Report to the NPOESS Integrated Program Office

on

Remote Sensing of Ocean Surface Wind Vectors by Passive Microwave Polarimetry - PSR Airborne Validation Study

Submitted by:

Dr. Albin J. Gasiewski
NOAA Environmental Technology Laboratory
Division of Ocean Remote Sensing - R/E/ET1
325 Broadway
Boulder, CO 80303
(303) 497-7275 (O)
(303) 497-3577 (F)
agasiwski@etl.noaa.gov

and

Dr. Jeffrey R. Piepmeier†
Microwave Instrument Technology Branch
NASA Goddard Space Flight Center
Mail Code 555
Greenbelt, MD 20771
(301) 286-5597 (O)
(301) 286-1750 (F)
jeff.piepmeier@gsfc.nasa.gov

Co-investigators:

Dr. Marian Klein (University of Colorado CIRES/NOAA)
Mr. Volker Bohm (University of Karlsruhe, Germany)

December 20, 1999

Covering contract work during FY 1998 and FY 1999

†Affiliation during this work: Georgia Institute of Technology,
School of Electrical and Computer Engineering, Atlanta, GA 30332-0250

Forward

This report summarizes an experimental study of the capability to measure ocean surface wind direction from space using a conical-scanning passive microwave polarimeter. The study was originally undertaken to provide corroboration of the evidence obtained using the DMSP SSM/I sensor that suggested that ocean surface winds impart deterministic and measurable brightness temperature anisotropies on the upwelling radiation field, and that these anisotropies can be used to remotely sense ocean surface wind direction. The study extends the SSM/I work by developing a geophysical model function (GMF) for additional frequencies and polarizations, demonstrating a maximum likelihood wind vector mapping algorithm, and illustrating the potential accuracy of satellite-based measurements of ocean surface winds through simulations using real downsampled aircraft data.

By focusing on high-resolution imaging of the ocean surface using a new airborne polarimetric imaging radiometer (the Polarimetric Scanning Radiometer, or PSR), the SSM/I measurements were corroborated in the mean over mesoscale sized regions of $\sim$30 km extent. The PSR is the first radiometer instrument to provide high-resolution ($\sim$1-2 km spot size) multiband (10.7, 18.7, 37, and 89 GHz) polarimetric (first three Stokes parameters: T_v, T_h, and T_U) imagery of the ocean surface. The results in this report are based on extensive aircraft observations made using the PSR over the Labrador Sea and other eastern U.S. offshore sites.

The PSR Labrador Sea flights provided data to develop an extended GMF for ocean surface thermal emission for T_v, T_h, and T_U at 10.7 and 37.0 GHz, and for T_v and T_h at 18.7 GHz. When the raw data were averaged over a large number of scans to reduce both instrument and geophysical noise, excellent agreement between the PSR and SSM/I 37 GHz azimuthal harmonic amplitudes was obtained for the range of wind speeds from near

calm to $\sim$16 m s^{-1} over large footprint areas and for an ensemble of ocean-atmosphere states. The GMF also shows excellent consistency between amplitudes and phases of the azimuthal harmonics for the 10.7, 18.7, and 37.0 GHz channels, with harmonic amplitudes monotonically increasing by $\sim$50% from 10.7 to 37.0 GHz.

On smaller spatial scales, the T_v and T_h data often showed local brightness variations of up to 10-15 K that are related to the presence of convection and/or unstable air-sea conditions. Atmospheric conditions suggest that these brightness perturbations are caused by surface wave spectrum variations. Such conditions did not influence the T_U imagery nearly as much, and in many instances virtually no impact was seen in T_U. The degree to which T_U rejects such convection-related perturbations indicates that the polarization signature will provide valuable information on surface wave, and hence wind, direction.

The PSR GMF was used to demonstrate the first aircraft-based passive microwave maps of ocean surface wind fields using a maximum likelihood (ML) estimator with adaptive channel weights. One-dimensional wind line plots were developed using full 360° azimuthal scans, and two-dimensional wind field maps over a region of $\sim$14$\times$100 km were developed using a two-look technique. Both one- and two-dimensional techniques show that ocean wind direction signatures over mesoscale-sized regions of $\sim$15 km or greater size are consistent enough for satellite mapping using a two-look polarimetric technique that includes T_U. Moreover, adaptive channel weighting allows use of all radiometric channels during conditions where the azimuthal harmonics have high signal-to-noise ratio (SNR), but emphasizes the lower frequency channels during conditions when the higher frequency channels become perturbed by either clouds or surface roughness.

Satellite simulations using the PSR data downsampled to spot sizes similar to that of the SSM/I, but including both tri-polarimetric channels (T_v, T_h, and T_U) and two-looks show retrieval accuracies of $\pm$8.4° and $\pm$0.8 m s^{-1} without directional ambiguities. These results strongly support the concept of satellite-based passive ocean surface wind vector mapping. When the third Stokes parameter is removed the simulated retrieval accuracy was reduced to $\pm$12.6° and $\pm$1.0 m s^{-1}, with a significant increase in ambiguity rate (11.1%).

When a tri-polarimetric system is used but with only one look, the accuracy is $\pm 14°$ and $\pm 1.6\ \mathrm{m\,s^{-1}}$, although the ambiguity rate is slightly lower (7.7%). It is noted that these simulation accuracies are consistent with error values predicted using the Cramer-Rao error bound for retrievals of multichannel sinusoidal signal phases in the presence of satellite radiometer measurement noise. The simulations also show that wind direction information significantly benefits the retrieval of wind speed by resolving small azimuthal brightness perturbations that would otherwise produce wind speed errors.

The hardware development effort under this contract also resulted in several innovations useful for spaceborne passive microwave wind direction sensing. The use of a 1 GS/sec three-level digital polarization correlator in the PSR showed for the first time that accurate calibrated polarimetric measurements can be made using only standard unpolarized ambient and cold calibration targets. Such calibration standards are readily available in a space environment. The correlator demonstration also required the development of new expression for the response of a digital correlator to the input correlation coefficient, correlator A/D converter offset, and A/D converter hysteresis. The utility of a polarized calibration standard for ground-based pre-flight calibration of the three first three Stokes parameters was demonstrated. Such a calibration standard should be useful for pre-launch calibration of polarimetric sensors such as WindSat and CMIS.

The airborne validation study also provided the first scanned polarimetric imaging radiometer suitable for post-launch satellite calibration and validation of a variety of future spaceborne passive microwave sensors. The capabilities of the PSR for airborne simulation are continuously being expanded through the development of new mission-specific scan-heads to provide airborne post-launch simulation of a variety of existing and future U.S. sensors, including CMIS, ATMS, AMSU, SSMIS, WindSat, TMI, RAMEX, and GEM.

In essence, this report is the thesis of Dr. Jeffrey Piepmeier[1], and is arranged as follows: Chapter 2 describes digital correlation polarimetry and the correlation hardware used in the PSR. Chapter 3 describes the PSR hardware and data processing and includes

[1] Piepmeier, J. R. *Remote Sensing of Ocean Wind Vectors by Passive Microwave Polarimetry.* Ph.D. thesis, Georgia Institute of Technology, 1999.

observed imagery obtained during the Labrador Sea experiment. Chapter 4 describes the PSR calibration. Chapter 5 describes the ocean surface GMF developed from the Labrador Sea measurements. Chapter 6 describes the ML wind vector retrieval algorithm, the adaptive channel weighting algorithm, and the ML Cramer-Rao error bound. Wind vector maps retrieved using PSR brightness imagery as shown. Chapter 7 describes the results of several simulated satellite retrievals.

Additional information on the PSR and updates on the analysis of PSR data from several related experiments can be found on the internet at the NOAA/ETL web page http://www1.etl.noaa.gov/radiom/psr.html. PSR data from the 1997 Hurricane Winds Experiment (HOWEX) and the 1998 Third Convection and Moisture Experiment (CAMEX-3) are currently being analyzed to extend the Labrador Sea GMF to higher wind speed regimes.

Acknowledgements: The development of the PSR motor drive and calibration system, aircraft hardware for integrating the PSR into the NASA P-3B aircraft, and processing of the PSR data was funded by contract # SMC185-96-N0109 from the NPOESS Integrated Program Office. A major portion of this study, including the original design and development of the PSR and the P-3 aircraft flight operations was funded by the U.S. Office of Naval Research under grant # N0014-98-F-0071 and ASSERT award # N00014-96-1007. The development of the PSR digital correlator modules was funded under NASA grant NAGW 4191.

Contents

Forward **ii**

List of Tables **ix**

List of Figures **x**

1 Introduction **1**

2 Digital Correlation Polarimetry **10**
2.1 Background 10
2.2 Digital Correlation Radiometry 16
2.2.1 Mean Statistics 16
2.2.2 Sensitivity 21
2.3 Systematic Errors 23
2.3.1 Sampler Offsets 23
2.3.2 Input Correlation Offset 29
2.3.3 Sampler Hysteresis and Timing Skew 32
2.4 Digital Correlation Hardware 35
2.5 Discussion 41

3 Polarimetric Scanning Radiometer **42**
3.1 Polarimetric Scanning Radiometer 42
3.1.1 Microwave and IF systems 46
3.1.2 Data System and Motion Control 53
3.2 Data Post Processing 57
3.3 Pitch and Roll Correction 61
3.4 Labrador Sea Experiment 73
3.4.1 PSR Microwave Imagery of the Ocean Surface 75
3.4.2 Detection of Sun Glint 88
3.5 Summary 93

4 Calibration **95**
4.1 Antenna 96
4.1.1 Rotation error 99
4.1.2 Cross-polarization coupling 101
4.1.3 Composition of $\overline{\overline{S}}_R$ and $\overline{\overline{S}}_X$ 105

4.1.4 Design Implications . . . 108
4.2 Digital Radiometer Calibration . . . 110
4.2.1 Total-Power Radiometer Calibration . . . 111
4.2.2 Correlator Calibration . . . 112
4.2.3 Verification of Polarimetric Calibration . . . 114
4.3 In-Flight Calibration . . . 118
4.3.1 Steady-State Model . . . 122
4.3.2 Transient Model . . . 126
4.3.3 Comparison of PSR brightness temperatures and the cold sky . . . 129

5 Geophysical Model Function 131
5.1 Background . . . 131
5.2 Aircraft Measurements . . . 134
5.3 Discussion . . . 139

6 Retrieval of Ocean Surface Wind Vectors 147
6.1 Introduction . . . 147
6.2 ML Estimation of Wind Vectors . . . 148
6.2.1 Wind direction retrieval . . . 149
6.2.2 Wind speed and atmospheric transmissivity . . . 151
6.2.3 Iterative Solution . . . 152
6.3 Modeling Error and Adaptive Channel Weighting . . . 155
6.4 Wind Vector Measurements . . . 160
6.4.1 Full-Scan Retrievals . . . 162
6.4.2 Two-Look Retrievals . . . 166
6.5 Discussion . . . 172

7 Simulated Satellite Retrievals 174
7.1 Design Considerations . . . 174
7.2 Simulations . . . 176

8 Conclusions 189
8.1 Summary of Thesis . . . 190
8.2 Suggestions for Future Research . . . 193

A Correlation Coefficient Inversion 195

B Digital Radiometer Sensitivity 197
B.1 Cross-correlator Sensitivity . . . 197
B.2 Total-power Sensitivity . . . 199

C Threshold Offset Effects 202

D Simulated Satellite Retrievals **208**

Bibliography **221**

List of Tables

2.1 Sensitivities of the PSR Digital Correlation Polarimeters. 41

3.1 PSR Radiometer Specifications. 48
3.2 PSR motion system hardware trigger states. 60
3.3 PSR Level 2.3 data types. 62
3.4 Elevational brightness sensitivities. 63

4.1 Correlator hardware constants and residual $\widehat{T}_U$ offsets. 114
4.2 Thermal properties of urethane foam. 123
4.3 Values of x_0 and γ for three PSR radiometer bands. 125
4.4 Comparisons of PSR brightness temperatures and modeled cold sky temperatures. 130

5.1 PSR wind direction harmonic observations during the OWI/Labrador Sea experiment 136
5.2 Quadratic fit coefficients for the wind speed dependence of the harmonic amplitudes as determined from PSR OWI Labrador Sea flights. 141

6.1 PSR Labrador Sea experiment Observations on March 7, 1997. 160
6.2 Wind direction statistics for the transect on March 7, 1997 across the polar low. 164

7.1 Hypothesized effects of polarization selection and number of looks on mean surface wind vector retrieval ambiguity and RMS error. 175
7.2 SSM/I and WindSat Nyquist spot size and the equivalent PSR hex-cross aperture size (for a 9 km $\times$ 15 km spot) at 10.7, 18.7, and 37.0 GHz. 176
7.3 Four data sets used to study the three satellite design cases. 177
7.4 Observation parameters used to study the three satellite design cases. 178
7.5 Retrieved direction distribution and ambiguity statistics of the four data sets. 183
7.6 Retrieved wind vector statistics for the four data sets and 3 design cases. . . 185

List of Figures

1.1 Passive microwave azimuthal wind-direction harmonics. 6
1.2 Passive microwave satellite sensor in two-look conically-scanning configuration. 8

2.1 Block diagram of a typical additive polarimeter. 11
2.2 Block diagram of a direct correlating polarimeter. 12
2.3 Block diagram of a typical digital polarimetric radiometer. 15
2.4 Ideal transfer function of three-level A/D converter. 17
2.5 The digital variance as a function of input RMS voltage. 18
2.6 The digital covariance versus the input correlation coefficient 20
2.7 Transfer function of three-level A/D converter with threshold offset v_δ. . . . 24
2.8 Noise model for dual channel, single LO, superheterodyne receiver. 30
2.9 Transfer function of three-level A/D converter with hysteresis magnitude v_{hys}. 33
2.10 The reduction in the digital correlator output as a function of hysteresis amplitude. 34
2.11 Digital correlator module. 36
2.12 Clock control and distribution module. 37
2.13 TTL counter/interface boards and ribbon cable bus. 39

3.1 The PSR situated in the support stand. 44
3.2 PSR scanhead installed in the NASA P-3. 45
3.3 The PSR and bomb-bay faring installed on the NASA P-3. 47
3.4 The PSR antennas and radiometers. 49
3.5 The IF plate. 51
3.6 IF subband division hardware. 52
3.7 The scanhead 486 embedded computer system. 53
3.8 Block diagram of the scanhead data system. 55
3.9 Example of brightness temperature sensitivity to incidence angle for X-band. 64
3.10 Same as Figure 3.9 except for K-band. 65
3.11 Same as Figure 3.9 except for Ka-band. 66
3.12 Sample of P-3 pitch and roll data from 2014 UTC on March 4, 1997. 67
3.13 The five rotational operations used to compute the PSR pointing and polarization vectors in the world coordinate frame. 69
3.14 Third Stokes parameter data illustrating the need for pitch and roll correction. 71
3.15 Uncorrected and corrected brightness temperatures versus elevation angle. . 72

3.16 PSR averaged azimuthal scans from 1632-1642 UTC on March 4, 1997. . . 76
3.17 PSR 10.7 GHz polarimetric microwave imagery of the ocean surface. . . . 78
3.18 Same as Figure 3.17 except the frequency is 18.7 GHz. 79
3.19 Same as Figure 3.17 except the frequency is 37.0 GHz. 80
3.20 Geolocated PSR 10.7 GHz polarimetric microwave imagery of the ocean surface. 82
3.21 Same as Figure 3.20 except the frequency is 18.7 GHz. 83
3.22 Same as Figure 3.20 except the frequency is 37.0 GHz. 84
3.23 Geolocated PSR 10.7 GHz residual (see lower images in Figure 3.17) microwave imagery of the ocean surface. 85
3.24 Same as Figure 3.23 except the frequency is 18.7 GHz. 86
3.25 Same as Figure 3.23 except the frequency is 37.0 GHz. 87
3.26 Sun glint in PSR X-band T_h raster image. 89
3.27 Sun glint in PSR X- and K-band average azimuthal scans. 90
3.28 Modeled brightness temperature perturbation due to sun glint. 92

4.1 Cascaded four port networks modeling both rotation and cross-polarization effects. 97
4.2 Plot of 37.0 GHz polarized target measurements. 117
4.3 Three-dimensional CAD model of the calibration targets and the scanhead. The vertical support structure was not rendered for clarity. 119
4.4 The PSR calibration loads and elevation motor viewed from below the ring bearing with the scanhead not installed. 120
4.5 PSR calibration targets: (a) cross-section of PSR calibration load, (b) steady-state temperature profile for the steady-state model, (c) finite-difference grid for the transient thermal model. 121
4.6 Computed calibration load emission temperatures for the Labrador Sea flight on March 7. 128

5.1 Polar coordinate system for the GMF. The azimuth coordinate ϕ is aligned with the compass rose. 133
5.2 Hex-cross flight pattern. 135
5.3 Map of PSR hex-cross measurement locations. 137
5.4 PSR azimuthal harmonics from March 9, 1997. 138
5.5 Microwave brightness temperature harmonic amplitudes versus wind speed. 140
5.6 Third Stokes parameter harmonic amplitudes versus wind speed. 144

6.1 Block diagram of the iterative wind speed and direction ML estimation algorithm. 148
6.2 Example of wind direction objective function. 154
6.3 Block diagram of the adaptive channel weights recursion algorithm. 156
6.4 Minimum bound on the retrieved wind direction standard deviation. 159

6.5 The NOAA-12 AVHRR infrared (channel 4, 10.9 μm) imagery at 1128 UTC on March 7, 1997. 161
6.6 Full-scan wind vector retrieval. 163
6.7 Adapted weighting of T_U relative to T_v and T_h. 165
6.8 High-resolution 2-dimensional wind map and brightness imagery for region east of wind direction shift. 167
6.9 Same as Figure 6.8 for the region west of the wind direction shift. 168
6.10 Same as Figure 6.8 for the region containing the wind direction shift. 170

7.1 Results of the four-fold search for ML solutions before ambiguity removal. 180
7.2 Four-fold search results after ambiguity selection. 182
7.3 Scatter plots of final retrieved wind vectors for data set 1. 185
7.4 Sensitivity of retrieved wind direction to ΔT_{RMS} 187

D.1 Results of the four-fold search before ambiguity removal - data set 1. 209
D.2 Four-fold search results after ambiguity selection - data set 1. 210
D.3 Scatter plots of final retrieved wind vectors for data set 1. 211
D.4 Same as Figure D.1 except for data set 2. 212
D.5 Same as Figure D.2 except for data set 2. 213
D.6 Same as Figure D.3 except for data set 2. 214
D.7 Same as Figure D.1 except for data set 3. 215
D.8 Same as Figure D.2 except for data set 3. 216
D.9 Same as Figure D.3 except for data set 3. 217
D.10 Same as Figure D.1 except for data set 4. 218
D.11 Same as Figure D.2 except for data set 4. 219
D.12 Same as Figure D.3 except for data set 4. 220

CHAPTER 1

Introduction

Passive microwave remote sensing is a valuable tool for providing global, all weather, day and night observations of the Earth's oceans. Such observations are valuable to the scientific, defense, and industrial communities. Ocean observations are used to initialize and/or verify ocean circulation, air-sea interaction, and atmospheric models. Improved performance of such models facilitates operational weather forecasting and modeling necessary to predict global climate change. The United States Navy relies heavily upon microwave satellite environmental products in carrying out tactical operations. Global observations of ocean winds and waves can aid the international shipping industry in operations planning, for example. Hence, there is a need for a system to provide timely, accurate, high-resolution ocean surface observations with global coverage.

Remote sensing of the boundary-layer wind speed using satellite based microwave radiometers has been an established technique for nearly two decades (e.g., [44, 28]). The technique is based upon the relationship between ocean surface emissivity and near-surface wind speed. Horizontal flow applies stress to the surface, which becomes increasingly disturbed and roughened with higher wind speeds. The surface roughening and the presence of foam (caused by wave breaking) increases the surface's microwave emissivity (e.g., [56, 15, 65]), resulting in a measurable increase in brightness temperature of $\sim$1 K per $\mathrm{m\,s^{-1}}$. The radiometric technique is most viable for wavelengths of $\sim$1-3 cm because the transmissivity over this range is reasonably high through most clouds and water vapor, and the satellite antenna sizes required to achieve mesoscale footprint sizes ($\sim$20-30 km) are

moderate (∼1-2 m). The Special Sensor Microwave/Imager (SSM/I), flown on the Defense Meteorological Satellite Program (DMSP) Block 5D-2 satellites is used operationally to globally map scalar wind speed.

Spaceborne scatterometers are the only sensors currently capable of providing global observation of the ocean surface wind vector, that is, both speed *and* direction. Examples include the NASA scatterometer (NSCAT[1]) (launched in August 1996) [45], the European Space Agency's ERS-1 and -2 scatterometers (launched in 1991 and 1995, respectively) [3], and the SeaWinds scatterometer (planned launch in mid-2000) [68]. While such sensors provide operational capability, they incorporate microwave transmitters, which require significant electrical power, and utilize complex signal processing hardware that must fly onboard the spacecraft. In the retrieval of wind vectors from scatterometer data there also exists a problem, namely dual directional ambiguity of the solutions (e.g., [55]). The complex hardware requirements and retrieval ambiguity problems are undesirable characteristics in a low-cost operational wind vector sensor.

A potential alternative to scatterometry is passive microwave polarimetry. Development of passive microwave polarimetry for measurement of boundary layer wind vectors has only recently received attention (e.g., [66, 71, 50]). The latency in development of the polarimetric wind direction technique stems from the relatively small azimuthal brightness signatures produced by a wind-driven ocean surface (typically ∼0.5-3 K in amplitude), as well as the somewhat increased complexity of a microwave polarimeter *vis-à-vis* a conventional radiometer[2]. A distinction is drawn between a polarimeter and a radiometer by considering a complete description of the radiation field as defined by the modified Stokes

[1]NSCAT provided 10 months of data before the failure of the ADEOS spacecraft terminated the data stream in June 1997 [29].

[2]Also of note is that the investigators who made the early efforts at modeling the sea-surface emissivity purposefully averaged over the azimuthal anisotropy of the wind-driven ocean surface to make the computational problem tractable.

vector [60]:

$$\overline{T}_B = \begin{bmatrix} T_v \\ T_h \\ T_U \\ T_V \end{bmatrix} = \frac{\lambda^2}{\eta k} \begin{bmatrix} \langle |E_v|^2 \rangle \\ \langle |E_h|^2 \rangle \\ 2\mathrm{Re}\langle E^v E_h^* \rangle \\ 2\mathrm{Im}\langle E^v E_h^* \rangle \end{bmatrix} \tag{1.1}$$

where E_v and E_h are the complex vertical and horizontal field amplitudes for a narrow band of frequencies about f, η is the wave impedance, λ the wavelength, and $k = 1.38 \cdot 10^{-23}$ J K^{-1} is Boltzmann's constant. The units of $\overline{T}_B$ are all Kelvin. While a conventional radiometer measures the first two elements of the Stokes vector (T_v and T_h), a polarimeter measures at least one of the third or fourth through an appropriate cross-correlation technique.

The first two modified Stokes parameters T_v and T_h can be measured using standard linearly-polarized total-power radiometers [61]. Detection of the third and fourth Stokes parameters, however, requires two additional measurements to effectively perform the correlations in (1.1). Polarimeters fall into one of two basic categories: additive polarimeters and direct correlating polarimeters. The additive polarimeter uses measurements of the brightness temperature of at least two additional polarization states, e.g., 45° linearly polarized ($T_{45°}$) and either left- or right-hand circularly polarized (T_l or T_r). The third and fourth Stokes parameters can be found using the sums and differences of the four measured brightness temperatures. The direct correlating polarimeter, on the other hand, estimates T_U and T_V by cross-correlating the instantaneous voltage signals of the vertical and horizontal channels. The actual correlation can be performed by either analog or digital multiplying circuitry.

Several mechanisms can contribute to polarimeter calibration errors. In the additive polarimeter, receiver and signal combining network imbalances can cause mixing of all four Stokes parameters, the amount of which must be known. One method for comprehensive calibration of the first three modified Stokes parameters uses a rotating polarized calibration standard [20]. Use of the polarized standard in space, however, requires addi-

tional hardware beyond the conventional ambient and cold blackbody standards that are commonly used. Thus, it is desirable to design systems requiring minimal amounts of calibration hardware. While an analog correlator can be used to determine T_U or T_V, its response generally will require the in-situ identification of gains and offsets of multiplication and detection circuitry. Such effects can be minimized by proper tuning and balancing, but elimination of long term drift in detection and video components can be prohibitively expensive.

To simplify the calibration problem digital correlation is presented in Chapter 2 as a solution for precise measurement of T_U or T_V. Here, horizontal and vertical IF signals are sampled at the Nyquist rate, the digital samples cross-correlated using fast multiplication circuitry, and the resulting products integrated via digital accumulation. Provided that the digitized signal contains no DC component and the A/D conversion is performed ideally, the correlation coefficient can be obtained without offset and leakage components. A further advantage (discussed in Chapter 4) of using a digital correlator with more than one bit (or two levels) of quantization is that in-situ calibration can be performed using only conventional unpolarized views of two targets.

The first measurement of the brightness temperature dependence on boundary layer wind direction was performed by Bespalova *et al.* [5][3]. Nadir aircraft observations revealed a 5 K increase in brightness temperature when the polarization vector was aligned in the along-wind direction versus the cross-wind direction. These observations confirmed the model predictions made by Kravstov *et al.* [39]. Later studies by Etkin *et al.* [16] and Irisov *et al.* [35] confirmed and more thoroughly investigated the nadir brightness temperature anisotropy of the ocean surface and its relationship to boundary layer winds.

In the late 1980's, satellite wind speed measurements made using the SSM/I at an off nadir incidence angle of 53.1° were observed by Wentz to have an error that was dependent upon the wind direction [66]. From the analysis, T_v and T_h at 19 and 37.0 GHz were shown to have ∼1-3 K directional variation. As illustrated in Figure 1.1(a-

[3]It is notable that Russian scientists made the initial theoretical and observational developments about 20 years ago.

b), T_v exhibits a first-order azimuthal harmonic variation (indicative of upwind-downwind surface asymmetry), while T_h exhibits a second-order harmonic variation (evidence of the along-wind and cross-wind surface anisotropy).

In addition to T_v and T_h, the third Stokes parameter T_U was observed using a nadir-viewing polarimeter aboard an aircraft by Dzura *et al.* [14] and was found to have significant dependence on wind direction. Subsequent wave-tank and aircraft measurements using fixed-beam radiometers confirmed the presence of the T_U signature at off-nadir viewing angles [21, 70]. While similar in amplitude to T_v and T_h, the third Stokes parameter is in phase-quadrature with respect to the wind direction, as seen in Figure 1.1(c). Recent observations of the fourth Stokes parameter have revealed its phase-quadrature nature as well [25]. Because of this characteristic, T_U (and possibly T_V) can provide key information necessary to remove ambiguities in the wind direction signatures of T_v and T_h. These polarization parameters have also been shown to be less affected by the presence of clouds and local convection than the first two parameters [22]. Finally, these parameters are effectively zero mean, and less subject to misinterpretation caused from fluctuating baseline values.

Although several investigators have measured the microwave wind-direction harmonics, the use of fixed-beam radiometers has precluded the acquisition of polarimetric *imagery* of the wind-driven ocean. An airborne conically-scanned polarimeter, the Polarimetric Scanning Radiometer (PSR), has been developed as part of this dissertation research to observe more fully the polarimetric emission of the ocean surface (see Chapter 3). The PSR was the first airborne conically-scanning polarimeter, and was first flown during the Labrador Sea experiment in March 1997 on the NASA Wallops Flight Facility's Orion P-3B research aircraft [48, 24, 19]. For the Labrador Sea experiment, the PSR was configured with four radiometers at 10.7, 18.7, 37.0, and 89.0 GHz. A unique 1 GS/s digital correlator [49] provided measurements of the third Stokes parameter T_U at 10.7 and 37.0 GHz.

The PSR imagery reveals the systematic wind-direction signature as well as a variable component which arises from cloud (and possibly surface roughness) inhomogeneities.

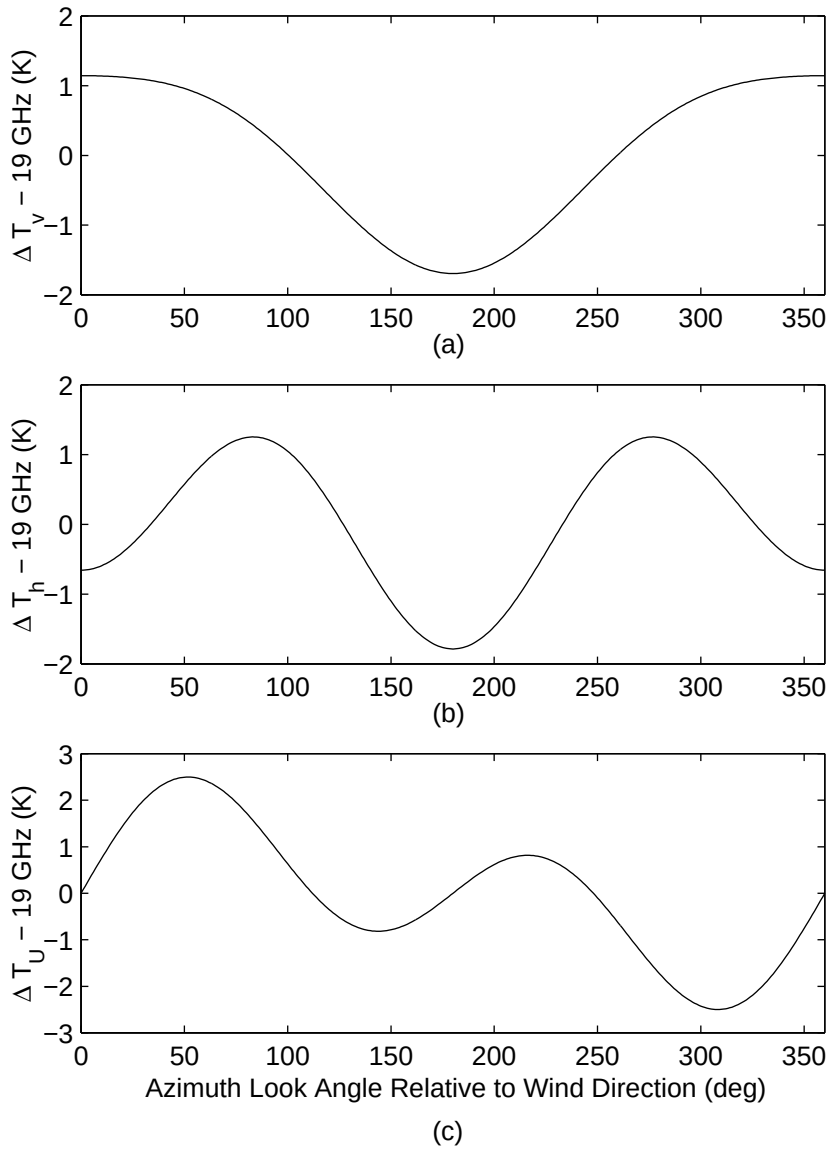

Figure 1.1: Passive microwave azimuthal wind-direction harmonics for 12 m s^{-1} winds: (a-b) vertical and horizontal polarization at 19 GHz and 53.1° incidence [66], (c) third Stokes parameter at 19 GHz and 50° incidence [70].

Using the imagery, wind-direction harmonics were measured over a wide range of wind speeds and a geophysical model function (GMF) for azimuthal brightness was developed (see Chapter 5). Over wide regions ($\sim$30 km in size) the Labrador Sea GMF model is shown to compare favorably with the model function found by Wentz using SSM/I data [66]. Comparison of the PSR GMF with a recent SSM/I investigation by Bates *et al.* [4] reveal discrepancies (particularly in the T_h harmonic amplitudes), which suggest that additional processes beyond the surface wind speed have influence upon the brightness temperature harmonic amplitudes.

Passive microwave wind vector retrieval algorithms appearing in the literature include a sum-of-squares (SOS) minimization algorithm [66] and a neural network based estimator [18]. The SOS algorithm is sub-optimal because the relative noises of the various input channels are not used to weight the channels appropriately. The neural network based estimator essentially approximates the inversion of the GMF by learning from training data; however, an estimate of the retrieval error variance is not directly calculable from the neural network. Therefore, a multi-look retrieval method based upon the maximum likelihood (ML) principle [62] was developed (see Chapter 6) to simultaneously retrieve both the speed and direction components of the wind. The standard ML method was modified to allow for the adaptation of channel weights to compensate for GMF modeling error. Another favorable attribute of the ML wind vector estimator is the ability to compute a minimum bound on the error standard deviation (i.e., the Cramer-Rao bound). The utility of the multi-look retrieval technique in both one-dimensional and two-dimensional wind field mapping is demonstrated using conically-scanned polarimetric microwave brightness imagery obtained during the Labrador Sea experiment. The conically-scanning configuration of the PSR, as opposed to a fixed-beam radiometer, makes possible the measurement of a two-dimensional wind vector field from the aircraft.

The configuration of a passive microwave wind vector satellite was initially proposed by Wentz [66] to use two looks at each surface cell because at the time the utility of the third Stokes parameter was as of yet not clear. With the known properties of T_U (and

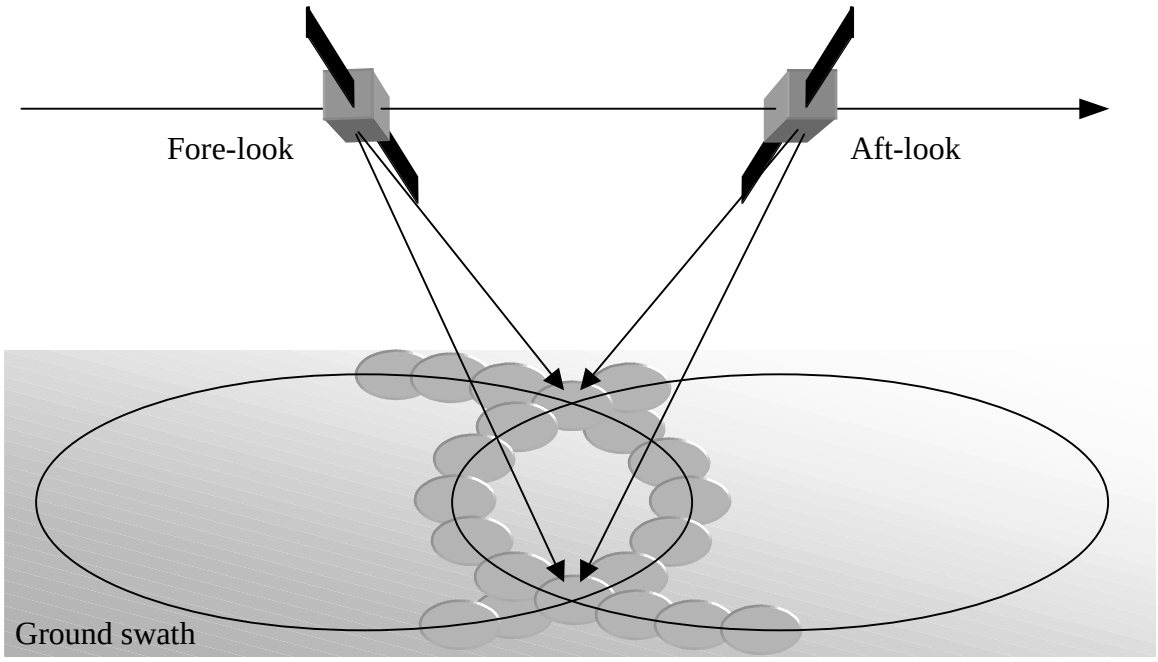

Figure 1.2: Passive microwave satellite sensor in two-look conically-scanning configuration.

T_V), however, a spaceborne polarimeter system might only need one look at a surface cell to measure the wind vector. The two-look surface coverage of a conically-scanning satellite sensor is illustrated in Figure 1.2. Satellite sensors currently planned include WindSat [17] and the Conical Microwave Imager/Sounder (CMIS) of the National Polar-orbiting Operation Environmental Satellite System (NPOESS). WindSat configuration is designed (because of calibration load placement) for two-look mapping along one-half of its swath and one-look mapping along the other half. The scanning configuration and polarization selection is an open question. Simulations in Chapter 7 help to quantitatively measure three cases: a two-look polarimeter, a two-look radiometer, and a one-look polarimeter. The measures used include the RMS retrieval accuracy and the directional ambiguity rate. The sensitivity of the two-look polarimeter is also compared to the retrieval Cramer-Rao bound for a range of radiometric sensitivities and three frequency band combinations.

The thesis is arranged as follows: Chapter 2 describes digital correlation polarime-

try and the correlation hardware used in the PSR. Chapter 3 describes the PSR hardware and data processing, as well as some observed imagery obtained during the Labrador Sea experiment. Chapter 4 describes the PSR calibration. Chapter 5 describes the ocean surface GMF developed from Labrador Sea measurements. Chapter 6 describes the ML wind vector retrieval algorithm and its associated Cramer-Rao error bound. Wind vector maps are retrieved from brightness imagery obtained using the PSR. Chapter 7 describes the results of several simulated satellite retrievals.

This thesis describes a system for high-resolution wind vector field mapping using passive microwave polarimetry. Contributions to passive microwave polarimetry include development and successful operation of a high-speed digital correlator for third Stokes parameter detection, as well as the precise calibration of the digital correlation polarimeter using views of two unpolarized targets. Contributions to passive polarimetric microwave remote sensing of the ocean include measurements of wind direction harmonics for T_v, T_h, and T_U, and the ML wind vector retrieval algorithm.

CHAPTER 2

Digital Correlation Polarimetry

The fundamentals of digital polarimetric radiometry are described in this chapter. The digital polarimeter uses a digital correlator to perform the correlations required to measure the third and/or fourth Stokes parameter(s). The relationships between the signal input statistics and the correlator outputs are derived and used to compute the associated radiometric sensitivities. Systematic errors due to system nonidealities and their mitigation through design are also discussed. Using these developments, the first wideband digital correlating polarimeter was built and demonstrated. The performance of the polarimeter is described here.

2.1 Background

The modified Stokes vector can be used to fully describe the second-order statistics of the quasi-monochromatic radiation field at a point in space. The elements of the modified Stokes vector, in units of brightness temperature (Kelvin), are directly related to the following ensemble averages of the incident transverse electric field components [60]:

$$\overline{T}_B = \begin{bmatrix} T_v \\ T_h \\ T_U \\ T_V \end{bmatrix} = \frac{\lambda^2}{\eta k} \begin{bmatrix} \langle |E_v|^2 \rangle \\ \langle |E_h|^2 \rangle \\ 2\mathrm{Re}\langle E_v E_h^* \rangle \\ 2\mathrm{Im}\langle E_v E_h^* \rangle \end{bmatrix} \tag{2.1}$$

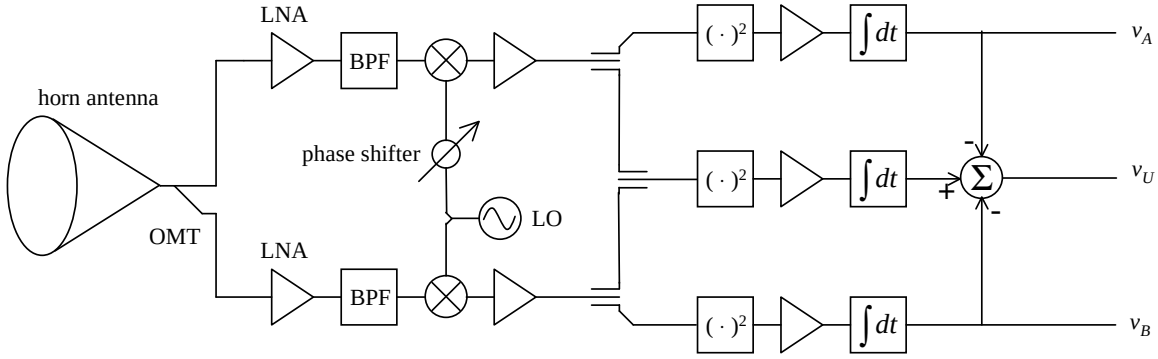

Figure 2.1: Block diagram of a typical additive polarimeter.

where λ is the wavelength, η is the impedance of the medium, and k is Boltzmann's constant. Here, E_α is the phasor amplitude for polarization α ($= v$ or h) per unit solid angle and bandwidth. The first two parameters, T_v and T_h, are the intensity in the vertical and horizontal polarizations and their sum is the total radiation intensity. The remaining two parameters contain information about the polarization characteristics of the radiation field. Specifically, T_U indicates the degree and sense of linear polarization and T_V of circular polarization. Partially polarized thermal radiation is specified by nonzero T_U or T_V.

The parameters T_v and T_h can be measured using standard linearly-polarized total-power radiometers [61]. Detection of the third and fourth Stokes parameters, however, requires two additional measurements to effectively perform the correlations in (2.1). The various types of polarimetric radiometers fall into two basic categories: additive polarimeters (AP) and direct correlating polarimeters (DCP). The additive polarimeter uses measurements of the brightness temperature of at least two additional polarization states e.g., 45° linearly polarized (T_{45°) and either left- or right-hand circularly polarized (T_l or T_r). From the four measured brightness temperatures and using the Stokes parameter rotational transformation [8], the third and fourth Stokes parameters can be found. For example:

$$T_U = 2T_{45^\circ} - T_v - T_h \tag{2.2}$$

$$T_V = 2T_r - T_v - T_h \tag{2.3}$$

The AP architecture was the first type to be implemented and used on an aircraft

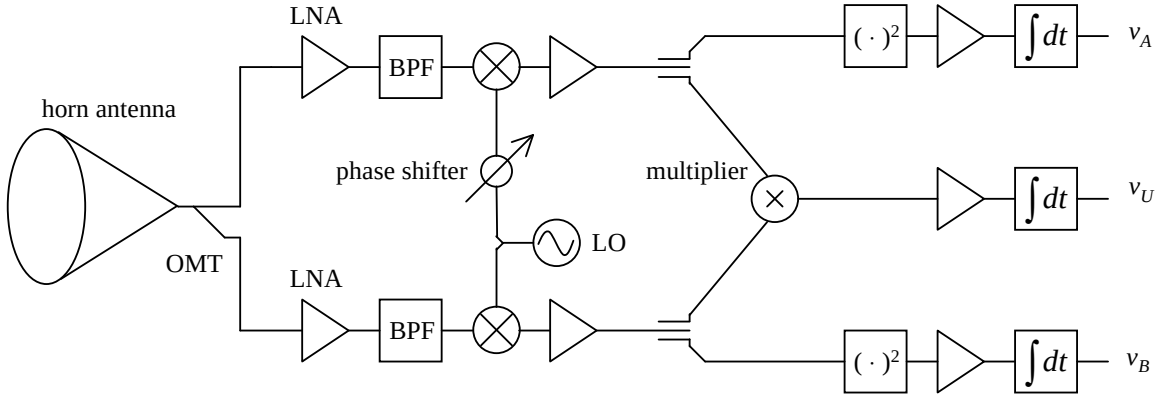

Figure 2.2: Block diagram of a direct correlating polarimeter.

to observe the ocean surface emission at nadir [14]. Subsequent measurements at off nadir angles were made by Kunkee using a W-band AP [42] and Yueh *et al.* using a K-band AP [70]. The block diagram of such a system is seen in Figure 2.1. A signal combiner (or magic-T) is used to synthesize the 45° polarization using the vertically and horizontally polarized signals. The subtractions in (2.2) are carried out using post-detection difference amplifiers.

The DCP estimates T_U and T_V by cross-correlating the instantaneous voltage signals of the vertical and horizontal channels (see Figure 2.2). The actual correlation can be performed by either analog or digital multiplying circuitry. A dual-channel superheterodyne receiver with a coherent local oscillator (LO) may be required to downconvert the RF band of interest to accommodate the bandwidth and/or operating frequency of the analog multiplier or the digital correlator A/D converters. If the time-varying voltages $v_v(t)$ and $v_h(t)$ are assumed to be stationary and ergodic [54], then the covariance estimate $\widehat{R}_{vh}$ is:

$$\widehat{R}_{vh} = \frac{1}{\tau}\int_0^{\tau} v_v(t)v_h(t)dt \tag{2.4}$$

where τ is the integration time. Since the IF voltages are related to the incident field quantities by the receiving antenna's effective area and the receiver's signal transfer char-

acteristics, measuring R_{vh} is equivalent to measuring T_U:

$$\widehat{T}_U = 2\widehat{\rho}\sqrt{\widehat{T}_{v,sys}\widehat{T}_{h,sys}}, \tag{2.5}$$

where $\widehat{\rho} = \frac{\widehat{R}_{vh}}{\widehat{\sigma}_v\widehat{\sigma}_h}$ is the correlation coefficient and $\widehat{T}_{\alpha,sys}$ are the system temperatures of the total-power radiometers for polarizations $\alpha = v$ and h. If the IF signals are downconverted in-phase, T_U is estimated; however, if the receiver is single-sideband and the signals are downconverted in phase-quadrature, then T_V is estimated.

Several mechanisms can contribute to calibration errors in either (2.2-2.3) or (2.4-2.5). Imbalances in signal combiners can cause Stokes parameter mixing in the AP. Differences between the detectors and the video amplifiers can also cause unwanted mixing between the individual Stokes parameters. While error produced by the combiners and summing amplifiers can be avoided by using an analog DCP, detection hardware is still required, and other errors can be caused by the signal splitters and the analog multiplier itself. The errors (to which the AP and analog DCP are both susceptible) in effect cause unwanted gains and offsets in the detector outputs of the polarimeter. The detector output voltages can be expressed as follows:

$$\begin{bmatrix} v_v \\ v_h \\ v_U \\ v_V \end{bmatrix} = \begin{bmatrix} g_{vv} & g_{vh} & g_{vU} & g_{vV} \\ g_{hv} & g_{hh} & g_{hU} & g_{hV} \\ g_{Uv} & g_{Uh} & g_{UU} & g_{UV} \\ g_{Vv} & g_{Vh} & g_{VU} & g_{VV} \end{bmatrix} \begin{bmatrix} T_v \\ T_h \\ T_U \\ T_V \end{bmatrix} + \begin{bmatrix} o_v \\ o_h \\ o_U \\ o_V \end{bmatrix} \tag{2.6}$$

Proper calibration of the AP or analog DCP requires the determination of the gain and offset terms by an appropriate technique.

The AP described in [70] was calibrated by carefully measuring *a-priori* the various amplitude imbalances of the combining and post-detection networks. The system was also temperature stabilized to minimize the effects of drift. While this technique can mitigate the effects of system imbalances on the gain and offset terms, elimination of long-term drift in operational systems, however, can be prohibitively expensive. An *in-situ* calibration method can address this problem.

One method for comprehensive calibration of the first three modified Stokes parameters uses a rotating polarized calibration standard [20]. The polarized standard presents to the receiver a strongly polarized but precisely determined radiation field and allows complete determination of the gains and offsets for the first three Stokes parameters. Calibration of the fourth Stokes parameter channel can be accomplished by insertion of an appropriate 90° shift in RF path using, e.g., a quarter wave plate. Use of the polarized standard in space, however, requires additional hardware beyond the conventional ambient and cold blackbody standards that are commonly used.

In the implementation of (2.1), it is desirable to design a system that requires a minimal amount of calibration hardware. A solution to precise measurement of T_U or T_V can be found through digital correlation. Here the RF (or IF) signals are sampled at the Nyquist rate, the digital samples cross-correlated using fast multiplication circuitry, and the correlation integral (2.4) performed via digital accumulation. Provided that the digitized signal contains no DC component and the A/D conversion is performed ideally, the correlation coefficient $\hat{\rho}$ can be obtained without offset of leakage. Because the signals are digitized, the gain and offset errors created by signal splitter and detection hardware imbalances are eliminated. The system equation, therefore, is nearly in the ideal form:

$$\begin{bmatrix} v_v \\ v_h \\ v_U \\ v_V \end{bmatrix} = \begin{bmatrix} g_{vv} & 0 & 0 & 0 \\ 0 & g_{hh} & 0 & 0 \\ 0 & 0 & g_{UU} & 0 \\ 0 & 0 & 0 & g_{VV} \end{bmatrix} \begin{bmatrix} T_v \\ T_h \\ T_U \\ T_V \end{bmatrix} + \begin{bmatrix} o_v \\ o_h \\ 0 \\ 0 \end{bmatrix} \tag{2.7}$$

where v_v, v_h, v_U and v_V are the linearized outputs of the digital correlation hardware. A further advantage of using a digital correlator with more than one bit (or two levels) of discretization is that in-situ calibration can be performed using only conventional ambient and cold unpolarized views, for example, an ambient blackbody target and cold space.

Digital correlation radiometry was first suggested by Weinreb [64] for use in autocorrelation spectrometers for radio astronomy. As shown by Weinreb in autocorrelation spectroscopy of Gaussian signals, only a single bit of quantization (i.e., two-level A/D

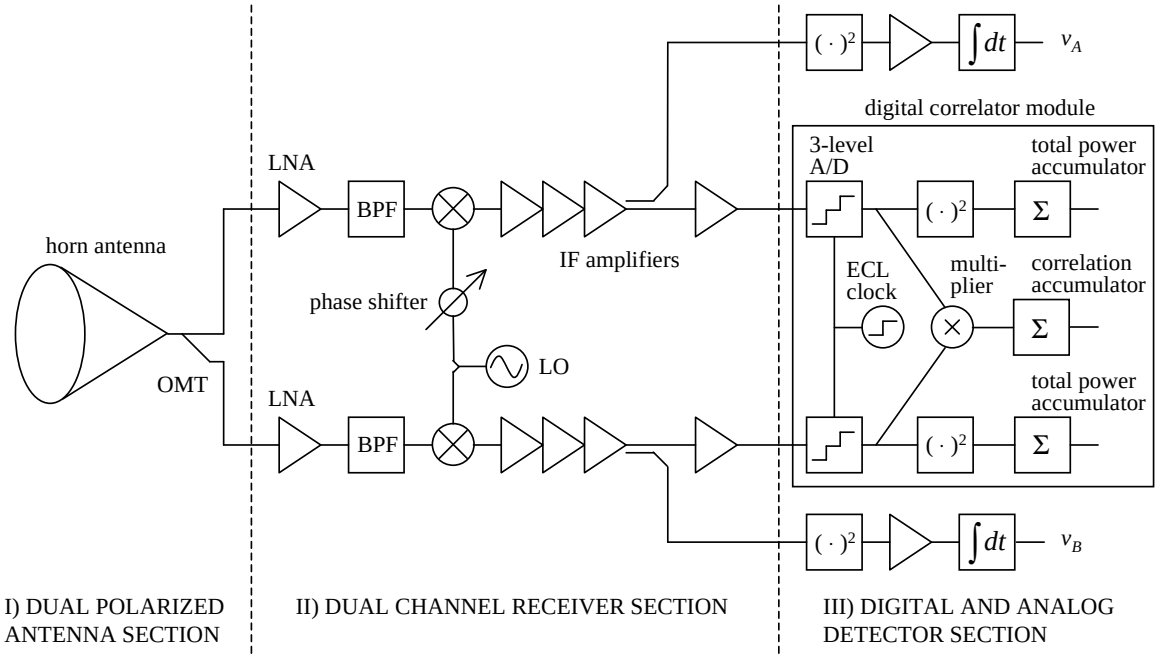

Figure 2.3: Block diagram of a typical digital polarimetric radiometer. This direct correlating polarimeter utilizes a dual polarized antenna, dual channel superheterodyne receiver, and a 3-level digital correlator. The IF signals are also coupled to conventional square law detectors and video amplifiers.

conversion) is required to achieve ∼64% of the detection sensitivity of a perfect analog correlator system. As fast digital logic became widely available, the single-bit systems were replaced with three-level (reduced 2-bit or 1.6-bit) systems. The two-bit correlator can obtain up to 88% of the detection sensitivity of the analog system [11]. The increasing availability of discrete high-speed digital logic has facilitated development of spectrometers operating over wide bandwidths, and both single-bit and two-bit correlators have now been implemented at clock-rates as high as 2 GS/s (e.g., [47, 7, 31, 59, 46]).

In this chapter we present the first digital correlator designed and constructed for use in microwave polarimetry. The block diagram of the digital polarimeter is shown in Figure 2.3. The major components are a dual-polarized antenna (I), a superheterodyne SSB phase coherent dual channel receiver (II), and a three-level digital correlator (III). We begin in Section 2.2 with a description of digital correlation radiometry and discuss

in Section 2.3 an investigation of systematic errors along with design implications. The digital correlator hardware is described in Section 2.4. (The operation and calibration of the system is described in Chapters 3 and 4.)

2.2 Digital Correlation Radiometry

The digital direct-correlating polarimeter has as its main distinguishing component a zero-lag digital cross-correlator. The digital correlator is made up of three main sections: A/D converters, a digital multiplier, and accumulators. To understand how the accumulated signals are used to determine T_U, it is instructive to examine the relationship between the input signal statistics and the accumulator outputs. These relationships also provide a measure of the digital correlator sensitivity.

2.2.1 Mean Statistics

The input signals to a correlator, $v_a(t)$ and $v_b(t)$, are modeled as jointly-Gaussian stationary random processes with root mean square (RMS) voltages σ_{v_a} and σ_{v_b} and correlation coefficient $\rho = \frac{R_{v_a v_b}}{\sigma_{v_a}\sigma_{v_b}}$. If the processes are sampled at or below their Nyquist rate with period T, then each sequence consists of independently and identically distributed samples with the following joint Gaussian probability density function (pdf):

$$f(v_a, v_b; \rho) = \frac{1}{2\pi\sigma_{v_a}\sigma_{v_b}\sqrt{1-\rho^2}} \exp\left[-\frac{\left(\frac{v_a}{\sigma_{v_a}}\right)^2 - 2\rho\frac{v_a v_b}{\sigma_{v_a}\sigma_{v_b}} + \left(\frac{v_b}{\sigma_{v_b}}\right)^2}{2\left(1-\rho^2\right)}\right]. \tag{2.8}$$

The three-level quantization performed by the A/D converter on the input signals is modeled by the transfer function:

$$h(v) = \begin{cases} 1 & \text{if } v > v_{th_\alpha}, \\ -1 & \text{if } v < -v_{th_\alpha}, \\ 0 & \text{otherwise.} \end{cases} \tag{2.9}$$

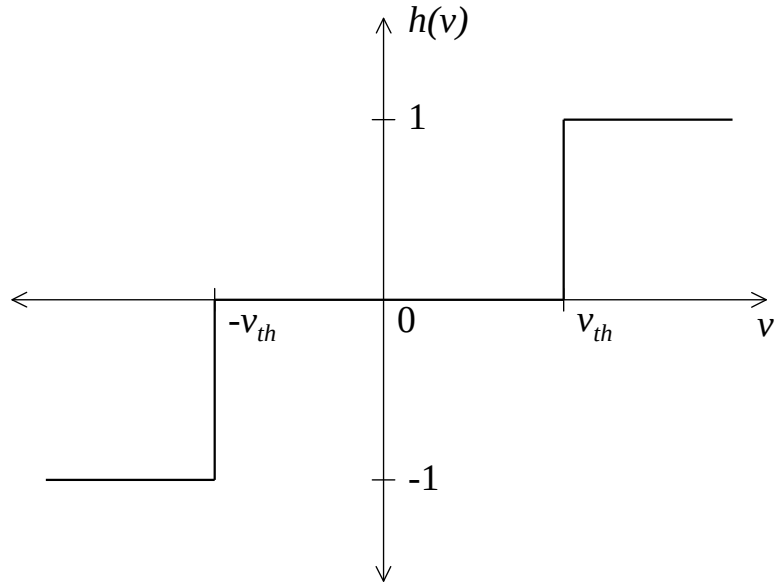

Figure 2.4: Ideal transfer function of three-level A/D converter.

where the quantities $\pm v_{th_\alpha}$ are the threshold levels of the quantization process (also see Figure 2.4). The subscript α denotes either channel a or b. For typical CMOS or ECL logic, $v_{th_\alpha} \approx 0.05$ to 0.50 volts; therefore, the microwave signal power is -12 to $+8$ dBm in a 50Ω system. The outputs from the quantizers form a new pair of joint-random processes, denoted $h(v_a(nT))$ and $h(v_b(nT))$, where sample n is taken at time nT. The second-order statistics of these sampled and quantized joint processes are the digital variances and covariance and are nonlinearly related to the first three Stokes parameters.

For a measurement of N samples, the estimated digital variances and covariance, denoted $\hat{s}_\alpha^2$ and $\hat{r}_{ab}$, are:

$$\hat{s}_\alpha^2 = \frac{1}{N}\sum_{n=1}^{N} h(v_\alpha(nT))^2 \tag{2.10}$$

$$\hat{r}_{ab} = \frac{1}{N}\sum_{n=1}^{N} h(v_a(nT))h(v_b(nT)) \tag{2.11}$$

These three statistical parameters are measured by a simple accumulation. The statistics

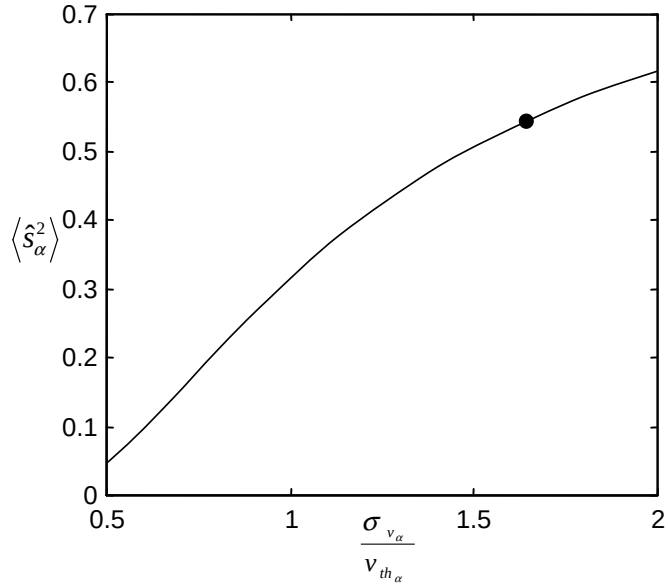

Figure 2.5: The digital variance as a function of input RMS voltage at a fixed threshold level. The optimal threshold level $\sigma_\alpha = 0.61$ occurs at $\sigma_{v_\alpha}/v_{th_\alpha} = 1.64$.

of $\hat{s}_a^2$, $\hat{s}_b^2$, and $\hat{r}_{ab}$ and their relationship to T_a, T_b, and T_U are obtained by integrating the right-hand sides of (2.10) and (2.11) against the pdf (2.8).

The expected value of the digital variance is

$$\langle \hat{s}_\alpha^2 \rangle = 2\left[1 - \Phi(\theta_\alpha)\right] \tag{2.12}$$

where $\theta_\alpha = v_{th_\alpha}/\sigma_{v_\alpha}$ and

$$\Phi(x) = \frac{1}{\sqrt{2\pi}} \int_{-\infty}^{x} e^{-t^2/2} dt \tag{2.13}$$

is the normal cumulative distribution function. Figure 2.5 is a plot showing the relationship between the digital variance and RMS input voltage at a fixed threshold voltage. As will be shown, for maximum sensitivity in T_U the value of θ_α should be close to 0.61.

Inverting (2.12) yields a simple estimate for the signal standard deviation given a measured digital signal variance:

$$\hat{\theta}_\alpha = \Phi^{-1}\left(1 - \frac{\langle \hat{s}_\alpha^2 \rangle}{2}\right) \tag{2.14}$$

or, in terms of antenna brightness temperature:

$$\begin{aligned}\hat{T}_{ANT,\alpha} &= \frac{\hat{\sigma}^2_{v_\alpha}/R_0}{kBG_\alpha} - T_{REC,\alpha} \\ &= \frac{v^2_{th_\alpha}}{R_0 kBG_\alpha}\left[\Phi^{-1}\left(1-\frac{\langle \hat{s}^2_\alpha\rangle}{2}\right)\right]^{-2} - T_{REC,\alpha}\end{aligned} \tag{2.15}$$

where R_0 is the system impedance, B is the bandwidth, G_α is the system gain, and $T_{REC,\alpha}$ is the receiver noise temperature. In general, the parameters $\frac{v^2_{th_\alpha}}{R_0 kBG_\alpha}$, and $T_{REC,\alpha}$ are slowly time varying and represent system gains and offsets that must be identified via periodic calibration.

The relationship between the input correlation coefficient ρ and the expected value of the digital covariance $r_{ab} = \langle \hat{r}_{ab}\rangle$ is similarly straightforward and can be obtained by integrating the right-hand side of (2.11) against the joint pdf. The problem, however, can be reduced to an integration over one dimension using Price's theorem [51, 30]. Price's theorem relates the covariance of the input signals to the digital correlation coefficient:

$$\begin{aligned}\frac{\partial r_{ab}}{\partial R_{v_a v_b}} &= \left\langle \frac{dh(v_a)}{dv_a}\frac{dh(v_b)}{dv_b}\right\rangle \\ &= \langle[\delta(v_a+v_{th_a})+\delta(v_a-v_{th_a})]\,[\delta(v_b+v_{th_b})+\delta(v_b-v_{th_b})]\rangle \\ &= f(v_{th_a},v_{th_b};\rho)+f(v_{th_a},-v_{th_b};\rho)+f(-v_{th_a},v_{th_b};\rho)+f(-v_{th_a},-v_{th_b};\rho) \\ &= f(\sigma_{v_a}\theta_a,\sigma_{v_b}\theta_b;\rho)+f(-\sigma_{v_a}\theta_a,\sigma_{v_b}\theta_b;\rho)+ \\ &\qquad f(\sigma_{v_a}\theta_a,-\sigma_{v_b}\theta_b;\rho)+f(-\sigma_{v_a}\theta_a,-\sigma_{v_b}\theta_b;\rho)\end{aligned} \tag{2.16}$$

The input covariance can be related to the input correlation coefficient using the chain rule:

$$\frac{\partial r_{ab}}{\partial \rho} = \frac{\partial r_{ab}}{\partial R_{v_a v_b}}\frac{\partial R_{v_a v_b}}{\partial \rho} = \sigma_{v_a}\sigma_{v_b}\frac{\partial r_{ab}}{\partial R_{v_a v_b}} \tag{2.17}$$

The digital correlation coefficient, therefore, is a one-dimensional integral of the pdf over ρ:

$$\begin{aligned}r_{ab} = \sigma_{v_a}\sigma_{v_b}\int_0^\rho &[f(\sigma_{v_a}\theta_a,\sigma_{v_b}\theta_b,\rho')+f(\sigma_{v_a}\theta_a,-\sigma_{v_b}\theta_b,\rho')+ \\ &f(-\sigma_{v_a}\theta_a,\sigma_{v_b}\theta_b,\rho')+f(-\sigma_{v_a}\theta_a,-\sigma_{v_b}\theta_b,\rho')]\,d\rho'.\end{aligned} \tag{2.18}$$

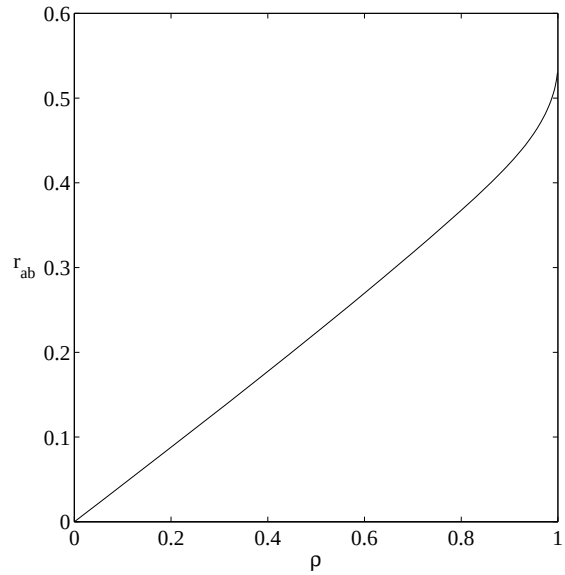

Figure 2.6: The digital covariance r_{ab} versus the input correlation coefficient ρ for $\theta = 0.61$.

In practice θ_a and θ_b are taken to be $\hat{\theta}_a$ and $\hat{\theta}_b$ from (2.14). The relationship between the input correlation coefficient and the digital covariance is plotted in Figure 2.6 for a fixed threshold level $\theta_\alpha = 0.61$.

For a given $\hat{r}_{ab}$, the correlation estimate $\hat{\rho}$ is determined by nonlinear inversion of (2.18). The inversion technique must be carefully chosen so that systematic errors arising from the approximation are not larger than the statistical uncertainty of the estimate. This requirement is quite stringent. For example, from (2.5), a radiometer with a system temperature of $T_{sys} = 500$ K and an integration noise requirement of $\Delta T_{RMS} = 0.1$ K for the third or fourth Stokes parameter would require a measurement of ρ with absolute error less than $0.1\text{K}/(2 \cdot 500\text{K}) = 1 \times 10^{-4}$. The two existing inversion techniques for three-level correlators are based upon power series inversions of either the bivariate normal integral [12] or the one-dimensional integral (2.18) [40]. In the former method [12] the inversion was derived for the cross-correlator, while for the latter method it was derived for the auto-correlator. Both share similar convergence characteristics, e.g., third-order expansions are required to obtain 0.1% accuracy or an absolute error of 10^{-4} for $|\rho| \lesssim 0.6$. The

latter technique is mathematically simpler and allows an analysis of the effects of system nonidealities, which will be considered in Section 2.3.1. Since this expression was originally derived for the autocorrelator, a new and more accurate expression tailored to the cross-correlator is presented here (the derivation is presented in Appendix A). First, the integrand of (2.18) is approximated by a Taylor series about $\rho' = 0$. Next, the series is integrated to obtain:

$$\langle \hat{r}_{ab} \rangle = \frac{2}{\pi} \exp\left[-\frac{1}{2}\left(\theta_a^2 + \theta_b^2\right)\right] \times \left[\rho + \frac{1}{6}\left(\theta_a^2 - 1\right)\left(\theta_b^2 - 1\right)\rho^3 + \frac{1}{120}\left(3 - 6\theta_a^2 + \theta_a^4\right)\left(3 - 6\theta_b^2 + \theta_b^4\right)\rho^5\right] + O(\rho^7). \quad (2.19)$$

Finally, a fifth-order power series reversion [1, (3.6.25)] is carried out on (2.19). The resulting estimate maps $\hat{r}_{ab}$ into $\hat{\rho}$ with absolute error $\sim 10^{-5}$ for $|\rho| \lesssim 0.5$ and normalized threshold levels θ_a, θ_b of $0.61 \pm 10\%$:

$$\hat{\rho} = \frac{1}{c_1}\hat{r}_{ab} - \frac{c_3}{c_1^4}\hat{r}_{ab}^3 + \left(3\frac{c_3^2}{c_1^7} - \frac{c_5}{c_1^6}\right)\hat{r}_{ab}^5, \quad (2.20)$$

where

$$\begin{aligned} c_1 &= \frac{2}{\pi}\exp\left[-\frac{1}{2}\left(\theta_a^2 + \theta_b^2\right)\right] \\ c_3 &= \frac{1}{3\pi}\exp\left[-\frac{1}{2}\left(\theta_a^2 + \theta_b^2\right)\right]\left(\theta_a^2 - 1\right)\left(\theta_b^2 - 1\right) \\ c_5 &= \frac{1}{60\pi}\exp\left[-\frac{1}{2}\left(\theta_a^2 + \theta_b^2\right)\right]\left(3 - 6\theta_a^2 + \theta_a^4\right)\left(3 - 6\theta_b^2 + \theta_b^4\right) \end{aligned} \quad (2.21)$$

Using a fifth-order power series acceptable inversion errors for polarimetry are attainable.

2.2.2 Sensitivity

A radiometer's sensitivity is fundamentally limited by the available bandwidth, observation time, and receiver noise. The radiometric sensitivity of a polarization correlating radiometer is:

$$\Delta T_{U,RMS} = \frac{\sigma_{\hat{\rho}}}{\partial\hat{\rho}/\partial\hat{T}_U}, \quad (2.22)$$

where $\sigma_{\widehat{\rho}}$ is the standard deviation of the estimate $\widehat{\rho}$. For continuous (analog) correlation using N independent samples and small values of ρ it can be shown that $\lim_{\rho \to 0} \sigma_{\widehat{\rho}} = 1/\sqrt{N}$ [11]. Using (2.5) and (2.22) the fundamental sensitivity is:

$$\Delta T_{U,RMS} = \frac{2\sqrt{T_{v,sys} T_{h,sys}}}{\sqrt{N}} \tag{2.23}$$

In the case of a digital correlator, the quantization noise of the A/D converter increases $\Delta T_{U,RMS}$. The increase in $\sigma_{\widehat{\rho}}$ due to quantization noise is a function of both the number of A/D converter levels and the threshold voltages. The impact of quantization noise can be minimized by proper selection of the threshold voltages v_{th_α}. Using a digital correlator we have:

$$\Delta T_{U,RMS} = \frac{\sigma_{\widehat{r}_{ab}}}{\partial \widehat{r}_{ab} / \partial \widehat{T}_U}. \tag{2.24}$$

For the three level system with balanced channels $(\theta_a = \theta_b = \theta)$, the sensitivity for vanishingly small correlation is (see Appendix B.1):

$$\lim_{\rho \to 0} \Delta T_{U,RMS} = 2\pi \left[1 - \Phi(\theta)\right] e^{\theta^2} \frac{\sqrt{T_{v,sys} T_{h,sys}}}{\sqrt{N}} \tag{2.25}$$

The above can be minimized numerically with respect to θ to find the threshold level required for minimum measurement uncertainty. The optimal value of θ is 0.61 with a corresponding sensitivity of:

$$\Delta T_{U,RMS} = 2.47 \frac{\sqrt{T_{v,sys} T_{h,sys}}}{\sqrt{N}} \tag{2.26}$$

Comparing this expression to the continuous correlator noise in (2.23), we find that the digital correlator achieves 81% of the sensitivity provided by an ideal analog correlator.

The total-power channels are useful for normalized threshold level estimation. The sensitivity of the total-power channel can be calculated in a similar fashion by

$$\Delta T_{\alpha,RMS} = \frac{\sigma_{\widehat{s}^2_\alpha}}{\partial (\widehat{s}^2_\alpha) / \partial \widehat{T}_\alpha} \tag{2.27}$$

With the threshold levels $\theta_a = \theta_b = 0.61$ (i.e., set for optimal cross-correlator sensitivity), the total-power channels have a radiometric sensitivity of (see appendix B.2)

$$\Delta T_{\alpha,RMS} = 2.20 \frac{T_{sys,\alpha}}{\sqrt{N}}. \tag{2.28}$$

The ideal total-power radiometer has a sensitivity of $T_{sys}/\sqrt{N}$. A three-level digital total-power radiometer can achieve 41% the sensitivity of an ideal analog total-power detector when the threshold voltages are optimized for the cross-correlation channel. It is noted that in (2.28) the optimal sensitivity for the total-power channels is not used because the threshold voltages were chosen to optimize the cross-correlation channel. In other words, the threshold level value of 0.61 is the optimum value for small cross correlations; however, this value is not optimal for the total power channels. This choice is acceptable, however, because in the polarization correlating radiometer the total-power channels are primarily used to measure the relative threshold level values. If the thresholds were set for optimal sensitivity for total-power detection, then the digital total-power radiometer achieves 78% of the sensitivity of the analog radiometer with $\theta_\alpha = 1.58$.

2.3 Systematic Errors

Three different sources of systematic errors are treated in this section. The first section deals with errors caused by threshold asymmetries in the A/D converters. Second, a correlation coefficient offset generated by downconverted LO thermal noise is described. Finally, the effects of A/D hysteresis and timing skew on the correlator gain are characterized. Within the treatment of each systematic error, some design suggestions that mitigate the error in a polarimetric radiometer are discussed.

2.3.1 Sampler Offsets

Threshold level asymmetries in the correlator A/D converters produce systematic errors in the variance and correlation measurements. When extreme accuracy is not required, the

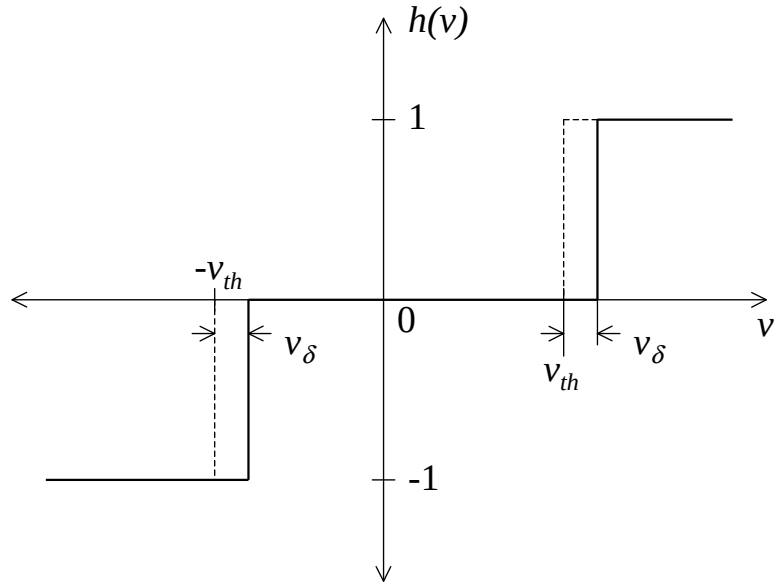

Figure 2.7: Transfer function of three-level A/D converter with threshold offset v_δ.

effects of these relatively small DC biases can be neglected. However, for high accuracy applications, such as found in microwave polarimetry for wind vector measurement, asymmetric threshold levels cause attenuation and offset variations that require compensation. An analysis is presented here that illustrates the second-order behavior of bias effects and leads to a simple analytical correction which can be included in the radiometer calibration.

The ideal three-level A/D converter has the transfer function (2.9). Typically, there can be a small DC voltage offset v_{δ_α} at the A/D input, which effectively causes the threshold levels to be asymmetric about ground. The normalized threshold asymmetry is defined as $\delta_\alpha = v_{\delta_\alpha}/\sigma_{v_\alpha}$. Incorporating this offset into the transfer function we have (see Figure 2.7):

$$h(v) = \begin{cases} 1 & \text{if } v > (\theta_\alpha + \delta_\alpha)\sigma_{v_\alpha} \\ -1 & \text{if } v < (-\theta_\alpha + \delta_\alpha)\sigma_{v_\alpha} \\ 0 & \text{otherwise} \end{cases} \tag{2.29}$$

The relations (2.10) and (2.11) can be recomputed to reveal the effects of threshold level

offsets. For example, the digital correlation coefficient becomes:

$$r_{ab} = r_{ab}|_{\rho=0} + \sigma_{v_a}\sigma_{v_b}\int_0^{\rho}[f(\sigma_{v_a}(\theta_a+\delta_a),\sigma_{v_b}(\theta_b+\delta_b),\rho') + f(\sigma_{v_a}(\theta_a+\delta_a),\sigma_{v_b}(-\theta_b+\delta_b),\rho') + f(\sigma_{v_a}(-\theta_a+\delta_a),\sigma_{v_b}(\theta_b+\delta_b),\rho') + f(\sigma_{v_a}(-\theta_a+\delta_a),\sigma_{v_b}(-\theta_b+\delta_b),\rho')]\,d\rho' \quad (2.30)$$

Throughout this analysis it is assumed that δ_a and δ_b are small with respect to θ_a and θ_b and only first-order terms in δ_a and δ_b are significant.

2.3.1.1 Correlation channel

Threshold level asymmetries will cause gain and offset perturbations of the digital correlator output. We show here that the gain error is negligible if the input correlation coefficient is small. In contrast, the offset error is found to be an order of magnitude larger than the gain error. This correlation offset, however, is parameterized in terms of the threshold level offset and may be compensated by calibration using two unpolarized standards.

The correlator offset error arises from the constant of integration in (2.30). This constant was not explicitly shown in (2.18) because ideally it is zero; however, the threshold level offsets cause it to become non-zero. The constant of integration $r_{ab}|_{\rho=0}$ can be evaluated by taking the expected value of (2.11) with $\rho = 0$ and using the modified definition of $h(v)$:

$$r_{ab}|_{\rho=0} = \langle h'(v_a)h'(v_b)\rangle|_{\rho=0} \quad (2.31)$$

Clearly, when either threshold level is ideal (that is, $\delta_\alpha = 0$) this term vanishes. A shift in both threshold levels, however, causes the offset error to become non-zero. The expected value may be separated into a product of two expected values because v_a and v_b are statistically independent when $\rho = 0$. If the threshold levels for channels a and b are offset by δ_a and δ_b, respectively, then the resulting offset in correlation is

$$r_{ab}|_{\rho=0} = [1 - \Phi(-\theta_a+\delta_a) - \Phi(\theta_a+\delta_a)]\,[1 - \Phi(-\theta_b+\delta_b) - \Phi(\theta_b+\delta_b)] \quad (2.32)$$

Assuming δ_a and δ_b are small allows the above to be approximated using Taylor series expansions about $\pm\theta_a$ and $\pm\theta_b$. The first term in the product is

$$\begin{aligned}
1-\Phi(-\theta_a+\delta_a)-\Phi(\theta_a+\delta_a) = & \\
& 1-\left[\Phi(\theta_a)+\frac{1}{2}\sqrt{\frac{2}{\pi}}e^{-\frac{1}{2}\theta_a^2}\delta_a-\frac{1}{4}\sqrt{\frac{2}{\pi}}e^{-\frac{1}{2}\theta_a^2}\theta_a\delta_a^2+O\left(\delta_a^3\right)\right] \\
& -\left[\Phi(-\theta_a)+\frac{1}{2}\sqrt{\frac{2}{\pi}}e^{-\frac{1}{2}\theta_a^2}\delta_a+\frac{1}{4}\sqrt{\frac{2}{\pi}}e^{-\frac{1}{2}\theta_a^2}\theta_a\delta_a^2+O\left(\delta_a^3\right)\right] \\
& =-\sqrt{\frac{2}{\pi}}e^{-\frac{1}{2}\theta_a^2}\delta_a+O\left(\delta_a^3\right)
\end{aligned} \tag{2.33}$$

The δ_a^2 terms cancel leaving an odd valued function. The $O(\delta_a)$ behavior of the above makes the threshold asymmetry a significant source of error. The second term, the b channel contribution, is identical to the above. The constant of integration is the product of these two terms:

$$\begin{aligned}
r_{ab}\big|_{\rho=0} &= \left[-\sqrt{\frac{2}{\pi}}e^{-\frac{1}{2}\theta_a^2}\delta_a+\left(\delta_a^3\right)\right]\left[-\sqrt{\frac{2}{\pi}}e^{-\frac{1}{2}\theta_b^2}\delta_b+\left(\delta_b^3\right)\right] \\
&= \frac{2}{\pi}\theta_a\theta_b\exp\left[-\frac{1}{2}\left(\theta_a^2+\theta_b^2\right)\right]\pi_\delta+O\left(\delta_a\delta_a^3,\delta_b\delta_a^3\right)
\end{aligned} \tag{2.34}$$

where

$$\pi_\delta=\left(\frac{\delta_a}{\theta_a}\frac{\delta_b}{\theta_b}\right) \tag{2.35}$$

The threshold asymmetries affect the digital correlation offset by an amount proportional to the normalized offset product π_δ. Expressed using voltages,

$$\pi_\delta=\frac{v_{\delta_a}v_{\delta_b}}{v_{th_a}v_{th_b}} \tag{2.36}$$

The above threshold-offset product is a slowly time varying hardware constant. As will be shown in Section 4.2, the threshold-offset product can be estimated using a traditional two-look unpolarized calibration.

The correlator gain is found by expanding the integrand of (2.30) in a three-dimensional power series in ρ', δ_a and δ_b, then integrating the resulting expansion with respect to

ρ'. The algebra involved (see Appendix C) is cumbersome, although the digital correlation coefficient can be expressed as a sum of two series. The first series $r_{ab}|_{\delta_a=\delta_b=0}$ is the ideal relationship between ρ and r given in (2.18). The second series is an error series $\delta r_{ab}(\delta_a, \delta_b, \rho)$ caused by nonzero threshold offsets δ_a and δ_b. Thus,

$$\begin{aligned} r_{ab} = r_{ab}|_{\rho=0} + r_{ab}|_{\delta_a=\delta_b=0} + \frac{2}{\pi}\exp\left[-\frac{1}{2}\left(\theta_a^2+\theta_b^2\right)\right] \times \\ \left[-\frac{1}{2}\left[\left(1-\theta_a^2\right)\delta_a^2+\left(1-\theta_b^2\right)\delta_b^2\right]\rho+\frac{1}{4}\delta_a\delta_b\left(1-2\theta_a^2\right)\left(1-2\theta_b^2\right)\rho^2+\right. \\ \left.-\frac{1}{6}[\left(6\theta_a^2+\theta_a^4+3\right)\left(1-\theta_b^2\right)\delta_a^2+\left(1-\theta_a^2\right)\left(6\theta_b^2+\theta_b^4+3\right)\delta_b^2]\rho^3\right]+O\left(\rho^4,\delta^3\right) \end{aligned} \tag{2.37}$$

The above series is truncated at $O(\rho^4)$ and $O(\delta^3)$. Assuming that the nominal threshold levels are equal to the optimal value $\theta_\alpha = 0.61$, the error series becomes

$$\delta r_{ab}(\delta_a, \delta_b, \rho) \approx -0.3140\left(\delta_a^2+\delta_b^2\right)\rho + 0.0164\delta_a\delta_b\rho^2 + -0.5621\left(\delta_a^2+\delta_b^2\right)\rho^3 \tag{2.38}$$

The error series is a sum of components that are $O(\delta^2\rho)$, $O(\delta^2\rho^2)$, and $O(\delta^2\rho^3)$, respectively. To determine which components of the error series are significant, we assume that $\rho = 0.1$ and $\delta_\alpha \sim O(\delta)$. The magnitudes of the three components become

$$\begin{aligned} -0.3140\left(\delta_a^2+\delta_b^2\right)\rho &\approx 0.044\delta^2 \\ 0.0164\delta_a\delta_b\rho^2 &\approx 0.00016\delta^2 \\ -0.5621\left(\delta_a^2+\delta_b^2\right)\rho^3 &\approx 0.00079\delta^2 \end{aligned}$$

To render these error terms insignificant, the magnitude of δ^2 must be sufficiently small. Using the criterion that all errors $\lesssim 10^{-5}$ are negligible, the threshold offsets should be no larger than 10^{-2}, in other words, $v_{\delta_\alpha} \leq 10^{-2}\sigma_{v_\alpha}$. This is readily attainable using precision electronics for $\sigma_{v_\alpha} \sim 0.5$ V. If threshold offsets are not small enough, then the offsets should at least be controlled to render insignificant the higher-order terms (e.g., ρ^2, $\rho^3 \ldots$). For this latter case, it is sufficient for $v_{\delta_\alpha} \leq 10^{-1}\sigma_{v_\alpha}$, which causes the magnitude of the ρ^3 term to be $< 10^{-5}$. The remaining error is linear in ρ and can be modeled as an effective

change in the correlator gain:

$$r_{ab} = r_{ab}\big|_{\rho=0} + \frac{2}{\pi}\exp\left[-\frac{1}{2}\left(\theta_a^2+\theta_b^2\right)\right]\left(1-\frac{1}{2}\left[\left(1-\theta_a^2\right)\delta_a^2+\left(1-\theta_b^2\right)\delta_b^2\right]\right)\rho + O(\rho^2,\delta_b^3) \quad (2.39)$$

Typically the threshold offsets are small enough so that the gain perturbation is a few percent or less.

2.3.1.2 Total-power channel

The effect of threshold asymmetry on the total-power channels is an additional system gain and offset along with a residual nonlinearity that will be shown to be negligible. Consider the expected value of the total-power output:

$$\langle \hat{s}_\alpha^2 \rangle = \Phi\left(-\theta_\alpha+\delta_\alpha\right) + 1 - \Phi\left(\theta_\alpha+\delta_\alpha\right) \quad (2.40)$$

This expression is simply an extension of (2.12), but includes the threshold asymmetry. The above can be approximated in δ_α as

$$\langle \hat{s}_\alpha^2 \rangle = \Phi\left(-\theta_\alpha\right) + 1 - \Phi\left(\theta_\alpha\right) + \frac{1}{2}\sqrt{\frac{2}{\pi}}e^{-\theta_\alpha^2/2}\theta_\alpha\delta_\alpha^2 + O\left(\delta_\alpha^4\right) \quad (2.41)$$

Similar to the correlation channel, the expected value of the total-power channel is a sum of the ideal output and an additional error series. We can now show that part of the error series can be combined with the ideal output to compute a modified system gain and offset, with the residual component being insignificant. If all functions of θ_α are approximated by a power series expansion

$$\Phi\left(-\theta_\alpha\right) + 1 - \Phi\left(\theta_\alpha\right) = 1 - \sqrt{\frac{2}{\pi}}\theta_\alpha + \frac{1}{6}\sqrt{\frac{2}{\pi}}\theta_\alpha^3 + O\left(\theta_\alpha^5\right) \quad (2.42)$$

$$e^{-\theta_\alpha^2/2} = 1 - \frac{1}{2}\theta_\alpha^2 + O\left(\theta_\alpha^4\right) \quad (2.43)$$

then (2.40) can be written

$$\begin{aligned}
\langle \widehat{s}_\alpha^2 \rangle &= \left[1 - \sqrt{\frac{2}{\pi}}\theta_\alpha + \frac{1}{6}\sqrt{\frac{2}{\pi}}\theta_\alpha^3 + O\left(\theta_\alpha^5\right)\right] + \frac{1}{2}\sqrt{\frac{2}{\pi}}\left[\theta_\alpha - \frac{1}{2}\theta_\alpha^3 + O\left(\theta_\alpha^5\right)\right]\delta_\alpha^2 + O\left(\delta_\alpha^4\right) \\
&= 1 - \sqrt{\frac{2}{\pi}}\left(1 - \frac{1}{2}\delta_\alpha^2\right)\theta_\alpha + \frac{1}{6}\sqrt{\frac{2}{\pi}}\left(1 - \frac{3}{2}\delta_\alpha^2\right)\theta_\alpha^3 + O\left(\theta_\alpha^5, \delta_\alpha^4\right) \\
&= \left(1 - \frac{1}{2}\delta_\alpha^2\right)\left[1 - \sqrt{\frac{2}{\pi}}\theta_\alpha + \frac{1}{6}\sqrt{\frac{2}{\pi}}\theta_\alpha^3 + O\left(\theta_\alpha^5\right)\right] + \frac{1}{2}\delta_\alpha^2 - \frac{1}{6}\sqrt{\frac{2}{\pi}}\delta_\alpha^2\theta_\alpha^3 + O\left(\delta_\alpha^4\right) \\
&= \left(1 - \frac{1}{2}\delta_\alpha^2\right)\langle \widehat{s}_\alpha^2 \rangle_{\delta_\alpha = 0} + \frac{1}{2}\delta_\alpha^2 - \frac{1}{6}\sqrt{\frac{2}{\pi}}\delta_\alpha^2\theta_\alpha^3 + O\left(\delta_\alpha^4\right)
\end{aligned} \tag{2.44}$$

There is a gain term affecting the total-power channel output by a factor of $\left(1 - \frac{1}{2}\delta_\alpha^2\right)$ and an offset of approximately $\frac{1}{2}\delta_\alpha^2$. This additional system gain and offset is easily identified via a standard two-look calibration. The nonlinear residual is

$$-\frac{1}{6}\sqrt{\frac{2}{\pi}}\delta_\alpha^2\theta_\alpha^3 + O\left(\delta_\alpha^4\right). \tag{2.45}$$

Assuming the optimal value for the threshold levels ($\theta_\alpha = 0.61$), the above residual is found to be $\sim 10^{-2}\delta_\alpha^2$. If $\delta_\alpha \lesssim 0.02$, then the nonlinear residual term becomes $< 10^{-5}$, which is insignificant.

2.3.2 Input Correlation Offset

Any correlated noise in the IF signals will cause an unwanted correlation offset at the digital correlator inputs. If the digital polarimetric radiometer utilizes a dual channel receiver with a common local oscillator (LO), downconverted LO noise in both IF signals will be highly correlated. The phase noise of the LO could also affect a correlation bias; however, the low frequency cutoff of IF bands is generally high enough so that the phase noise is significantly smaller than the downconverted thermal noise. Systems with LOs that have high noise temperatures, such as Gunn diode oscillators, and those with single diode mixers will be most susceptible to the downconverted noise. To study the magnitude of this effect, the noise signal model in Figure 2.8 is used in the calculation of the correlation coefficient.

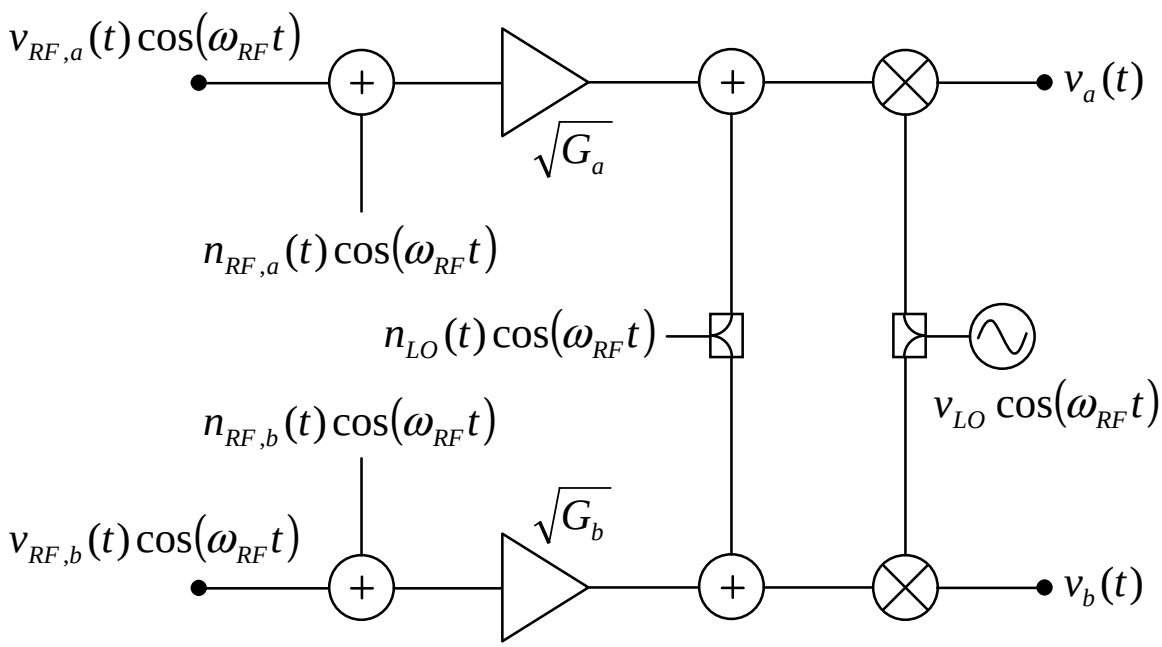

Figure 2.8: Noise model for dual channel, single LO, superheterodyne receiver. The input referred RF noise signals $n_{RF,a}(t)\cos(\omega_{RF}t)$ and $n_{RF,b}(t)\cos(\omega_{RF}t)$ are uncorrelated. The system voltage gains are represented by $\sqrt{G_a}$ and $\sqrt{G_b}$. The local oscillator thermal noise $n_{LO}(t)\cos(\omega_{RF}t)$ and signal $\cos(\omega_{LO}t)$ are modeled by common sources, which are split equally between both channels. The outputs signals $v_a(t)$ and $v_b(t)$ are the downconverted sums of the RF signals, RF noise, and LO thermal noise.

The IF signals $v_\alpha(t)$, $\alpha = a$ or b, at the mixer output can be described by

$$v_\alpha(t) = \left[v_{RF,\alpha}(t) + n_{RF,\alpha}(t)\right]\sqrt{G_\alpha} + n_{LO}(t)\sqrt{\frac{1}{L_{LO-IF}}} \tag{2.46}$$

where $v_{RF,\alpha}(t)$ is the signal at the antenna output, $n_{RF,\alpha}(t)$ is the input referred system noise (excluding the LO noise), $\sqrt{G_\alpha}$ is the RF voltage gain, $n_{LO}(t)$ is the LO noise, and L_{LO-IF} is the conversion loss from the LO to IF paths of the mixer. A first approximation of L_{LO-IF} is the product of the LO-to-RF isolation and the RF-to-IF conversion loss of the mixer. The correlation coefficient of the IF signals is

$$\begin{aligned}\rho &= \frac{\langle v_a(t) v_b(t)\rangle}{\sigma_{v_a}\sigma_{v_b}} \\ &= \frac{\langle v_{RF,a}(t) v_{RF,b}(t)\rangle\sqrt{G_a G_b} + \sigma^2_{n_{LO}}\frac{1}{L_{LO-IF}}}{\sigma_{v_a}\sigma_{v_b}}\end{aligned} \tag{2.47}$$

where $\sigma_{n_{LO}}$ is the RMS voltage of the LO noise signal. Or in terms of noise and brightness temperatures, ρ is

$$\rho = \frac{\frac{1}{2}T_{ANT,U} + T_{LO}/\left(L_{LO-IF}\sqrt{G_a G_b}\right)}{\sqrt{T_{sys,a}T_{sys,b}}} \tag{2.48}$$

where T_{LO} is the noise temperature of the LO. The correlation bias is identified as:

$$\rho_0 = \frac{T_{LO}/\left(L_{LO-IF}\sqrt{G_a G_b}\right)}{\sqrt{T_{sys,a}T_{sys,b}}} \tag{2.49}$$

To illustrate the magnitude of ρ_0, consider two examples. For a system with a mixer front-end:

$$\begin{aligned}T_{LO} &= 30,000 \text{ K } (\sim\text{20 dB ENR}) \\ L_{LO-IF} &= 500 \text{ (27 dB)} \\ G_\alpha &= 1 \\ T_{sys,\alpha} &= 500 \text{ K}\end{aligned}$$

Using these values, the correlation bias $\rho_0 = 0.12$. If LNAs are placed before the mixers,

then typical system parameters might be

$$T_{LO} = 30,000 \text{ K } (\sim 20 \text{ dB ENR})$$
$$L_{LO-IF} = 500 \text{ (27 dB)}$$
$$G_{\alpha} = 100 \text{ (20 dB)}$$
$$T_{sys,\alpha} = 200 \text{ K}$$

In this case the correlation bias $\rho_0 = 0.003$ and is greatly reduced by the addition of the LNAs.

Other techniques, in addition to front-end LNAs, can be utilized to reduce the correlation bias. For example, in a balanced mixer the LO and IF ports are well isolated, which greatly reduces the amount of down-converted LO thermal noise at the IF output [10, p. 866]. If further reduction is needed, the LO thermal noise in each channel can be reduced by placing attenuators in each arm of the dual output LO at the expense of LO power. A third, and almost certain, method is to use two separate LOs phase-locked to a single reference. Since thermal noise signals generated by two different sources are uncorrelated, there will be no correlation bias caused by the downconverted LO noise.

It is not, however, necessary to completely eliminate ρ_0 provided that in-situ radiometric calibration is available. In this case the offset can be identified by presenting to the system an uncorrelated input stimulus such as a view of an unpolarized blackbody target or cold space (see Section 4.2). The correlation bias, however, should be reduced as much as possible using the methods described above so that the value of ρ will remain within the range of validity of (2.20).

2.3.3 Sampler Hysteresis and Timing Skew

Analog-to-digital converter hysteresis acts to reduce the correlation output by an amount proportional to the magnitude of the hysteresis. This effect has been modeled by D'Addario, *et al.* [12] assuming a uniformly distributed region of uncertainty about the nominal threshold. However, this statistical model underestimates the attenuation effect, because the hys-

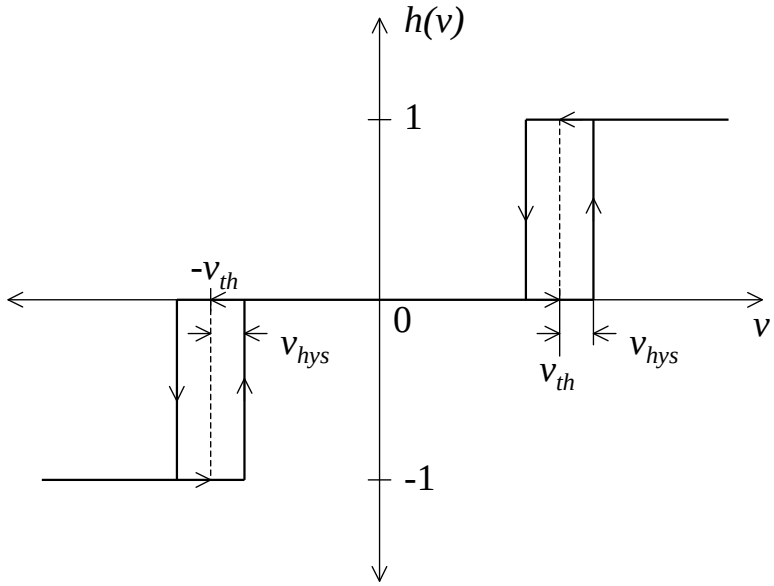

Figure 2.9: Transfer function of three-level A/D converter with hysteresis magnitude v_{hys}.

teresis is treated as a uniformly distributed region centered about the threshold level. More precisely, hysteresis is a nonstationary process in which the current threshold level is dependent upon the previous value of the input signal. To make more accurate assessment of hysteresis, a Monte-Carlo simulator was constructed to demonstrate the effect on the gain of the correlation channel. The simulator is based upon an A/D converter transfer function:

$$h(v(nT)) = \begin{cases} 1 & \text{if } v(nT) > \quad v_{th_\alpha} + v_{hys,\alpha} \text{ AND } h[v((n-1)T)] \neq 1, \\ 1 & \text{if } v(nT) > \quad v_{th_\alpha} - v_{hys,\alpha} \text{ AND } h[v((n-1)T)] = 1, \\ -1 & \text{if } v(nT) < -v_{th_\alpha} + v_{hys,\alpha} \text{ AND } h[v((n-1)T)] = -1, \\ -1 & \text{if } v(nT) < -v_{th_\alpha} - v_{hys,\alpha} \text{ AND } h[v((n-1)T)] \neq -1, \\ 0 & \text{otherwise.} \end{cases} \tag{2.50}$$

where $v_{hys,\alpha}$ is the hysteresis voltage. The transfer function is graphically illustrated in Figure 2.9. Input correlation coefficients in the range $-0.1 < \rho < 0.1$ were tested with varying levels of hysteresis. In Figure 2.10, the correlator output r_{ab} is plotted for values of hysteresis in the range $0 \leq v_{hys,\alpha}/\sigma_{v_\alpha} \leq 0.333$. The computed relative attenuation on

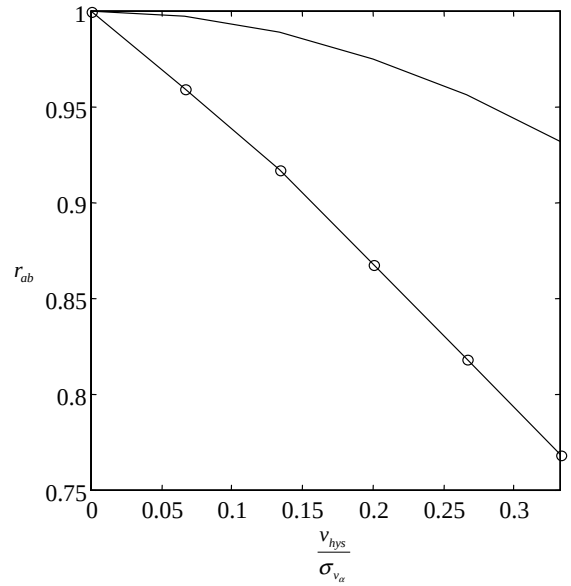

Figure 2.10: The reduction in the digital correlator output as a function of hysteresis amplitude. The results of the Monte-Carlo model (solid line with open circles) shows that the statistical model [12] (solid line) under estimates the effect.

r_{ab} due to the hysteresis is practically independent of ρ for this region. The results of the statistical model of [12] for the same conditions are also plotted. Compared to the Monte-Carlo simulations, the statistical model appears to underestimate the attenuation effect by a factor of $\sim$10 at $v_{hys,\alpha}/\sigma_{v_\alpha} = 0.1$.

According to the simulation, hysteresis has a discernible effect on the correlator output. A reduction in correlator gain of 1% is caused by a hysteresis voltage equal to 2% of the RMS signal voltage. For a 0 dBm signal into 50 Ω, a hysteresis voltage of 4.4 mV would cause this. Care must be taken to design the A/D converter circuitry without significant hysteresis. Alternatively, a-priori correction using a polarimetric calibration system or precise knowledge of the hysteresis levels must be performed.

Timing skew between the A/D converters or (equivalently) additional delay in one of the RF or IF paths has a similar effect of reducing the correlator output. The baseband

signals at the correlator input can be modeled by

$$v_a(t) = v_a^0(t) + v_c(t) \tag{2.51}$$

$$v_b(t) = v_b^0(t - \Delta t) + v_c(t - \Delta t) \tag{2.52}$$

where $v_a^0(t)$, $v_b^0(t)$, and $v_c(t)$ are mutually uncorrelated and wide-sense stationary, and Δt is an additional path delay or timing skew. If $v_c(t)$ is bandlimited then the cross-correlation function is:

$$R_{v_a v_b}(\Delta t) = \rho \sigma_{v_a} \sigma_{v_b} \text{sinc}(2\pi B \Delta t) \tag{2.53}$$

where B is the bandwidth or bandlimiting cutoff frequency of $v_c(t)$, and the function $\text{sinc}(x) \triangleq \frac{\sin x}{x}$. Timing skew will reduce the measured correlation coefficient. For example, a 1% reduction would be caused by $\Delta t = 0.039 B^{-1}$. For a 500 MHz bandwidth, this corresponds to $\Delta t = 78$ ps or ~ 24 mm of free-space path delay.

2.4 Digital Correlation Hardware

The digital correlator hardware includes three modules: the high-speed correlators, the clock module, and the counter/interface module. The high-speed correlators process the eight 500 MHz IF channel pairs by performing signal sampling, quantization, multiplication, and accumulation. The operations of the correlators are controlled by the clock module output. The clock module generates a 1000 MHz clock signal for input to the correlators. The clock signal is output in controlled 16.8 ms bursts that are initiated by computer. When a 16.8 ms pulse train is completed, a computer reads the correlator outputs from the counter/interface module and then initiates a new correlation sequence.

The four correlator modules each contain two identical correlator circuits for a total of eight correlators. A photograph of a digital correlator module is shown in Figure 2.11. Each correlator comprises three functional blocks: the A/D converters, the multipliers, and the accumulators. The high-speed A/D converters are dual window comparators yielding

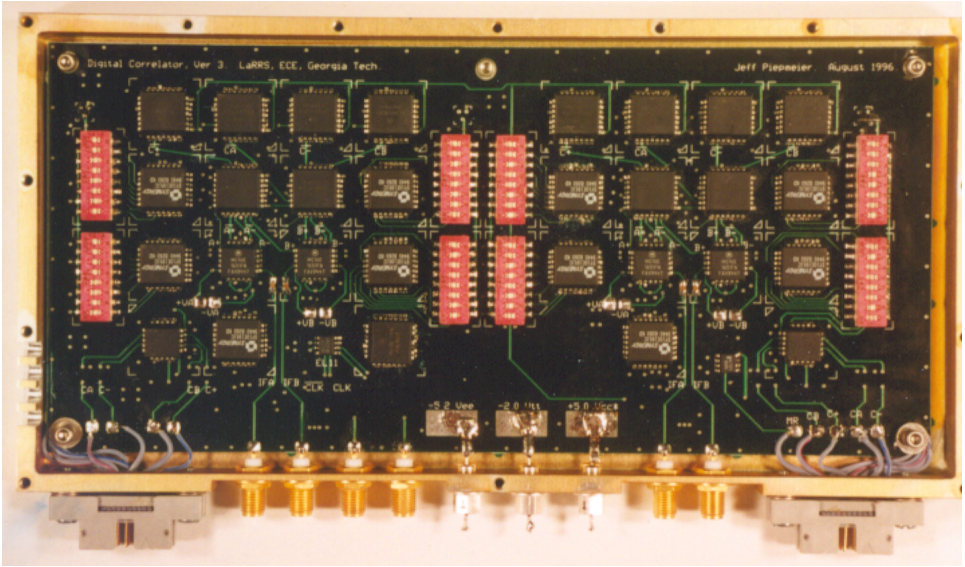

Figure 2.11: Photograph of a digital correlator module. The PSR contains four of these modules and each module has two correlator circuits.

three levels of quantization at a 1 GS/s rate. The comparator threshold levels are dynamically adjusted to track slowly-varying drifts in IF signal power. Threshold level adjustment using eight-bit D/A converters provides (for Gaussian signals) a 48 dB A/D converter input dynamic range. Limiting the operating dynamic range to approximately 30 dB, however, by setting a minimum allowable threshold level ensures a good signal-to-noise ratio. The typical threshold level is $\sim$0.3 V. The total-power of an individual channel is measured by counting the number of times the input signal exceeds either the positive or negative threshold levels as in (2.10). This operation is achieved by NANDing the dual comparator's complement outputs. The correlation coefficient is similarly determined by separately counting the number of positive and negative correlation counts. The products required for the correlation operation are formed using two NAND and four AND gates. A total of eight AND/NAND gates compose the entire three-level multiplier circuitry. The outputs of the digital multiplier are accumulated in four 24-bit counters. The counter input stages

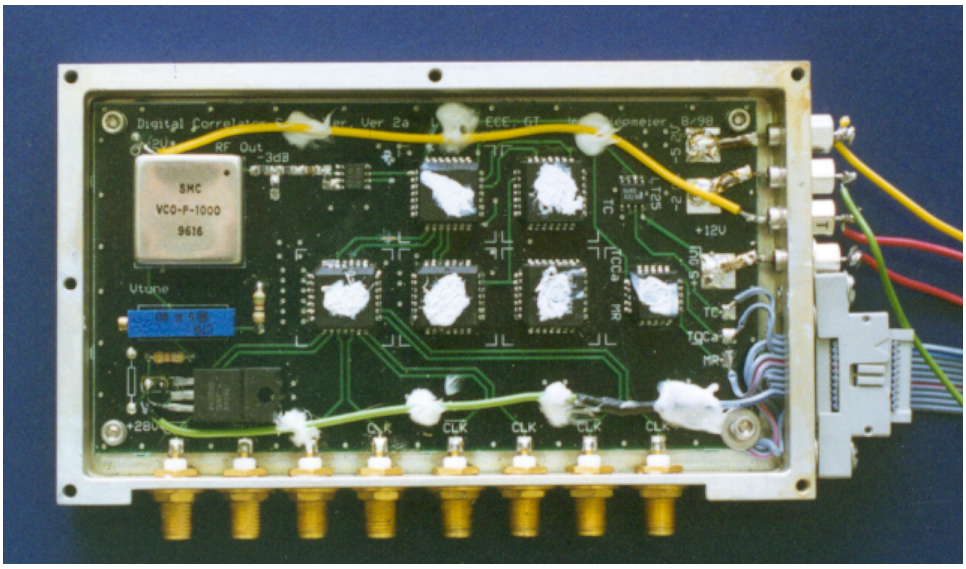

Figure 2.12: Photograph of the clock control and distribution module, the central component of the digital correlation system.

are high-speed 8-bit ECL ripple counters. The outputs from these counters are carried to 16-bit TTL counters in the counter/interface module. The system clock (generated by the clock module) is received by an ECL receiver buffer and further distributed throughout the correlator circuitry. A differential clock pair is sent to each of the four counters and the two A/D converters. Programmable delay chips are used to synchronize the clock signals with the digital multiplier signals. The delay chips are programmed with dip switches and are capable of 128 different levels of delay distributed in $\sim$20 ps steps.

A photograph of the clock module is shown in Figure 2.12. The clock signal is generated by a 2000 MHz voltage controlled oscillator (VCO). The output of the VCO is attenuated by a 3 dB T-network attenuator and capacitively coupled to a $\div 2$ ECL counter. The input to the ECL chip is biased by the counter's reference voltage output, which brings the 2000 MHz sinewave into ECL input voltage range. The output of the $\div 2$ counter is a 50% duty cycle 1000 MHz ECL square wave. The counter output, or the clock signal,

is then gated and sent to a 24-bit counter. The 24-bit counter is realized using three 8-bit counters in series. After a reset is sent to the 24-bit counter, the clock gate is enabled, which allows the clock signal to increment the counter. When the carry bits of the two most significant 8-bit counters are sent high, the 24-bit counter latches itself and the clock gate at a count of $(2^{24} - 256)$. The gated clock signal is also distributed to the correlator modules using an ECL clock buffer/distribution chip with the differential outputs transmitted over coaxial cables.

The clock module and high-speed correlators are fabricated using discrete high-speed emitter-coupled logic (ECL) components, which are surface mounted on six layer PC boards. The ECL discrete logic chips are mounted to the top layer. The top and bottom layers of the circuit boards hold the microstrip interconnects. Both 50 Ω termination chip resistors and 0.01 μF chip capacitors for power filtering are surface-mounted on the bottom layer. Via holes transmit signals and current from the top to the bottom layers. The middle layers are heavy 2 ounce copper planes: ground planes on the 2nd and 5th layers, and -5.2 V and -2 V power supply planes are sandwiched in the middle. Plated-through via holes are used to supply power and ground connections to the top and bottom layers from these internal layers. Because of the high-speed signals and the possibility of their radiation from the circuit boards, aluminum enclosures were machined to contain the boards. The enclosures include conductive stand-offs on which to mount the circuit boards. The mounting holes on the boards where plated through and connected to the ground planes to ensure a good electrical connection between the circuit and enclosure. Digital ECL signals carried off the clock board to other modules are transmitted in differential pairs on two coaxial cables. There are SMA connectors mounted to the aluminum enclosures to which these cables are connected. The TTL output signals produced by the correlator modules are transmitted over twisted pair ribbon cables to the counter/interface module.

The counter/interface module has eight TTL counter boards, each containing four 16-bit counters that are triggered by the output signals from the correlator modules. Photographs of the TTL counter boards are shown in Figure 2.13. These counters are operated

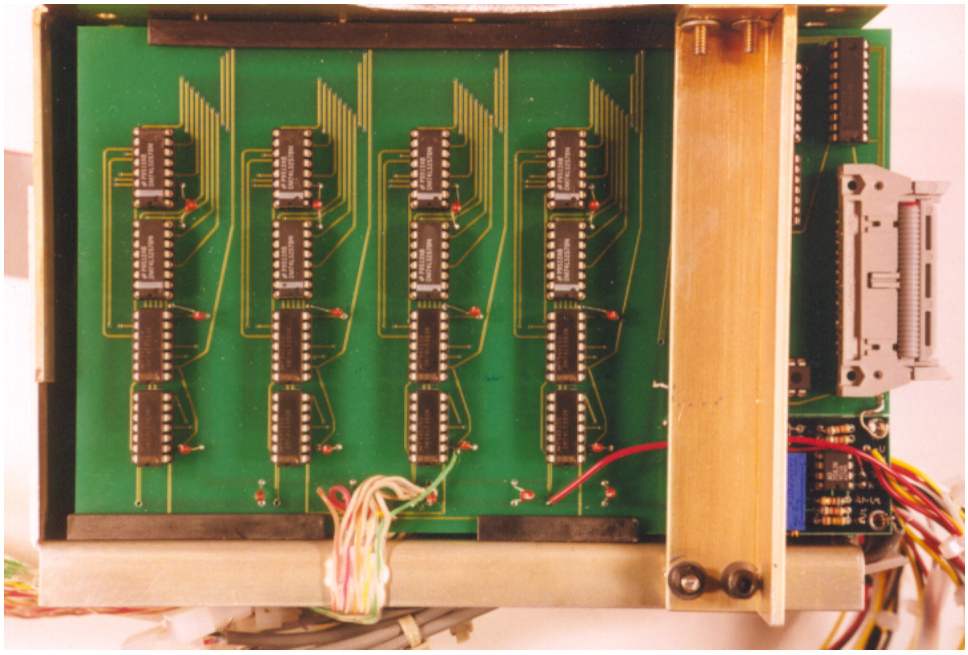

(a) top view

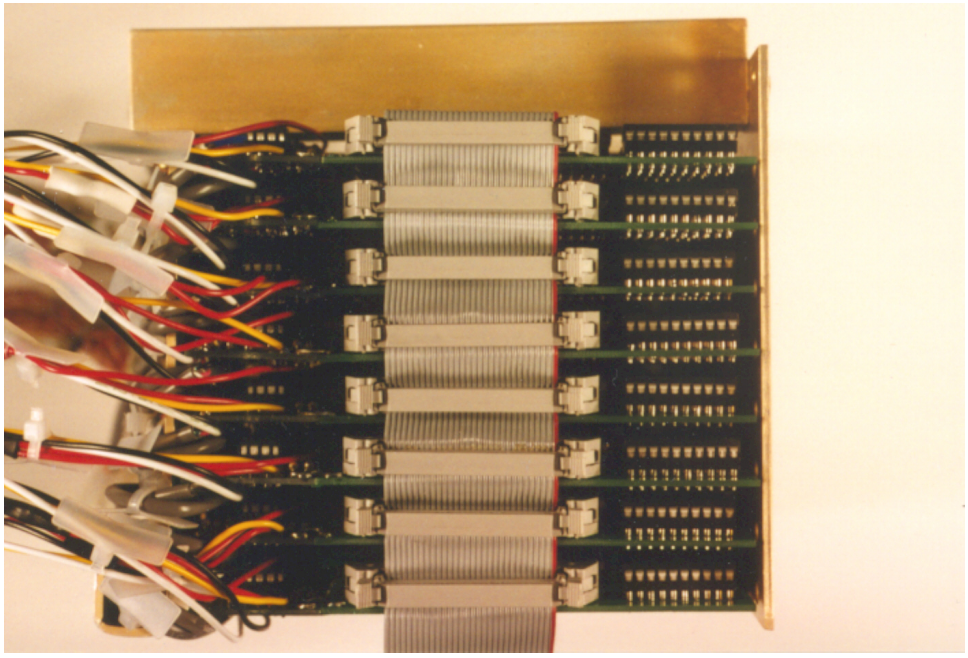

(b) end view

Figure 2.13: TTL counter/interface boards and ribbon cable bus.

in free-running asynchronous mode. The outputs of the counters are organized into high- and low-bytes by 2-to-1 multiplexers with tri-state outputs. The tri-state outputs are connected in parallel to an eight-bit data bus, which allows the high- or low-bytes of any of the 32 counters (four counters per board on the eight boards) to be read by the PC with an eight-bit input port. A six-bit address allows the scanhead computer to select any of these 64 bytes. The address is organized with three bits for the board address, two bits for the counter address, and 1 bit for the high- or low-byte address. The counter/interface module bus is a flat ribbon cable with locking connectors.

In addition to the counter and interface circuitry, the threshold level generators for the correlator A/D converters reside on the TTL counter boards. A threshold level generator includes a dual eight-bit D/A converter and buffering and inverting op-amps, which generate the positive and negative threshold voltages. Any of the eight D/A converters can be selected by using the three-bit board address. The desired data is placed on an additional eight-bit bus, which is connected to the inputs of all eight D/A converters. By triggering a latch enable line, the data is loaded into the appropriate D/A converter as determined by the 3-bit board address.

These three modules together compose the digital correlation system for detecting the first three Stokes parameters for the four different radiometer bands. Because of the large number of discrete ECL devices used, the power consumption is $\sim$100 W. The correlation system, along with the supporting IF system, occupies $\sim$30% of the space used within the scanhead. Table 2.1 lists the theoretical and practical sensitivities for the PSR X-band, Ka subband-1, and Ka subband-2 digital correlation polarimeters. The measured sensitivities were estimated by computing the standard deviation of a sample set of brightness temperature data. In general the actual sensitivities are $\sim$2 times the fundamental limits. The increased noise is attributed to RF and IF amplifier gain fluctuations (due to aircraft vibrations) and possibly bit-errors in the multiplication and accumulating circuitry.

Table 2.1: Sensitivities of the PSR Digital Correlation Polarimeters.

Channel	Theoretical	Measured
X-v	0.48	0.89
X-h	0.48	2.05
X-U	0.43	0.77
Ka_1-v	0.54	1.08
Ka_1-h	0.54	1.10
Ka_1-U	0.60	1.39
Ka_2-v	0.54	1.15
Ka_2-h	0.54	1.06
Ka_2-U	0.60	0.74

2.5 Discussion

The design techniques and correlator hardware described here were used in the airborne scanning polarimeter described in Chapter 3. Other polarimeter topologies are available such as the analog correlator based polarimeter or the additive polarimeter. Such systems, however, can exhibit Stokes parameter mixing that is not easily identifiable without sophisticated calibration techniques [20]. On the contrary, the digital polarimeter, if built to the proper design specifications, has the distinct advantage of negligible Stokes parameter cross-coupling and affords in-flight periodic calibration (see Chapter 4) of all polarimetric channel parameters.

Because of the relatively wide bandwidths required for earth remote sensing applications (typically tens to thousand of MHz), the digital correlator has not been considered for use in space until recently. With the advent of high-speed radiation-hardened digital logic, bandwidths of hundreds of MHz have now become realizable in sensitive, short integration-time, digital correlating radiometers. For example, a mixed-signal integrated circuit or multichip-module with the radiation hardened RF, IF, and CMOS digital subsystems could be readily developed for spaceborne polarimetry. The successful design and demonstration of this digital correlation polarimeter suggest that such a pursuit be undertaken.

CHAPTER 3

Polarimetric Scanning Radiometer

A description of the Polarimetric Scanning Radiometer (PSR) hardware, data processing, and the Labrador Sea experiment are presented in this chapter. The PSR is an airborne microwave imaging radiometer developed to obtain polarimetric microwave emission imagery of the ocean. The two-axis gimbal positioner provides conical, cross-track, and fixed-angle stare scanmodes. The PSR polarimetric radiometers were the first to utilize direct digital correlation for third Stokes parameter detection. During the Labrador Sea experiment, the PSR was used to obtain the first high-resolution ($\sim$1 km) multiband, polarimetric, conically-scanned microwave imagery of the ocean surface. The observations reveal the presence of both a systematic wind direction signature and a natural geophysical variability in the microwave emission over the ocean.

3.1 Polarimetric Scanning Radiometer

The Polarimetric Scanning Radiometer (PSR) is a versatile airborne imaging radiometer developed for the primary purpose of obtaining polarimetric microwave emission imagery of the ocean[1]. The design of the PSR is based upon the following set of scientific objectives:

- Radiometric objectives
  - Frequency coverage from X- to W-bands

[1]The PSR as used in this thesis was designed and built by the author, Prof. A.J. Gasiewski, with assistance from the following individuals: C. Campbell, E. Panning, E. Thayer, P. Chauhan, and M. Klein (of Georgia Tech); J. Baloun, M. Tucker, and B. Davidson (of Raytheon); and D. Brown (of GTRI).

  - Polarimetric capability (at least T_U)

- Imaging objectives

  - Scan modes: conical, cross-track, nadir stare and sky view
  - Field of view: nadir to 70° with full fore and aft views
  - Spatial resolution: 100 to 1500 meters (depending on altitude)
  - Pointing knowledge: $\lesssim 0.1°$ in elevation, $\lesssim 0.5°$ in azimuth

In addition to the requirements introduced by the scientific objectives, the following engineering constraints were also considered in the design:

- Aircraft platforms

  - NASA/DFRC DC-8 (smallest envelope)
  - NASA/WFF P-3B (first flights)
  - NASA/DFRC ER-2 (possible adaptation)

- Aerodynamic and environmental conditions

  - Dynamic pressure $\sim$ 570 psf maximum
  - Ambient temperature range from -40° to +40° C
  - Condensing and moist atmosphere

The PSR design effort resulted in a two-axis gimbal positioner with the radiometer hardware contained inside a moving scanhead. The scanhead houses four tri-polarimetric (first three Stokes parameters) microwave radiometers, the data system, and a video camera. The scanhead can be positioned so that the radiometers can view any angle within 70° elevation of nadir at any azimuthal angle, as well as external hot and ambient calibration targets. This configuration supports full conical (primary mode), cross-track, and fixed-angle stare scan modes.

Figure 3.1: The PSR situated in the support stand. The stand holds the PSR at the horizontal mounting plate.

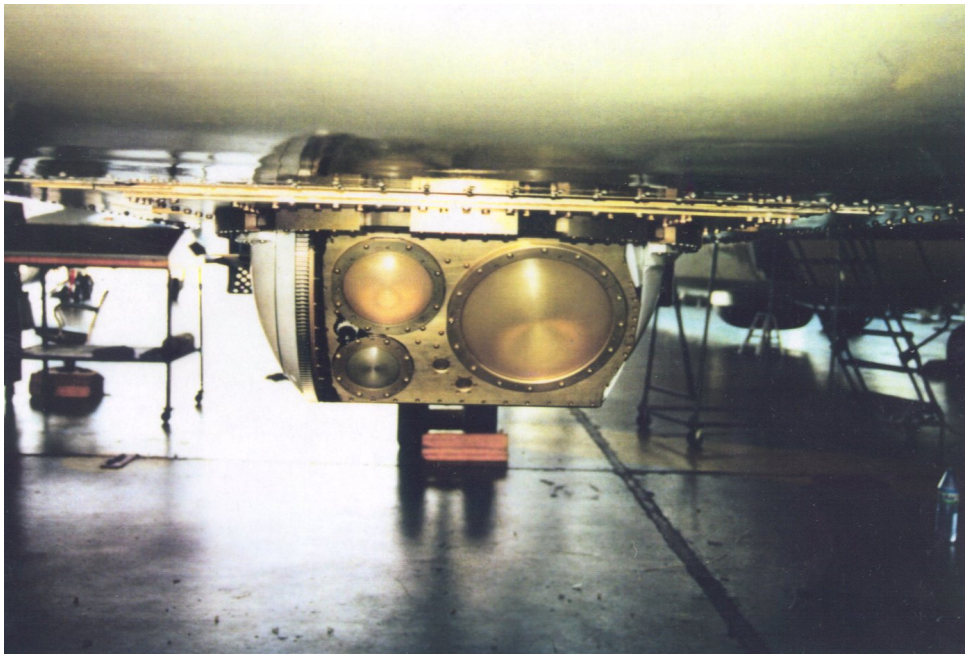

Figure 3.2: PSR scanhead installed in the NASA P-3. The three lenses visible on the face-plate are, in decreasing size, the X/Ka dual-band, K-band, and W-band antenna apertures, respectively.

The full positioner and scanhead are shown in Figure 3.1. In this photograph the PSR is sitting in its stand that is used for storage when not installed on the aircraft. The stand supports the PSR at its horizontal mounting plate. When installed in the aircraft, the horizontal plate is mounted flush with the aircraft body. Below the horizontal plate, approximately one half of the scanhead is exposed to the slip stream. This protrusion allows the radiometers an unoccluded view of the scene to $\sim 70^\circ$ from nadir. A photograph of the scanhead is displayed in Figure 3.2. All electrical power and signals going to and from the scanhead are transmitted through slip rings on both axes. The slip rings allow unrestricted angular motion of the scanhead about its azimuth and elevation axes.

The elevation axis of the scanhead is connected to a large 76 cm (30 inch) diameter ring bearing, which is mounted to the horizontal plate. The ring bearing assembly is designed to withstand the horizontal loading due to windage and aircraft acceleration. The

scanhead is attached to the azimuth axis by a yoke-like mount, which is also attached to the inner race of the ring bearing. Above the horizontal plate is the vertical support structure, which bears the vertical load of the azimuthal drive motor, calibration targets, and yoke. The load of the yoke and scanhead is distributed to the structure through the ring bearing and an additional upper bearing located at the top of the azimuth axis. Within the vertical support structure are the ambient and heated calibration loads. The loads are mounted to the fore and aft walls of the structure. The scanhead antennas view the targets when pointed either fore or aft and at 45° above the horizontal plane.

All of the PSR components are placed out of the aircraft slip stream, except for the bottom half of the scanhead. To reduce the dynamic pressure to ∼30% of its freestream value, a perforated fence is attached to the aircraft in front of the scanhead. This arrangement greatly reduces the drag on the scanhead, which also reduces the required motor torque. The P-3 integration is completed by an experimenter's-bay (actually the bomb-bay) faring that replaces the bay doors. The PSR and faring are shown installed on the P-3 in Figure 3.3.

3.1.1 Microwave and IF systems

The four microwave radiometers operate in the X (10.7 GHz), K (18.7 GHz), Ka (37.0 GHz), and W (89.0 GHz) frequency bands[2]. The typical radiometer comprises a dual polarization antenna, a dual channel superheterodyne receiver, IF amplifiers and square-law detectors with video amplifiers. There are eight analog radiometer outputs corresponding to 4 bands $\times$ 2 polarizations. The IF amplifiers also have outputs that are connected to the IF processing and high-speed digital correlation system for third Stokes parameter detection as well as dual-polarization total power detection. In the IF processing stage, the IF bands of the 37 and 89 GHz systems are sub-divided into six 500 MHz subbands. Including the 10.7 and 18.7 GHz systems there are a total of 24 digital radiometer outputs corresponding to 8 subbands $\times$ 3 Stokes parameters. Table 3.1 lists the characteristics for each of the four

[2]The W-band radiometer operated only for the transit flight from WFF to the Labrador Sea.

Figure 3.3: The PSR and bomb-bay faring installed on the NASA P-3.

Table 3.1: PSR Radiometer Specifications.

Band	X	K	Ka	W
Frequency (GHz)	10.4-10.8	18.4-19.0	36-38	86-92
Receiver type	SSB/HEMT	SSB/HEMT	DSB/LO	DSB/LO
IF bandwidth (MHz)	250	500	1000	2000
Receiver temp. (K)	1000	350	800	800
Sensitivity (K) for				
8 ms integration	0.7	0.18	0.28	0.18
3-dB beamwidth	8°	8°	2.3°	2.3°
3-dB spot size (km)				
at 5 km altitude:				
nadir	0.70	0.70	0.20	0.20
53° incidence	1.1×1.9	1.1×1.9	0.32×0.55	0.32×0.55

radiometers.

The antennas for the four radiometer systems can be seen in the photographs of the scanhead faceplate in Figure 3.4. The X- and Ka-band systems share a dual-band, dual-polarization, antenna. The X-band ortho-mode transducer (OMT) is a turnstyle type waveguide junction and has external coaxial cable and stripline signal combining, while the Ka-band OMT is a thru- and side-port waveguide structure. Single band antennas with thru- and side-port OMTs are used for the K- and W-band systems. To compensate for the relatively small focal lengths ($f/D \sim 1$) required to fit the various antennas in the scanhead, each antenna has a dielectric lens that increases the beam efficiency to $\gtrsim$90%. The lenses have concentric inside grooves for impedance matching and also serve as aerodynamically-shaped physical barriers between the outside air and the feedhorn cavities.

Connected to the antenna OMT output ports are the four dual-channel radiometers. The PSR radiometers are based upon the prototypical digital polarimeter as discussed in Chapter 2. The X-band radiometer is a single-sideband (SSB) superheterodyne receiver with 20 dB gain low noise amplifiers (LNAs) and 250 MHz band-pass filters (BPFs) in the RF paths. The mixers are double balanced and driven by common LO signals generated by a dielectric resonant oscillator (DRO). The LNAs, BPFs, mixers, and LO are discrete

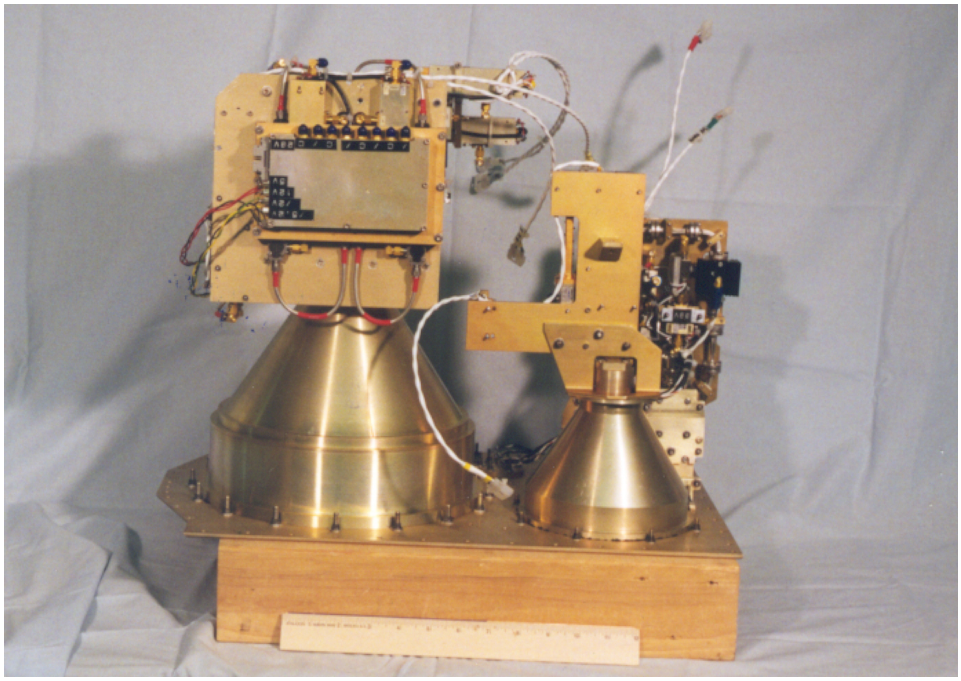

(a) front view

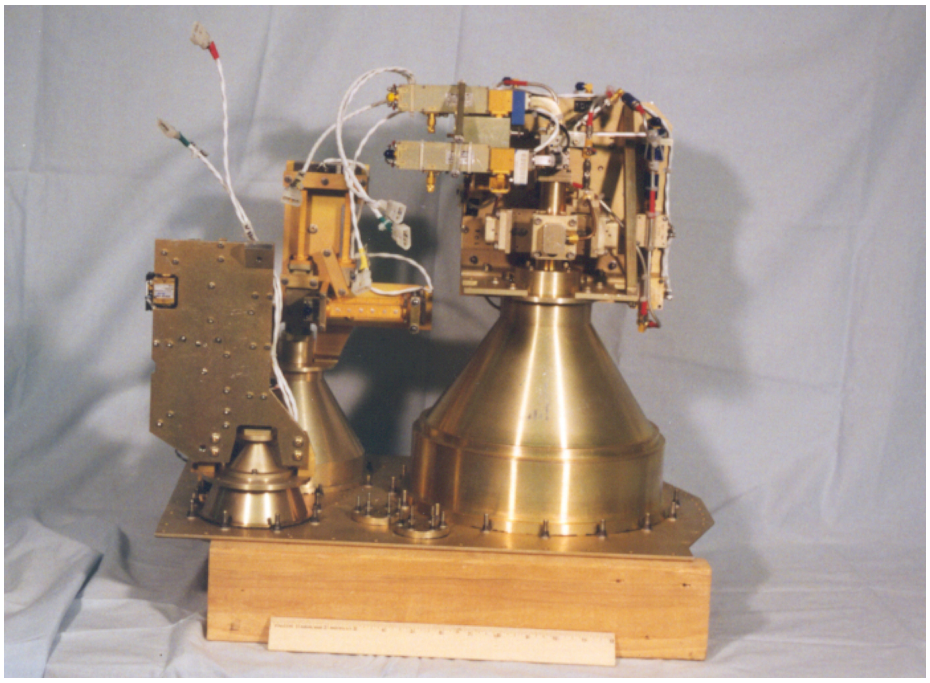

(b) back view

Figure 3.4: The PSR antennas and radiometers installed on the faceplate before installation into the scanhead.

components connected using SMA adaptors and coaxial cables. The mixer outputs are connected to IF amplifier modules with built in square-law detectors and video amplifiers. The video amplifier voltage output is from 0-10 V. Additional IF outputs are coupled off at $\sim$-20 dBm power level and fed to the IF processing and digital correlation system. The IF and power detection components described here are also replicated in the other three radiometers.

The K-band radiometer uses waveguide BPFs connected to the OMT outputs. After the first filter stage, the signals are fed to LNAs and image reject filters. The outputs of the second filter stage are sent to single-diode waveguide mixers, which are driven by a common Gunn diode LO. The phase of the LO signals in the K-, Ka-, and W-band radiometers can be adjusted to account for phase differences in the OMT arms and connecting waveguides. (A phase shifter is not needed in the X-band system because of the inherent symmetry of the turnstyle OMT.) The phase shifters are placed in one of the two LO paths and work by inserting a dielectric card into the waveguide, thus increasing the phase delay through the waveguide. Unlike the X- and K-band systems, the Ka- and W-band radiometers are based on double-sideband (DSB) receivers with single diode mixer front-ends. Preceding the mixers are waveguide isolators, which prevent LO leakage from the antennas. Such leakage has been shown to be a potential cause of radiometer gain modulation by reflection from, e.g., imperfect calibration targets [36]. Like the K-band radiometer, the mixers are driven by a single Gunn diode oscillator and the IF signals are processed as described above.

The intermediate frequency (IF) processing system uses IF (L-band and lower frequency) amplifier chains and subband division hardware to condition the IF output signals of the four radiometers for processing by the digital correlators. The IF amplifier chains are required to provide the necessary $\sim$5 dBm power to the digital correlators. The subband division hardware is required because the correlators have a Nyquist bandwidth $\lesssim$ 500 MHz while the Ka- and W-band IF signals have more than 500 MHz bandwidth. Referring to Table 3.1, a total of 4000 MHz of radiometric bandwidth distributed between the four

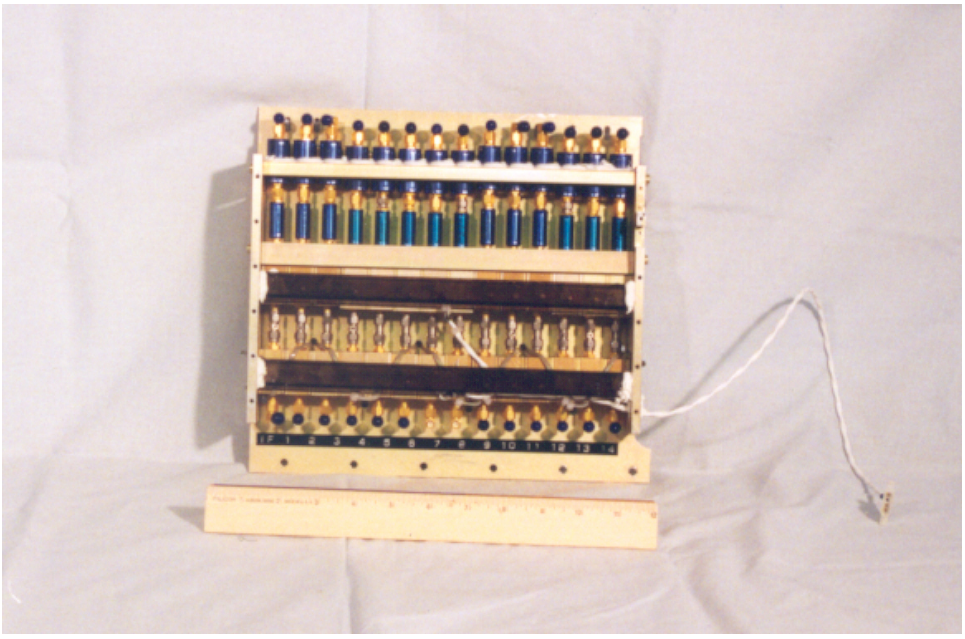

Figure 3.5: The IF plate contains the amplifiers and filters that prepare the IF signals for input to the digital correlators.

frequency bands is divided into eight 500 MHz subband channel pairs. The IF systems were fabricated using standard connectorized amplifiers, mixers, oscillators, and attenuators. All components were connected using female-female SMA adaptors or aluminum clad semi-rigid SMA coaxial cables.

The IF amplifier chains were composed of two discrete amplifiers and a low-pass filter (LPF) (see Figure 3.5). The first amplifier increases the -20 dBm signal from the radiometer to $\sim$ 0 dBm. A second medium-power amplifier adds an additional 10 dB of gain. This second amplifier has a 1dB compression point of $\sim$ 12 dBm which is sufficient for the correlator inputs. Following the output of the second amplifier stage is a 3 dB attenuator and LPF. The LPF has a 1 dB cutoff of 450 MHz, which ensures that there is no significant signal power above 500 MHz. A attenuator is needed because the high reflection coefficient of the LPF above 500 MHz could make the preceding amplifier unstable. With the insertion loss of the attenuator and the filter the power output is $\sim$ 5 dBm.

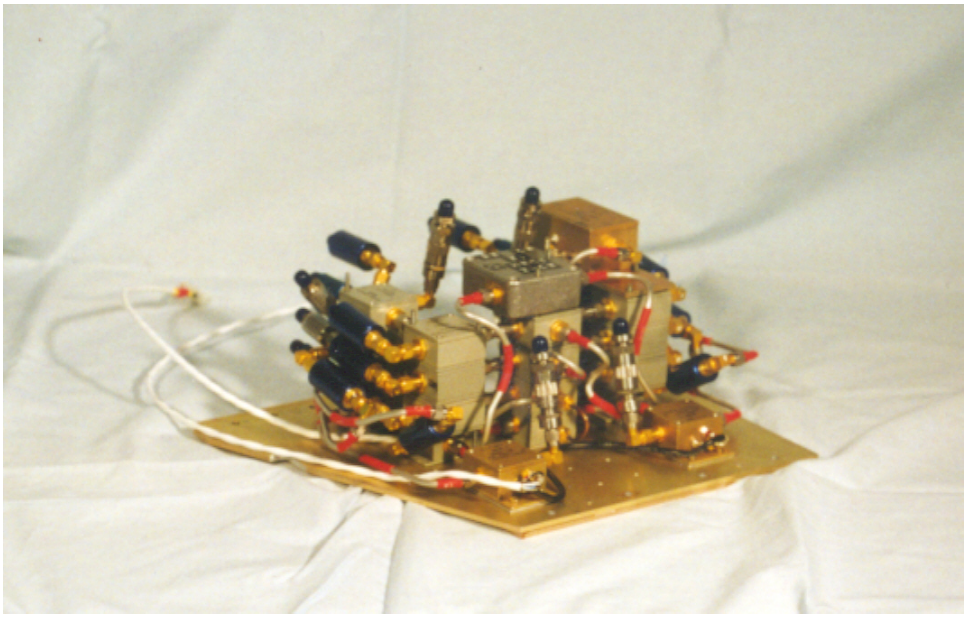

Figure 3.6: IF subband division hardware. This module demultiplexes the 1000 MHz IF of the Ka-band radiometer and the 2000 MHz IF of the W-band radiometer into six 500 MHz sub-bands.

The subband division hardware converts the 1000 MHz IF band of the 37 GHz radiometer into two 500 MHz sub-bands and converts the 2000 MHz IF band of the 89 GHz radiometer into four 500 MHz sub-bands. A photograph of the subband division hardware is shown in Figure 3.6. The Ka-band system includes a signal splitter, mixer and LO. The IF output of the Ka-band radiometer is sent to the signal splitter. One of the splitter outputs is connected directly to an IF amplifier chain (as described above). The filter in the IF chain truncates the IF bandwidth to include only the lower 500 MHz. The other output is mixed with a 1000 MHz LO signal. This operation reverses the frequency spectrum of the 1000 MHz IF band. The mixer output is then sent to an IF chain, which amplifies and passes the lower 500 MHz. Because of the frequency inversion performed by the mixer circuit, this second 500 MHz subband contains the content of the upper half of the 1000 MHz Ka-band radiometer output.

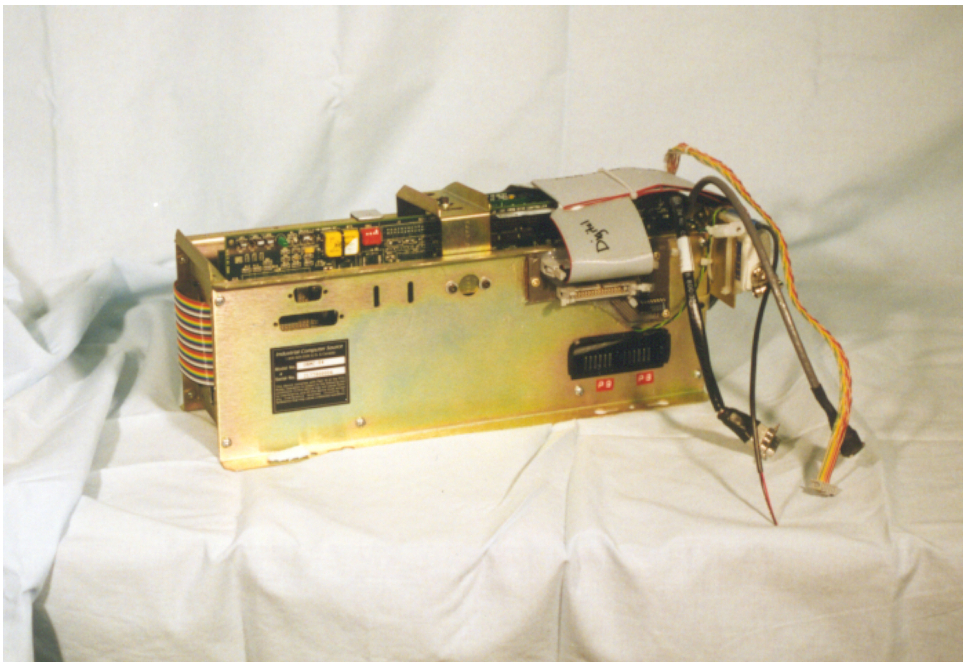

Figure 3.7: The scanhead 486 embedded computer system.

3.1.2 Data System and Motion Control

The analog and digital radiometer outputs are read and recorded by the data system, which includes three computers: one in the scanhead and two in the aircraft cabin. The main computer in the cabin provides the user interface, mass data storage, and motion control. The purpose of the scanhead computer is to acquire radiometer data and to control the digital correlators. The secondary cabin PC is used to control and store the output of the calibration load temperature measurement system. The three computers are linked via a 10 base-2 ethernet and time synchronized to better than 1 msec using a single IRIG-B time code source.

The scanhead computer system is based on an embedded 486 PC running the MS-DOS operating system. A photograph of the computer is shown in Figure 3.7. The PC has a four slot passive backplane architecture with the following hardware components:

- 486 single board computer with 8 MB RAM

- PCMCIA adaptor with
  - 4 MB SRAM solid state disk drive (SSDD)
  - 10 base-2 ethernet adaptor
- IRIG-B time code receiver
- Multi-function I/O card
  - 24-bit digital I/O interface
  - 16 channel 12-bit A/D converter interface

The configuration of these components is shown in Figure 3.8. The 486 computer boots from the 4 MB SSDD, which holds the disk and network operating systems. Sixteen bits of the digital I/O interface are used for the digital correlators. The remaining eight bits are used to address and set analog offset level generators which are used to shift the eight analog radiometer video outputs into the input voltage range of the scanhead PC 12-bit A/D converter. Three of the remaining A/D converter channels are used to measure the temperature via thermistors at three places within the scanhead. A fourth analog input is used as a receiver for a DC level shift signal, called the hardware trigger, that is generated by the motion controller.

The scanhead PC runs a Pascal data acquisition program, the main function of which is to operate the correlators and acquire radiometer data. The program's basic operation is given in Algorithm 1. Basic operation is as follows: the computer reads the radiometer data and stores it to the RAM disk. The output from the IRIG-B time code receiver is used to time-stamp all acquired data to 1 msec resolution. If the radiometers are not pointing at the scene or calibration loads, then housekeeping data is read and stored as well. Data are transferred from the RAM disk to the cabin PC approximately every 15 minutes or on command of the user via the hardware trigger. Secondary functions of the Pascal program are to set the digital correlator threshold levels and the analog radiometer

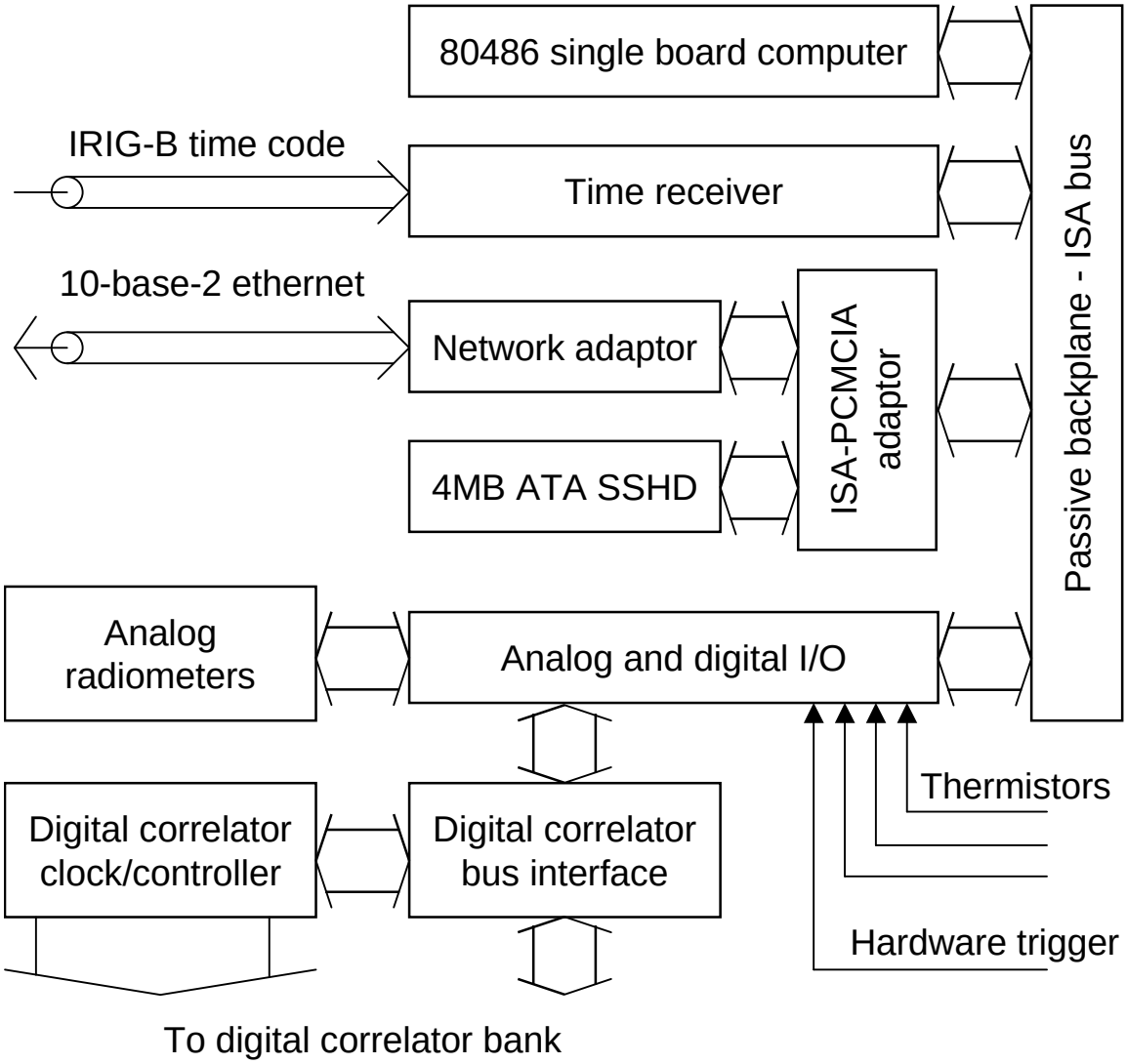

Figure 3.8: Block diagram of the scanhead data system.

offset voltages. This operation is done a few minutes after take-off and generally does not need to be repeated.

Algorithm 1 Main function of scanhead PC

```
loop
  repeat
    enable the correlator clock output
    write the previous sampled data onto the RAM disk
    read the analog radiometer data
    wait until correlator counting is complete
    read the digital correlator data
    if hardware trigger indicates transit state then
      read housekeeping data
      store housekeeping data
    end if
  until RAM disk full
  transfer RAM disk data to cabin PC hard disk drive
end loop
```

The main and secondary cabin computers are mounted in an equipment rack inside the aircraft cabin.A graphical user interface (GUI) was written in Microsoft Visual Basic for Windows 3.11 and is run on the main computer. The GUI allows the user to control the radiometer data acquisition; specify, start and stop different scanmodes; and view both housekeeping and radiometer data files. The secondary cabin computer controls and stores data from the calibration load temperature measurement system.

The motion control system is a microprocessor-based two-axis stepper motor controller with incremental encoder feedback. The high-torque stepper motors are driven by microstepping motor amplifiers and have 135 N-m (100 ft-lbf) output torque, which is sufficient to accelerate the scanhead during the scanning sequences and to overcome the drag from the aircraft slip-stream. Additionally, the motors are oil filled and designed to withstand a condensing atmosphere and temperatures ranging from -40 to +40°C. The azimuth motor has a 29:1 gear head integrated into the motor casing. A 1024 line optical encoder is driven via a 1:1 low backlash gear set for position feedback. An incremental encoder interface that operates using quadrature decoding provides 12-bits or (0.088°) of

position resolution. The elevation stepper motor also has an 11:1 reduction gear head and uses an additional pair of external gears to rotate the scanhead about the elevation axis. An additional 1024 line optical encoder is directly driven by the scanhead and provides elevation position feedback. The encoders are equipped with sealed bearings and an extended temperature range specification.

The programmable motor controller is mounted in the main cabin PC and receives commands from the user through the main computer GUI interface. Upon system startup, several motion control programs are downloaded to the controller's memory. These programs are executed at the operator's direction and include commands for homing the scanner and starting the different scan modes. Homing the scanner is achieved by using absolute position marks internal to the two encoders. The motion sequences for the two scan modes are described in Algorithms 2 and 3. During the scanning sequences the encoder counts are continuously read, timestamped, and stored on the hard disk by the main cabin computer. These data are used during post-processing to determine the pointing angles of the radiometers.

A final task of the motion controller is to set the voltage of the hardware trigger signal that is sent to the scanhead computer. The hardware trigger is a DC signal that specifies the state of the scanner during the scan sequence. For example, hardware trigger tags for the hot and cold calibration looks are used to extract the calibration measurements from a radiometer data file. The different hardware trigger states are listed in Table 3.2.

3.2 Data Post Processing

The PSR data processing is divided into several levels designated from Level 1.0 data through Level 2.3. The initial Level 1.0 data are the raw binary or ASCII files containing data recorded from different sources such as the analog and digital radiometers and the aircraft navigation system. The final data Level 2.3 contains fully calibrated radiometer data organized into flight segments. The various data levels and the processes required to

Algorithm 2 Conical Scanning Routine

```
reset motion system
begin motion azimuth ⇒ 180°, elevation ⇒ 45° {cold load}
hardware trigger ⇐ transit
loop
    wait until scanner motion complete
    hardware trigger ⇐ cold load
    pause 500 ms
    begin motion elevation ⇒ scene look angle {typically 53.1° off nadir}
    begin motion azimuth + ⇒ 1.5 revolutions {1 turn for scene, 0.5 for calibration}
    hardware trigger ⇐ transit
    wait azimuth == 270° {start of scan}
    hardware trigger ⇐ fore-scan
    wait azimuth == 90° {midpoint of scan}
    hardware trigger ⇐ aft-scan
    wait azimuth == 270° {end of scan}
    begin motion elevation ⇒ 45° {calibration look angle}
    hardware trigger ⇐ transit
    wait for motion to stop {azimuth now at 0° }
    hardware trigger ⇐ hot load
    pause 500 ms
    begin motion azimuth ⇒ 180° {move to cold load}
    hardware trigger ⇐ transit
end loop
```

Algorithm 3 Cross-track Scanning Routine

```
reset motion system
begin motion azimuth ⇒ 180°, elevation ⇒ 45° {cold load}
hardware trigger ⇐ transit
loop
    wait until scanner stops at cold load
    hardware trigger ⇐ cold load
    pause 500 ms
    begin motion azimuth ⇒ 90° {port side look}
    hardware trigger ⇐ transit
    wait azimuth == 115° {almost to port look}
    begin motion elevation + ⇒ 0.75 revolutions {0.5 turn for scene, 0.25 for calibra-
    tion}
    wait elevation == 70° off nadir {start of scan looking port}
    hardware trigger ⇐ port-scan
    wait elevation == nadir {midpoint of scan}
    hardware trigger ⇐ starboard-scan
    wait elevation == 70° off nadir {end of scan looking starboard}
    begin motion azimuth ⇒ 0° {hot load}
    hardware trigger ⇐ transit
    wait for motion to stop
    hardware trigger ⇐ hot load
    pause 500 ms
    begin motion azimuth ⇒ 180° {move to cold load}
    hardware trigger ⇐ transit
end loop
```

Table 3.2: PSR motion system hardware trigger states.

State	Description	Voltage (V)
0	stand-by	0.1
1	hot calibration look	0.8
2	cold calibration look	1.5
3	scanner transit (not scene or calibration data)	2.2
4	fore-look in conical scan	2.6
5	aft-look in conical scan	3.3
6	port side of cross-track scan	4.1
7 and 8	home position	4.8 and 4.6
9	starboard side of cross-track scan	5.4
10	cold sky calibration look	6.2
11	nadir look	6.9
12	reserved for expansion	7.5
13	not used	8.3
14	terminate data acquisition signal	9.1
15	system in startup mode	9.9

move from each level to the next are described in this section.

Before processing, all the aircraft sorties are segmented into a standard set of maneuvers, serialized and recorded in a maneuver flight catalog[19, Appendix L][3]. Each catalog entry is a specific maneuver associated with a serial number and designated by a date, range of times, and description. Typical flight maneuvers for the catalog entries are straight-and-level flight, constant altitude turns, and ascending and descending spirals. The Level 1.0 data are separated into segments according to serial number and all the data streams are compiled into individual files (one for each segment) that compose the Level 1.1 data. The Level 1.1 data is converted to Level 1.2 by linearizing the total-power digital radiometer output and registering all data streams to a common time grid by interpolation. Level 1.2 data is converted to Level 1.3 by organizing the time sequenced data into raster images. A raster image is a matrix with the scan number along one dimension and scan samples along the second dimension. The raster images are indexed along a third dimension according to

[3]R. C. Lum of Georgia Tech meticulously composed the flight catalog for the Labrador Sea experiment.

data type (e.g., radiometer channel, pitch, roll, timestamp, etc.). The digital data is quality checked for anomalous bit-errors (spikes) during conversion from Level 1.3 to Level 1.4.

The step from Level 1.4 to Level 2.0 or 2.1 is the first major calibration step. Level 2.0 data are calibrated brightness temperatures generated using single scan gains and offsets. Level 2.1 data are similar but calibrated using Wiener-filtered gains and offsets [2]. The digital correlator data are also linearized, corrected for offsets, and converted to calibrated third Stokes parameter brightness temperatures. Level 2.0 and 2.1 data are corrected for pitch and roll variations, which results in Level 2.2 and 2.3 data, respectively. Level 2.3 is the highest quality level of PSR calibrated brightness temperatures available. Table 3.3 lists the different data types available in the Level 2.3 indexed raster format.

3.3 Pitch and Roll Correction

Deviations in elevation and polarization rotation angles from their nominal values will introduce unwanted perturbations in the measured Stokes vector. Such deviations are continuously present and changing throughout a conical scan due to variations in the aircraft attitude (i.e., pitch and roll angle variations). To facilitate the interpretation of brightness imagery, it is advantageous to reference all brightness temperature measurements obtained during a conical scan in level flight to a constant elevation angle (e.g., the SSM/I nadir angle of 53.1°). A first-order correction can be made such that the corrected brightness temperature is:

$$T_B(\theta_0) = T_B(\theta) - (\theta - \theta_0) \left. \frac{dT_B}{d\theta} \right|_{\theta=\theta_0} \tag{3.1}$$

where θ_0 and θ are the nominal and true elevation angles, respectively.

The elevational sensitivity of brightness temperature (the derivative $dT_B/d\theta$) was measured using the cross-track scan mode during the spiral flight patterns over the Labrador Sea. The spirals were flown with a constant bank angle and the PSR radiometers were scanned across the aircraft heading. This configuration produced brightness measurements

Table 3.3: PSR Level 2.3 data types.

Index	Description	Units
1	X-band, V-pol, analog radiometer	K
2	X-band, H-pol, analog radiometer	K
3	K-band, V-pol, analog radiometer	K
4	K-band, H-pol, analog radiometer	K
5	Ka-band, V-pol, analog radiometer	K
6	Ka-band, H-pol, analog radiometer	K
7	W-band, V-pol, analog radiometer	K
8	W-band, H-pol, analog radiometer	K
9	X-band, V-pol, digital radiometer	K
10	X-band, H-pol, digital radiometer	K
11	X-band, U-channel, digital radiometer	K
12	K-band, V-pol, digital radiometer	K
13	K-band, H-pol, digital radiometer	K
14	K-band, U-channel, digital radiometer	K
15	Ka-band, V-pol, digital radiometer; subband 1	K
16	Ka-band, H-pol, digital radiometer; subband 1	K
17	Ka-band, U-channel, digital radiometer; subband 1	K
18-20	same as 15-17, except subband 2	K
21	W-band, V-pol, digital radiometer; subband 1	K
22	W-band, H-pol, digital radiometer; subband 1	K
23	W-band, U-channel, digital radiometer; subband 1	K
24-26	same as 21-23, except subband 2	K
27-29	same as 21-23, except subband 3	K
30-32	same as 21-23, except subband 4	K
33	azimuth encoder	deg
34	elevation encoder	deg
35	aircraft latitude	deg N
36	aircraft longitude	deg E
37	aircraft heading	deg
38	pressure altitude	feet
39	GPS altitude	feet
40	aircraft pitch	deg
41	aircraft roll	deg
42	IRIG-B time stamp	ms past midnight
43	pointing azimuth angle	deg
44	pointing nadir angle	deg
45	polarization rotation	deg

Table 3.4: Elevational brightness sensitivities for X- through Ka-bands at 53.1° as measured by PSR during the Labrador Sea experiment.

Date	3/3/97	3/4/97	3/7/97	3/9/97
Time (UTC)	1515	1645	1630	1455
X-v	1.61	1.55	1.82	1.86
X-h	-0.910	-0.809	-0.931	-0.919
K-v	1.50	1.42	1.76	1.82
K-h	-0.843	-0.794	-0.933	-0.926
Ka-v	1.23	1.16	1.33	1.54
Ka-h	-0.622	-0.412	-0.370	-0.642

for elevation angles from nadir to ∼70° incidence. For example, the March 9, 1997 measurements of T_v and T_h versus θ are plotted in Figures 3.9-3.11. These measurements were made at 1455 UTC at an altitude of ∼450 m (1500 ft). The elevational sensitivities of the brightness temperatures at $\theta = 53.1°$ for several representative flights are listed in Table 3.4.

The third Stokes parameter is primarily sensitive to polarization rotation rather than elevation angle variations. Like T_v and T_h, T_U can be rotationally corrected using the appropriate terms from the polarization basis transform [8]:

$$T_U(\alpha = 0) = T_U(\alpha) + (T_h - T_v)\sin(-2\alpha) \tag{3.2}$$

where α is the polarization rotation angle.

Aircraft pitch and roll variations are the primary source of elevation angle and polarization rotation deviations. Sample records of the P-3 pitch and roll from 2014 UTC on March 4, 1997 as acquired from the aircraft's ARINC 429 10 Hz data stream are plotted in Figure 3.12. The ∼0.3° pitch and roll variations can cause brightness perturbations of ∼0.3-0.6 K. A pitch and roll data correction algorithm was developed to compensate for unplanned aircraft attitude variations.

The correction algorithm is based on calculating the true elevation angle and polarization rotation given the PSR position encoder values and the aircraft pitch and roll data. First, the antenna pointing and horizontal polarization vectors are transformed into

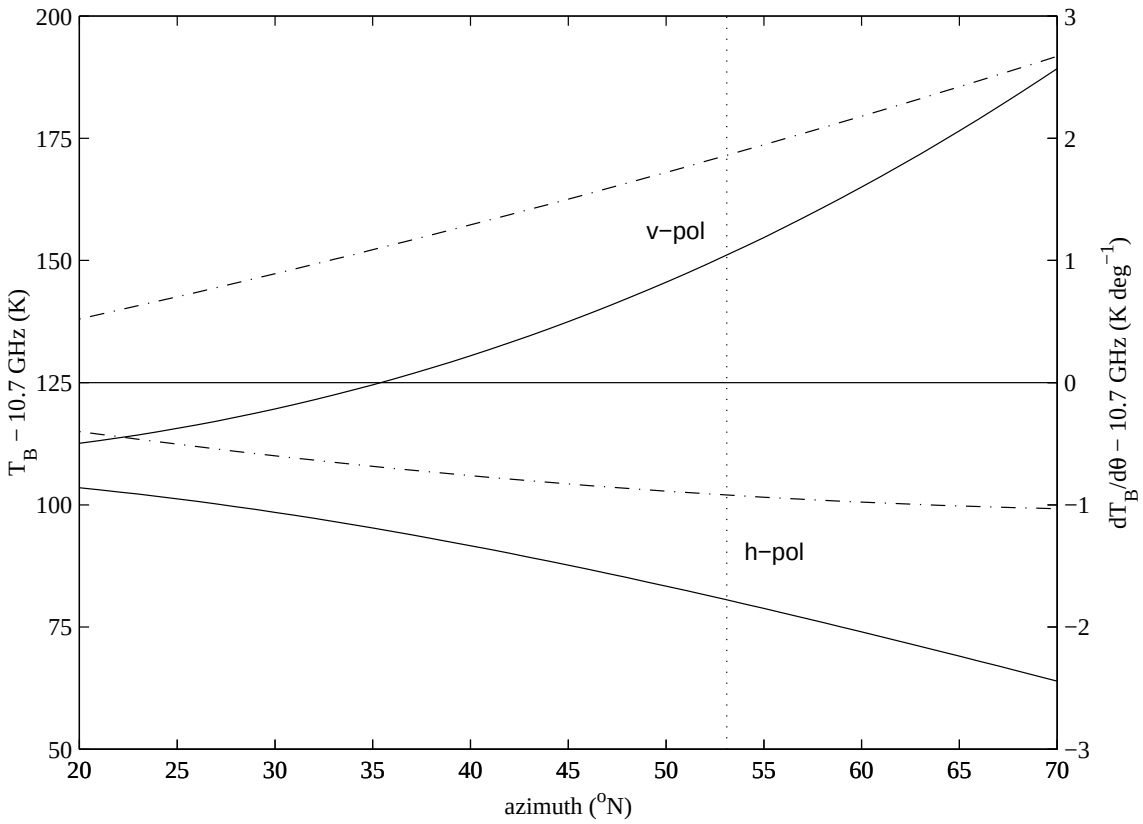

Figure 3.9: Example of brightness temperature sensitivity to incidence angle for X-band. The solid lines represent the actual brightness temperature and are keyed to the left axis. The dashed lines are the elevational sensitivities and are keyed to the right axis. The vertical dotted line denotes the typical incidence angle of 53.1°. The numerical values for the sensitivities are tabulated in Table 3.4. These data were measured at 1455 UTC on March 9, 1997 at an altitude of ∼450 m.

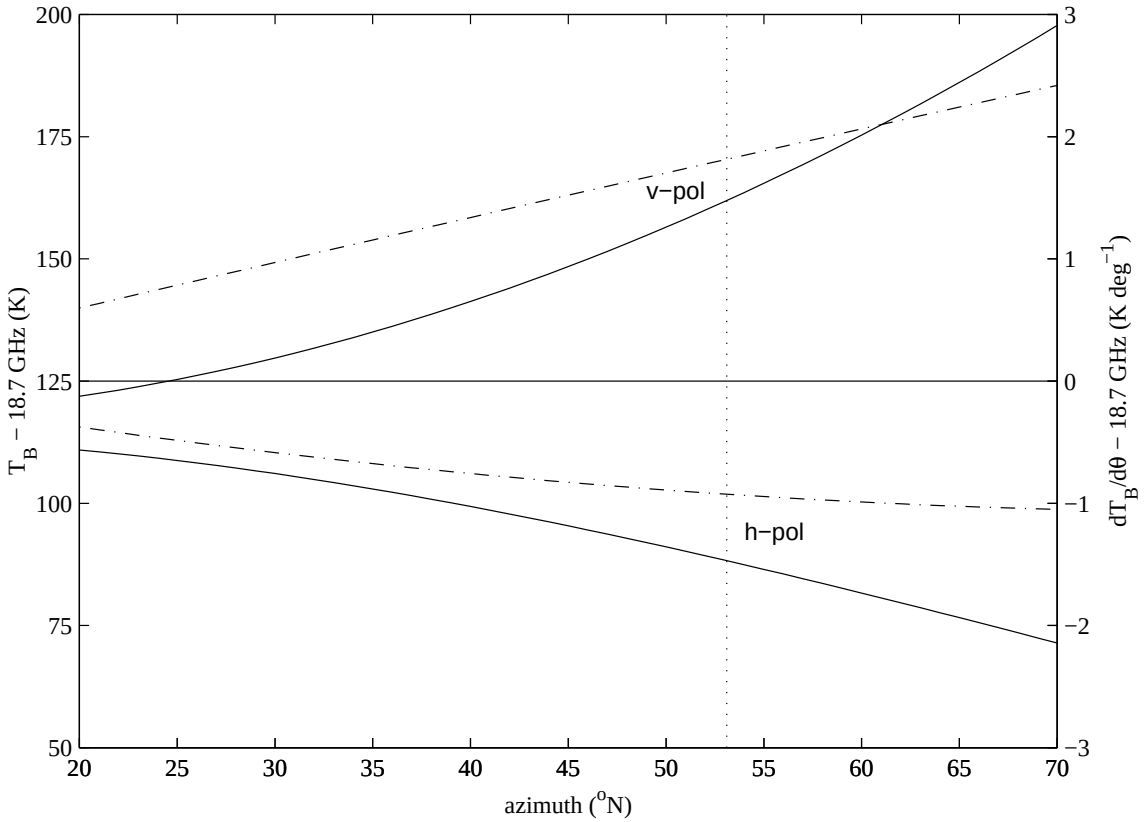

Figure 3.10: Same as Figure 3.9 except for K-band.

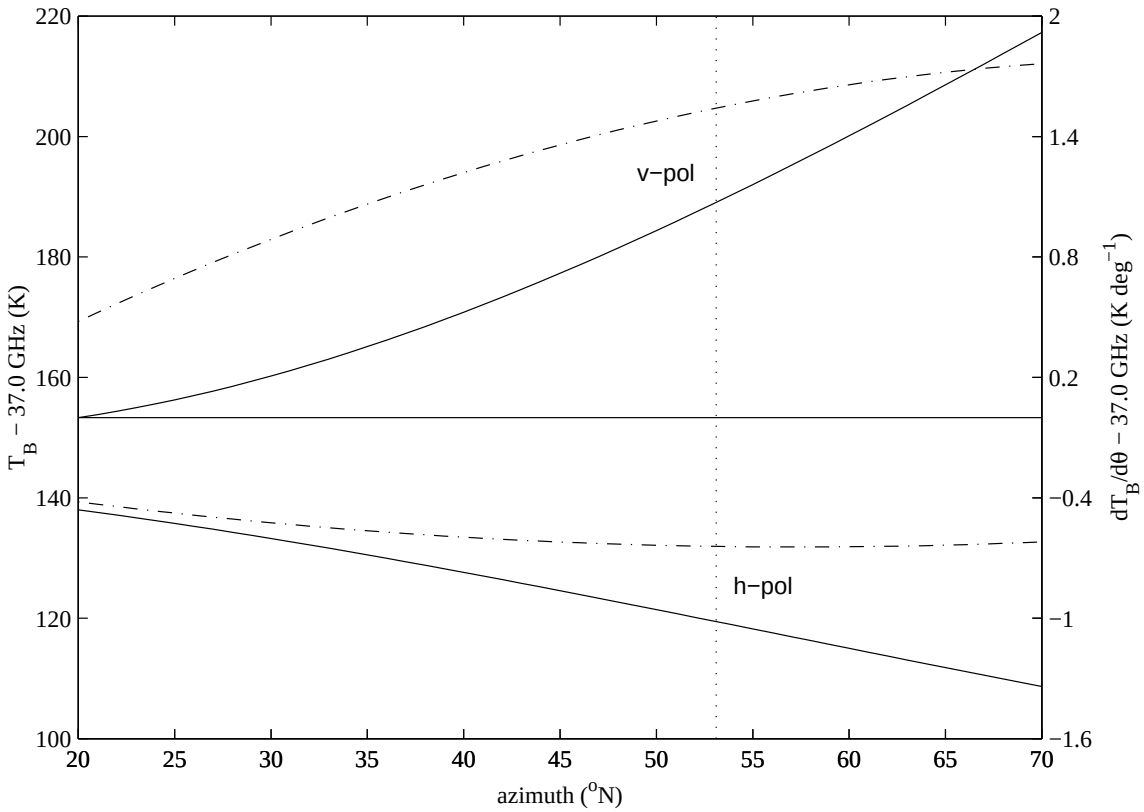

Figure 3.11: Same as Figure 3.9 except for Ka-band.

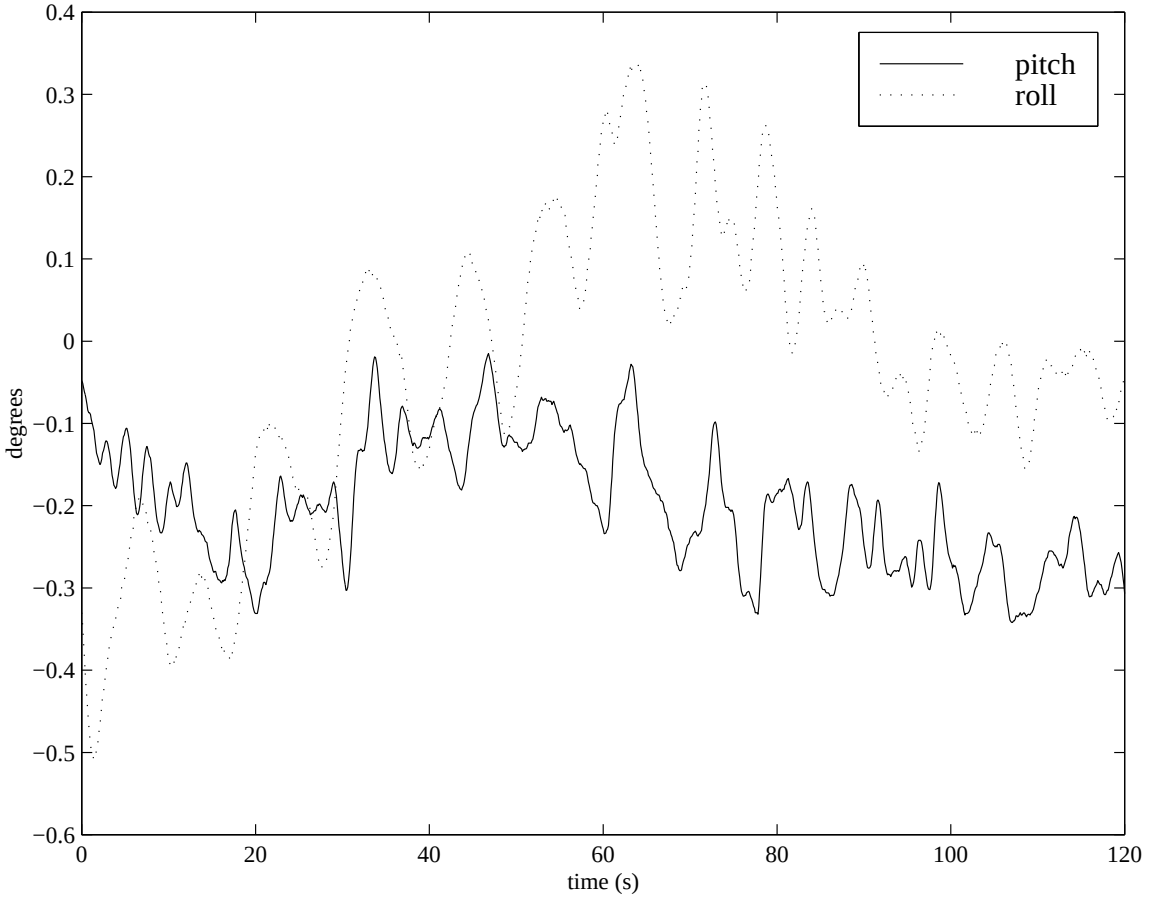

Figure 3.12: Sample of P-3 pitch and roll data from 2014 UTC on March 4, 1997.

the Earth's (world) coordinate frame using five rotational transforms. Then, the azimuth, elevation (from nadir), and polarization rotation angles are computed from the output vectors. Once these angles are found, the corrections to the brightness temperatures can be made using (3.1) and (3.2).

The transformation of the antenna pointing and polarization vectors to the world coordinate frame is achieved using five rotational transform operations [26]. These rotations are performed about the scanhead elevation and azimuth axes, the aircraft roll and pitch axes, and finally the compass heading axis. Figure 3.13 illustrates each of these coordinate frame rotations. In vector notation the compound transformation is

$$\widehat{\overline{X}} = \overline{\overline{R}}_z^{-1}(\gamma_{\text{head}}) \cdot \overline{\overline{R}}_y^{-1}(\gamma_{\text{pitch}}) \cdot \overline{\overline{R}}_x^{-1}(\gamma_{\text{roll}}) \cdot \overline{\overline{R}}_z^{-1}(\gamma_{\text{az}}) \cdot \overline{\overline{R}}_y^{-1}(\gamma_{\text{el}}) \cdot \widehat{\overline{x}} \tag{3.3}$$

where $\widehat{\overline{x}}$ is the pointing or polarization unit vector in the antenna coordinate frame and $\widehat{\overline{X}}$ is the respective unit vector in the world coordinate frame. The antenna pointing unit vector is $\hat{k}_A = (0, 0, 1)^T$ and the horizontal polarization unit vector is $\hat{h} = (0, 1, 0)^T$. The rotation operators are given by the following:

$$\overline{\overline{R}}_x^{-1}(\gamma) = \begin{bmatrix} 1 & 0 & 0 \\ 0 & \cos\gamma & -\sin\gamma \\ 0 & \sin\gamma & \cos\gamma \end{bmatrix} \tag{3.4}$$

$$\overline{\overline{R}}_y^{-1}(\gamma) = \begin{bmatrix} \cos\gamma & 0 & \sin\gamma \\ 0 & 1 & 0 \\ -\sin\gamma & 0 & \cos\gamma \end{bmatrix} \tag{3.5}$$

$$\overline{\overline{R}}_z^{-1}(\gamma) = \begin{bmatrix} \cos\gamma & -\sin\gamma & 0 \\ \sin\gamma & \cos\gamma & 0 \\ 0 & 0 & 1 \end{bmatrix} \tag{3.6}$$

The azimuth, elevation, and polarization angles can be found from the different

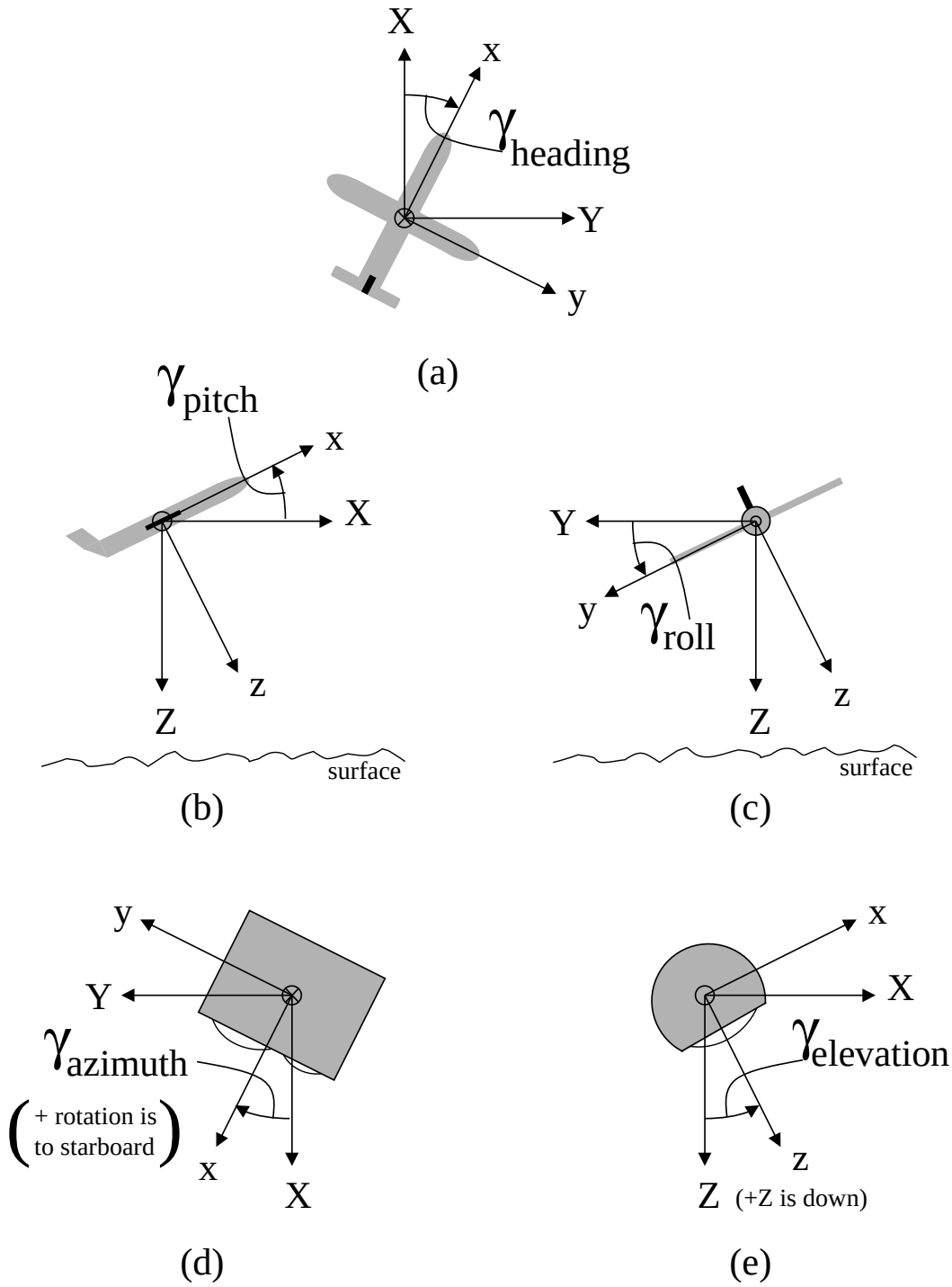

Figure 3.13: The five rotational operations used to compute the PSR pointing and polarization vectors in the world coordinate frame.

vector components. The true elevation angle θ is

$$\theta = \tan^{-1}\left(\frac{\sqrt{(\hat{k}_x^2 + \hat{k}_y)^2}}{\hat{k}_z}\right) \tag{3.7}$$

where $\hat{k}_x$, $\hat{k}_y$, and $\hat{k}_z$ are the x, y, and z components of the antenna pointing vector in the world coordinate frame. The true azimuth angle ϕ, in the compass rose orientation, is

$$\phi = \tan^{-1}\left(\frac{\hat{k}_y}{\hat{k}_x}\right) \tag{3.8}$$

The polarization rotation angle is found by projecting the polarization vector in world coordinate frame $\hat{\bar{p}} = (\hat{h}_x, \hat{h}_y, \hat{h}_z)^T$ into the spherical world coordinates and using the inverse tangent function:

$$\alpha = \tan^{-1}\frac{\hat{h}_x \cos\theta\cos\phi + \hat{h}_y \cos\theta\sin\phi - \hat{h}_z \sin\theta}{-\hat{h}_x \sin\phi + \hat{h}_y \cos\phi} \tag{3.9}$$

The angle α has a righthanded sense about the $\hat{k}_A$-axis. Note that the azimuth angle ϕ is undefined if the true elevation angle is zero ($\theta \equiv 0$). In this case, the polarization angle is defined as

$$\phi = \tan^{-1}\left(\frac{\hat{h}_y}{\hat{h}_x}\right) \tag{3.10}$$

The need for pitch and roll correction is strikingly illustrated in Figure 3.14. In this figure, the solid curve is the average T_U azimuthal signature, corrected for polarization basis rotations, over the Labrador Sea at 1555 UTC on March 4, 1997. The surface winds were reported to be 279° at 16 m s^{-1}, which coincides well with the observed T_U variation. The zero-crossing and steep slope near 279° is characteristic of the the upwind direction. The dotted curve, however, is the average uncorrected T_U azimuthal signature. Note, that the character of the two curves is quite different. The pitch and roll correction removes polarization rotation errors that mask the true nature of the signal. To further verify the performance of the pitch and roll correction, the squared-correlation coefficient between T_v (or T_h) and θ was computed before and after correction for several flight tracks throughout

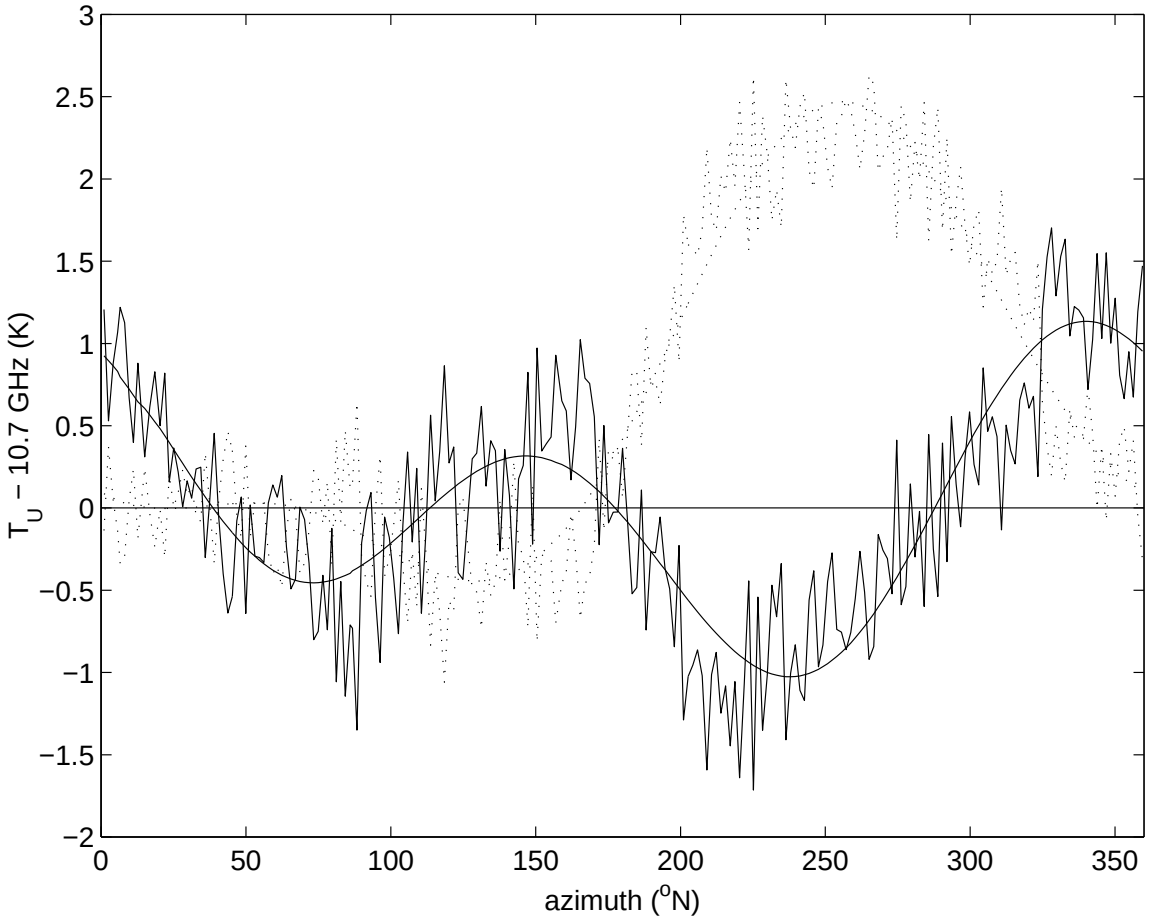

Figure 3.14: Third Stokes parameter data illustrating the need for pitch and roll correction. The data drawn with the dashed line is an average scan output of T_U without pitch and roll correction. The solid line is T_U with pitch and roll correction. The wind direction was 279° according to *Knorr* measurements and the corrected T_U measurements agree. The characteristic of the T_U curve that indicates the upwind direction is its zero-crossing and steep slope near 279°. The down wind direction is indicated by a zero-crossing but gradual slope near 99°.

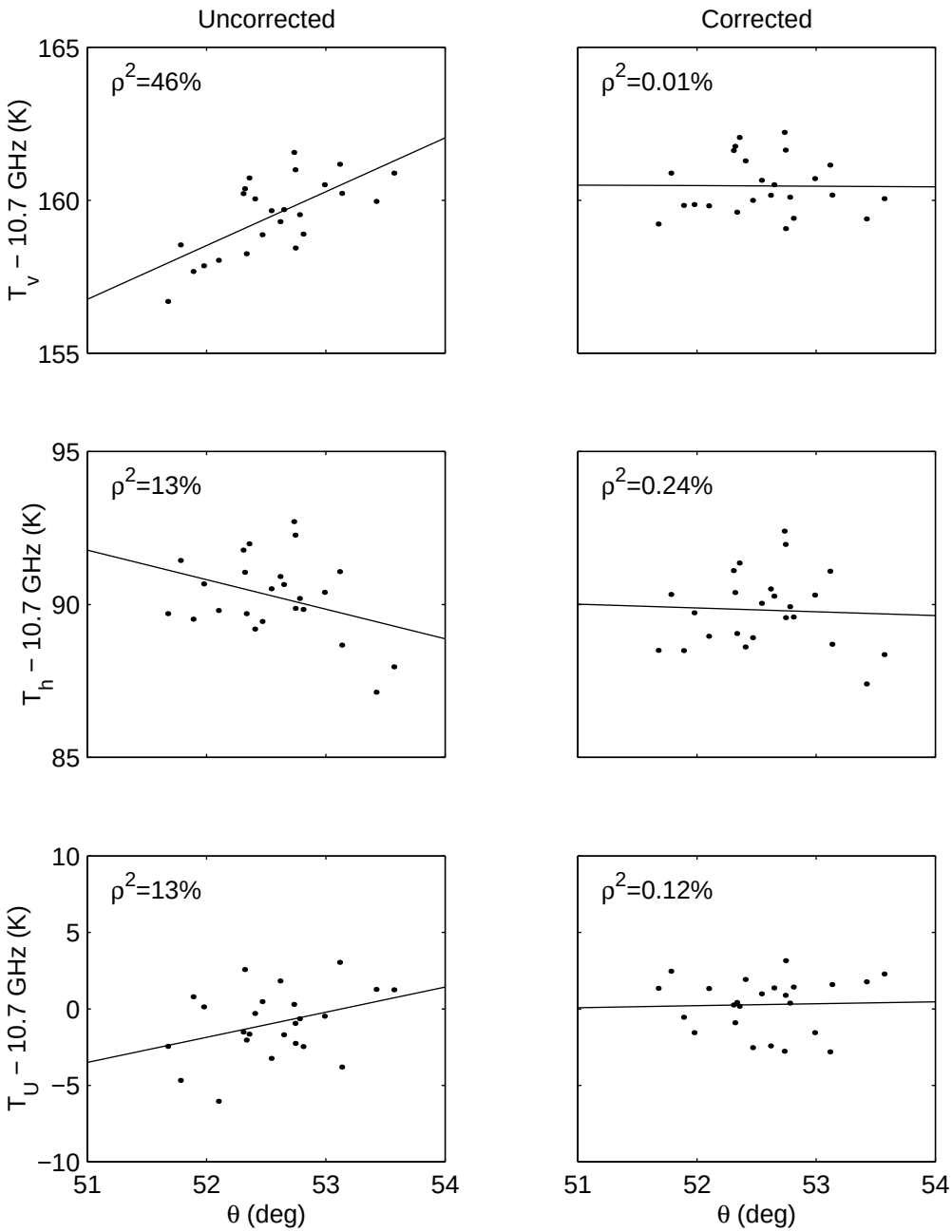

Figure 3.15: Uncorrected and corrected X-band brightness temperatures versus elevation angle. The data brightness data, denoted by the scattered points, were collected on March 9 from 14:12-14:20 UTC. The linear regression is plotted by a solid line. As indicated by the values of ρ^2, the correction algorithm reduced the contribution of aircraft attitudinal variations from 13%-64% to 0.24%-0.01%.

the Labrador Sea data set (see Figure 3.15). As seen in the left column of plots, 13%-46% of the variation in the uncorrected brightness temperatures is attributable to aircraft attitudinal changes. The correction algorithm reduced this dependence to 0.24%-0.01%, which is illustrated by the nearly horizontal lines in the right hand plots.

3.4 Labrador Sea Experiment

The Labrador Sea experiment consisted primarily of six data flights from March 1 to March 10, 1997 over the Labrador Sea along with three local data flights of the Atlantic Ocean near Wallops Island, Virginia. The objective of the experiment was to observe high wind speed ($\gtrsim$10 m s^{-1}) conditions to verify the utility of passive polarimetric wind vector sensing in high seas. The primary data products were the ocean surface emission harmonics and high-resolution polarimetric microwave imagery of the ocean. The imagery provided unique observations with which to demonstrate the retrieval of ocean wind vector fields using a variety of channel and viewing two-look configurations. Flight patterns were conducted at ~6.1 km (20,000 ft) altitude and included hex-cross patterns (described in Chapter 5), patrols (coincident flight legs flown on opposite headings), ascending and descending spirals with constant bank angle, and long (>100 km) transects. The March 1 flight departed from the NASA Wallops Flight Facility (WFF), Wallops Island, Virginia and terminated in Goose Bay, Labrador, Canada. Sorties on March 3, 4, 7 and 9 originated from Goose Bay. The March 9 flight terminated in Brunswick, Maine. The return flight to WFF on March 10 included maneuvers over two ocean buoys off the eastern shores of Virginia and Maryland.

During the Labrador Sea experiment, the NASA WFF P3-B Orion aircraft was not only outfitted with the PSR, but also included the follow instruments:

- CSCAT: C-band scatterometer (University of Massachusetts)
- KASPR: Ka-band conically-scanning polarimeter (UMASS)

- KAPOL: Ka-band nadir viewing polarimeter (NOAA/Environmental Technology Laboratory)
- CWVR: 21 and 31 GHz zenith viewing cloud and water vapor radiometer (ETL)
- ROWS: radar ocean wave spectrometer (NASA/WFF)
- GPS dropsonde station - NCAR

The flights concentrated over the Woods Hole Oceanographic Institute's *R. V. Knorr*. Scientists aboard the *Knorr* operated a suite of surface meteorological instruments and launched daily radiosondes[4]. The flights were also coordinated to underfly DMSP SSM/I, NSCAT, and ERS-2 scatterometer.

The PSR scanning mechanism operated reliably for all data flights. Ambient conditions met design expectations with temperatures as low as -50°C. The internal temperature of the scanhead was typically near 0°C at altitude. The following PSR radiometer systems provided quality data for the six flights:

- X-band analog and digital
- K-band analog
- Ka-band analog (H-pol) and digital subbands 1 and 2

The primary cause for the malfunction of the remaining systems was the mechanical coupling of the scanning motion to RF components. This phenomenon was evidenced by large ($\sim$10-50 K) and somewhat systematic output variations correlated to azimuth encoder values. The W-band radiometer was non-operational due to mixer and LO failure. The digital correlation system performed well, with the exception of a few instances when the aircraft DC voltage supply dropped below the expected 28 VDC. Otherwise the operation of the

[4]Peter Guest of the Naval Postgraduate School provided surface truth and radiosonde data measured from aboard the *Knorr*.

digital correlation system was a successful technology demonstration and provided important new polarimetric observations at 10.7 and 37.0 GHz. A comprehensive description of the Labrador Sea experiment, including a detailed flight catalog, can be found in [19].

3.4.1 PSR Microwave Imagery of the Ocean Surface

Radiometric brightness imagery obtained using the PSR reveals both a systematic wind direction signature and stochastic variability of geophysical origin. The data presented herein were obtained from 1632-1642 UTC during the Labrador Sea flight on March 4 and contains 37 azimuthal scans processed according the to procedures detailed in the previous sections and calibrated as described in Chapter 4. The wind speed and direction were 16.2 $\mathrm{m\,s^{-1}}$ at 270° as measured using *Knorr* wind sensors and the ocean swell was ∼5 m (16 ft) from 275° according to observers aboard the *Knorr*.

As was introduced in Chapter 1 (Figure 1.1) and will be thoroughly discussed in Chapter 5, the elements of the Stokes vector contain systematic ∼1-2 K azimuthal variations over the ocean at a fixed elevation angle that are highly correlated to the near-surface wind direction. Such variations can be seen in the average azimuthal scans for the March 4 data as shown in Figure 3.16. The vertical polarization exhibits a first-order harmonic variation in the azimuth coordinate. The harmonic variation is even-valued with respect to the wind direction (i.e., it is cosinusoidal) and has its peak value near the upwind azimuth angle of 270°. The horizontal polarization also exhibits a cosinusoidal variation with respect to the wind direction, however, the variation has a dominant second-order harmonic dependence that is negative in sign. This characteristic is illustrated by the nulls in brightness temperature near the upwind (270°) and downwind (90°) directions and the peaks in the cross-wind directions (0 and 180°). The third Stokes parameter, conversely, is in phase quadrature with T_v and T_h. The averaged T_U scans have a dominant first-order harmonic character, but are sinusoidal with respect to the wind direction in nature. These properties are evident in the righthand plots of Figure 3.16. The value of T_U is zero near the upwind and downwind directions, while the positive peak is seen to be 90° clockwise from upwind

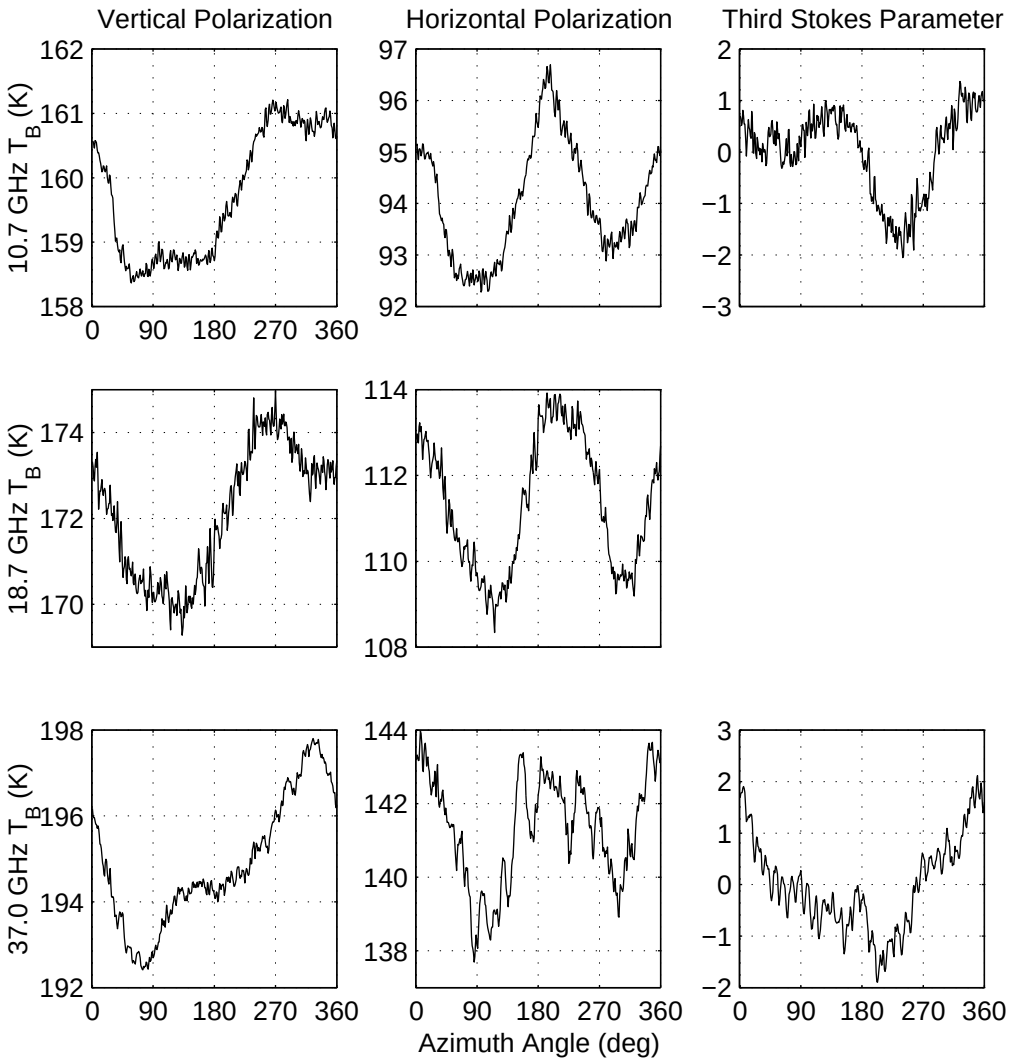

Figure 3.16: PSR averaged azimuthal scans from 1632-1642 UTC on March 4, 1997 illustrating the systematic wind direction dependence of the first three Stokes parameters at 10.7, 18.7, and 37.0 GHz. (Data for T_U at 18.7 GHz was unavailable.) The wind was 16.2 $\mathrm{m\,s^{-1}}$ at 270° as reported by the *Knorr*.

(0°) and the negative is 90° counterclockwise (180°). This cross-wind asymmetry is indicative of the phase-quadrature nature of T_U compared to T_v and T_h. All of the average features of T_v, T_h, and T_U can be seen not only in the average scan plots of Figure 3.16, but in the brightness imagery described in the remainder of this section.

The systematic wind direction signature is revealed in the PSR X, K, and Ka band raster images presented in Figures 3.17 through 3.19. The two coordinates in the raster format are the azimuth look angle and the along track position or scan number and the color of the pixels represents the brightness temperature as indicated by the accompanying key. In the T_v imagery (upper left image within each figure), the first-order harmonic dependence is clearly evidenced by brightening in the upwind direction (recall the cosinusoidal characteristic). The second-order azimuthal harmonic is evident in the T_h images and can be seen as increased brightness temperature in the cross-wind directions, while the two streaks of lower brightness temperatures are in the up and downwind directions. Finally, the odd symmetry of the T_U signature is seen in the third Stokes parameter imagery as positive values to the right of the wind direction and negative values to the left.

The wind direction signature can also be seen in the geolocated imagery display in Figures 3.20 through 3.22. The information for each polarization is divided into fore- and aft-looks, such that two swaths are displayed for each polarization. In the T_v imagery, the effect of the west wind on the brightness temperature can be seen as a warming along the western edge of the swath because the radiometers are pointed to the west. Because the 215° flight track heading is nearly cross-wind, the T_h imagery exhibits increased values along the middle of the swath (with the radiometers pointing cross-wind) and decreased amplitude along the swath edges (with the radiometers pointing upwind and downwind). Furthermore, the T_U imagery possesses a strong fore/aft-look contrast and values near zero along the swath edges. These characteristics are indicative of the quadrature phase of the azimuthal dependence of the third Stokes parameter, with positive and negative extrema in the cross-wind look directions. Note, that while the wind direction signature is not obvious in the 37.0 GHz T_U raster imagery, the geolocated imagery clearly reveals the cross-wind

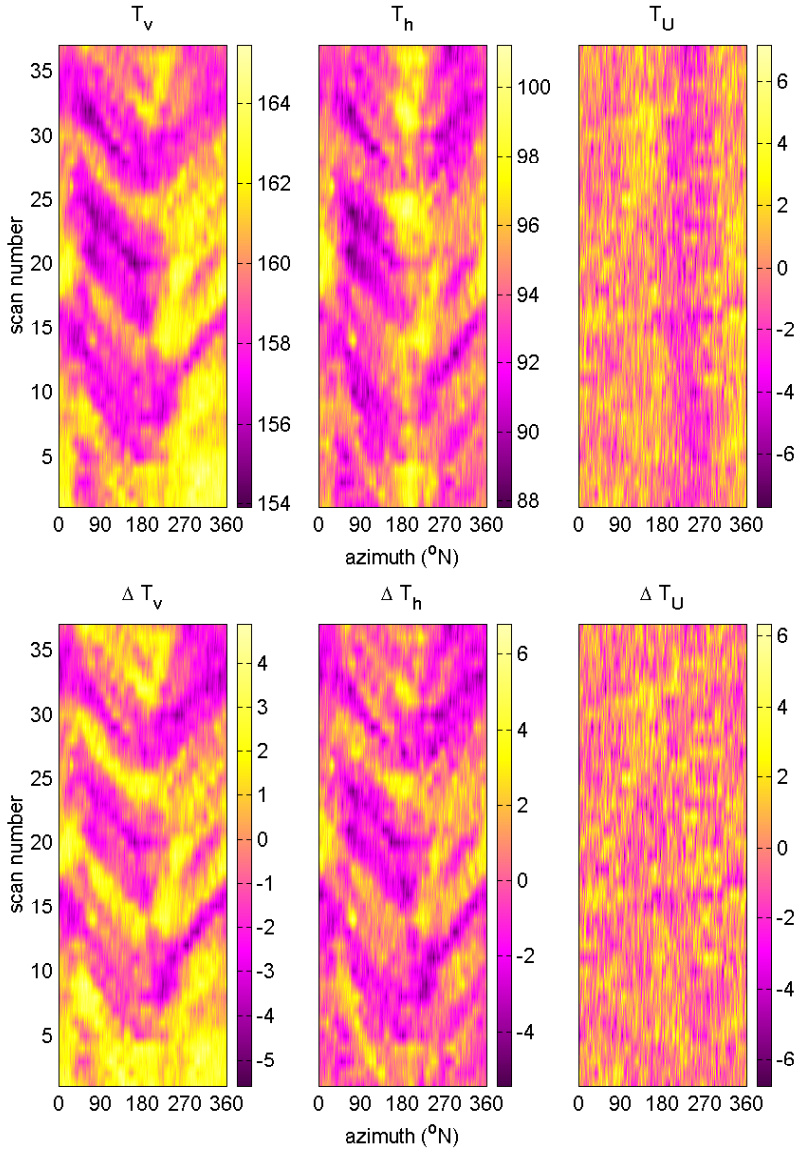

Figure 3.17: PSR 10.7 GHz polarimetric microwave imagery of the ocean surface.

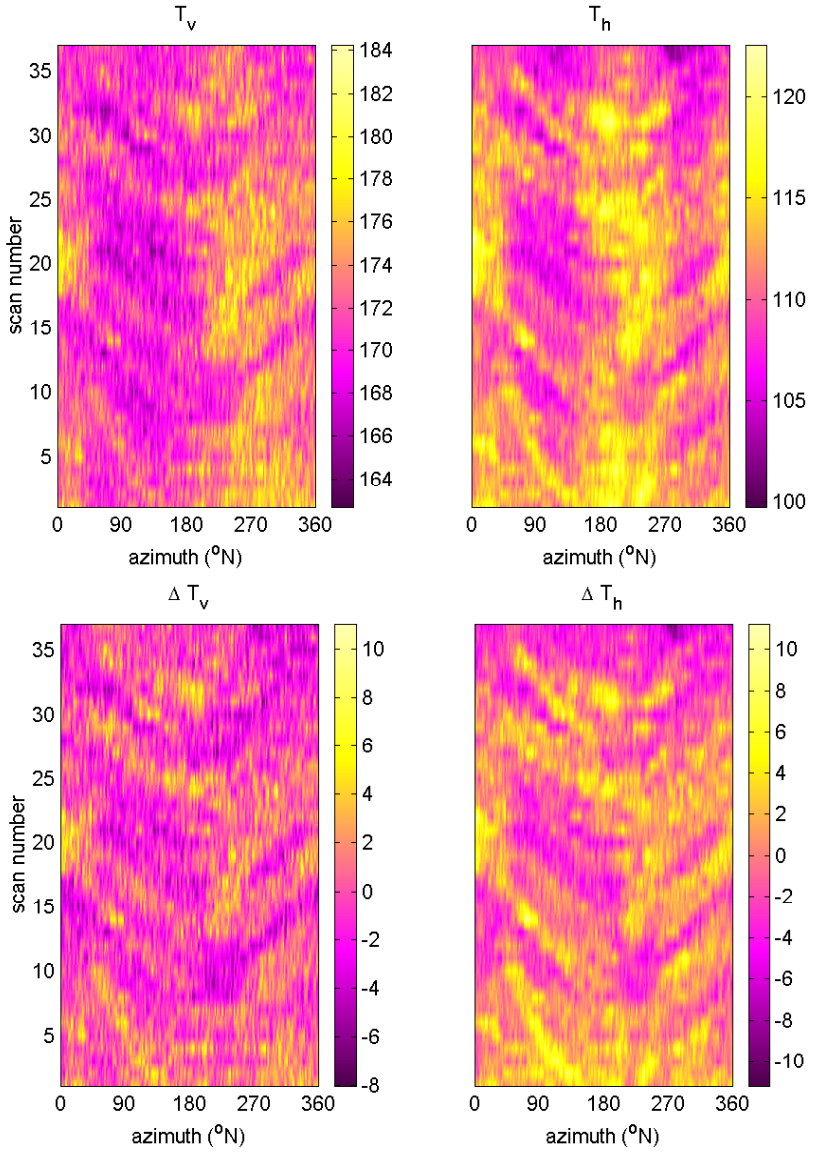

Figure 3.18: Same as Figure 3.17 except the frequency is 18.7 GHz.

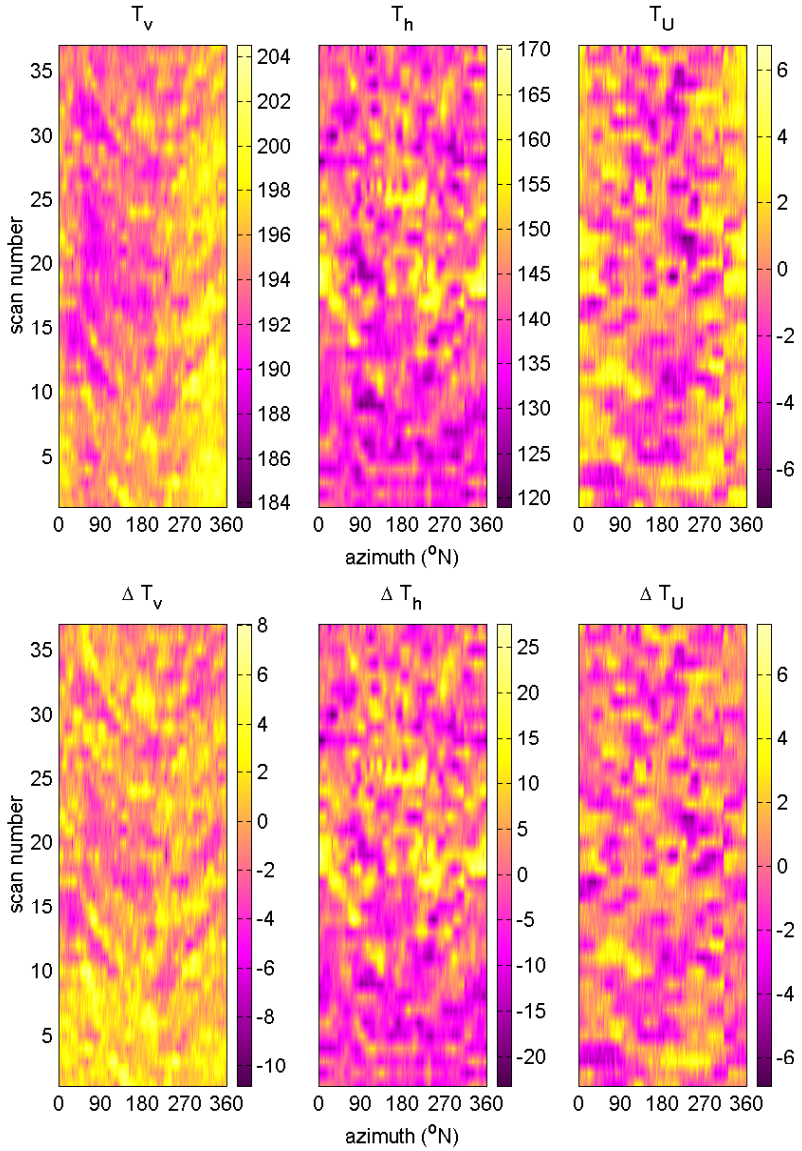

Figure 3.19: Same as Figure 3.17 except the frequency is 37.0 GHz.

asymmetry.

In addition to the systematic wind direction signature, there are stochastic variations in the brightness temperatures seen in the raster imagery. These variations are clearly revealed by removing the azimuthal means (from Figure 3.16 and displaying the residual brightness deviations as was done in the lower images in Figures 3.17 through 3.19. The deviations from the mean are a sum of both instrument noise and α-mesoscale geophysical variability. The two different sources can be distinguished because instrument noise is independent from one pixel to the next. The spatial variability of the geophysical noise, however, extends over a larger area than one pixel. Diagonal streaks that span $\sim$5 scans appear in the residual raster imagery and are correlated between polarizations and across radiometer bands. Because of their geophysical nature, these features are better illustrated using geolocated imagery.

Figures 3.23 through 3.25 contain the fore and aft-looking geolocated residual brightness imagery for X, K, and Ka-bands. The diagonal streaks in the raster imagery are mapped to spots of $\sim$5 km in size in the geolocated imagery. Not only are these spots present across both polarizations and the three bands, they are repeated in both fore and aft-looking imagery. Their presence in the two polarizations and absence in T_U is evidence that the excess emission is primarily unpolarized. The emission also appears to be isotropic as evidenced by the repeatability in both fore and aft-looks. The presence in both azimuthal looks also indicates that the temporal constancy of the features is $\gtrsim$100 sec. The cloud tops were well below the aircraft at $\sim$2.1 km (7000 ft) altitude (as determined during a spiral decent performed immediately after the flight track) and the cloud ceiling was $\sim$1 km (3300 ft) (as reported by the *Knorr*). In total, these characteristics suggest that variability in the cloud field is one mechanism possibly responsible for the observed brightness temperature variability. Other contributing factors could be variability in the atmospheric water vapor or the wind field which perturbs the ocean surface roughness.

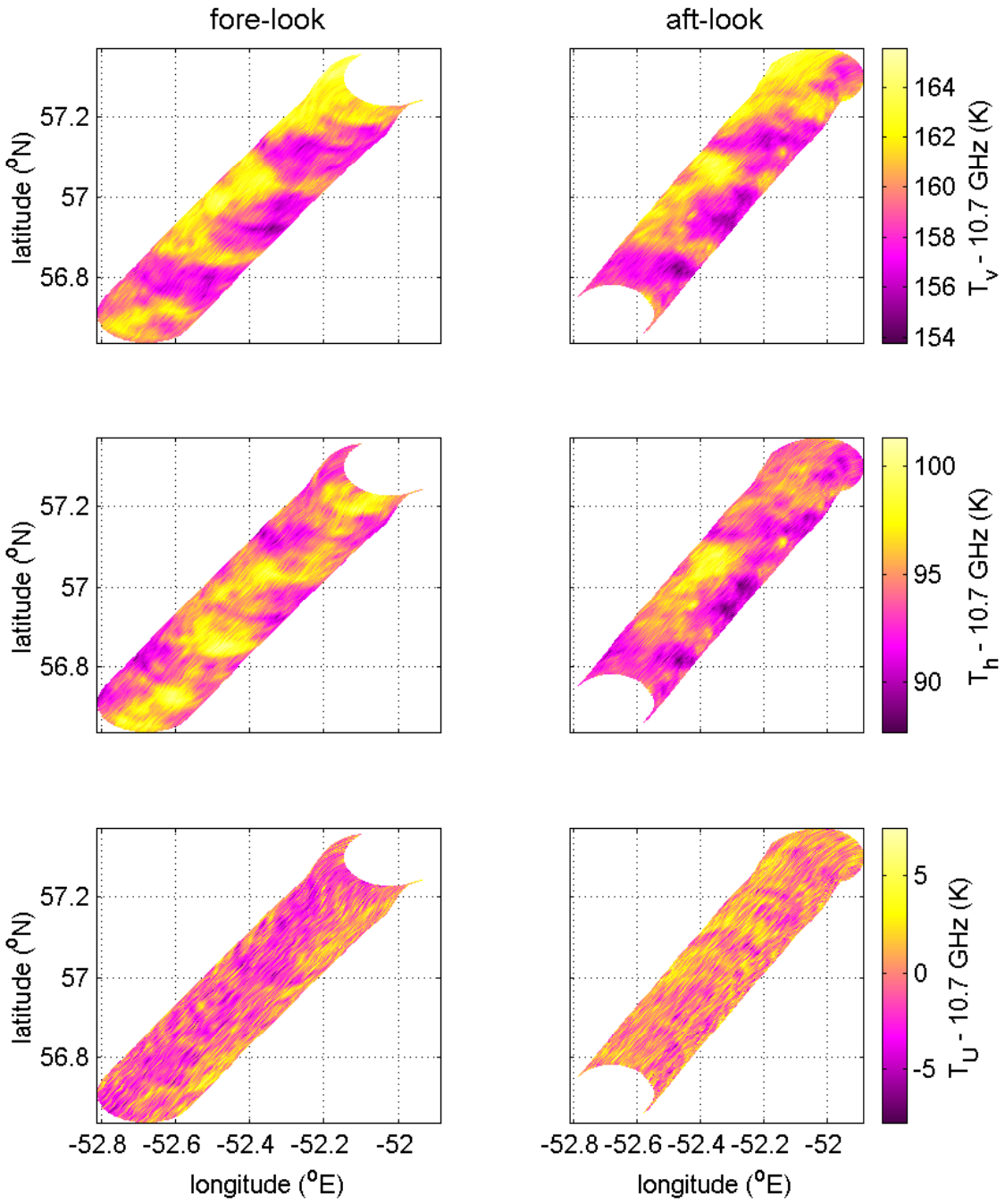

Figure 3.20: Geolocated PSR 10.7 GHz polarimetric microwave imagery of the ocean surface.

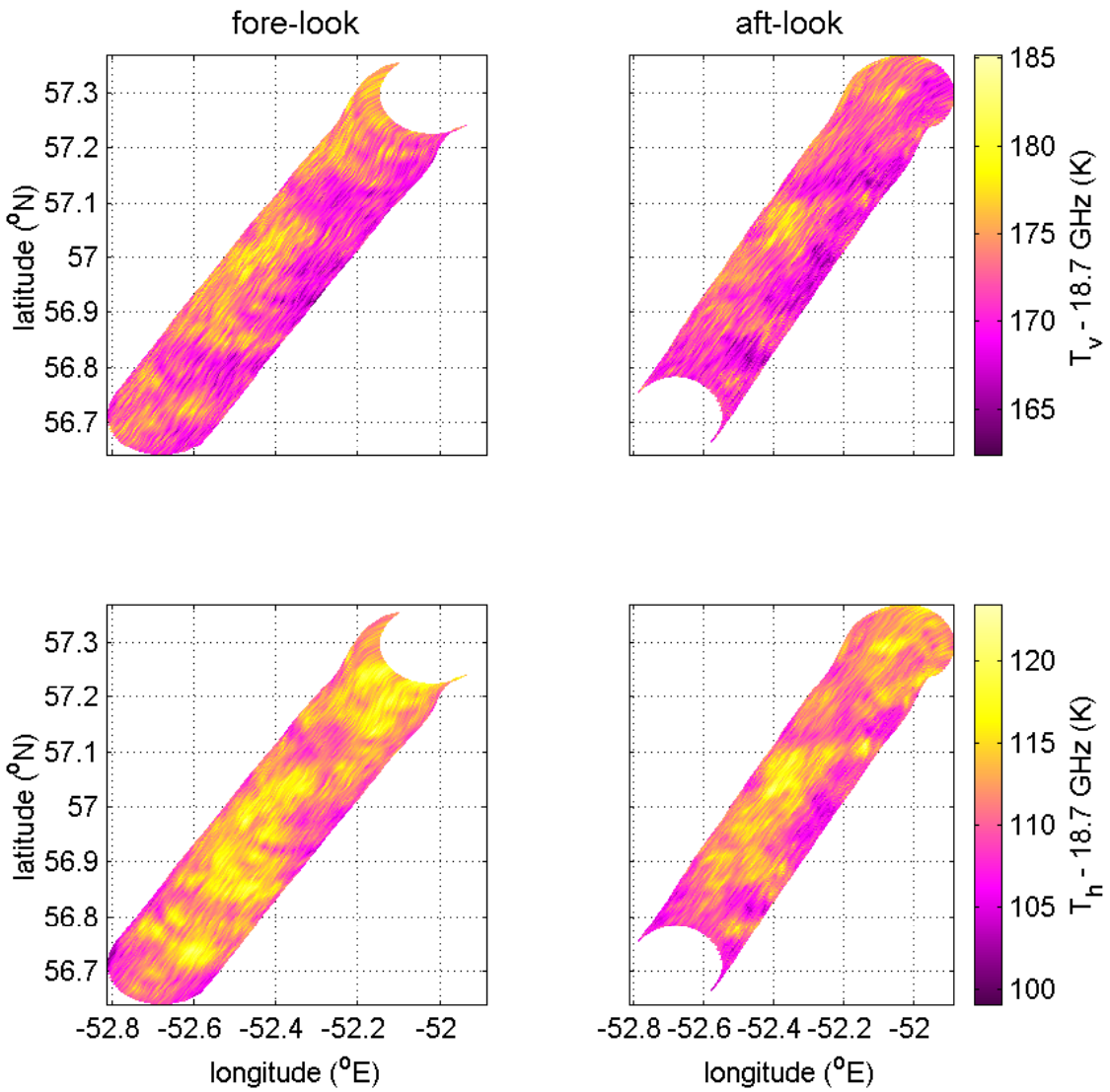

Figure 3.21: Same as Figure 3.20 except the frequency is 18.7 GHz.

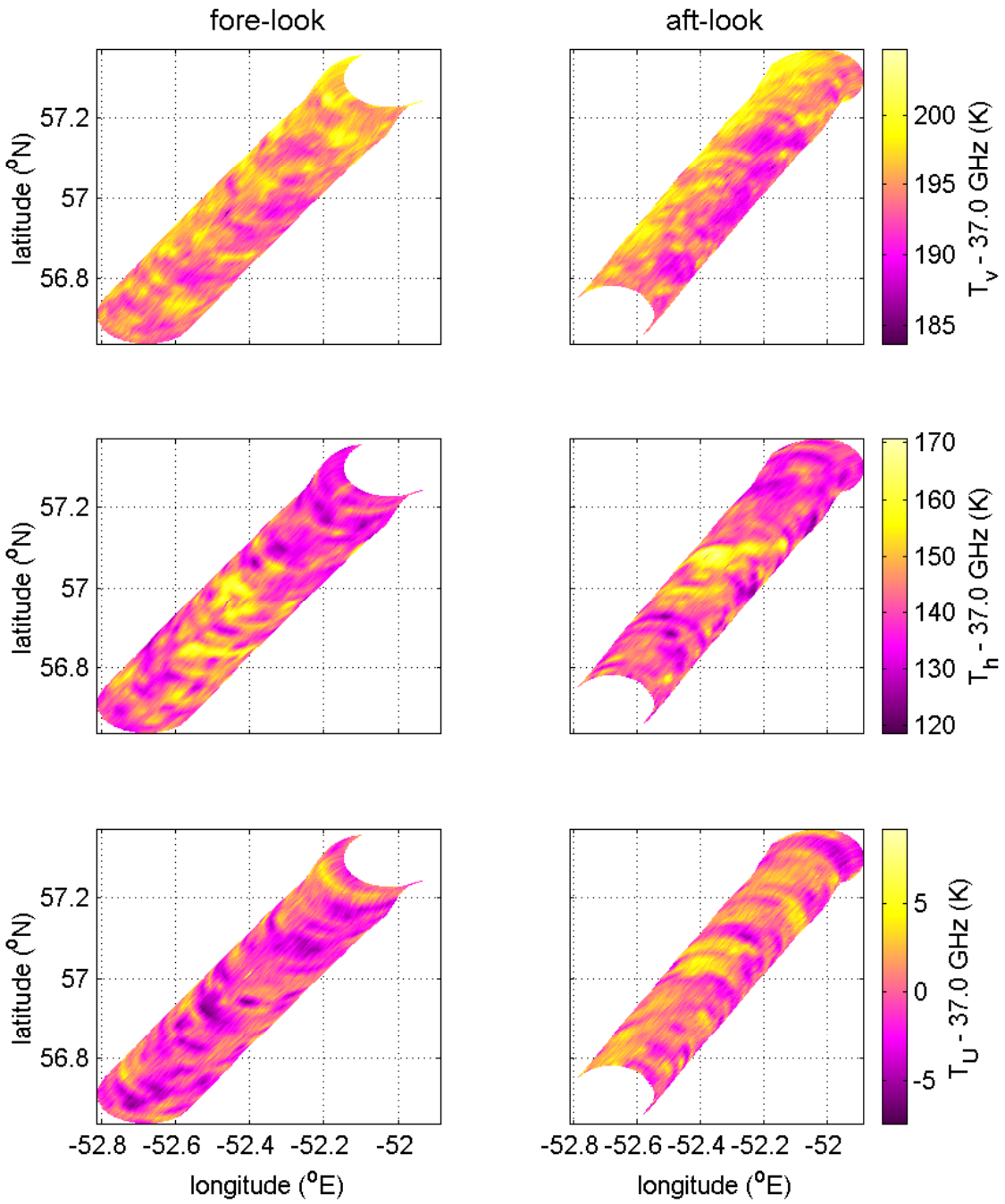

Figure 3.22: Same as Figure 3.20 except the frequency is 37.0 GHz.

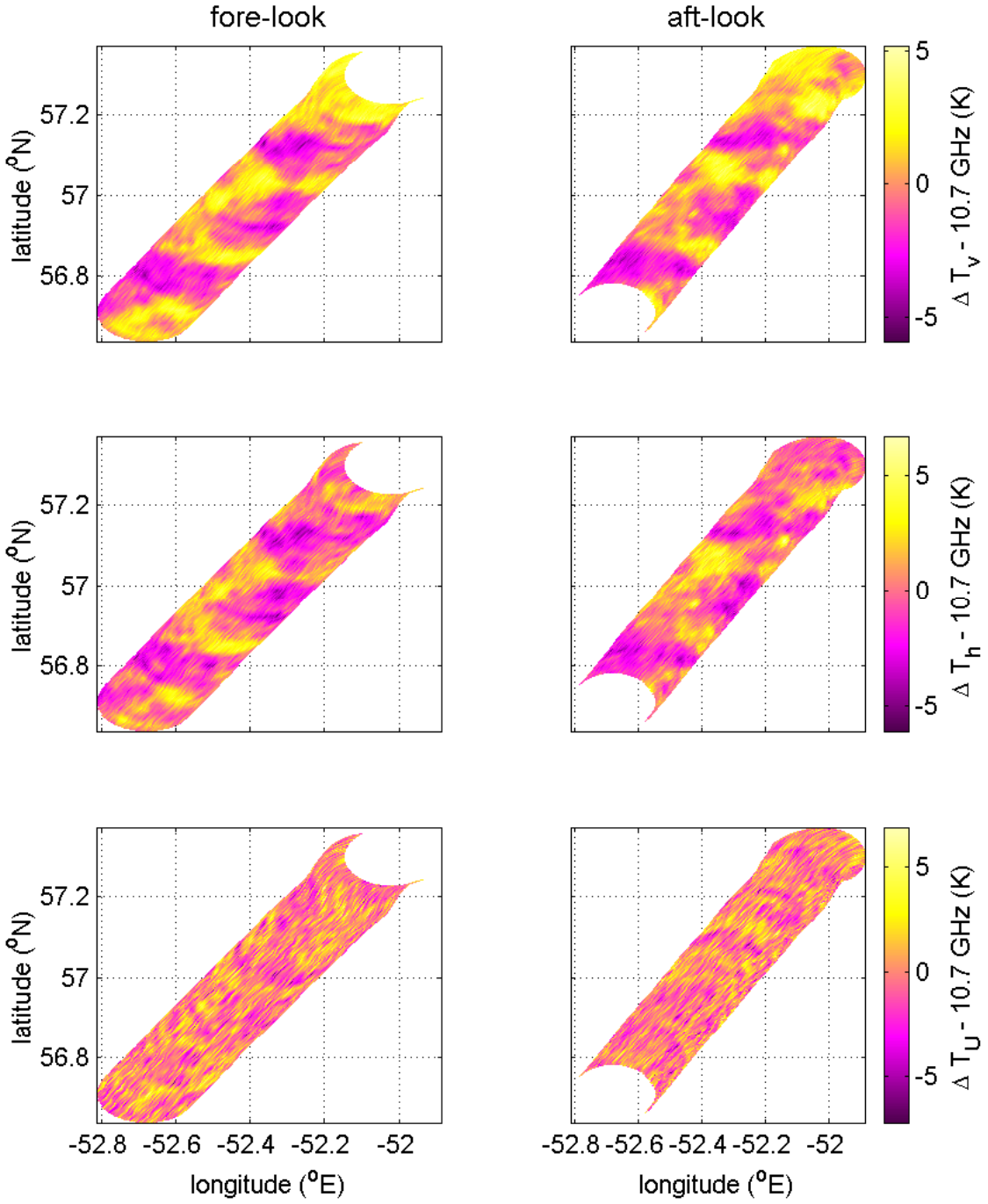

Figure 3.23: Geolocated PSR 10.7 GHz residual (see lower images in Figure 3.17) microwave imagery of the ocean surface.

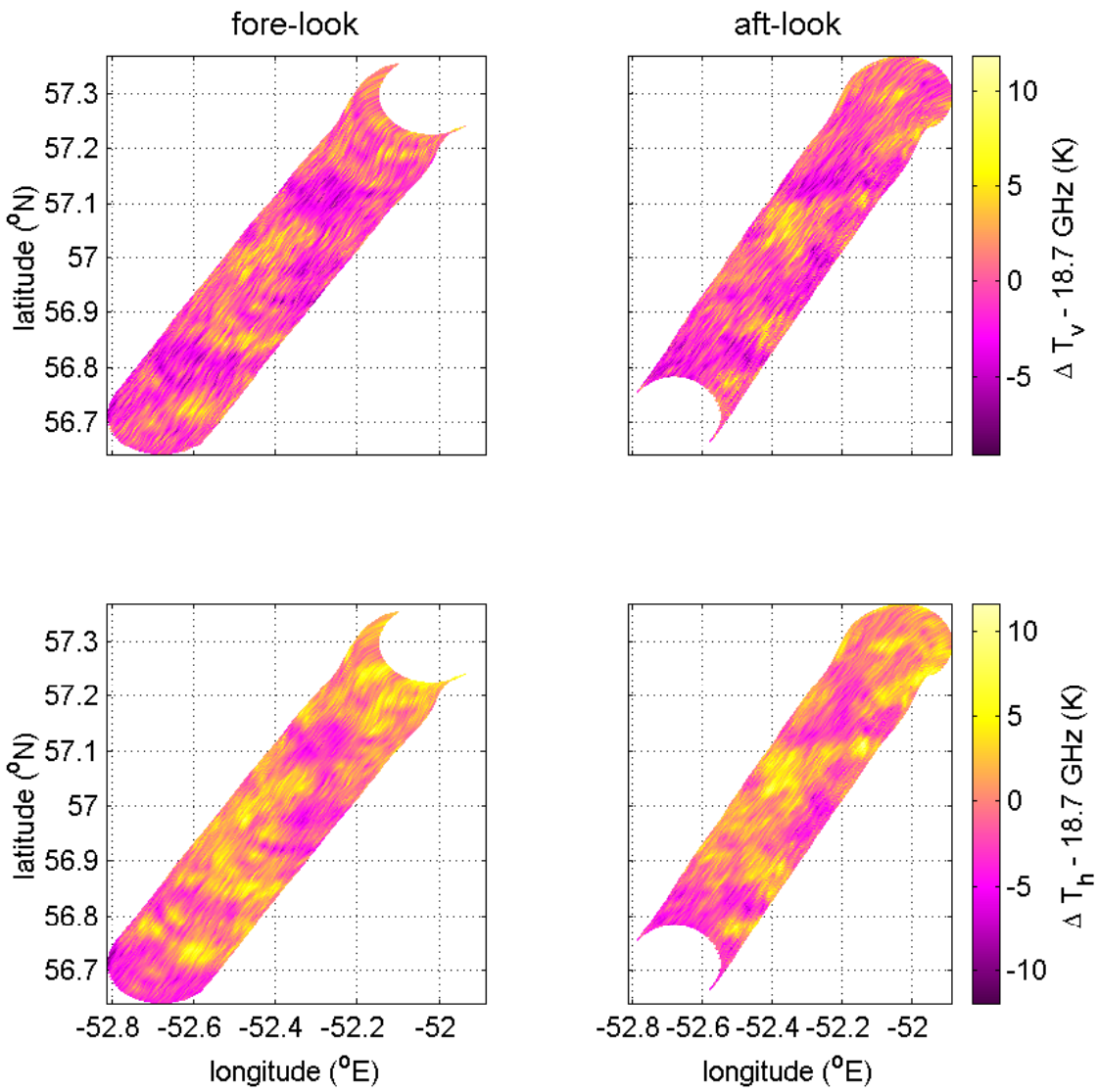

Figure 3.24: Same as Figure 3.23 except the frequency is 18.7 GHz.

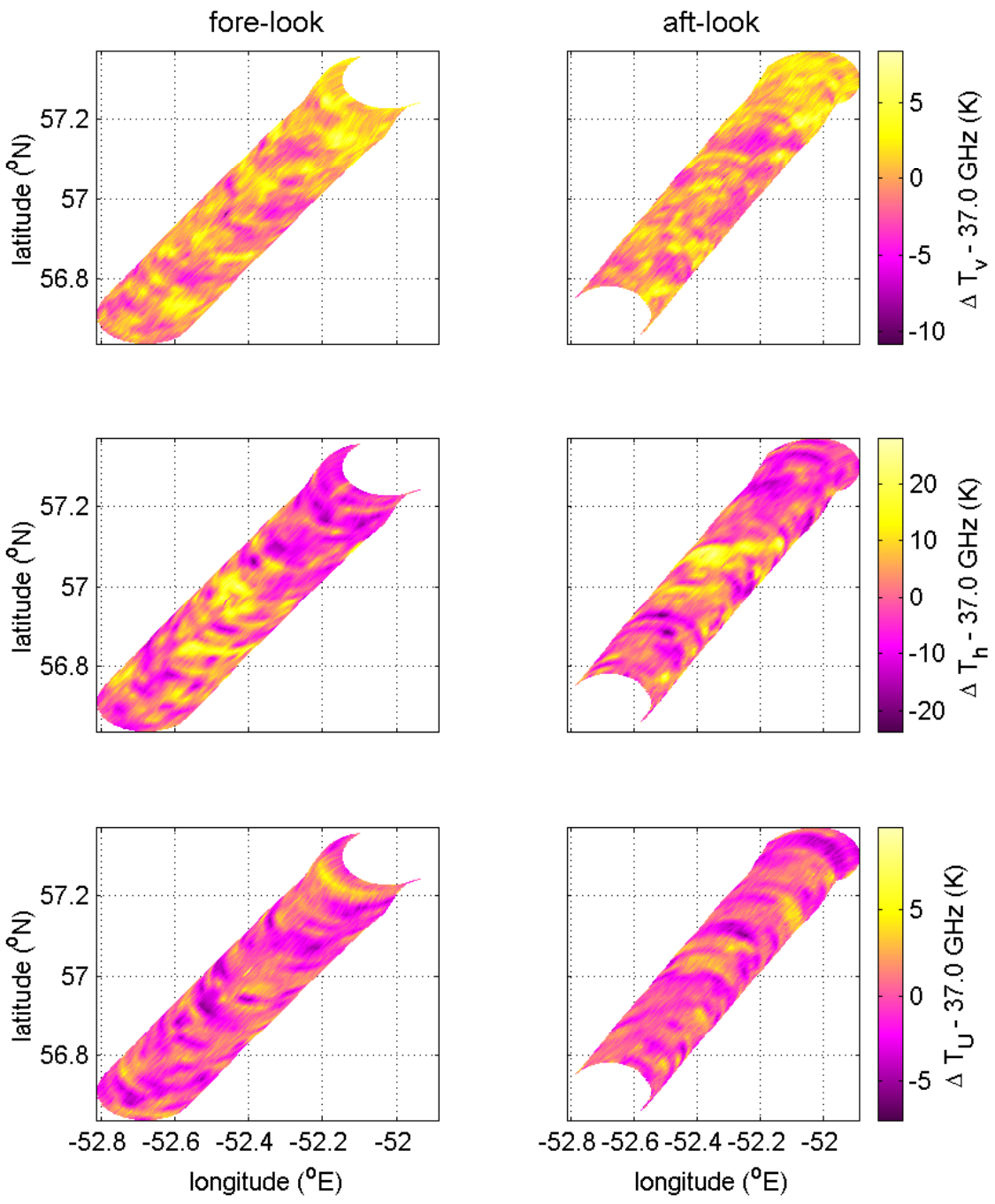

Figure 3.25: Same as Figure 3.23 except the frequency is 37.0 GHz.

3.4.2 Detection of Sun Glint

The microwave emission from the sun can reflect off the ocean surface into the radiometer feedhorn given the right geometry. Even when clouds are present, this reflection can increase the measured brightness temperature by a few Kelvin. The presence of sun glint in PSR data is evidenced by the radiometric imagery in Figure 3.26. In this image, a 10.7 GHz T_h raster image is displayed in grayscale. The sunglint can be seen in the left image as a slight increase in brightness along $\sim$170° azimuth. The left and right images are identical except that a line was superimposed on the right image to emphasize the azimuthal track of the sun glint over time. These data were collected during a hex-cross pattern from 1430-1515 UTC on March 3. There is a distinct bright track running from $\sim$160° N at scan 1 to $\sim$173° N at scan 129, which coincides with the solar azimuth. The solar azimuth can be calculated using the methods in [13].

Plotted in Figure 3.27 are the vertical and horizontal brightness temperatures at 10.7 and 18.7 GHz averaged over the raster imagery. The two vertical dashed lines in each plot delineate the solar azimuths at the start and end of the hex-cross pattern. Note that there is a distinct $\sim$0.3 K perturbation between these boundaries. Sun glint was not detected in the Ka-band imagery.

In addition to correlating the bright track of Figure 3.26 with the solar azimuth, a model is presented here that quantitatively verifies that sun glint is a probable candidate for the observed perturbation. The sun glint is modeled by assuming a flat ocean and lossless atmosphere and the antenna pattern is approximated by a Gaussian beam. The antenna temperature can be calculated by the following:

$$T_A = \frac{\int_0^{2\pi}\int_0^{\pi} T_B(\theta',\phi')G(\theta',\phi')\sin\theta' d\theta' d\phi'}{\int_0^{2\pi}\int_0^{\pi} G(\theta',\phi')\sin\theta' d\theta' d\phi'} \tag{3.11}$$

where $T_B(\theta',\phi')$ is the brightness temperature and $G(\theta',\phi')$ is the antenna gain pattern in the direction (θ',ϕ'). The coordinate system is referenced to the radiometer boresight $(\theta',\phi') = (0,0)$. Because the sun is relatively small in the sky ($\sim$0.5°), the antenna tem-

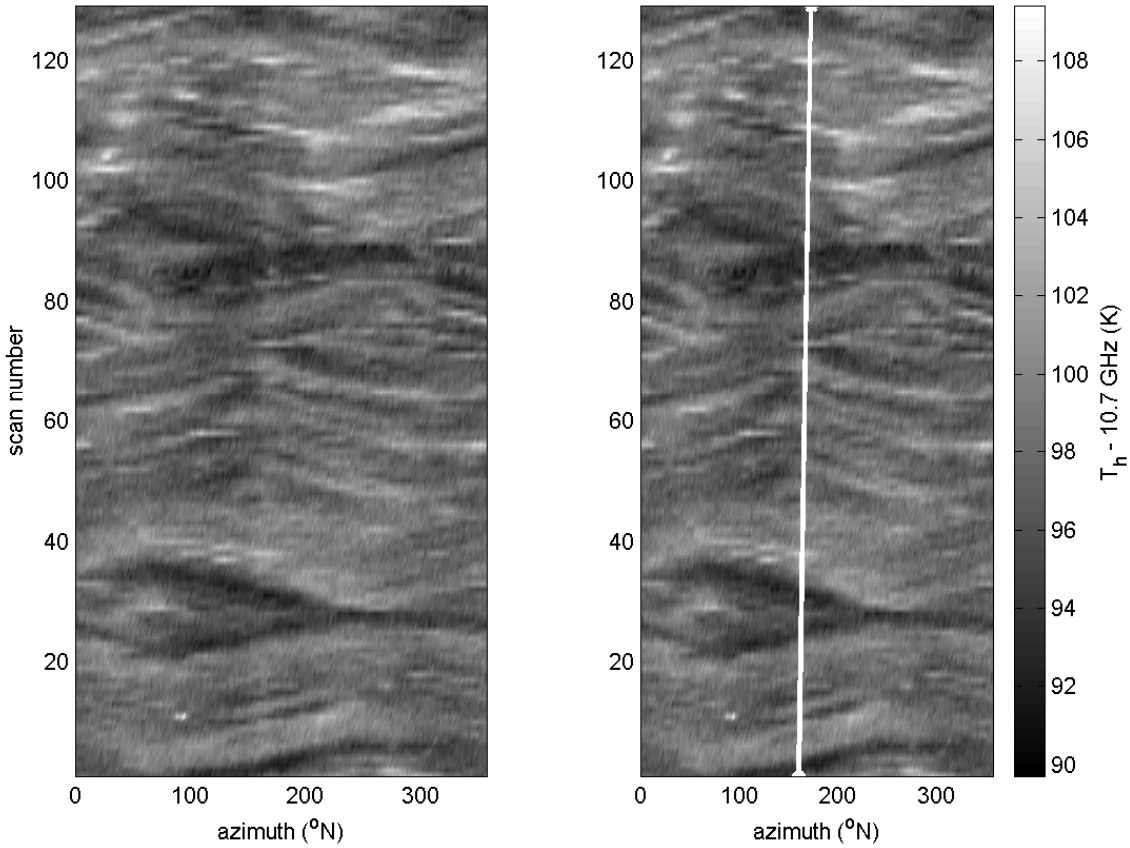

Figure 3.26: PSR X-band T_h raster image illustrating the presence of sun glint in radiometer imagery. The left and right images are identical except that a line was superimposed on the right image to emphasize the azimuthal track of the sun glint over time. These data were gathered from 1430-1515 UTC on March 3, 1997 over the Labrador Sea.

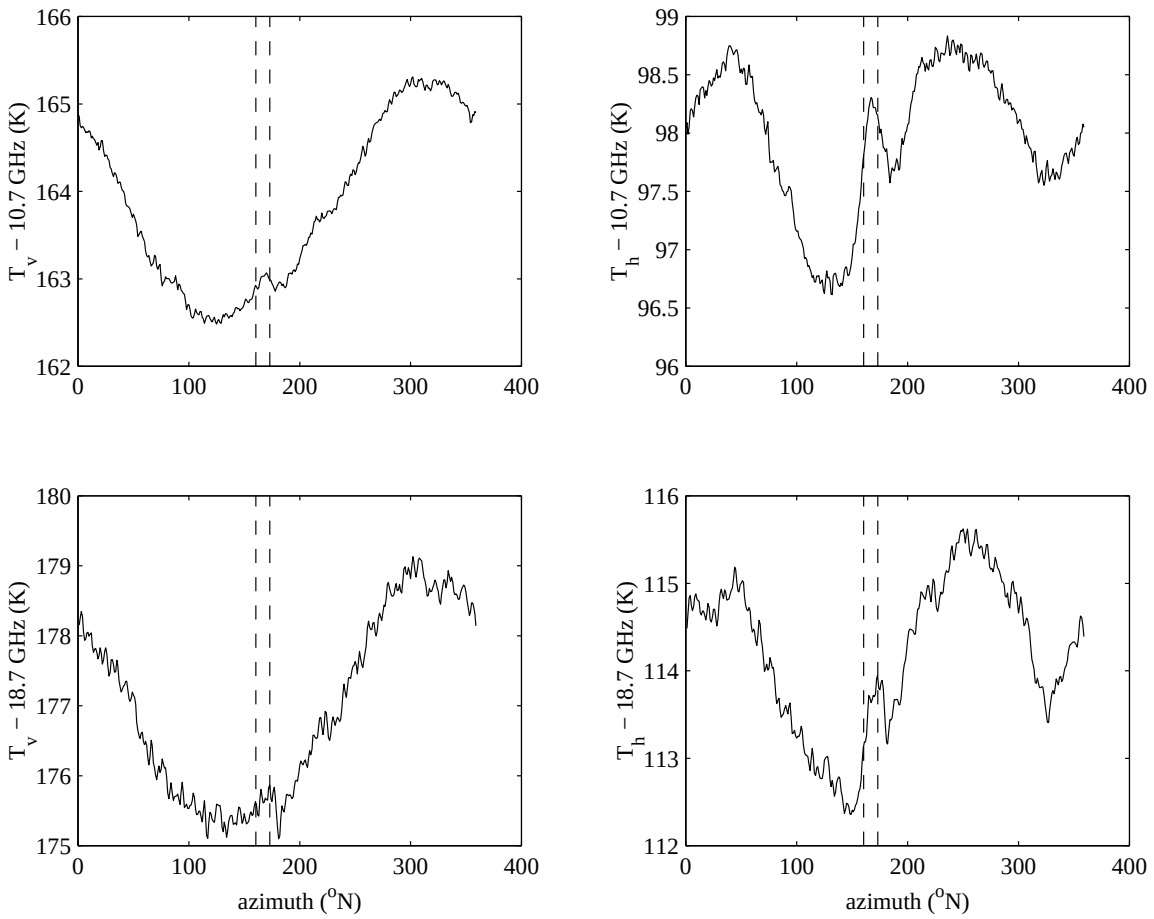

Figure 3.27: Sun glint in PSR X- and K-band average azimuthal scans. The averages were made over the data set used in Figure 3.26. The vertical lines represent the solar azimuth at the start and end of the given time range.

perature can be approximated:

$$T_A = \frac{T_\odot \left|R_\alpha(\theta_\odot)\right|^2 G(\theta'_\odot) d\Omega_\odot}{\int_0^{2\pi}\int_0^{\pi} G(\theta',\phi')\sin\theta' d\theta' d\phi'} \tag{3.12}$$

where $T_\odot$ is the brightness temperature of the sun, R_α is the Fresnel reflection coefficient of the ocean surface for polarization $\alpha = v$ or h, $\theta_\odot$ is the solar incidence angle from nadir, $\theta'_\odot$ is the off-boresight angle of the sun glint in the antenna coordinate frame, and $d\Omega_\odot$ is the solid angle subtended by the sun ($\sim (\pi/360)^2$ Sr).

The radiobrightness of the sun is approximately 6000 K at wavelengths shorter than 1 cm (or frequencies greater than 30 GHz) and greater than 6000 K for longer wavelengths [38]. For example, the quiet sun (i.e., low sun spot activity) is ~10,000 K near 3 cm wavelength (or 10 GHz). The Fresnel reflection coefficients at the ocean surface are

$$R_v(\theta) = \frac{\epsilon_w \cos\theta - \sqrt{\epsilon_w - \sin^2\theta}}{\epsilon_w \cos\theta + \sqrt{\epsilon_w - \sin^2\theta}} \tag{3.13}$$

$$R_h(\theta) = \frac{\cos\theta - \sqrt{\epsilon_w - \sin^2\theta}}{\cos\theta + \sqrt{\epsilon_w - \sin^2\theta}} \tag{3.14}$$

where ϵ_w is the dielectric constant of sea water as given by [37]. The antenna pattern is approximated with a Gaussian beam pattern:

$$G(\theta') = \exp\left[-\frac{1}{2}\left(\frac{\theta'}{\gamma}\right)^2\right] \tag{3.15}$$

where the parameter γ is related to the 3 dB beamwidth Θ_{3dB} by

$$\gamma^2 = \frac{\ln 2}{8}\Theta_{3dB}^2 \tag{3.16}$$

The sun glint direction in the antenna coordinate frame is

$$\theta'_\odot = \cos^{-1}(\sin\theta_0\cos\phi_0\sin\theta_\odot\cos\phi_\odot + \sin\theta_0\sin\phi_0\sin\theta_\odot\sin\phi_\odot + \cos\theta_0\cos\theta_\odot) \tag{3.17}$$

where θ_0 and ϕ_0 are the antenna incidence and azimuth angles, and $\theta_\odot$ and $\phi_\odot$ are the solar incidence and azimuth angles in the world coordinate frame.

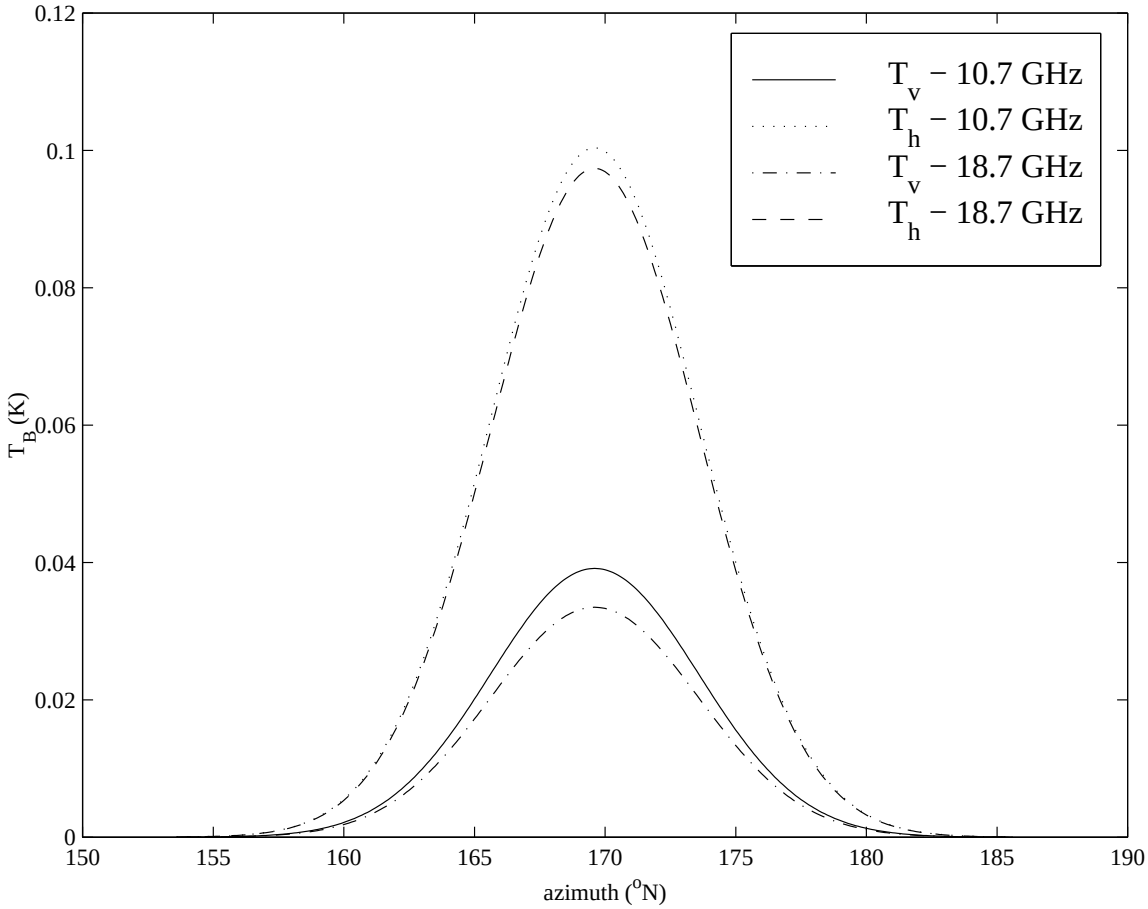

Figure 3.28: Modeled brightness temperature perturbation due to sun glint for X- and K-bands. The radiometer is viewing the surface at 53.1° with an 8° beamwidth. The solar azimuth and elevation angles are 169.6° and 64.5°, respectively.

Figure 3.28 shows the modeled sun glint for the experiment flown on March 3, 1997 (same case as for Figures 3.26 and 3.27). At 1500 UTC the P-3 was at 57.5586° N and 51.5670° W and the solar azimuth and incidence angles were 169.6° and 64.5°, respectively. The computed perturbations are similar to those that were measured and plotted in Figure 3.27. The model, however, does underestimate the sun glint because it is assuming a Fresnel reflection from the ocean rather than reflection from a rough ocean. The rough ocean would effectively broaden the antenna beam, thus increasing the predicted sun glint perturbation. Nonetheless, this simple model, coupled with the solar azimuth data, helps to validate the hypothesis that sun glint will perturb the measured brightness temperature of the ocean.

3.5 Summary

Descriptions of the PSR hardware, data processing, and Labrador Sea experiment were presented in this chapter. The PSR was the first microwave polarimeter to utilize a digital correlator for detection of the third Stokes parameter. The unique two-axis gimbal design facilitated the first multiband polarimetric imaging observations of ocean surface emission. The data processing algorithms, in particular the compensation method for aircraft pitch and roll perturbations, were discussed. The pitch and roll correction algorithm was demonstrated to reduce the contributions of attitude variations in the PSR imaging from $> 10\%$ to $< 1\%$. During the Labrador Sea experiment, the PSR was used to obtain the first high-resolution ($\sim$1 km) multiband, polarimetric, conically-scanned microwave imagery of the ocean surface. After calibration (which is discussed in Chapter 4) the imagery revealed the expected systematic wind direction signature as well as natural geophysical variability in the microwave emission over the ocean. The geophysical variability is hypothesized to arise from cloud, water vapor, and surface emission variations. The Labrador Sea data will be used in Chapter 5 to develop an empirical geophysical model function for ocean brightness temperature over the Labrador Sea. This model function will be applied in Chapter 6 to

retrieve surface wind vector fields from imagery obtained during the Labrador Sea March 7 flight over a polar low. The ocean surface imagery obtained by the PSR during the five sorties flown in March 1997, provide an important data set to use for the technical development and demonstration of ocean surface wind vector field measurement by passive microwave polarimetry.

CHAPTER 4

Calibration

The PSR in-flight calibration algorithms are discussed in this chapter. The calibration of the PSR entails the estimation and removal of systematic gains and offsets from the different radiometer outputs, and is carried out in-flight using heated and ambient temperature calibration targets. The success of using unpolarized targets to calibrate the digital microwave polarimeter depends partially upon the design of the radiometer antenna, in which polarization purity is the primary consideration. Accordingly, an analysis considering antenna rotational and polarization effects is presented, and a set of design principles (on which the PSR design was based) is derived from the analysis.

The ability to properly estimate the hardware constants of the digital correlator is also necessary so that the first three Stokes parameters, in particular T_U, can be measured without instrument bias. Total-power radiometer calibration for both the analog and digital systems is straightforward. The radiometer is presented with two known temperature stimuli (the hot and ambient loads) from which measurements of the gain and offset parameters are computed. The method is specifically derived for the digital total-power channels to include the linearization of the digital counter outputs in the calibration equations. A novel calibration scheme for the third Stokes parameter channel that uses the hot and ambient loads is described. Because of A/D converter threshold offsets and input correlation bias, there are non-zero offsets in the correlator output. These effects can be compensated by using measurements from the two unpolarized calibration looks. A fully polarimetric calibration standard was utilized to verify the effectiveness of the technique and the absolute

calibration of the U-channel was found to be ~ 0.4 K.

Finally, the in-flight calibration algorithms using the two unpolarized targets are described. In particular, the total-power radiometer calibration is augmented with a third calibration reference, the cold-sky, to correct for thermal gradients within the PSR's calibration targets. Post-calibration brightness temperature comparisons with several cold-sky looks reveal an absolute calibration $\Delta T_{abs} \lesssim 4$ K.

4.1 Antenna

The PSR's radiometers use dual-polarization lens-feedhorn antennas. The dual-polarization antenna couples the incident partially polarized radiation from free space to two orthogonally polarized guided modes and uses an ortho-mode transducer (OMT) to couple these modes into two signals ports. The antenna's cross-polarization discrimination (XPD) characteristics affect the amount of contamination in a measurement due to inclusion of unwanted energy in an orthogonal polarization. Poor XPD will result in unacceptable Stokes parameter mixing at the radiometer outputs. Careful consideration, therefore, must be given to XPD specifications when designing the antenna for a polarimeter. In addition, rotational misalignments due to antenna mounting or uncertainty in the polarization alignment will cause polarization basis rotation errors. Beginning with a basic antenna model, several design rules, which may be used to specify antenna characteristics, are found in this section.

The antenna system can be modeled as a four port device that couples the incident horizontally and vertically polarized electric fields (denoted E_v^+ and E_h^+) to two output ports. The fields at the output ports are denoted E_a^- and E_b^-, respectively. Ideally, the antenna and output ports would be perfectly matched and have infinite XPD (i.e., E_v^+ and

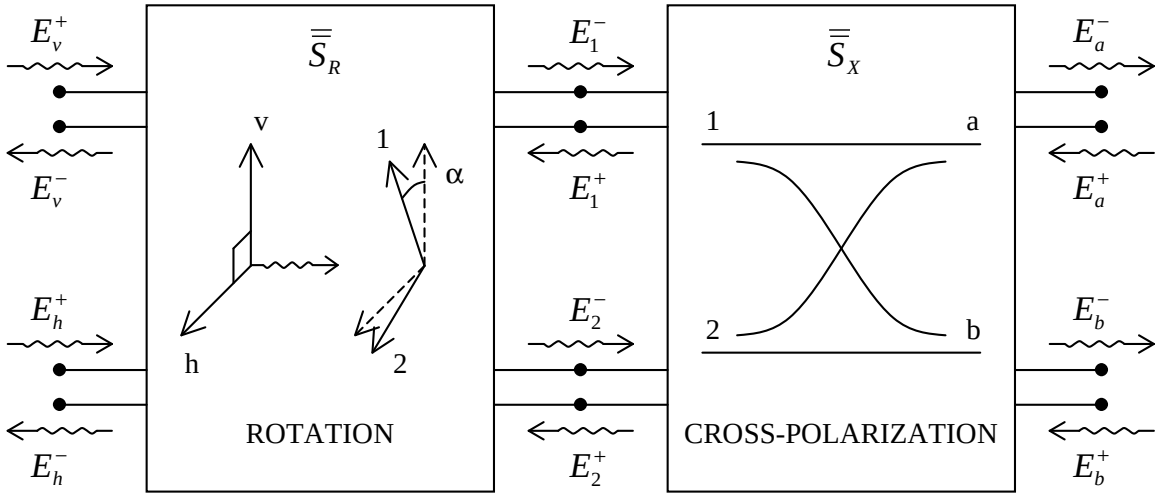

Figure 4.1: Cascaded four port networks modeling both rotation and cross-polarization effects within a dual-polarized antenna system. The first network, described by the scattering matrix $\overline{\overline{S}}_R$, acts as a rotation of the polarization basis from the natural basis. The second network, modeled by scattering matrix $\overline{\overline{S}}_X$, introduces impedance mismatches, port-to-port isolation, and cross-polarization coupling.

E_h^+ would couple directly to E_a^- and E_b^-). In scattering matrix notation the ideal case is:

$$\begin{bmatrix} 0 \\ 0 \\ E_a^- \\ E_b^- \end{bmatrix} = \begin{bmatrix} 0 & 0 & 1 & 0 \\ 0 & 0 & 0 & 1 \\ 1 & 0 & 0 & 0 \\ 0 & 1 & 0 & 0 \end{bmatrix} \begin{bmatrix} E_v^+ \\ E_h^+ \\ 0 \\ 0 \end{bmatrix} \tag{4.1}$$

Unfortunately, antenna alignment errors, OMT imperfections, and cross-polarization mixing in the feed antenna itself render the idealized assumption invalid. To assess the effects of such defects, the nonidealities can be decomposed into two error modes: (1) a polarization basis rotation and (2) a cross-polarization coupling. The properties of these two error modes can be modeled using passive, lossless, and reciprocal four port networks (see Figure 4.1) with scattering matrices $\overline{\overline{S}}_R$ (for rotation) and $\overline{\overline{S}}_X$ (for coupling):

$$\overline{\overline{S}}_R = \begin{bmatrix} 0 & 0 & \cos\alpha & -\sin\alpha \\ 0 & 0 & \sin\alpha & \cos\alpha \\ \cos\alpha & \sin\alpha & 0 & 0 \\ -\sin\alpha & \cos\alpha & 0 & 0 \end{bmatrix}, \tag{4.2}$$

where α is an effective clockwise rotation of the antenna about its boresight; and

$$\overline{\overline{S}}_X = \begin{bmatrix} R & I & T & C \\ I & R & C & T \\ T & C & R & I \\ C & T & I & R \end{bmatrix}, \tag{4.3}$$

where the four scattering parameters are defined as follows: C is the cross-polarization coupling coefficient, I is the port-to-port isolation coefficient, R is the reflection coefficient, and T is the co-polarized transmission coefficient. The matrix $\overline{\overline{S}}_X$ contains only three independent scattering parameters, which are related to actual antenna measurements (in dB) as follows:

$$RL = -20\log|R| \qquad \text{(return loss)} \tag{4.4}$$

$$XPD = -20\log|C| \qquad \text{(cross-polarization discrimination)} \tag{4.5}$$

$$PPI = -20\log|I| \qquad \text{(port-to-port isolation)} \tag{4.6}$$

Both of these device models are assumed to be reciprocal, passive and lossless. These assumptions impose two mathematical criteria on the scattering parameter matrices. First, the scattering matrix of a reciprocal device is symmetric under transposition. Accordingly, we see from (4.2) and (4.3) that $\overline{\overline{S}}_R = \overline{\overline{S}}_R{}^T$ and $\overline{\overline{S}}_X = \overline{\overline{S}}_X{}^T$. The second criterion is that the scattering matrix be unitary for a passive and lossless device, that is:

$$\overline{\overline{S}}_R\overline{\overline{S}}_R{}^\dagger = \overline{\overline{I}} \qquad \text{and} \qquad \overline{\overline{S}}_X\overline{\overline{S}}_X{}^\dagger = \overline{\overline{I}}, \tag{4.7}$$

where $\dagger$ denotes the conjugate transpose. It can be readily shown that $\overline{\overline{S}}_R$ satisfies this condition. For the cross-polarization coupling matrix, however, this requirement limits the number of independent parameters in $\overline{\overline{S}}_X$. These constraints are examined in Section 4.1.2.

Since the antenna is used to couple the incident Stokes vector (2.1) to the radiometer, any antenna errors will perturb the measurement of the true Stokes vector. The scattering matrices $\overline{\overline{S}}_R$ and $\overline{\overline{S}}_X$ will be analyzed independently to elucidate the effects of the individual error modes. The results will then be composed for a complete analysis.

4.1.1 Rotation error

Rotational errors can arise from the misalignment of the antenna with the platform, OMT/feedhorn or feedhorn/reflector misalignments, or platform attitude measurement errors. Given a plane wave incident upon a misaligned antenna, the fields at the output ports are determined by

$$\begin{bmatrix} E_v^- \\ E_h^- \\ E_1^- \\ E_2^- \end{bmatrix} = \begin{bmatrix} 0 & 0 & \cos\alpha & -\sin\alpha \\ 0 & 0 & \sin\alpha & \cos\alpha \\ \cos\alpha & \sin\alpha & 0 & 0 \\ -\sin\alpha & \cos\alpha & 0 & 0 \end{bmatrix} \begin{bmatrix} E_v^+ \\ E_h^+ \\ E_1^+ \\ E_2^+ \end{bmatrix} = \begin{bmatrix} 0 \\ 0 \\ \cos\alpha E_v^+ + \sin\alpha E_h^+ \\ \cos\alpha E_h^+ - \sin\alpha E_v^+ \end{bmatrix} \tag{4.8}$$

This equation is the result of rotating the polarization basis, and leads to the Stokes vector rotational transform [8]. Rather than measuring the true Stokes vector, the radiometer measures the antenna brightness vector $\overline{T}_{ANT}$ which is associated with the output fields E_1^- and E_2^-:

$$\overline{T}_{ANT} = \begin{bmatrix} T_{ANT,v} \\ T_{ANT,h} \\ T_{ANT,U} \\ T_{ANT,V} \end{bmatrix} = \frac{\lambda^2}{\eta k} \begin{bmatrix} \langle |E_1^-|^2 \rangle \\ \langle |E_2^-|^2 \rangle \\ 2\mathrm{Re}\langle E_1^- E_2^{-*} \rangle \\ 2\mathrm{Im}\langle E_1^- E_2^{-*} \rangle \end{bmatrix} \tag{4.9}$$

where λ is the wavelength, η is the wave impedance, and k is Boltzmann's constant. Making the substitutions for E_1^- and E_2^- in terms of E_v^+ and E_h^+ results in the following:

$$\begin{aligned}\overline{T}_{ANT} &= \frac{\lambda^2}{\eta K}\begin{bmatrix} \langle|\cos\alpha E_v^+ + \sin\alpha E_h^+|^2\rangle \\ \langle|\cos\alpha E_h^+ - \sin\alpha E_v^+|^2\rangle \\ 2\mathrm{Re}\langle\left(\cos\alpha E_v^+ + \sin\alpha E_h^+\right)\left(\cos\alpha E_h^+ - \sin\alpha E_v^+\right)^*\rangle \\ 2\mathrm{Im}\langle\left(\cos\alpha E_v^+ + \sin\alpha E_h^+\right)\left(\cos\alpha E_h^+ - \sin\alpha E_v^+\right)^*\rangle \end{bmatrix} \\ &= \frac{\lambda^2}{\eta K}\begin{bmatrix} \cos^2\alpha\langle|E_v^+|^2\rangle + \sin^2\alpha\langle|E_h^+|^2\rangle + \sin 2\alpha\mathrm{Re}\langle E_v^+E_h^{+*}\rangle \\ \sin^2\alpha\langle|E_v^+|^2\rangle + \cos^2\alpha\langle|E_h^+|^2\rangle - \sin 2\alpha\mathrm{Re}\langle E_v^+E_h^{+*}\rangle \\ -\sin 2\alpha\langle|E_v^+|^2\rangle + \sin 2\alpha\langle|E_h^+|^2\rangle + 2\cos 2\alpha\mathrm{Re}\langle E_v^+E_h^{+*}\rangle \\ 2\mathrm{Im}\langle E_v^+E_h^{+*}\rangle \end{bmatrix}\end{aligned} \tag{4.10}$$

The above result can be decomposed into a matrix-vector product by separating a rotation operator:

$$\overline{T}_{ANT} = \overline{\overline{L}}(\alpha)\cdot\frac{\lambda^2}{\eta k}\begin{bmatrix} \langle|E_v^+|^2\rangle \\ \langle|E_h^+|^2\rangle \\ 2\mathrm{Re}\langle E_v^+E_h^{+*}\rangle \\ 2\mathrm{Im}\langle E_v^+E_h^{+*}\rangle \end{bmatrix}, \tag{4.11}$$

where

$$\overline{\overline{L}}(\alpha) = \begin{bmatrix} \cos^2\alpha & \sin^2\alpha & \frac{1}{2}\sin 2\alpha & 0 \\ \sin^2\alpha & \cos^2\alpha & -\frac{1}{2}\sin 2\alpha & 0 \\ -\sin 2\alpha & \sin 2\alpha & \cos 2\alpha & 0 \\ 0 & 0 & 0 & 1 \end{bmatrix}. \tag{4.12}$$

The matrix operator $\overline{\overline{L}}(\alpha)$ is the Stokes vector rotational transform, and the antenna brightness vector $\overline{T}_{ANT}$ is simply a transformation of the Stokes vector under a rotation of angle α:

$$\overline{T}_{ANT} = \overline{\overline{L}}(\alpha)\overline{T}_B. \tag{4.13}$$

Several observations can be made about the errors that occur from antenna rotation. First, the fourth Stokes parameter is invariant under polarization basis rotation. This is expected because T_V contains information about the circular polarization. To quantitatively identify the effects of mixing among the other Stokes parameters, the sensitivity to small polarization rotations about the nominal $\alpha = 0$ is defined as:

$$\left.\frac{\partial}{\partial \alpha}\overline{T}_{ANT}\right|_{\alpha=0} = \begin{bmatrix} T_U \\ -T_U \\ 2\left(T_h - T_v\right) \\ 0 \end{bmatrix} \mathrm{K\,rad}^{-1} = \frac{\pi}{180}\begin{bmatrix} T_U \\ -T_U \\ 2\left(T_h - T_v\right) \\ 0 \end{bmatrix} \mathrm{K\,deg}^{-1} \tag{4.14}$$

Small polarization misalignments will produce mixing between T_v (or T_h) and T_U that are $\sim\ O(\alpha)$. Second, notice that T_v and T_h do not mix, at least to $O(\alpha)$, for small deviations about the ideal alignment. Obviously, the magnitude of naturally occurring polarized emissions greatly affects the amount of Stokes parameter mixing caused by polarization misalignment. For example, with $T_U = 1$ K and $(T_v - T_h) = 60$ K, the rotational sensitivity is

$$\begin{bmatrix} 0.02 \\ -0.02 \\ -2.1 \\ 0 \end{bmatrix} \mathrm{K\,deg}^{-1}. \tag{4.15}$$

Small values of the third Stokes parameter have a negligible effect on T_v and T_h; however, large polarization differences, such as seen over the ocean, can greatly affect T_U when rotational errors exist.

4.1.2 Cross-polarization coupling

The effects of cross-polarization coupling are analyzed in this section, separately from antenna rotation, using the definition of $\overline{\overline{S}}_X$ from (4.3). It is assumed that the antenna is

perfectly matched to the receiver so that $E_a^+ = E_b^+ = 0$. The output field amplitudes are:

$$\begin{bmatrix} E_1^+ \\ E_2^+ \\ E_a^- \\ E_b^- \end{bmatrix} = \begin{bmatrix} R & I & T & C \\ I & R & C & T \\ T & C & R & I \\ C & T & I & R \end{bmatrix} \begin{bmatrix} E_1^- \\ E_2^- \\ 0 \\ 0 \end{bmatrix} = \begin{bmatrix} RE_1^- + IE_2^- \\ IE_1^- + RE_2^- \\ TE_1^- + CE_2^- \\ CE_1^- + TE_2^- \end{bmatrix} \tag{4.16}$$

Using the results for E_a^- and E_b^- from above, the measurable antenna temperature vector is

$$\overline{T}_{ANT} = \frac{\lambda^2}{\eta K} \begin{bmatrix} |T|^2\langle|E_1^-|^2\rangle + |C|^2\langle|E_2^-|^2\rangle + 2\mathrm{Re}\{TC^*\langle E_1^- E_2^{-*}\rangle\} \\ |T|^2\langle|E_2^-|^2\rangle + |C|^2\langle|E_1^-|^2\rangle + 2\mathrm{Re}\{TC^*\langle E_1^- E_2^{-*}\rangle\} \\ 2(|T|^2 + |C|^2)\mathrm{Re}\{\langle E_1^- E_2^{-*}\rangle\} + 2\mathrm{Re}\{TC^*\}(\langle|E_1^-|^2\rangle + \langle|E_2^-|^2\rangle) \\ 2(|T|^2 - |C|^2)\mathrm{Im}\{\langle E_1^- E_2^{-*}\rangle\} + 2\mathrm{Im}\{TC^*\}(\langle|E_1^-|^2\rangle - \langle|E_2^-|^2\rangle) \end{bmatrix}. \tag{4.17}$$

If the antenna is not rotated, then $E_1^- = E_v^+$ and $E_2^- = E_h^+$ and the above antenna brightness vector can be rewritten by using the Stokes parameters:

$$\overline{T}_{ANT} = \begin{bmatrix} |T|^2 T_v + |C|^2 T_h + \mathrm{Re}\{TC^*\}T_U - \mathrm{Im}\{TC^*\}T_V \\ |T|^2 T_h + |C|^2 T_v + \mathrm{Re}\{TC^*\}T_U + \mathrm{Im}\{TC^*\}T_V \\ (|T|^2 + |C|^2)T_U + 2\mathrm{Re}\{TC^*\}(T_v + T_h) \\ (|T|^2 - |C|^2)T_V + 2\mathrm{Im}\{TC^*\}(T_v - T_h) \end{bmatrix}. \tag{4.18}$$

The above can be expressed as a transformation of the true Stokes vector to the measurable antenna temperatures at the output ports:

$$\overline{T}_{ANT} = \begin{bmatrix} |T|^2 & |C|^2 & \mathrm{Re}\{TC^*\} & -\mathrm{Im}\{TC^*\} \\ |C|^2 & |T|^2 & \mathrm{Re}\{TC^*\} & \mathrm{Im}\{TC^*\} \\ 2\mathrm{Re}\{TC^*\} & 2\mathrm{Re}\{TC^*\} & |T|^2 + |C|^2 & 0 \\ 2\mathrm{Im}\{TC^*\} & -2\mathrm{Im}\{TC^*\} & 0 & |T|^2 - |C|^2 \end{bmatrix} \overline{T}_B \tag{4.19}$$

Before the effects of cross-polarization coupling can be discussed, the constraints on the scattering parameters T and C must be identified. Under the unitary condition,

$\overline{\overline{S}}_X \overline{\overline{S}}_X{}^{\dagger} = \overline{\overline{I}}$, the following relations are required:

$$|T|^2 + |C|^2 + |R|^2 + |I|^2 = 1 \tag{4.20}$$

$$TC^* + T^*C + RI^* + R^*I = 0 \tag{4.21}$$

$$TR^* + T^*R + IC^* + I^*C = 0 \tag{4.22}$$

$$TI^* + T^*I + RC^* + R^*C = 0 \tag{4.23}$$

Relation (4.20) is simply a statement of conservation of power. The other three relations constrain the real and imaginary parts of the four scattering parameters. These conditions can be used to determine the behavior of the Stokes transformation in (4.19), which has four parameters: $|T|^2$, $|C|^2$, Re$\{TC^*\}$, and Im$\{TC^*\}$.

The case of $R = I = 0$ (i.e., the antenna ports are perfectly matched and isolated) is an informative one. For this case, the relations (4.20-4.23) reduce to

$$|T|^2 + |C|^2 = 1 \tag{4.24}$$

$$TC^* + T^*C = 0 \tag{4.25}$$

Upon examination of (4.25) we see that Re$\{TC^*\} = 0$, i.e., C and T are 90° out of phase. Furthermore, by conservation of power, $|T| = \sqrt{1 - |C|^2}$. Using the substitutions $C = |C|e^{j\xi}$ and $T = \pm \mathrm{j}\sqrt{1 - |C|^2}e^{j\xi}$ the transformation matrix in (4.19) can be rewritten:

$$\begin{bmatrix} 1 - |C|^2 & |C|^2 & 0 & \mp|C|\sqrt{1 - |C|^2} \\ |C|^2 & 1 - |C|^2 & 0 & \pm|C|\sqrt{1 - |C|^2} \\ 0 & 0 & 1 & 0 \\ \pm|C|\sqrt{1 - |C|^2} & \mp|C|\sqrt{1 - |C|^2} & 0 & 1 - 2|C|^2 \end{bmatrix} \tag{4.26}$$

Here we see that cross-polarization mixing between T_v and T_h is $O(|C|^2)$; however, the degree of mixing between the fourth Stokes parameter and T_v and T_h is $O(|C|)$. Likewise, there is also a $(T_v - T_h)$ coupling of $O(|C|)$ into T_V. Notice that T_U is immune to cross-polarization effects for this specific case.

If the assumption that $R = I = 0$ is not made, then the real part of the product TC^* becomes important. That is, a mixing of T_v, T_h, and T_U will occur. This additional restric-

tion does not change the mixing between T_v, T_h and T_V; however, T_U is no longer immune to cross-polarization coupling. In fact, the inter-channel mixing with T_U is governed by the magnitude of $\text{Re}\{TC^*\}$. Fortuitously, the real part of TC^* can be bounded. From unitary relation (4.21),

$$\begin{aligned} TC^* + T^*C + RI^* + R^*I &= 0 \\ 2\text{Re}\{TC^*\} &= -\left(RI^* + R^*I\right) \\ |\text{Re}\{TC^*\}| &\leq \frac{1}{2}|RI^* + R^*I| \\ &\leq \frac{1}{2}(|RI^*| + |R^*I|) \\ &\leq |R||I| \end{aligned} \tag{4.27}$$

One only need specify the maximum values of $|R|$ and $|I|$ to limit the mixing of T_v and T_h into T_U.

The imaginary part of TC^* (which determines the mixing of T_v and T_h into T_V) can be bounded as well:

$$|T|^2|C|^2 \geq |\text{Im}TC^*|^2 = |T|^2|C|^2 - |\text{Re}TC^*|^2 \tag{4.28}$$

$$|T|^2|C|^2 \geq |\text{Im}TC^*|^2 \geq |T|^2|C|^2 - |R|^2|I|^2 \tag{4.29}$$

where $|T|^2 = 1 - |C|^2 - |R|^2 - |I|^2$ (by conservation of power). By specifying the three common antenna measurements, RL, XPD, and PPI, the degree of Stokes parameter mixing caused by cross-polarization coupling can be controlled and known to within some bound.

4.1.3 Composition of $\overline{\overline{S}}_R$ and $\overline{\overline{S}}_X$

The two scattering matrices $\overline{\overline{S}}_R$ and $\overline{\overline{S}}_X$ can be composed to relate the output fields E_a^- and E_b^- to the aperture fields E_v^+ and E_h^+. The composite scattering matrix is:

$$\overline{\overline{S}}_{XR} = \begin{bmatrix} R\cos^2\alpha - I\sin\alpha\cos\alpha & I\cos^2\alpha + R\sin\alpha\cos\alpha & T\cos\alpha - C\sin\alpha & C\cos\alpha - T\sin\alpha \\ I\cos^2\alpha + R\sin\alpha\cos\alpha & R\cos^2\alpha + I\sin\alpha\cos\alpha & C\cos\alpha + T\sin\alpha & T\cos\alpha + C\sin\alpha \\ T\cos\alpha - C\sin\alpha & C\cos\alpha + T\sin\alpha & R & I \\ C\cos\alpha - T\sin\alpha & T\cos\alpha + C\sin\alpha & I & R \end{bmatrix} \tag{4.30}$$

The order of the matrix composition is chosen such that the rotation operator is applied before the cross-polarization operator, which is physically justified because the received fields encounter the antenna aperture before the OMT. Assuming the receiver is perfectly matched to the antenna, the output fields are

$$\begin{bmatrix} E_v^- \\ E_h^- \\ E_a^- \\ E_b^- \end{bmatrix} = \overline{\overline{S}}_{XR} \begin{bmatrix} E_v^+ \\ E_h^+ \\ 0 \\ 0 \end{bmatrix} = \begin{bmatrix} (R\cos^2\alpha - I\sin\alpha\cos\alpha)\,E_v^+ + (I\cos^2\alpha + R\sin\alpha\cos\alpha)\,E_h^+ \\ (I\cos^2\alpha + R\sin\alpha\cos\alpha)\,E_v^+ + (R\cos^2\alpha + I\sin\alpha\cos\alpha)\,E_h^+ \\ (T\cos\alpha - C\sin\alpha)\,E_v^+ + (C\cos\alpha + T\sin\alpha)\,E_h^+ \\ (C\cos\alpha - T\sin\alpha)\,E_v^+ + (T\cos\alpha + C\sin\alpha)\,E_h^+ \end{bmatrix} \tag{4.31}$$

The measurable antenna brightness vector can be computed using the results for E_a^- and E_b^- from above; however, it is simpler to cascade the two Stokes vector transformations (4.12) and (4.19) and achieve the same result. The composite Stokes vector transformation, which accounts for both rotational and cross-polarization coupling error modes, can be

expressed as the product of two matrices:

$$\begin{bmatrix} |T|^2 & |C|^2 & \mathrm{Re}\{TC^*\} & -\mathrm{Im}\{TC^*\} \\ |C|^2 & |T|^2 & \mathrm{Re}\{TC^*\} & \mathrm{Im}\{TC^*\} \\ 2\mathrm{Re}\{TC^*\} & 2\mathrm{Re}\{TC^*\} & |T|^2+|C|^2 & 0 \\ 2\mathrm{Im}\{TC^*\} & -2\mathrm{Im}\{TC^*\} & 0 & |T|^2-|C|^2 \end{bmatrix} \cdot \begin{bmatrix} \cos^2\alpha & \sin^2\alpha & \frac{1}{2}\sin 2\alpha & 0 \\ \sin^2\alpha & \cos^2\alpha & -\frac{1}{2}\sin 2\alpha & 0 \\ -\sin 2\alpha & \sin 2\alpha & \cos 2\alpha & 0 \\ 0 & 0 & 0 & 1 \end{bmatrix} \quad (4.32)$$

The elements of this matrix product describe the mixing of the four Stokes parameters due to the composition of $\overline{\overline{S}}_R$ and $\overline{\overline{S}}_X$. Similar to (4.30), the order of the matrix multiplication is chosen such that the rotation operator is applied before the cross-polarization operator. Changing the order of multiplication will change the outcome of the following equations (4.33)-(4.36). This change, however, does not change the conclusions in Section 4.1.4 assuming both the polarization rotation angle α and polarization cross-coupling C are small. Each of the four Stokes parameters will be discussed briefly.

The measurable antenna temperatures at the vertical and horizontal polarization output ports are

$$\begin{aligned} T_{ANT,v} = &\left(|T|^2\cos^2\alpha + |C|^2\sin^2\alpha - \mathrm{Re}\{TC^*\}\sin 2\alpha\right)T_v + \\ &\left(|T|^2\sin^2\alpha + |C|^2\cos^2\alpha + \mathrm{Re}\{TC^*\}\sin 2\alpha\right)T_h + \\ &\left[\frac{1}{2}\left(|T|^2-|C|^2\right)\sin 2\alpha + \mathrm{Re}\{TC^*\}\cos 2\alpha\right]T_U - \mathrm{Im}\{TC^*\}T_V \end{aligned} \quad (4.33)$$

$$\begin{aligned} T_{ANT,h} = &\left(|T|^2\sin^2\alpha + |C|^2\cos^2\alpha - \mathrm{Re}\{TC^*\}\sin 2\alpha\right)T_v + \\ &\left(|T|^2\cos^2\alpha + |C|^2\sin^2\alpha + \mathrm{Re}\{TC^*\}\sin 2\alpha\right)T_h + \\ &\left[-\frac{1}{2}\left(|T|^2-|C|^2\right)\sin 2\alpha + \mathrm{Re}\{TC^*\}\cos 2\alpha\right]T_U + \mathrm{Im}\{TC^*\}T_V \end{aligned} \quad (4.34)$$

In these equations there are three modes of Stokes parameter mixing. The first mode is mixing between the vertical and horizontal channels. The contribution of T_h to $T_{ANT,v}$, or vice-versa, is $\left[|T|^2 \sin^2\alpha + |C|^2 \cos^2\alpha \pm \mathrm{Re}\{TC^*\} \sin 2\alpha\right]$. The first component $|T|^2 \sin^2\alpha$ is primarily due to polarization rotation and the second term $|C|^2 \cos^2\alpha$ is due to cross-polarization coupling. The third component $\pm\mathrm{Re}\{TC^*\} \sin 2\alpha$ is the product of both rotation and polarization coupling effects. The second mixing mode, the addition of the third Stokes parameter T_U to $T_{ANT,v}$ and $T_{ANT,h}$, has two components. The first component is $\pm\frac{1}{2}\left(|T|^2 - |C|^2\right) \sin 2\alpha$ and is due mainly to the rotation error mode; the second term is $\mathrm{Re}\{TC^*\} \cos 2\alpha$ and is caused mostly by cross-polarization coupling within the antenna. The final error mode is fourth Stokes parameter mixing into $T_{ANT,v}$ and $T_{ANT,h}$. Because T_V is invariant under polarization basis rotation, this mixing $\mp\mathrm{Im}\{TC^*\}$ is solely due to cross-polarization contamination.

The measurable in-phase correlation antenna temperature $T_{ANT,U}$ observed at the output ports is

$$T_{ANT,U} = 2\mathrm{Re}\{TC^*\}(T_v + T_h) - \left(|T|^2 + |C|^2\right) \sin 2\alpha (T_v - T_h) + \left(|T|^2 + |C|^2\right) \cos 2\alpha T_U \quad (4.35)$$

There are two modes of brightness temperature mixing that occur here. First, the sum $(T_v + T_h)$ is added to $T_{ANT,U}$ with a scaling factor of $\mathrm{Re}\{TC^*\}$. (Note, that if the antenna is perfectly matched and its ports are isolated, then $\mathrm{Re}\{TC^*\} = 0$.) This mixing is solely due to cross-polarization coupling. Second, the polarization difference $(T_v - T_h)$ is mixed in with a coefficient of $-\left(|T|^2 + |C|^2\right) \sin 2\alpha$. This contamination, on the other hand, is predominantly an effect of the rotational error mode and can be removed using electronic polarization basis rotation [20]. It is notable that the fourth Stokes parameter does not appear in the in-phase correlation brightness temperature. As seen in the next section, this is not true for the opposite case.

The quadrature-phase correlation antenna temperature $T_{ANT,V}$ measured at the out-

put ports is

$$T_{ANT,V} = 2\text{Im}\{TC^*\}\left(\cos^2\alpha - \sin^2\alpha\right)(T_v - T_h) + \\ 2\text{Im}\{TC^*\}\sin 2\alpha T_U + \left(|T|^2 - |C|^2\right)T_V \quad (4.36)$$

The polarization difference contribution has a coefficient of $2\text{Im}\{TC^*\}\left(\cos^2\alpha - \sin^2\alpha\right)$. It is clear that cross-polarization coupling is principally responsible for $(T_v - T_h)$ mixing into $T_{ANT,V}$. The other error component is the in-phase correlation brightness T_U with a magnitude of $2\text{Im}\{TC^*\}\sin 2\alpha$. The introduction of T_U into $T_{ANT,V}$ is interesting because it requires the combination of both the rotational and cross-polarization coupling error modes. Each of these modes acting individually does not cause third and fourth Stokes parameter mixing. If either C or α becomes zero, then the contribution vanishes.

4.1.4 Design Implications

The above relations can be used to compute the antenna specifications sufficient for remote sensing of observed brightness temperatures from a given scene class. Four parameters should be specified: return loss, cross-polarization discrimination, port-to-port isolation, and antenna rotation error. Known antenna rotations due to platform attitude variations can be compensated using a polarization basis transformation of the measured Stokes vector [20]. The unknown antenna rotation α_0 is assumed to be small enough that the following small angle approximations can be used:

$$\cos 2\alpha_0 \approx 1 \qquad \sin 2\alpha_0 \approx 2\alpha_0$$
$$\cos^2\alpha_0 \approx 1 \qquad \sin^2\alpha_0 \approx 0$$

Using these approximations the measured antenna temperatures (4.33)-(4.36) are

$$T_{ANT,v} = \left(|T|^2 - \text{Re}\{TC^*\}2\alpha_0\right)T_v + \left(|C|^2 + \text{Re}\{TC^*\}2\alpha_0\right)T_h + \\ \left[\frac{1}{2}\left(|T|^2 - |C|^2\right)2\alpha_0 + \text{Re}\{TC^*\}\right]T_U - \text{Im}\{TC^*\}T_V \quad (4.37)$$

$$T_{ANT,h} = \left(|C|^2 - \text{Re}\{TC^*\}2\alpha_0\right) T_v + \left(|T|^2 + \text{Re}\{TC^*\}2\alpha_0\right) T_h + \left[-\frac{1}{2}\left(|T|^2 - |C|^2\right) 2\alpha_0 + \text{Re}\{TC^*\}\right] T_U + \text{Im}\{TC^*\}T_V \quad (4.38)$$

$$T_{ANT,U} = 2\text{Re}\{TC^*\}(T_v + T_h) - \left(|T|^2 + |C|^2\right) 2\alpha_0(T_v - T_h) + \left(|T|^2 + |C|^2\right) T_U \quad (4.39)$$

$$T_{ANT,V} = 2\text{Im}\{TC^*\}(T_v - T_h) + 2\text{Im}\{TC^*\}2\alpha_0 T_U + \left(|T|^2 - |C|^2\right) T_V \quad (4.40)$$

One requirement arises from mixing of T_v and T_h, and three from possible contamination of T_U and T_V:

$$\left(|C|^2 \pm \text{Re}\{TC^*\}2\alpha_0\right) T_\alpha < \varepsilon \qquad \text{from (4.37) and (4.38)} \quad (4.41)$$

$$|2\alpha_0(T_v - T_h)| < \varepsilon \qquad \text{from (4.39)} \quad (4.42)$$

$$|2\text{Re}\{TC^*\}(T_v + T_h)| < \varepsilon \qquad \text{from (4.39)} \quad (4.43)$$

$$|2\text{Im}\{TC^*\}(T_v - T_h)| < \varepsilon \qquad \text{from (4.40)} \quad (4.44)$$

The choice of ε is up to the designer; however, the use of ΔT_{RMS} for ε will ensure that any systematic error will be smaller than random errors.

Typical values of T_v and T_h over the ocean, with 10 $\text{m}\,\text{s}^{-1}$ winds, and clear air at 53.1° from nadir have been computed using the microwave radiative transfer model of Gasiewski and Staelin [23]. At 18.7 GHz, $T_v + T_h \approx 308$ K and $T_v - T_h \approx 68$ K. Using these values and $\varepsilon = 0.1$ K, the constraints are:

$$|C|^2 < 5.3 \cdot 10^{-4} \quad (4.45)$$

$$|\alpha_0| < 7.4 \cdot 10^{-4} \quad (4.46)$$

$$|\text{Re}\{TC^*\}| < 1.6 \cdot 10^{-4} \quad (4.47)$$

$$|\text{Im}\{TC^*\}| < 7.4 \cdot 10^{-4} \quad (4.48)$$

These constraints can be used to determine antenna design specifications. The constraint (4.45) limits the cross-polarization mixing between the first two Stokes parameters. The following XPD specification will ensure less than 0.1 K mixing between T_v and T_h:

$$XPD > 32.7 \text{ dB} \quad (4.49)$$

This specification is typically attainable using precision symmetric microwave antennas. According to constraint (4.46), rotational errors should be known to within $\sim$0.05° in order that contributions of the polarization difference $T_v - T_h$ be kept to less than 0.1 K.

The magnitude of $|\mathrm{Re}\{TC^*\}|$ is constrained by (4.47). According to (4.27), $|\mathrm{Re}\{TC^*\}|$ is bounded by $|R||I|$. The following specification can be made about the return loss and port-to-port isolation:

$$RL + PPI > 75.8 \text{ dB} \tag{4.50}$$

This requirement can be met, for example, with 23 dB return loss (VSWR=1.15) and 53 dB port-to-port isolation. The isolation specification is attainable at lower frequencies; however, at 96 GHz an isolation of 30-40 dB is state-of-the-art [9].

Meeting these three constraints (4.45-4.47) is necessary for accurately measuring the first three Stokes parameters. To measure the fourth Stokes parameter, however, the remaining constraint (4.48) should be met because use of the less restrictive XPD specification (4.49) only limits mixing of the polarization difference into T_V by a factor of 0.058. For the given 68 K difference, the contamination would be 3.9 K. Thus, a more restrictive specification on XPD is required to accurately measure the fourth Stokes parameter. The new cross-polarization specification is found by combining (4.29) and (4.48) with the 23 dB return loss and 53 dB isolation specifications suggested above:

$$XPD > 62.4 \text{ dB} \tag{4.51}$$

This XPD requirement is not likely attainable and suggests that measurement of T_V using a linearly polarized antenna and direct polarization correlation is not optimal.

4.2 Digital Radiometer Calibration

Calibration of a digital polarimeter entails the periodic identification of slowly time varying system hardware constants. For the total-power channels, these constants are the system gain and offset. For the polarization correlating channel, two new parameters have been

introduced: the threshold-offset product (2.36) in Section 2.3.1.1 and the correlation bias (2.49) in Section 2.3.2. As will be shown, these new parameters can be estimated using the simple hot and cold looks of unpolarized blackbody standards as during conventional total-power channel calibration.

4.2.1 Total-Power Radiometer Calibration

From (2.15), the output of a total-power channel is related to the antenna temperature estimate by:

$$\left[\Phi^{-1}\left(1-\frac{\widehat{s}_\alpha^2}{2}\right)\right]^{-2} = g_\alpha\left(\widehat{T}_{ANT,\alpha}+T_{REC,\alpha}\right) \tag{4.52}$$

where the left hand side is the linearized digital variance, and g_α is the radiometer system gain. The receiver temperature $T_{REC,\alpha}$ is the system offset.

The gain and offset can be estimated by presenting the radiometer with two known antenna temperatures of differing values. The digital variance measurements corresponding to the calibration hot and cold antenna temperatures, denoted T_{CAL}^{hot} and T_{CAL}^{cold}, are:

$$\left[\Phi^{-1}\left(1-\frac{\widehat{s}_\alpha^{2\ hot}}{2}\right)\right]^{-2} = \widehat{g}_\alpha\left(T_{CAL}^{hot}+\widehat{T}_{REC,\alpha}\right) \tag{4.53}$$

$$\left[\Phi^{-1}\left(1-\frac{\widehat{s}_\alpha^{2\ cold}}{2}\right)\right]^{-2} = \widehat{g}_\alpha\left(T_{CAL}^{cold}+\widehat{T}_{REC,\alpha}\right) \tag{4.54}$$

This system is simple to solve for $\widehat{g}_\alpha$ and $\widehat{T}_{REC,\alpha}$:

$$\widehat{g}_\alpha = \frac{\left[\Phi^{-1}\left(1-\frac{\widehat{s}_\alpha^{2\ hot}}{2}\right)\right]^{-2} - \left[\Phi^{-1}\left(1-\frac{\widehat{s}_\alpha^{2\ cold}}{2}\right)\right]^{-2}}{T_{CAL}^{hot}-T_{CAL}^{cold}} \tag{4.55}$$

$$\widehat{T}_{REC,\alpha} = \frac{T_{CAL}^{hot}\left[\Phi^{-1}\left(1-\frac{\widehat{s}_\alpha^{2\ cold}}{2}\right)\right]^{-2} - T_{CAL}^{cold}\left[\Phi^{-1}\left(1-\frac{\widehat{s}_\alpha^{2\ hot}}{2}\right)\right]^{-2}}{\left[\Phi^{-1}\left(1-\frac{\widehat{s}_\alpha^{2\ hot}}{2}\right)\right]^{-2} - \left[\Phi^{-1}\left(1-\frac{\widehat{s}_\alpha^{2\ cold}}{2}\right)\right]^{-2}} \tag{4.56}$$

With the two system parameters properly identified, the estimated antenna temperature as measured by the total-power radiometer is

$$\widehat{T}_{ANT,\alpha} = \frac{1}{\widehat{g}_\alpha}\left[\Phi^{-1}\left(1-\frac{\widehat{s}_\alpha^2}{2}\right)\right]^{-2} - \widehat{T}_{REC,\alpha} \tag{4.57}$$

4.2.2 Correlator Calibration

Estimation of the digital correlator threshold-offset product (2.36) and correlation bias (2.49) system constants can be achieved using the hot and cold calibration looks required for the total-power radiometer calibration. The expected value of the correlator output given an unpolarized brightness field at the antenna input is

$$r_{ab}|_{T_U=0} = c_0\pi_\delta + c_1\rho_0 + c_3\rho_0^3 + c_5\rho_0^5 \tag{4.58}$$

where

$$c_0 = \frac{2}{\pi}\theta_a\theta_b \exp\left[-\frac{1}{2}(\theta_a^2 + \theta_b^2)\right] \tag{4.59}$$

and c_1, c_3, and c_5 are given by (2.21). The fifth-order term $c_5\rho_0^5$ can be ignored if $\rho_0 < 0.1$, which is usually the case.

The two calibration targets provide unpolarized emission at two different radiation intensities. Looking at both targets in sequence provides the digital correlation measurements $\widehat{r}_{ab}^{hot}$ and $\widehat{r}_{ab}^{cold}$ for the hot and cold looks, respectively. Using these two measurements the following system of equations can be formed:

$$\widehat{r}_{ab}^{hot} = c_0^{hot}\widehat{\pi}_\delta + c_1^{hot}\widehat{\rho}_0 + c_3^{hot}\widehat{\rho}_0^3 \tag{4.60}$$

$$\widehat{r}_{ab}^{cold} = c_0^{cold}\widehat{\pi}_\delta + c_1^{cold}\widehat{\rho}_0 + c_3^{cold}\widehat{\rho}_0^3 \tag{4.61}$$

The coefficients c_i^{hot} and c_i^{cold} are computed by using the relative threshold values θ_α^{hot} and θ_α^{cold}, respectively. Using only a third-order expansion in ρ_0 allows the above system to be solved analytically such that the estimate of the threshold-offset product can be found by

$$\widehat{\pi}_\delta = \frac{\widehat{r}_{ab}^{cold} - c_1^{cold}\widehat{\rho}_0 - c_3^{cold}\widehat{\rho}_0^3}{c_0^{cold}} \tag{4.62}$$

and an estimate of the correlation bias is a root of the following cubic:

$$\left(-\widehat{r}_{ab}^{hot} + \frac{c_0^{hot}}{c_0^{cold}}\widehat{r}_{ab}^{cold}\right) + \left(c_1^{hot} - \frac{c_0^{hot}}{c_0^{cold}}c_1^{cold}\right)\widehat{\rho}_0 + \left(c_3^{hot} - \frac{c_0^{hot}}{c_0^{cold}}c_3^{cold}\right)\widehat{\rho}_0^3 = 0 \tag{4.63}$$

The solution of a cubic equation is given in [1, (3.8.2)]. For this particular cubic there is typically one real root and a pair of complex conjugate roots. The real root is the desired solution for $\widehat{\rho}_0$ and is given by:

$$\widehat{\rho}_0 = \left[r + \left(q^3 + r^2\right)^{\frac{1}{2}}\right]^{\frac{1}{3}} \left[r - \left(q^3 + r^2\right)^{\frac{1}{2}}\right]^{\frac{1}{3}} \tag{4.64}$$

where q and r are defined as

$$q = \frac{1}{3}\frac{\left(c_1^{hot} - \frac{c_0^{hot}}{c_0^{cold}} c_1^{cold}\right)}{\left(c_3^{hot} - \frac{c_0^{hot}}{c_0^{cold}} c_3^{cold}\right)} \tag{4.65}$$

$$r = \frac{1}{2}\frac{\left(\widehat{r}_{ab}^{hot} - \frac{c_0^{hot}}{c_0^{cold}} \widehat{r}_{ab}^{cold}\right)}{\left(c_3^{hot} - \frac{c_0^{hot}}{c_0^{cold}} c_3^{cold}\right)} \tag{4.66}$$

Care must be taken in choosing the proper branch of the cube roots; otherwise the solution is straightforward.

Once $\widehat{\pi}_\delta$ and $\widehat{\rho}_0$ have been determined, the correlation coefficient estimate $\widehat{\rho}$ can be computed as follows:

$$\widehat{\rho} = \left[\frac{1}{c_1}\left(\widehat{r}_{ab} - \widehat{r}_{ab}\big|_{\rho=0}\right) - \frac{c_3}{c_1^4}\left(\widehat{r}_{ab} - \widehat{r}_{ab}\big|_{\rho=0}\right)^3 + \left(3\frac{c_3^2}{c_1^7} - \frac{c_5}{c_1^6}\right)\left(\widehat{r}_{ab} - \widehat{r}_{ab}\big|_{\rho=0}\right)^5\right] - \widehat{\rho}_0 \tag{4.67}$$

where the estimated digital correlation bias is computed as in (2.34):

$$\widehat{r}_{ab}\big|_{\rho=0} = \widehat{\pi}_\delta \cdot \frac{2}{\pi}\theta_a\theta_b \exp\left[-\frac{1}{2}\left(\theta_a^2 + \theta_b^2\right)\right] \tag{4.68}$$

There are two required calibration offsets. The first is the correlation bias $\hat{\rho}_0$, which is caused by correlated LO thermal noise. The second is the digital correlation offset $r_{ab}\big|_{\rho=0}$, which is caused by threshold level asymmetry and is applied to the digital correlator output prior to conversion into the continuous correlation coefficient. An estimate of the third Stokes parameter can subsequently be computed using (2.5):

$$\widehat{T}_U = 2\widehat{\rho}\sqrt{\widehat{T}_{v,sys}\widehat{T}_{h,sys}} \tag{4.69}$$

Table 4.1: Correlator hardware constants and residual $\widehat{T}_U$ offsets.

Band	Date	Time UTC	$\widehat{\rho}_0$	$\widehat{\pi}_\delta$	ΔT_U^{hot} (K)	ΔT_U^{cold} (K)	$\sigma_{\Delta T_U}$ (K)
X	3/1/97	1757	-0.17	-0.048	-0.077	-0.11	0.65
	3/4/97	2027	-0.20	0.020	-0.55	0.22	0.33
	3/7/97	2132	-0.20	0.032	0.017	0.080	0.28
Ka_1	3/1/97	1757	0.053	-0.13	0.32	0.63	0.44
	3/4/97	2027	0.028	-0.060	0.35	-2.8	1.1
	3/7/97	2132	0.012	-0.016	-0.36	0.18	0.78
Ka_2	3/1/97	1757	-0.20	0.032	0.21	-0.044	0.23
	3/4/97	2027	0.012	-0.016	-0.36	-1.7	0.67
	3/7/97	2132	0.19	-0.006	0.069	0.19	0.54

The PSR operational calibration algorithms utilized the preceding technique for the Labrador Sea experiment. Table 4.1 lists several estimates of ρ_0 and π_δ made using unpolarized calibration looks acquired during flights on March 1, 4 and 7. Several $\widehat{T}_U$ measurements of the unpolarized calibration loads are also listed. The values of $\widehat{\rho}_0$ are similar to those predicted in Section 2.3.2 for radiometers with significant LO noise. As seen in Table 4.1, the bias in T_U is typically within $\sim \pm 0.4$ K with the exception of the Ka channels on March 4. As evidenced by the standard deviation, the Ka channels were particularly noisy at that time. Otherwise, these data verify the effectiveness of the calibration using two unpolarized looks.

4.2.3 Verification of Polarimetric Calibration

A fully polarimetric calibration using a polarized target similar to that described in [20] was performed to determine the effectiveness of the unpolarized calibration method for the T_U channel. The calibration target comprised an ambient load, a cold load, and a polarizing grid. The absorber material was carbon-impregnated urethane foam (similar to Eccosorb® brand). The cold load was constructed by immersing a 56 cm $\times$ 56 cm square of the convoluted absorber in liquid nitrogen. The liquid nitrogen bath covered the

absorber tips by at least 0.5 cm to ensure temperature uniformity. The ambient load was shrouded by a styrofoam jacket. The temperature difference was $T_{hot} - T_{cold} \approx 210$ K. The polarized target was mounted to a turntable that provided rotation about the feedhorn axis. The rotational position was measured using an optical encoder with 0.25° precision. The resulting polarized field that was presented to the radiometer is given by:

$$\begin{bmatrix} T_v \\ T_h \\ T_U \end{bmatrix} = \begin{bmatrix} \cos^2\alpha & \sin^2\alpha \\ \sin^2\alpha & \cos^2\alpha \\ -\sin 2\alpha & \sin 2\alpha \end{bmatrix} \begin{bmatrix} r_{||}T_{hot} + (1 - r_{||})T_{cold} \\ t_{\perp}T_{cold} + (1 - t_{\perp})T_{hot} \end{bmatrix} \tag{4.70}$$

where α is the angular position of the calibration target. The coefficients $r_{||}$ and $t_{\perp}$ are the parallel-polarized reflection and perpendicular-polarized transmission coefficients of the polarizing grid.

The estimated third Stokes parameter, as given in Section 4.2.2, can be related to the incident polarized field (4.70) by the relevant portion of (2.7):

$$\widehat{T}_U = 2\langle\widehat{\rho}\rangle\sqrt{T_{sys,v}T_{sys,h}} = g_{Uv}T_v + g_{Uh}T_h + g_{UU}T_U + o_U \tag{4.71}$$

where the gains g_{UU}, g_{Uv}, and g_{Uh} and offset o_U are unidentified system parameters that might have been left uncompensated by the two-look non-polarized calibration procedure. Ideally $g_{UU} = 1$ and $g_{Uv} = g_{Uh} = o_U = 0$. Comparison of measurements of $\widehat{T}_U$ (as provided by the calibration standard) with the expected polarized emission T_v, T_h, and T_U makes possible the determination of the level of any Stokes parameter mixing, residual correlation offset, and correlation coefficient attenuation.

Brightness vector measurements at several values of α and one unpolarized look allows a system of equations to be formed, which can be solved for the gains and offset:

$$\begin{bmatrix} \widehat{T}_U(\alpha_1) \\ \widehat{T}_U(\alpha_2) \\ \vdots \\ \widehat{T}_U(\alpha_n) \\ \widehat{T}_U(UP) \end{bmatrix} = \overline{\overline{C}}_U \begin{bmatrix} g_{Uv} \\ g_{Uh} \\ g_{UU} \\ o_U \end{bmatrix} + \overline{n} \tag{4.72}$$

where $\overline{\overline{C}}_U$ is the observation matrix and $\overline{n}$ is the random noise of the measurement. The observation matrix is constructed as follows:

$$\overline{\overline{C}}_U = \begin{bmatrix} T_v(\alpha_1) & T_h(\alpha_1) & T_U(\alpha_1) & 1 \\ T_v(\alpha_2) & T_h(\alpha_2) & T_U(\alpha_2) & 1 \\ \vdots & \vdots & \vdots & \vdots \\ T_v(\alpha_n) & T_h(\alpha_n) & T_U(\alpha_n) & 1 \\ T_{amb} & T_{amb} & 0 & 1 \end{bmatrix} \tag{4.73}$$

where the brightness temperatures T_v, T_h and T_U are determined by (4.70) and T_{amb} is the brightness temperature of the unpolarized look. The measurement vector was generated by the following procedure. Initially, the radiometer antenna was aligned with the polarized target such that the incident Stokes field was $T_v = T_1$, $T_h = T_2$ and $T_U = 0$. The measurements were taken while rotating the target over an angular range of ~420°. An additional piece of absorber at ambient temperature was used for the unpolarized look. Six hundred radiometer samples were recorded and averaged into two degree bins, resulting in 180 points (for a full 360° rotation) with ~28 ms integration time per point ($\Delta T_{RMS} \approx 0.4$ K). Using the calibration constants found from the two-look unpolarized method, the output of the digital correlator was converted into calibrated values of $\widehat{T}_U(\alpha_i)$ ($i = 1 \ldots n$) for the different angles and $\widehat{T}_U(UP)$ for the unpolarized look. The measurement vector and the columns of the observation matrix are plotted in Figure 4.2. By visual inspection, T_v and T_h mixing into $\widehat{T}_U$ appears to be nonexistent, but the correlator output is attenuated ~75% compared to T_U.

Given the measurement vector and the observation matrix, the gains and offset can be precisely found using the pseudo-inverse [57]:

$$\begin{bmatrix} \widehat{g}_{Uv} \\ \widehat{g}_{Uh} \\ \widehat{g}_{UU} \\ \widehat{o}_U \end{bmatrix} = \left(\overline{\overline{C}}_U{}^T \overline{\overline{C}}_U \right)^{-1} \overline{\overline{C}}_U{}^T \begin{bmatrix} \widehat{T}_U(\alpha = 1^\circ) \\ \widehat{T}_U(\alpha = 3^\circ) \\ \vdots \\ \widehat{T}_U(\alpha = 359^\circ) \\ \widehat{T}_U(UP) \end{bmatrix} \tag{4.74}$$

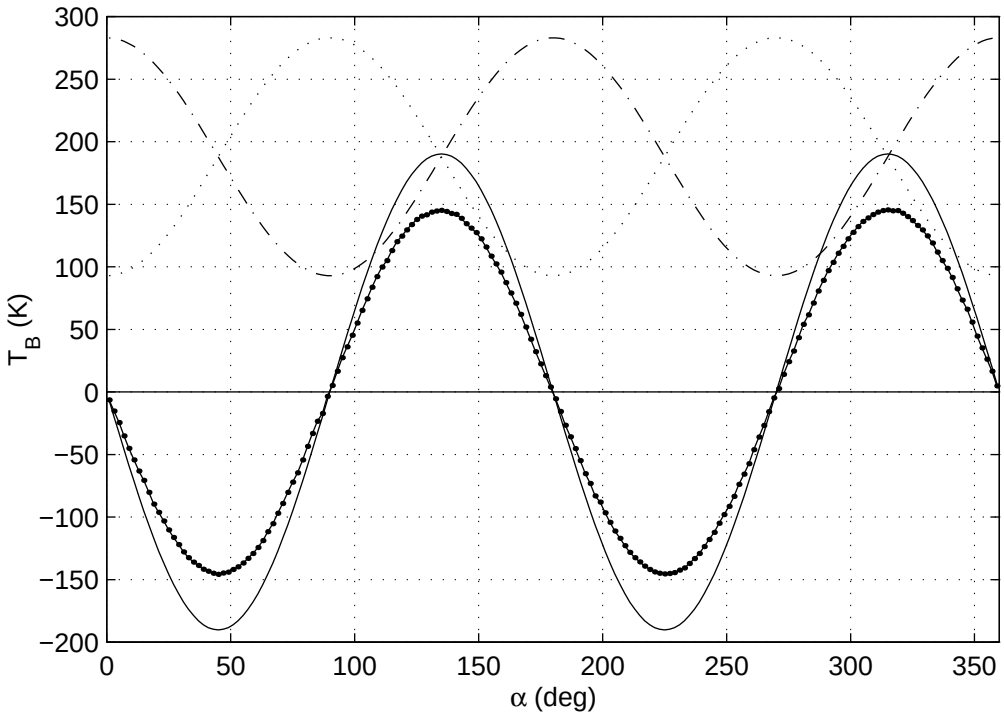

Figure 4.2: Plot of 37.0 GHz polarized target measurements $\widehat{T}_U(\alpha)$ (heavy dotted line) and the observation matrix. The columns of the observation matrix are plotted as follows: $T_v(\alpha)$ (dash-dot), $T_h(\alpha)$ (dotted), and $T_U(\alpha)$ (solid).

For the 37.0 GHz polarimeter, the following parameters were computed:

$$\begin{bmatrix} \widehat{g}_{Uv} \\ \widehat{g}_{Uh} \\ \widehat{g}_{UU} \\ \widehat{o}_U \end{bmatrix} = \begin{bmatrix} 1.01 \times 10^{-3} \\ 4.94 \times 10^{-4} \\ 0.764 \\ -0.444 \end{bmatrix} \tag{4.75}$$

First notable are the small ($\lesssim$0.1%) T_v and T_h cross-polarization gain terms. As predicted by (4.39), minimizing Re$\{TC^*\}$ prohibited substantial contamination from T_v and T_h. Second, the correlator output is seen to be attenuated by $\widehat{g}_{UU} = 0.764$, which is most likely due to sampler hysteresis, timing skew, and possibly threshold asymmetry effects. Subsequent polarimetric calibration experiments have shown that this attenuation does not vary by more than a few percent over several months, allowing a correlator gain coefficient to be included in the aircraft data processing routines. Finally, the offset $o_U = 0.444$ K is similar to the values listed in Table 4.1. Offsets of this size correspond to correlation coefficient offsets $\sim 10^{-4}$, which are close to the design goals set forth in Chapter 2.

4.3 In-Flight Calibration

In-flight calibration is carried out using the hot and ambient temperature unpolarized targets integral to the PSR vertical support structure. The calibration loads are recessed into the vertical support structure so that the radiometers can be pointed upwards at 45° and view either the hot or ambient load. Figure 4.3 shows a CAD model illustrating the position of the calibration loads with respect to the scanhead. The photograph in Figure 4.4 was taken looking up from below the ring bearing at the calibration loads with the scanhead removed. Each calibration load is constructed out of 45 mm (1.75 inch) convoluted foam absorber (similar to the Eccosorb® brand) with aluminum backplates (see Figure 4.5(a)). The aluminum frame and absorbing material are both shrouded in 13 mm (0.5 inch) styrofoam board. The hot load is heated to ∼65° C by heater strips that are glued to the aluminum backplates. Both calibration loads have eight resistive temperature detectors (RTD) at-

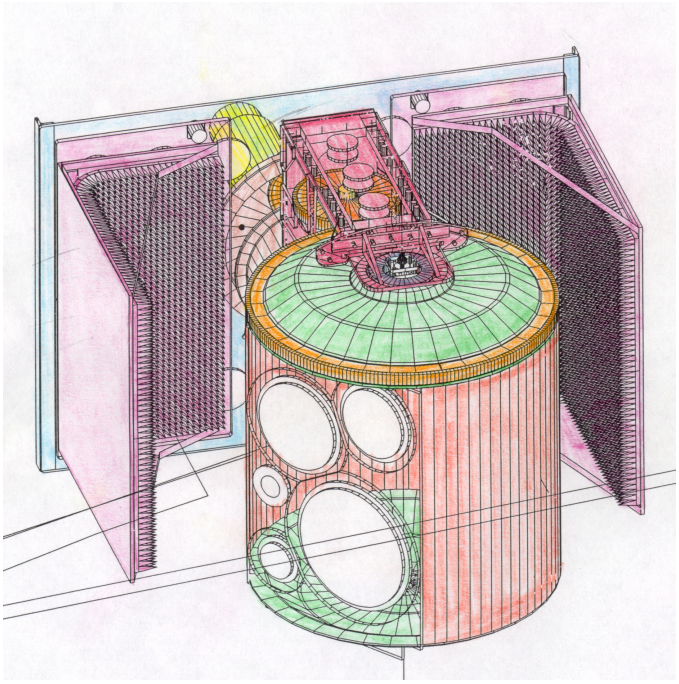

Figure 4.3: Three-dimensional CAD model of the calibration targets and the scanhead. The vertical support structure was not rendered for clarity.

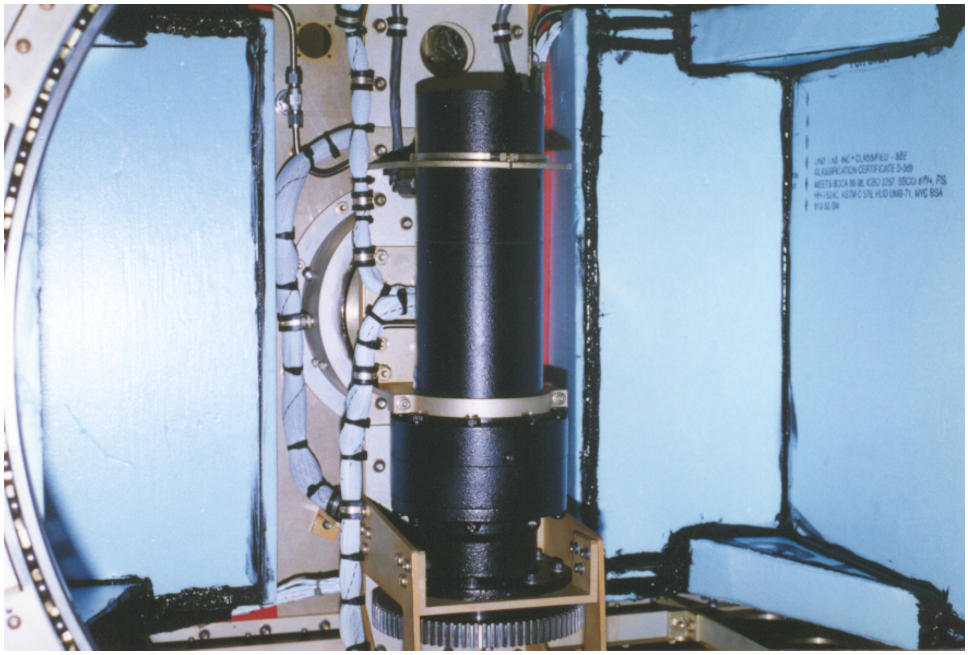

Figure 4.4: The PSR calibration loads and elevation motor viewed from below the ring bearing with the scanhead not installed.

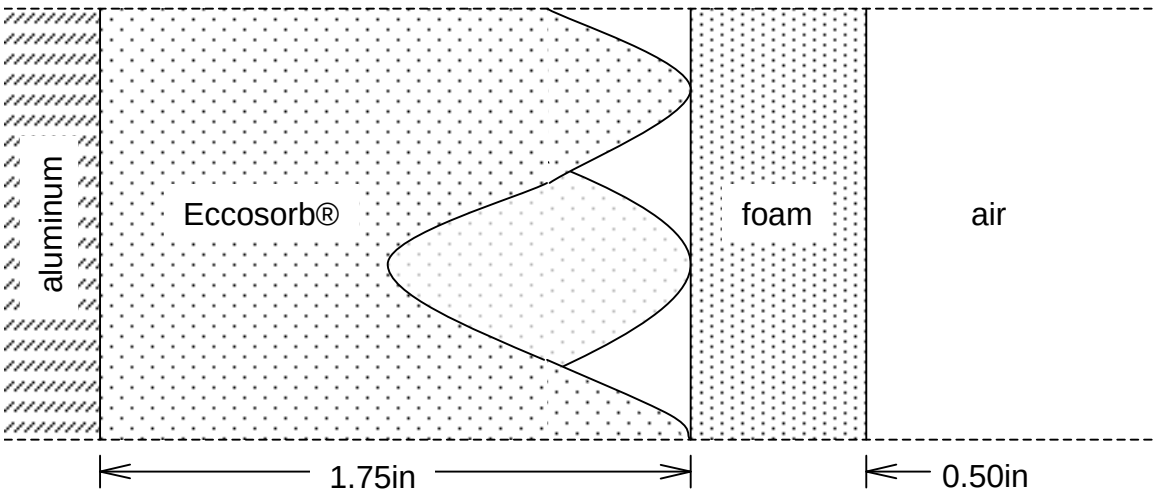

(a) cross-section of calibration load structure

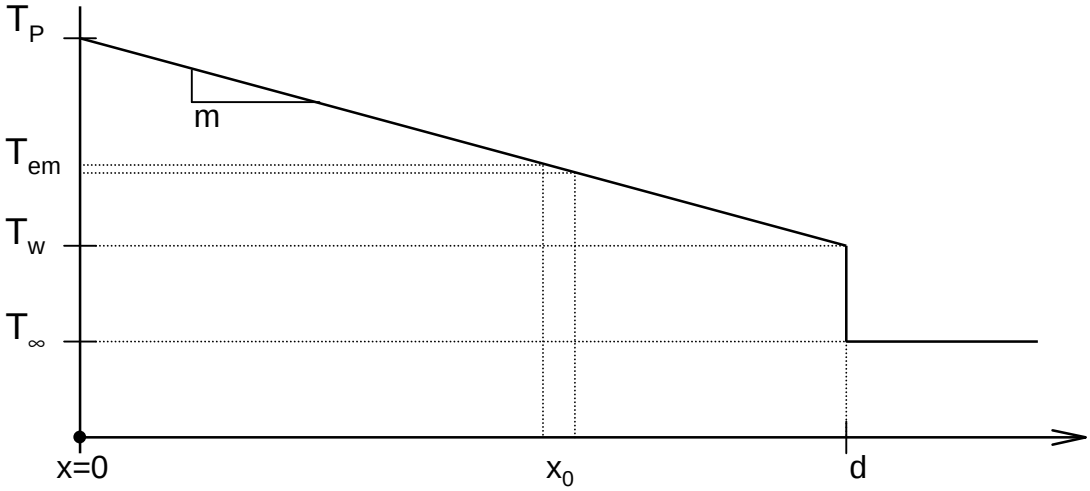

(b) steady-state temperature profile

(c) finite difference grid

Figure 4.5: PSR calibration targets: (a) cross-section of PSR calibration load, (b) steady-state temperature profile for the steady-state model, (c) finite-difference grid for the transient thermal model.

tached to the aluminum backplates. The RTDs are connected in three-wire configuration to a temperature measurement system called the Tempscan unit from Omega Engineering. The Tempscan is mounted to the top of the vertical support structure to keep the RTD wire lengths as short as possible. The Tempscan acquires temperature data every 15 seconds and transmits the data to the secondary cabin PC over an RS-232 serial data link. These data are stored on the hard drive for later usage by the radiometer calibration algorithms.

Because of time and cost constraints, the absorber material used had a low thermal conductivity, which caused a longitudinal temperature gradient to extend from the aluminum backplate through the absorber to the foam shroud. A third calibration point, the cold sky, is used to characterize the calibration loads so an accurate estimate of the emission temperatures can be made. The emission temperatures T_{em} of the loads can be modeled by:

$$T_{em} = \int_0^d W(x)T(x)dx \tag{4.76}$$

where $W(x)$ is the weighting function and $T(x)$ is the temperature profile. The weighting function is assumed to be simply

$$W(x) = \delta(x - x_0) \tag{4.77}$$

such that the emission temperature is $T_{em} = T(x_0)$. A steady-state thermal model is described here and used to find values of x_0 for each of the PSR's frequency bands. With the calibration loads characterized in steady-state, a finite difference model is used to calculate the unsteady-state temperature response within the calibration load during aircraft sorties. The backplate and ambient temperature data are used as forced boundary conditions to drive the temperature within the absorber. The time domain calculations of temperature at positions x_0 can then be used to calibrate the total-power radiometers.

4.3.1 Steady-State Model

The calibration load material and the styrofoam are both urethane foams and are assumed to have similar thermal properties (see Table 4.2). Using this assumption, the steady-state

Table 4.2: Thermal properties of urethane foam.

Symbol	Value	Description
ρ	$30\ \mathrm{kg\,m^{-3}}$	density
k	$0.024\ \mathrm{W\,m^{-1}\,{}^{\circ}C^{-1}}$	thermal conductivity
c	$1000\ \mathrm{J\,kg^{-1}\,{}^{\circ}C^{-1}}$	heat capacity

temperature profile through the load has a constant gradient (see Figure 4.5). At the styrofoam/air interface, however, the temperature profile is no longer linear because of convection. This transition can be modeled by a discontinuity. The steady-state temperature profile is

$$T(x) = \begin{cases} T_P + mx & 0 \leq x \leq d \\ T_\infty & x > d \end{cases} \tag{4.78}$$

where T_P is the backplate temperature and T_∞ is the ambient air temperature. The slope m or gradient of the temperature profile depends upon the heat flow at $x = d$. The temperature at $x = d$ is commonly called the wall temperature $T_w = T_P + md$. From Fourier's law of heat conduction and Newton's law of cooling, the steady-state heat flow equation at $x = d$ is

$$-km = h(T_w - T_\infty) \tag{4.79}$$

The coefficient of heat transfer h due to convection is difficult to model because the major influencing factor is the airflow at the interface. The calibration loads are recessed into the aircraft, and the effect upon the surrounding air from the passing slipstream at the scanhead and ring bearing is unknown. A method is developed here whereby the parameter h is identified in flight using the cold sky looks in addition to the hot and ambient target looks.

The emission temperature can be parameterized and evaluated using T_P and T_∞ by:

$$T_{em} = \gamma T_P + (1 - \gamma) T_\infty \tag{4.80}$$

where the parameter γ is related to the temperature gradient:

$$\gamma = m\frac{x_0}{T_P - T_\infty} + 1 \tag{4.81}$$

In this formulation, other effects such as calibration target reflectivity and beam spill-over are inherently included through the parameter γ. Since m, h, and γ are related by (4.79) and (4.81), the parameter γ will be determined by using the sky looks and then used to find h.

During the Labrador Sea experiment, several sky looks were executed. To point the radiometers at the sky, the scanner was positioned looking to starboard at a 60° nadir angle. The P-3 then commenced three successive 60° left rolls at ∼6.1 km (20,000') altitude, which pointed the antennas 30° above the horizon. The sky temperature was calculated using atmospheric profiles measured by five radiosondes that were launched from the *Knorr* from March 1 through 9. The radiosonde profiles terminated at ∼100 mb, so statistical data were used to augment to profiles to 5 mb. Using the microwave radiative transfer model of Gasiewski and Staelin [23], the sky temperature was computed for the elevation angles and altitudes of the PSR during the 60° rolls. The values of T_{sky} ranged from ∼4 to 8 K at 30° above the horizon for X- through Ka-bands. During a single 60° roll there were ∼500 radiometer samples recorded at 20°- 30° elevation.

Taking the hot, ambient, and sky looks together, an objective function can be formed whose minimizer is γ for each frequency band. When looking at the sky, the radiometer detector voltage v_d is related to the measured brightness temperature by

$$\hat{T}_{sky} = gv_d + o \tag{4.82}$$

where g and o are the system gain and offset. Using the hot and ambient calibration loads, the gain and offset are

$$g = \frac{T_c - T_h}{v_c - v_h} \qquad \text{and} \qquad o = \frac{v_c T_h - v_h T_c}{v_c - v_h} \tag{4.83}$$

The temperatures T_c and T_h are the emission temperatures of the hot and cold calibration

Table 4.3: Values of x_0 and γ for three PSR radiometer bands.

Band	X	K	Ka
x_0	31.6 mm	30.6 mm	33.1 mm
γ	0.6632	0.6739	0.6470
σ_γ	0.0156	0.0190	0.0303
ΔT_{abs}	2.4 K	2.8 K	4.7 K

loads and are found using (4.80)

$$T_c = \gamma T_{P,c} + (1-\gamma)T_\infty) \tag{4.84}$$

$$T_h = \gamma T_{P,h} + (1-\gamma)T_\infty) \tag{4.85}$$

By using the computed brightness temperatures for T_{sky}, and knowing T_∞ and the calibration load backplate temperatures, the parameter γ can be found by minimizing the following:

$$\sum_i \left(T_{sky,i} - \hat{T}_{sky,i}\right)^2 \tag{4.86}$$

where the sum is over all the sky look samples. The modeled sky temperature for the i-th sample is denoted $T_{sky,i}$, and the estimated sky temperature $\hat{T}_{sky,i}$ is given by (4.82)-(4.85).

Table 4.3 lists the values of γ found using the available sky looks for each channel. The absolute calibration of the radiometers is limited by the variability σ_γ of the estimates of γ:

$$\Delta T_{abs} = \frac{\sigma_\gamma}{\gamma}(T_P - T_\infty) \tag{4.87}$$

The standard deviation σ_γ for each frequency channel was found from the set of 20 values of γ that were computed using data from ten steep-rolls performed during five different flights. The absolute temperature uncertainties for the different PSR frequency bands are listed in Table 4.3 with $T_P - T_\infty \approx 100$K.

The heat flow equation (4.79) at the convective boundary can be rewritten using (4.78-4.81):

$$h = k\frac{(1-\gamma)/x_0}{1 - d(1-\gamma)/x_0} \tag{4.88}$$

The coefficient of heat transfer h due to convection is fundamentally independent of the microwave frequency, and the frequency dependence of γ and x_0 must cancel. To hold h constant, the term $(1-\gamma)x_0^{-1}$ must remain constant and is assumed to have an average broadband value:

$$\frac{1-\gamma}{x_0} = \frac{1-\overline{\gamma}}{\overline{x}_0} \tag{4.89}$$

where $\overline{\gamma}$ is the average of the values in Table 4.3 and $\overline{x}_0$ is the broadband emission point within the absorber profile. The value of $\overline{x}_0$ is assumed to be 38 mm (1.5 in), such that the broadband microwave emission originates at the midpoint between the tips and valleys of the convoluted foam absorber. This assumption is consistent with model results obtained for wedge absorber with a width to height ratio near unity [36]. With these assumptions, the value of h is calculated to be 0.6554 W m^{-2} °C^{-1}. The completed steady-state model comprises the two boundary conditions (the backplate, and the convection boundary) and the values of x_0 for each frequency band. During a sortie, however, the environment does not remain in steady-state; therefore, a transient model is needed to compute the temperature profile throughout the flight.

4.3.2 Transient Model

A one-dimensional finite-difference transient model has been developed to solve the time-dependent heat transfer problem for a calibration load during an aircraft sortie. The backplate and ambient temperatures are used as forced boundary conditions to drive the temperature profile within the absorber. Using the convection boundary and values of x_0 that were estimated using the steady-state model, the emission temperatures can be estimated for an entire flight. The following is the time-dependent heat equation, which is approximated and solved using the finite-difference technique:

$$k\frac{\partial^2 T}{\partial x^2} = \rho c \frac{\partial T}{\partial t} \tag{4.90}$$

where ρ is the material density and c is the specific heat (or heat capacity) of the material.

The finite difference grid is constructed using M equally spaced points between the calibration load backplate at $m = 0$ and the convection boundary at $m = M$ (see Figure 4.5(c)). The grid spacing was chosen to be $\Delta x = 1$mm. The spatial derivative at grid point m can be approximated using a central difference:

$$\frac{\partial^2 T}{\partial x^2} \approx \frac{T_{m+1} - 2T_m + T_{m-1}}{(\Delta x)^2} \tag{4.91}$$

The time derivative is approximated using a single sided forward difference:

$$\frac{\partial T}{\partial t} \approx \frac{T^{p+1} - T^p}{\Delta t} \tag{4.92}$$

These two differences can be substituted into (4.90) and the time step equation can be found. By setting

$$\frac{(\Delta x)^2}{\alpha \Delta t} = 2 \qquad \text{with} \qquad \alpha = \frac{k}{\rho c} \tag{4.93}$$

the timestep equation is

$$T_m^{p+1} = \frac{T_{m-1}^p + T_{m+1}^p}{2} \tag{4.94}$$

With Δx and α specified, the timestep is $\Delta t = 0.625$sec.

The boundary condition at $m = 0$ is enforced by assigning the node temperature at timestep p to the backplate temperature at $t = p\Delta t$:

$$T_0^p = T_P(p\Delta t) \tag{4.95}$$

The convection boundary condition is achieved by balancing the energy flow at the wall using single-sided difference approximations [33, eqn 4-33]:

$$T_M^p = \frac{T_{M-1}^p + \beta T_\infty^p}{1 + \beta} \qquad \text{with } \beta = \frac{h\Delta x}{k} \tag{4.96}$$

and $T_\infty^p = T_\infty(p\Delta t)$, which is the static air temperature as measured by the P-3 environmental system. The model is run for each flight and the calibration load emission temperatures are taken to be $T(x_0)$ as computed by the transient model. For example, Figure 4.6 shows the computed emission temperatures for the flight on March 7.

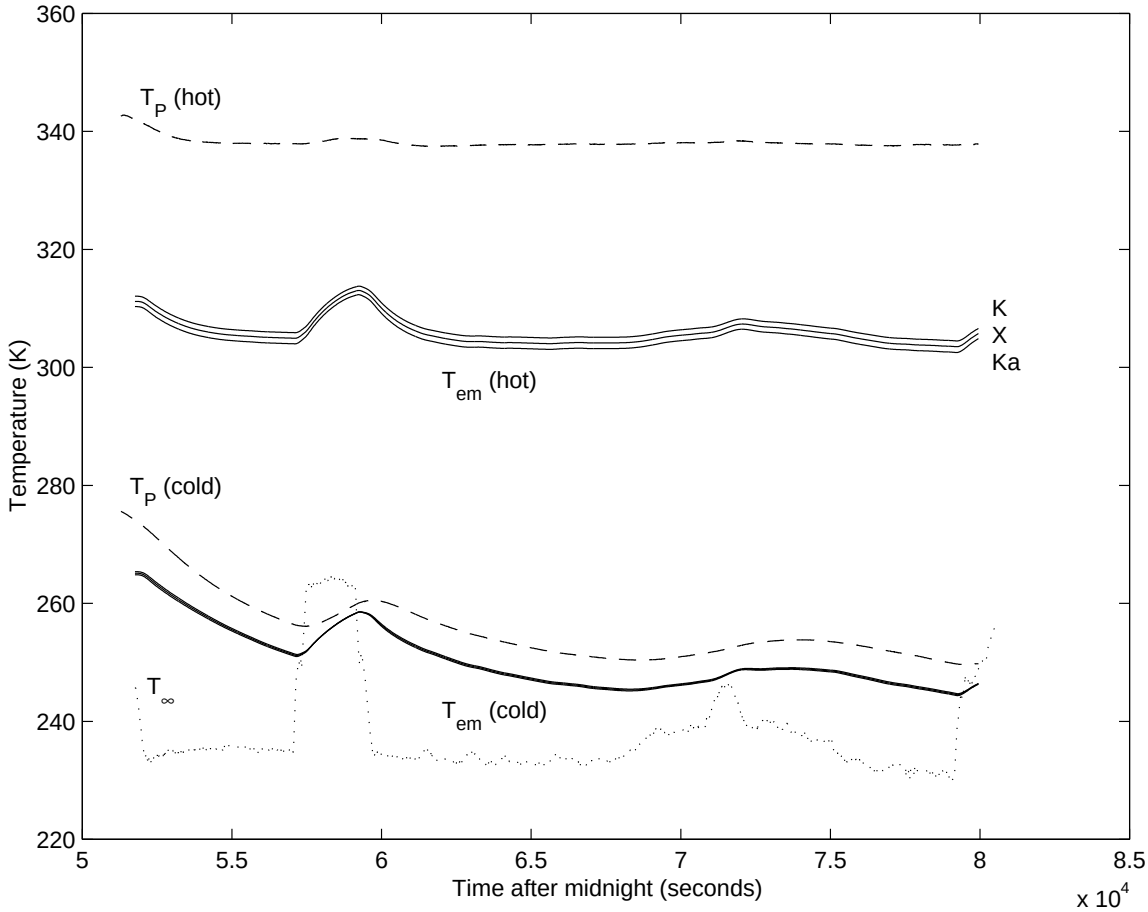

Figure 4.6: Computed calibration load emission temperatures for the Labrador Sea flight on March 7.

4.3.3 Comparison of PSR brightness temperatures and the cold sky

To verify the performance of the calibration algorithms, calibrated PSR brightness temperatures were compared with the modeled cold sky temperatures. The cold sky looks were used to obtain the parameter γ for the steady-state model, however, the comparison in this section verifies the utility of the time-domain model for calibrating the radiometers. Table 4.4 lists three representative cases for comparison. The mean difference between the calibrated and modeled brightness temperatures for $\sim$400 samples is $\lesssim$3 K, which is near the accuracy predicted in Table 4.3. The X-v, X-h, and Ka-h channels on March 9, however, exhibited a larger than normal offset of about twice the predicted accuracy. Thus, the accuracy of time-domain calibration algorithm is concluded to be 1-2 times the predicted accuracy or $\Delta T_{abs} \sim$ 4-8 K.

Table 4.4: Comparisons of PSR brightness temperatures and modeled cold sky temperatures for three representative 60°-roll observations during the Labrador Sea experiment. The T_h Ka-band channel exhibited a larger than normal offset during the flight on March 9, yet the offset was only ∼2.5 times the standard deviation predicted in Table 4.3.

3/7/97	scan 1, samples 640-1000 elevation angle = 61.4°, altitude=5.7 km			
PSR Channel	modeled T_{sky} (K)	measured T_{sky} (K)	mean difference (K)	standard deviation (K)
X-v	3.65	3.67	0.02	0.49
X-h	3.65	2.36	-1.29	0.76
K-v	4.05	1.89	-2.16	2.16
K-h	4.05	4.00	-0.05	1.55
Ka-v	7.20	6.91	-0.29	0.91
Ka-h	7.20	5.70	-1.51	0.41

3/7/97	scan 2, samples 570-1100 elevation angle = 60.3°, altitude=5.7 km			
PSR Channel	modeled T_{sky} (K)	measured T_{sky} (K)	mean difference (K)	standard deviation (K)
X-v	3.69	5.26	1.57	0.50
X-h	3.69	3.70	0.01	0.79
K-v	4.10	3.89	-0.21	2.22
K-h	4.10	4.82	0.72	1.60
Ka-v	7.38	6.73	-0.65	1.13
Ka-h	7.38	7.40	0.02	1.12

3/9/97	scan 1, samples 500-750 elevation angle = 59.9°, altitude=5.6 km			
PSR Channel	modeled T_{sky} (K)	measured T_{sky} (K)	mean difference (K)	standard deviation (K)
X-v	3.71	7.68	3.97	0.45
X-h	3.71	-1.67	-5.39	0.73
K-v	4.14	3.84	-0.30	2.05
K-h	4.14	4.30	0.16	1.46
Ka-v	7.49	9.73	2.24	1.18
Ka-h	7.49	-3.77	-11.27	0.56

CHAPTER 5

Geophysical Model Function

An empirical geophysical model function (GMF) for brightness temperature over the ocean is described in this chapter. The model contains both the azimuthal wind direction harmonics (for the full Stokes vector) and the azimuthally-averaged zeroeth-order components (for the first two Stokes parameters). The primary geophysical parameters in the model are wind speed, wind direction, and atmospheric transmissivity. The first- and second-order harmonic amplitude coefficients of the wind direction harmonics were measured using the PSR during the Labrador Sea experiment. These measurements were for the first three Stokes parameters at 10.7, 18.7, and 37.0 GHz at wind speeds from 0.4 through 16 $\mathrm{m\,s^{-1}}$. The T_v and T_h results are comparable to those obtained using the SSM/I satellite radiometer [66, 4], thus vindicating both measurement techniques. The T_U are comparable to recently published fixed-beam radiometer aircraft observations [69] for wind speeds below 5 $\mathrm{m\,s^{-1}}$. Similar trends are observed for wind speeds higher than 5$\mathrm{m\,s^{-1}}$, but the coefficients of the PSR first-order harmonic measurements are smaller compared to the other aircraft data.

5.1 Background

The PSR geophysical model function relates the wind speed and direction, typically referenced to 10 m above the surface, to the directionally dependent Stokes vector that is observed over the ocean. The observed brightness temperature depends upon the polarization and frequency, and at least the following geophysical parameters: wind speed, wind

direction, water temperature, and atmospheric transmissivity. Observations made using the SSM/I [66] along with wave tank data [21] and emission models [42] suggest that the azimuthal dependence of the brightness temperature can be well modeled by a second-order harmonic expansion including the effects of these variables. The general form of the GMF for a channel of one specific frequency is:

$$\overline{T}_B = \begin{bmatrix} \begin{pmatrix} a_{v0} \\ a_{h0} \end{pmatrix} + t \left[\begin{pmatrix} a_{v1} \\ a_{h1} \end{pmatrix} \cos\left(\phi - \phi_w\right) + \begin{pmatrix} a_{v2} \\ a_{h2} \end{pmatrix} \cos\left[2\left(\phi - \phi_w\right)\right] \right] \\ t \left[\begin{pmatrix} b_{U1} \\ b_{V1} \end{pmatrix} \sin\left(\phi - \phi_w\right) + \begin{pmatrix} b_{U2} \\ b_{V2} \end{pmatrix} \sin\left[2\left(\phi - \phi_w\right)\right] \right] \end{bmatrix} \tag{5.1}$$

where ϕ_w is the upwind direction, t is the atmospheric transmissivity, and ϕ is the azimuthal viewing direction defined by the righthand coordinate system in Figure 5.1. 5.1. The azimuthal coordinate is aligned with the compass rose such that 0° is north, 90° is east, etc. The first- and second-order harmonic coefficients $a_{\alpha i}$ and $b_{\beta i}$, $\alpha = v$ or h, $\beta = U$ or V, and $i = 1$ or 2 are primarily wind speed dependent and can be determined by either modeling or measurement. In this investigation, measurements using the PSR are analyzed to determine several of the $a_{\alpha i}$ and $b_{\beta i}$ coefficients.

Unlike the third and fourth Stokes parameters, the first two parameters contain a large zeroeth-order component of the harmonic expansion due to the combined bulk thermal emission from the ocean and atmosphere. These $a_{\alpha 0}$ terms are a strong function of wind speed and can be written:

$$\begin{pmatrix} a_{v0} \\ a_{h0} \end{pmatrix} = \begin{pmatrix} T_{B\uparrow} \\ T_{B\uparrow} \end{pmatrix} + t \left[\left\langle \begin{matrix} \varepsilon_v \\ \varepsilon_h \end{matrix} \right\rangle_\phi T_w + \left\langle \begin{matrix} 1-\varepsilon_v \\ 1-\varepsilon_h \end{matrix} \right\rangle_\phi T_{B\downarrow} \right] \tag{5.2}$$

where $T_{B\uparrow}$ and $T_{B\downarrow}$ are the upwelling and downwelling atmospheric nonpolarized brightness contributions, ε_α is the ocean surface emissivity and T_w is the physical temperature of the ocean skin. Within this expression, the surface emissivity is azimuthally averaged as denoted by $\langle\cdot\rangle_\phi$ and is assumed to model the radiative properties of wind-roughened sea water and foam.

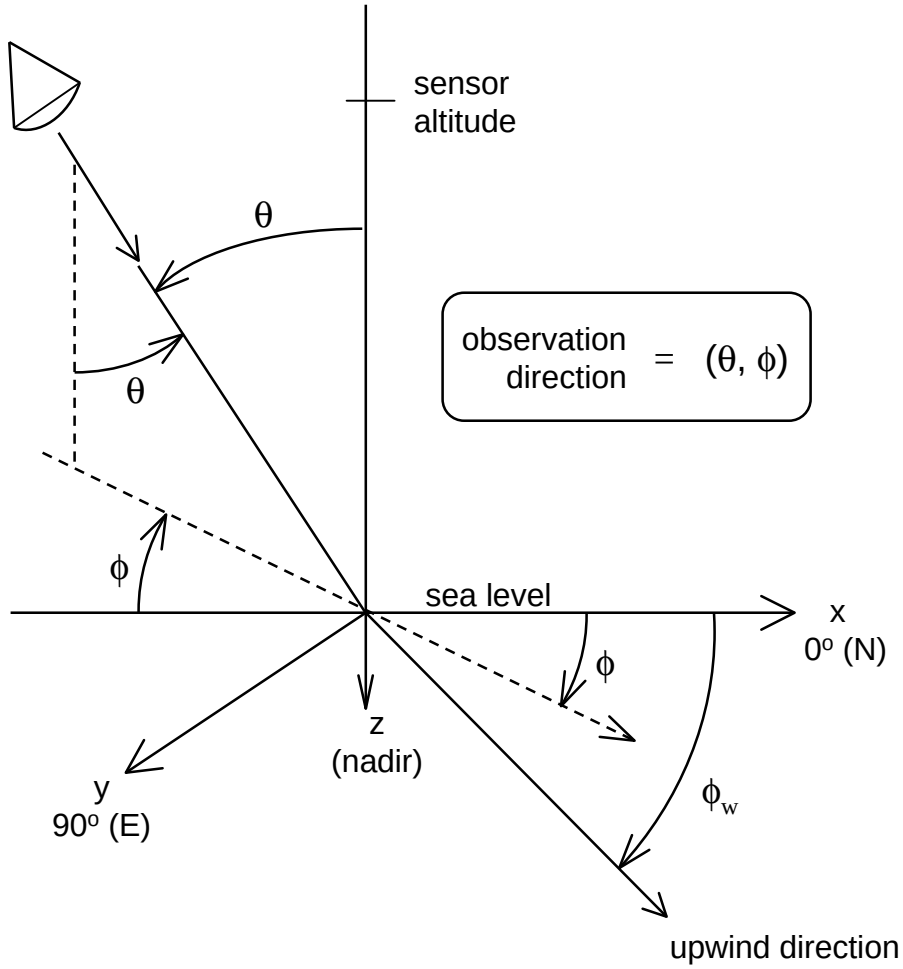

Figure 5.1: Polar coordinate system for the GMF. The azimuth coordinate ϕ is aligned with the compass rose.

Upon examination of the GMF in (5.1), two important signal characteristics are noted. First, the azimuthal dependence of the third and fourth Stokes parameters is in phase quadrature with respect to the dependence of the first two Stokes parameters. As will be shown in Section 6.4.2, this characteristic enables the retrieval algorithm to resolve most directional ambiguities. Second, small fluctuations in atmospheric transmission (and hence $T_{B\downarrow}$ and $T_{B\uparrow}$) due to water vapor or clouds do not substantially change the values of T_U and T_V; such variations occur only in amplitude through relatively small variations in t and $b_{\beta 1}$ and $b_{\beta 2}$. Furthermore, the third and fourth Stokes parameters are effectively zero mean with respect to azimuth angle[1]. From (5.2), however, the values of T_v and T_h are seen to be significantly affected by variations in the atmospheric transmission and emission.

5.2 Aircraft Measurements

The wind-speed dependence of the harmonic amplitudes was measured using the PSR at seven different wind speeds ranging from 0.4 to 16 m s^{-1} during both the Labrador Sea Experiment and associated flights over buoys off the eastern shores of Maryland and Virginia. The flight pattern used to measure the azimuthal brightness temperature signature for each case consisted of six straight and level flight legs organized in three pairs, each 60° apart in heading. Each such "hex-cross" pattern (see Figure 5.2) covered an area of ∼900 km^2 (a size similar to that of a satellite microwave radiometer footprint) and occurred over a ∼50 minute time period. Flying the three headings has the effect of minimizing any artifacts in the data that were dependent on the slip-stream flow across the scanhead. No such patterns were discernible in the channels used in this study, however, the Ka-band analog and K-band digital channels exhibited these type variations (as discussed in Chapter 3) and were not used in calculating the GMF. The data collected during a typical hex-cross pattern consisted of ∼150 full conical scans with ∼227 samples per scan and at an elevation angle of $53.1°$ from nadir (the SSM/I incident angle). Hex-cross patterns were flown at 6,100 m

[1]That T_U and T_V are azimuthally zero-mean is not an intrinsic property of all surfaces, but rather a physical property that appears to hold true for the ocean.

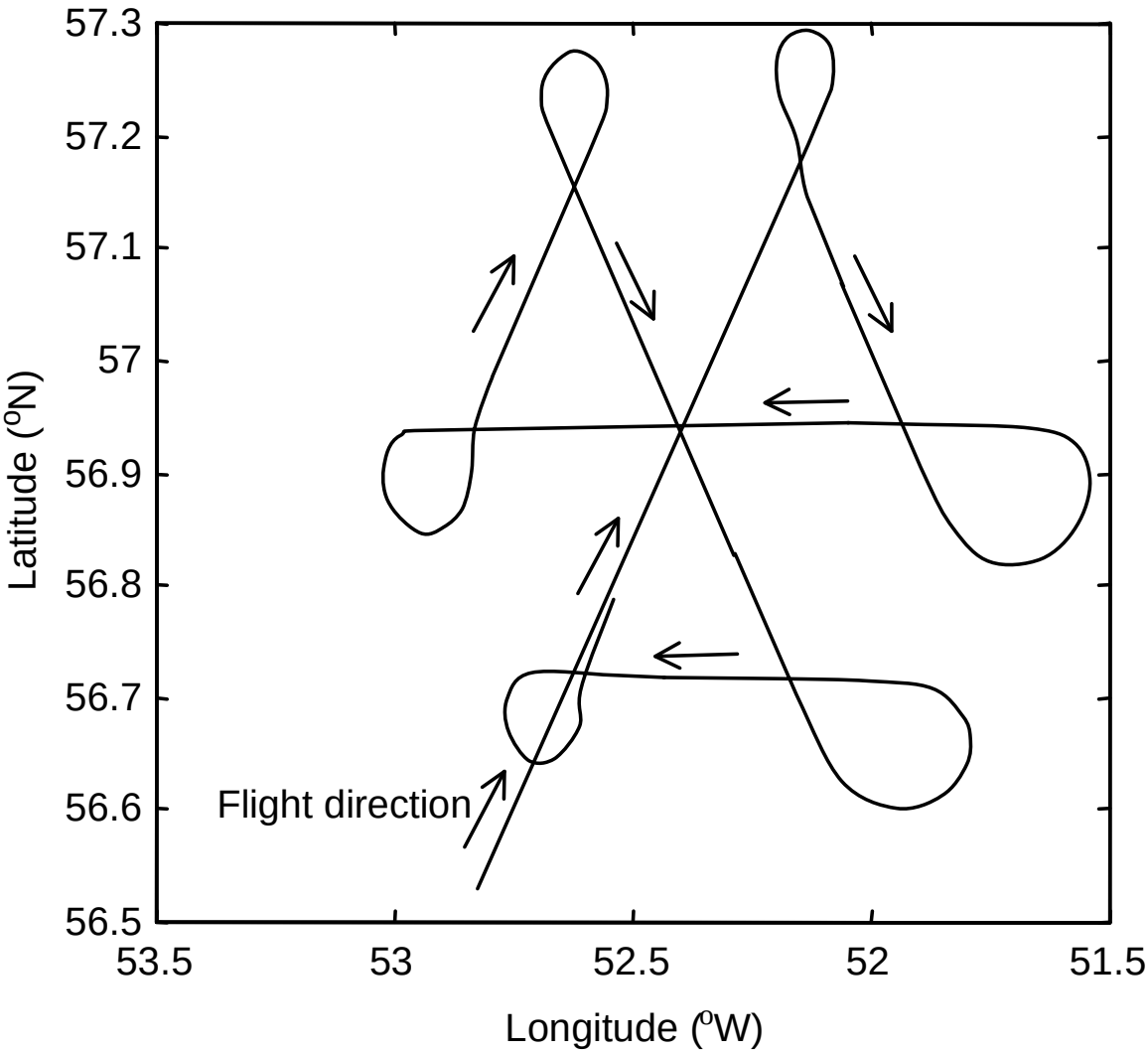

Figure 5.2: Hex-cross flight pattern used for PSR observations of ocean winds on March 4, 1997. This flight track is typical of the hex-cross patterns performed during the OWI Labrador Sea experiment.

Table 5.1: PSR wind direction harmonic observations during the OWI/Labrador Sea experiment

u_{10} (m s^{-1})	T_{air} (°C)	T_w (°C)	Date	Time (UTC)	Surface Truth
0.44	10	9	3/10/97	2200	Buoy #44014
3.4	10	7	3/10/97	2100	Buoy #44009
11 ± 0.5	-9	3	3/9/97	1530	*R.V. Knorr*
12 ± 0.4	-7	3	3/7/97	1700	”
12.6 ± 0.3	-7	4	3/7/97	1800	”
13.6 ± 1.6	-9	3	3/3/97	1500	”
16 ± 0.3	-12	3	3/4/97	1600	”

(20,000 ft) altitude on seven occasions and at six locations between March 3 and March 10, 1997, (Figure 5.3).

All hex-cross patterns were centered over a source of surface wind truth. For the Virginia flights the truth was obtained from fixed buoys operated by the NOAA National Data Buoy Center (NDBC), and for the Labrador Sea experiment the truth was obtained from meteorological sensors aboard the *R. V. Knorr*. The two locations overflown on March 10 were NDBC buoys #44009 and #44014 and the remaining locations were centered over the *Knorr* in the Labrador Sea. In-situ truth included measurements of surface winds and ocean and air temperatures. Atmospheric transmissivity was calculated using temperature and moisture profiles measurements from four radiosondes launched from the *Knorr* near the times of the aircraft overflights. The wind speed and environmental conditions for the seven measurements are presented in Table 5.1.

As an example, the mean azimuthal brightness temperature signatures and harmonic approximations measured on March 9 from 1500-1600 UTC are shown in Figure 5.4. The wind speed was 10 m s^{-1} $\pm$ 0.6 m s^{-1} during the data collection. The first- and second-order harmonic amplitudes were determined using a least-squares fit to the scan-averaged azimuthal signature. As illustrated by the $\pm 1\sigma$ fit-error curves, radiometric noise and brightness temperature variability of geophysical origin influenced the variances of the

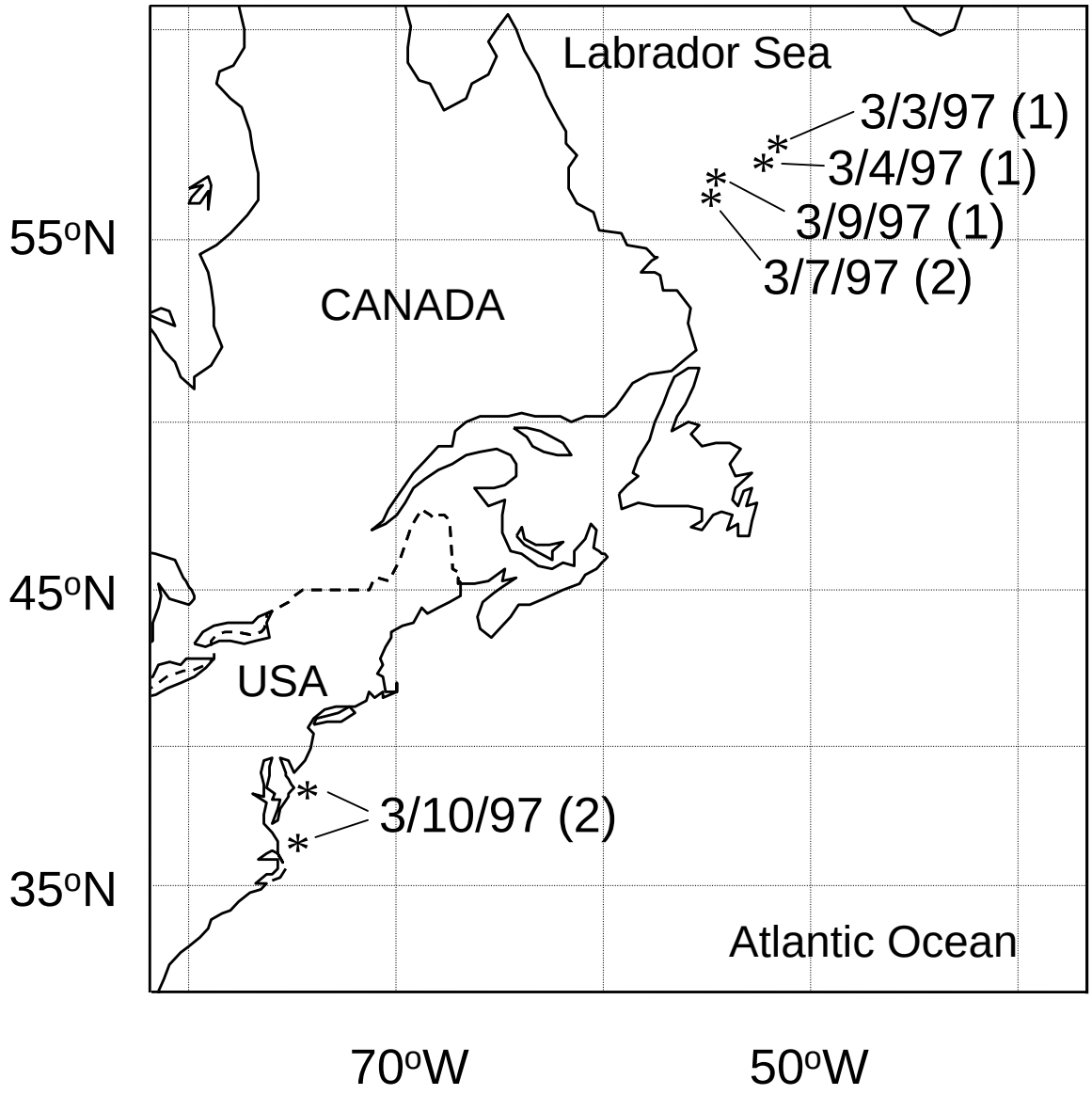

Figure 5.3: Map of PSR hex-cross measurement locations. Hex-cross patterns were executed at these six locations to develop the microwave azimuthal geophysical model function.

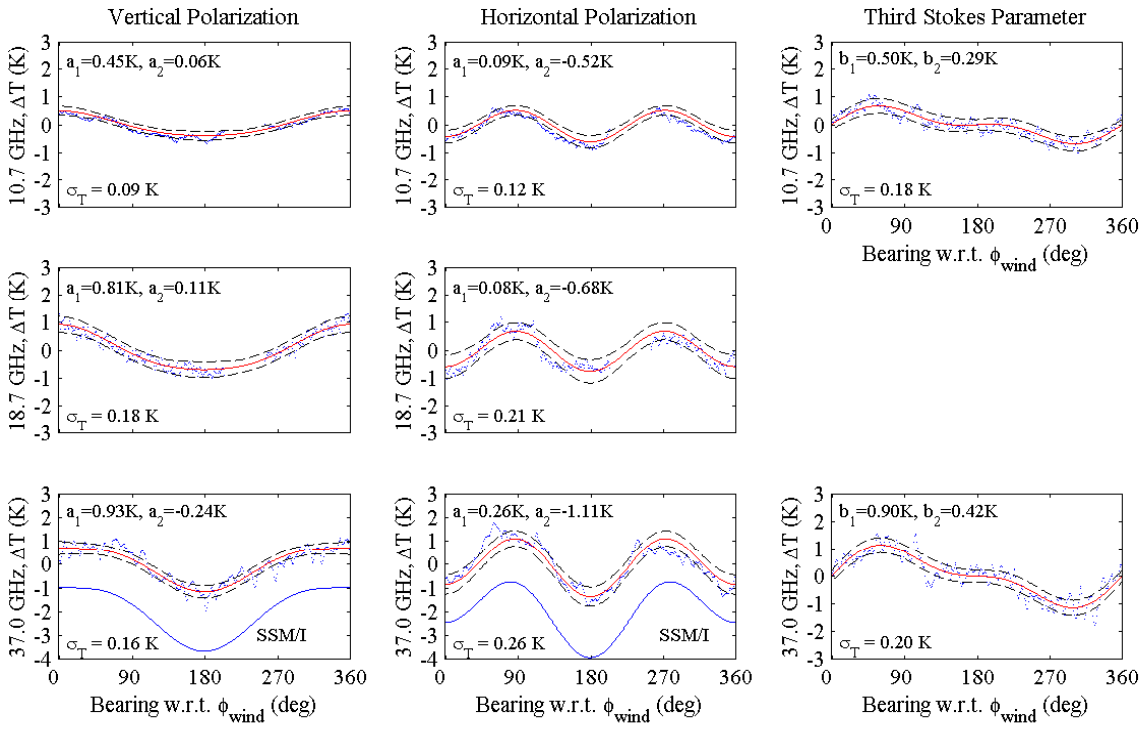

Figure 5.4: PSR azimuthal harmonics from March 9, 1997 exhibiting the wind direction dependence of the first three Stokes parameters at 10.7, 18.7, and 37.0 GHz. (Data for T_U at 18.7 GHz was unavailable.) The wind speed was 10 m s^{-1} $\pm$0.6 m s^{-1} from 1500 to 1600 UTC as measured by the *Knorr*. The solid lines represent the reconstructed second-order harmonic expansions and the dashed lines are the $\pm 1\sigma_T$ error curves for 170 full azimuthal scans. Individual points indicate mean measured brightness deviations. The 37.0 GHz SSM/I global average wind direction harmonics, denoted by solid lines, are shifted by -2 K for clarity.

harmonic amplitude measurements by less than ∼5%. For comparison, the 37 GHz SSM/I global average wind direction harmonics from [66] for a wind speed of 10 m s^{-1} are plotted with a -2 K offset.

The PSR GMF shows a distinct 2-3 K variation with strong first- and second-order harmonic dependence in the vertical and horizontal polarizations, respectively. For both polarizations, the amplitudes of the dominant harmonics (i.e., a_{v1} and a_{h1}) increase with frequency. Furthermore, the measured vertical and horizontal harmonic amplitudes at 18.7 GHz and 37.0 GHz exhibit excellent agreement with the SSM/I global average wind direction harmonics. Although slightly lower in amplitude, the PSR 10.7 GHz wind direction harmonics are otherwise comparable to the 37 GHz SSM/I harmonics. Of particular interest is the strong (∼1 K amplitude) first harmonic present in the third Stokes parameter signature. The large first harmonic content of this signature is indicative of a strong windward-leeward asymmetry in the ocean wave structure. The T_U signature is clearly in phase quadrature with the T_v and T_h azimuthal signatures. These measurements are similar to theoretical modeling results obtained by Kunkee and Gasiewski [41] using an asymmetric wave geometrical optics model.

The harmonic analysis of Figure 5.4 was performed for the remaining hex-cross patterns with the results compiled in Figure 5.5. The first- and second-order harmonic amplitudes are plotted as circles and squares (respectively) along with wind speed and amplitude error bars. The wind-speed dependence of the harmonic coefficients is estimated by a least-squares quadratic fit, as shown using solid lines. The parameters of these quadratics define the GMF and are detailed in Table 5.2.

5.3 Discussion

Several observations about the GMF harmonic coefficients (shown in Figure 5.5) can be made. First, the wind speed dependence of the harmonic coefficients is broadband in nature, that is, the same general trend is seen for each Stokes parameter over almost two octaves

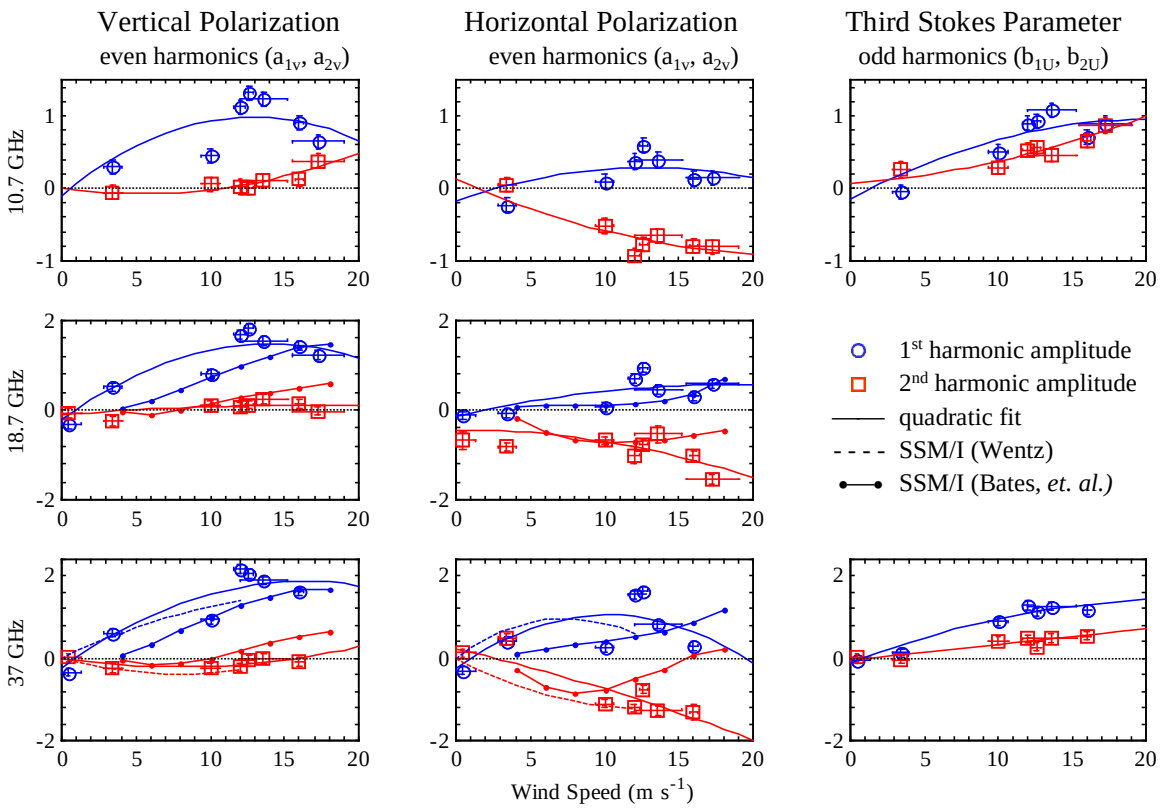

Figure 5.5: Microwave brightness temperature harmonic amplitudes versus wind speed at 10 meter height for the first three Stokes parameters at 10.7, 18.7, and 37.0 GHz. (Data for T_U at 18.7 GHz was unavailable.) Open circles and squares represent first- and second-order harmonic amplitudes, respectively, and the amplitude error bars represent the $\pm 1\sigma$ bounds on the estimate of the amplitude coefficients. The wind speed error bars are the $\pm 1\sigma$ bounds on the *Knorr* wind speed measurements or the gust speed of the buoy measurements. The solid lines are quadratic fits to the data. The dashed and dotted lines are the SSM/I measurements of Wentz [66] and Bates, *et al.* [4], respectively.

Table 5.2: Quadratic fit coefficients for the wind speed dependence of the harmonic amplitudes as determined from PSR OWI Labrador Sea flights.

f (GHz)	parameter	c_0 (K)	c_1 (K m^{-1}s)	c_2 (K m^{-2}s^2)
10.7	a_{v1}	-0.1022	0.1693	-0.0066
10.7	a_{v2}	0.0090	-0.0294	0.0026
10.7	a_{h1}	-0.1713	0.0715	-0.0028
10.7	a_{h2}	0.1245	-0.0906	0.0019
10.7	b_{U1}	-0.1532	0.1094	-0.0027
10.7	b_{U2}	0.0673	0.0154	0.0015
18.7	a_{v1}	-0.2229	0.2432	-0.0087
18.7	a_{v2}	-0.1115	0.0271	-0.0008
18.7	a_{h1}	-0.1336	0.0762	-0.0021
18.7	a_{h2}	-0.4398	0.0006	-0.0027
37.0	a_{v1}	-0.2243	0.2570	-0.0079
37.0	a_{v2}	-0.0124	-0.0526	0.0034
37.0	a_{h1}	-0.2433	0.2537	-0.0124
37.0	a_{h2}	0.2347	-0.0849	-0.0013
37.0	b_{U1}	-0.1062	0.1354	-0.0029
37.0	b_{U2}	-0.0265	0.0314	0.0003

in frequency. One distinguishing characteristic is that the coefficient values increase by $\sim$50% in amplitude from 10.7 to 37.0 GHz. The nearly identical values between 18.7 and 37.0 GHz, however, agree with the observation made by Wentz. A second feature pertains to the vertical polarization. Here, the first-order harmonic amplitude a_{v1} increases with wind speed and saturates at $\sim$12 m s^{-1}, while the second-order harmonic amplitude a_{v2} is almost zero except for wind speeds $\gtrsim$15 m s^{-1}. The horizontal polarization, however, has a dominant (negative) second-order harmonic whose amplitude a_{h2} increases monotonically with wind speed. The smaller first-order harmonic amplitude a_{h1} peaks at $\sim$12 m s^{-1}. The third Stokes parameter exhibits both significant first- and second-order harmonics, with the first-order harmonic being dominant. Both amplitude coefficients b_{U1} and b_{U2} increase with wind speed and exhibit no saturation over the range of available wind speeds.

Also shown in Figure 5.5 are satellite harmonic amplitude measurements from the SSM/I for comparison. Harmonic coefficients determined by Wentz [66] are shown as dashed lines for vertical and horizontal polarizations at 37 GHz, and those at 19 and 37 GHz as determined in an independent study by Bates *et al.* [4] are shown using dotted lines. The PSR harmonic coefficients compare favorably with satellite measurements made by Wentz and mostly so (but somewhat less so) with those of Bates *et al.*. In the vertical polarization, the PSR first-order harmonic amplitudes show general consistency with the amplitudes of both Wentz and Bates *et al.* over the full range of wind speeds. While there is excellent agreement with the Wentz SSM/I measurement at 3.4 m s^{-1} (as indicated by the $\pm 1\sigma$ error bars), there is, however, a $\sim$0.3 K discrepency with the Bates *et al.* result. This discrepency might be attributable to the fact that ocean surface wind speed for the Wentz study was measured using in-situ moored bouys, while the investigation in [4] relied heavily upon ERS-1 and -2 scatterometer retrievals for the surface wind speed measurements. However, the PSR first-order vertical harmonic amplitudes at 10 and 16 m s^{-1} agree well with the Bates *et al.* measurements and the PSR second-order vertical harmonic amplitudes agree closely with both satellite data sets. Additionally, the PSR second-order harmonic coefficients exhibit a zero crossing at $\sim$14 m s^{-1} similar to the zero

crossing of Bates *et al.* at $\sim$9 m s^{-1}.

In the horizontal polarization the PSR harmonic coefficients show general consistency (as indicated by the $\pm 1\sigma$ error bars in varying instances) with results from both satellite investigations. Here, the PSR first-order horizontal harmonic amplitudes agree best with Wentz for wind speeds $\lesssim$10 m s^{-1} and have some agreement with Bates *et al.* for wind speeds $\gtrsim$10 m s^{-1}. The PSR data do agree well with the Bates *et al.* measurements in the 19 GHz channels for wind speeds $\lesssim$14 m s^{-1}.

In contrast to the vertical polarization, however, the harmonic amplitudes as measured using the PSR and by Wentz and Bates *et al.* are seen to be more variable. The PSR second-order horizontal harmonic amplitude data match the trend of the Wentz amplitude measurements, however, the Bates *et al.* results exhibit a zero crossing at 15 m s^{-1} for 37 GHz that is not present in either the PSR or Wentz data. Indeed, the difference between the two satellite measurement sets at 37 GHz and 6 m s^{-1} is $\sim$0.4 K. The variability in the first-order harmonic amplitude at horizontal (and to some extent vertical) polarization suggests that the ocean wave hydrodynamic and air-sea interaction processes responsible for the upwind-downwind asymmetry in the surface wave structure are themselves highly variable. While the wind speed is fairly well correlated to the harmonic coefficients, additional processes that drive the ocean wave spectral development such as fetch, ocean currents, boundary layer stability, and the presence of longwaves and surfactants could be contributing factors to the environmental dependence of the azimuthal signatures.

The PSR 10.7 and 37 GHz T_U harmonic coefficients b_{U1} and b_{U2} are displayed in the righthand plots of Figure 5.5. Both the first- and second-order coefficients are significant, with b_{U1} being dominant. The 37 GHz measurements are about twice as large as the 10.7 GHz harmonic amplitudes. This characteristic is consistent with the frequency dependence observed for the vertical and horizontal polarizations. Quadratic fits were computed for these data and are shown as the solid lines. As indicated by the error bars, the PSR data are well modeled by the quadratic wind speed dependence. In fact, there appears to be little or no wind speed saturation up to $\sim$ 16 m s^{-1}. Comparison of satellite measurements

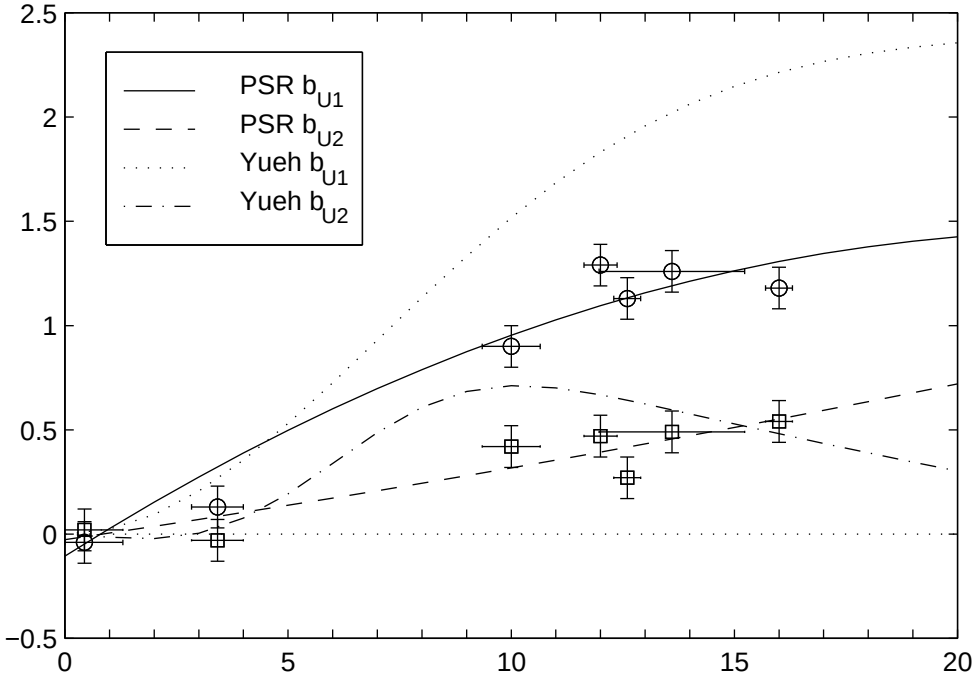

Figure 5.6: Third Stokes parameter harmonic amplitudes versus wind speed at 10 meter height for 37.0 GHz. Open circles and squares represent first- and second-order harmonic amplitudes b_{U1} and b_{U2}, respectively. The error bars are the same as for Figure 5.5. The solid and dashed lines are quadratic fits to the PSR data. The dotted and dash-dotted lines are the exponential function fits given by Yueh *et al.* [69].

to the PSR T_U model is currently not possible because satellite polarimeters are not yet in operation.

The PSR 37.0 GHz T_U measurements are plotted in Figure 5.6 for comparison with fixed-beam polarimetric measurements reported by Yueh *et al.* [69]. The same symbolic notation is used as for Figure 5.5. The Yueh *et al.* data were obtained using a 37 GHz fixed-beam polarimeter mounted to an aircraft. Circle flights were performed to allow the radiometer footprint to dwell on a single spot of the ocean surface at 55° incidence as the azimuth angle varied due to aircraft motion. Exponential function fits of b_{U1} and b_{U2} are given in [69] and plotted as the dotted and dash-dotted lines, respectively. The Yueh *et al.* b_{U1} function is ∼1.5-2 times the amplitude of the PSR GMF for wind speed $\gtrsim$10 m s^{-1}.

The b_{U2} curves exhibit this same characteristic at $\sim 10\ \mathrm{m\,s^{-1}}$. Otherwise, the two functions agree well for wind speeds $<5\ \mathrm{m\,s^{-1}}$ and the second-harmonic curves intersect at $15\ \mathrm{m\,s^{-1}}$. Several potential causes for the discrepancy at $10\ \mathrm{m\,s^{-1}}$ exist. First, there could be an error in estimating the atmospheric attenuation. Line of sight attenuation of $\sim$0.54 dB was reported by Yueh *et al.* compared to an estimate of $\sim$0.31 dB for the PSR measurements. According to (5.1), the amplitude of T_U variation is directly proportional to atmospheric transmissivity t; however, a 3 dB error in atmospheric attenuation would be necessary to generate the observed 100% difference. Such a gross error is unlikely. The size of the geographic area over which the measurements were made is a second possible cause for the difference. The footprint cast on the ocean surface by the fixed-beam polarimeter used by Yueh *et al.* was $\sim$1 km across. The PSR measurements, however, were made over an area of satellite footprint proportions ($\sim$30 km), and thus variations in wind speed were smoothed by averaging the PSR scans. Additionally, the Yueh *et al.* measurements were made off the coasts of California, Maryland, and Virginia, as opposed to the PSR high wind speed measurements over the Labrador Sea. Geographic and seasonal variations might play an important role in determining the signature. Finally, one must consider the existence of calibration error. The PSR digital correlators did exhibit a nonideal gain of <1, however, the author believes that the ground based polarimetric calibration (Chapter 4) successfully compensated for the effect. The consistency of the Labrador Sea measurements between sorties and between the X-band, Ka subband-1, and Ka subband-2 channels supports the stability of the calibration.

The model function agrees well in the mean with comparable anisotropic wind emission models from independent SSM/I satellite studies [66, 4]. This is not to say that the ocean surface emission phenomena is completely understood, even on an empirical basis. Indeed, it is noted that significant geophysical noise can occur within a given spot, in particular, for the higher frequency channels and first two Stokes parameters. Such noise is hypothesized to be the combined result of clouds and local surface wind and wave inhomogeneities, and is prevalent in spots of smaller size. The impact of such geophysical noise

from all sources is apparently much less on the third (and presumably) the fourth Stokes parameters since these observables are both effectively zero mean for the ocean and mostly undergo attenuation of their azimuthal harmonics by clouds. Nonetheless, the GMF is repeatable enough and provides a large enough brightness temperature signal for meaningful wind direction retrievals in Chapter 6.

CHAPTER 6

Retrieval of Ocean Surface Wind Vectors

6.1 Introduction

In this chapter, the retrieval of ocean surface wind vectors is investigated using the PSR GMF and high-resolution polarimetric microwave imagery of the ocean. To simultaneously retrieve both the speed and direction components of the wind, a multi-look retrieval method based upon the maximum likelihood (ML) principle [62] was developed. The ML retrieval problem is posed in a form allowing for the use of an arbitrary set of azimuth look angles, radiometric frequencies, and polarization states. The result is a nonlinear weighted least-squares minimization problem, which can be solved using any of several multivariate search techniques. An enhancement of the ML algorithm allows for adaptation of the channel weights based upon an estimate of the geophysical modeling error. The error estimate can also be used to study the relative informational content of the various channels, and clearly reveals the utility of the third Stokes parameter over convection. The utility of the multi-look retrieval technique in both one-dimensional and two-dimensional wind field mapping is demonstrated using conically-scanned polarimetric microwave brightness imagery observed during the passage of a polar low over the southern Labrador Sea.

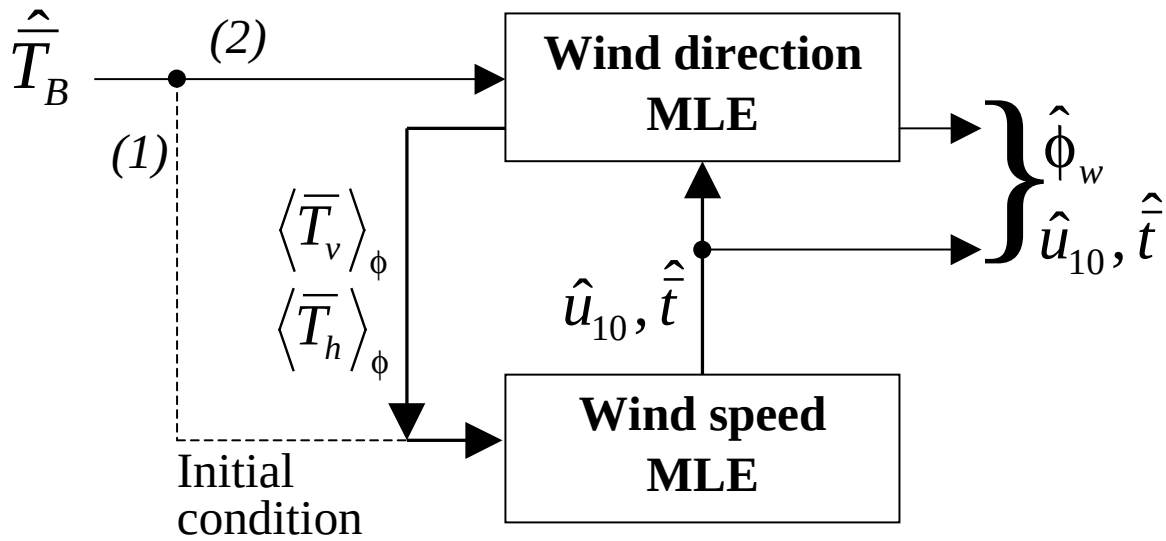

Figure 6.1: Block diagram of the iterative wind speed and direction ML estimation algorithm for passive microwave wind vector retrieval. The dashed line indicates the data flow path for the first iteration.

6.2 ML Estimation of Wind Vectors

The retrieval problem consists of estimating the wind speed and direction from measured brightness temperatures. In this section, an inversion method based on maximum likelihood (ML) estimation of wind speed and direction using measured brightness temperatures at a suitable set of azimuthal angles is presented. The solution is based on iteration between separate wind speed and wind direction retrieval algorithms (see Figure 6.1). The wind direction retrieval algorithm returns both the ML estimated wind direction and azimuthally-averaged brightness temperatures $a_{\alpha 0}$ using the GMF detailed in Chapter 5. In addition to a set of input brightness temperature measurements, the wind speed and atmospheric transmissivity are required for input to this algorithm. These two parameters, however, are generated by the wind speed algorithm. This retrieval algorithm is an inversion of (5.2) and uses estimated values for the zeroeth-order harmonic terms $a_{\alpha 0}$ as input. By iteratively feeding the output of each algorithm to the other's input the joint wind speed and direction estimate rapidly converges.

6.2.1 Wind direction retrieval

We assume that the brightness temperature measured by a radiometer is equal to the GMF in (5.1) evaluated for the specific ocean and atmospheric state plus two additional random components: instrument noise and geophysical modeling error. The instrument noise is a function of radiometer bandwidth, integration time, receiver noise figure and stability and can be quantified either experimentally after deployment or theoretically prior to deployment. For the PSR, the instrument noise is well modeled by integration noise from a total power radiometer with fixed system temperature:

$$\Delta T_{RMS} = \frac{T_{sys}}{\sqrt{B\tau}} \tag{6.1}$$

where B is the bandwidth and τ is the integration time. Sources of geophysical modeling error include radiothermal perturbations caused by variables such as stability, longwave amplitude, and fetch that are not considered in the present GMF. If the noise and modeling errors are assumed to be Gaussian, the measured brightness temperature vector $\widehat{\overline{T}}_B$ for a multi-frequency polarimetric radiometer with N channels can be modeled as an $N \times 1$ random vector that follows an N-dimensional joint Gaussian probability density function (pdf):

$$f\left(\widehat{\overline{T}}_B\right) = \frac{1}{(2\pi)^{N/2}\left[\det\left(\overline{\overline{K}}\right)\right]^{1/2}} \exp\left[-\frac{1}{2}\left(\widehat{\overline{T}}_B - \overline{T}_B\right)^T \overline{\overline{K}}^{-1}\left(\widehat{\overline{T}}_B - \overline{T}_B\right)\right], \tag{6.2}$$

where

$$\mathrm{E}\left[\widehat{\overline{T}}_B\right] \triangleq \overline{T}_B = (T_1, T_2, \cdots, T_N)^T$$

$$\overline{\overline{K}} = \begin{bmatrix} \Delta T_1^2 & & 0 \\ & \ddots & \\ 0 & & \Delta T_N^2 \end{bmatrix}$$

$$\det\left(\overline{\overline{K}}\right) = \prod_{i=1}^{N} \Delta T_i^2$$

and ΔT_i^2 is the combined instrumental and geophysical noise variance for the i-th brightness vector component and $(\cdot)^T$ denotes transpose. The vector $\overline{T}_B$ is the expected value of

the brightness vector and is equal to the multi-frequency GMF for the given atmospheric and ocean state. The multi-frequency GMF is found by concatenating several single-band GMFs (5.1) into a single vector:

$$\overline{T}_B = \left[\overline{T}_B^{\mathrm{X}\,T},\ \overline{T}_B^{\mathrm{K}\,T},\ \overline{T}_B^{\mathrm{K_a}\,T} \right]^T \tag{6.3}$$

where the superscripts denote the various frequency bands. For M independent looks (e.g., at various azimuth angles) the joint pdf of the observed brightness temperatures is simply the product of the respective pdfs (6.2) for each of the M looks:

$$f\left(\widehat{\overline{T}}_{B,1}, \widehat{\overline{T}}_{B,2}, \cdots, \widehat{\overline{T}}_{B,M}\right) = \prod_{m=1}^{M} f\left(\widehat{\overline{T}}_{B,m}\right) \tag{6.4}$$

Given measurements from M looks we can determine the wind direction and speed by maximizing the likelihood function [62], which is defined as the above joint pdf:

$$L\left(\widehat{\overline{T}}_{B,1}, \widehat{\overline{T}}_{B,2}, \cdots, \widehat{\overline{T}}_{B,M}; \overline{W}\right) \equiv f\left(\widehat{\overline{T}}_{B,1}, \widehat{\overline{T}}_{B,2}, \cdots, \widehat{\overline{T}}_{B,M}; \overline{W}\right) \tag{6.5}$$

where $\overline{W} = \left[\langle \overline{T}_B \rangle_\phi^T, \phi_w\right]$. The components of $\overline{W}$ are the wind direction ϕ_w and the mean azimuthal brightness temperatures $\langle \overline{T}_B \rangle_\phi \triangleq \overline{a}_0 = [a_{v0}^X,\ a_{h0}^X,\ a_{v0}^K,\ \ldots\ ]^T$. These components are assumed to be constant but unknown. The maximum likelihood estimator $\widehat{\overline{W}}$ is that value of $\overline{W}$ that either maximizes L:

$$\begin{aligned} L &= \prod_{m=1}^{M} \frac{1}{(2\pi)^{N/2}\left[\det\left(\overline{\overline{K}}\right)\right]^{1/2}} \times \exp\left[-\frac{1}{2}\left(\widehat{\overline{T}}_{B,m} - \overline{T}_{B,m}\right)^T \overline{\overline{K}}^{-1}\left(\widehat{\overline{T}}_{B,m} - \overline{T}_{B,m}\right)\right] \\ &= \left((2\pi)^{N/2}\left[\det\left(\overline{\overline{K}}\right)\right]^{1/2}\right)^{-M} \times \exp\left[-\frac{1}{2}\sum_{m=1}^{M}\left(\widehat{\overline{T}}_{B,m} - \overline{T}_{B,m}\right)^T \overline{\overline{K}}^{-1}\left(\widehat{\overline{T}}_{B,m} - \overline{T}_{B,m}\right)\right]. \end{aligned} \tag{6.6}$$

or (equivalently) $\ln L$ since the natural logarithm is monotonic:

$$\ln L = -M \ln\left((2\pi)^{N/2}\left[\det\left(\overline{\overline{K}}\right)\right]^{1/2}\right) - \frac{1}{2}\sum_{m=1}^{M}\left(\widehat{\overline{T}}_{B,m} - \overline{T}_{B,m}\right)^T \overline{\overline{K}}^{-1}\left(\widehat{\overline{T}}_{B,m} - \overline{T}_{B,m}\right). \tag{6.7}$$

The maximization of $\ln L$ is equivalent to the minimization of the objective function [62]:

$$\sum_{m=1}^{M} \left(\widehat{\overline{T}}_{B,m} - \overline{T}_{B,m}\right)^T \overline{\overline{K}}^{-1} \left(\widehat{\overline{T}}_{B,m} - \overline{T}_{B,m}\right). \tag{6.8}$$

If all measurement errors are assumed to be independent, then $\overline{\overline{K}}$ (and hence $\overline{\overline{K}}^{-1}$) is diagonal and (6.8) becomes:

$$\sum_{m=1}^{M} \sum_{i=1}^{N} \left(\widehat{T}_{i,m} - T_{i,m}\right)^2 \Delta T_i^{-2} \tag{6.9}$$

where the subscripts (i, m) are used to denote the i-th brightness component of the m-th azimuthal look. The ML solution is thus cast in the form of a non-linear weighted least-squares minimization problem with preference given to the less noisy channels.

6.2.2 Wind speed and atmospheric transmissivity

The wind speed and atmospheric transmissivity can be determined by non-linearly inverting the ML-estimated zeroeth-order coefficients a_{v0} and a_{h0} in (5.2). Parameterization of the zeroeth-order components in both t and u_{10} using a statistical wind speed emissivity model facilitates the ML estimation process. In this study, we compute the emissivity $\langle \varepsilon_\alpha \rangle_\phi$ using the hybrid Kirchoff approximation and ocean foam model described by Wilheit [67] along with the sea water dielectric constant model of Klein and Swift [37]. The emissivity calculation depends primarily on wind speed, and secondarily on water temperature and salinity. We assume these lattermost two to be known *a-priori*.

The upwelling and downwelling brightnesses $T_{B\uparrow}$ and $T_{B\downarrow}$ can be approximated using a two-layer atmosphere model parameterized in transmissivity:

$$T_{B\uparrow} = (1-t)T_{e\uparrow} \tag{6.10}$$

$$T_{B\downarrow} = (1-t)T_{e\downarrow} + tT'_{Bc} \tag{6.11}$$

where $T_{e\uparrow}$ and $T_{e\downarrow}$ are the effective upwelling and downwelling emission temperatures of the layer below the aircraft, and T'_{Bc} is the combined contribution of the atmosphere above

the aircraft and the microwave cosmic background. The effective emission temperatures are determined by:

$$T_{e\uparrow} = (T_a - T_{\delta_\uparrow}) \tag{6.12}$$

$$T_{e\downarrow} = (T_a - T_{\delta_\downarrow}) \tag{6.13}$$

where T_a is the surface air temperature and $T_{\delta_\uparrow}$ and $T_{\delta_\downarrow}$ are offset temperatures. The three temperatures T_a, $T_{\delta_\uparrow}$ and $T_{\delta_\downarrow}$ are all determined from ancillary data. For this investigation we used five radiosondes launched from the *Knorr* during the period from March 1 to March 9, 1997 to these quantities as follows. Using temperature, pressure, and humidity measurements from the sondes the atmospheric transmissivity t and the background upwelling and downwelling brightness temperatures $T_{B_\uparrow}$, $T_{B_\downarrow}$ and T'_{Bc} were computed using the microwave radiative transfer model of Gasiewski and Staelin [23]. These data along with the surface air temperature were used to determine the offset temperatures. Typical offsets were $T_{\delta_\uparrow} \sim 27°$C and $T_{\delta_\downarrow} \sim 26°$C, corresponding to effective emission temperatures $T_{e_\uparrow} \approx T_{e_\downarrow}$ equal to that of the air at an altitude of ~4 km.

Development of the wind speed estimator is similar to that of wind direction. The log likelihood function for wind speed is:

$$\ln L = -\ln\left((2\pi)^{N/2}\left[\det\left(\overline{\overline{K}}\right)\right]^{1/2}\right) - \frac{1}{2}\left(\widehat{\langle\overline{T}_B\rangle}_\phi - \overline{a}_0\right)^T \overline{\overline{K}}^{-1}\left(\widehat{\langle\overline{T}_B\rangle}_\phi - \overline{a}_0\right) \tag{6.14}$$

where the noise covariance matrix $\overline{\overline{K}}$ is the same as in (6.2). The resulting objective function, which is minimized over both wind speed and atmospheric transmissivity, uses the zeroeth-order brightness temperature components that were estimated by the wind direction algorithm:

$$\sum_{i=1}^{N}\left(\widehat{\langle T_i\rangle}_\phi - a_{0,i}\right)^2 \Delta T_i^{-2} \tag{6.15}$$

6.2.3 Iterative Solution

The individual wind direction and speed estimations are iterated to arrive at a joint minimization of both (6.9) and (6.15). The operation is illustrated in Figure 6.1 and is carried

out as follows. First, an initial wind speed estimate is made. The estimate is based on an average over the azimuthal looks rather than an estimate of $\langle T_i \rangle_\phi$ as in (6.15). For this step the objective function is:

$$\sum_{i=1}^{N} \left(\sum_{m=1}^{M} \widehat{T}_{i,m} - a_{0,i} \right)^2 \Delta T_i^{-2} \tag{6.16}$$

Once the first wind speed estimate is obtained, a wind direction can be estimated by minimizing (6.9). Both wind direction and speed minimizations are performed using a multivariable quasi-Newton method. The method requires about 30 function calls to converge to 10^{-5} because the Jacobian is computed using finite differences. If faster convergence is needed, the Jacobian could be analytically derived and used in a Gauss-Newton method. With the computational power available with inexpensive computers, the extra burden of the Jacobian approximation is trivial. A by-product of the wind direction estimation is $\widehat{\overline{a}}_0$, which is fed back to the wind speed algorithm to refine the estimate. The wind speed results are then fed to the wind direction algorithm and so fourth. The iterations are repeated until the wind vector converges to the desired precision. Experimentation shows that more than four iterations does not change the direction by more than $\sim$0.05° or the speed by $\sim$0.05 $\mathrm{m\,s^{-1}}$.

The objective function (6.9) inherently has several minima, one of which is the global minimum (i.e., the ML solution). A search, therefore, is required to find and distinguish the different points of convergence. This search was implemented by initializing the retrieval minimization algorithms with four different initial guesses of wind direction: 0°, 90°, 180° and 270°. An example plot of the wind direction objective function is shown in Figure 6.2. In this example there is a global minimum (the ML solution) at 348° and a local minimum at 117°. If the global search were not performed, the local minimum could be accepted at the ML solution resulting in an erroneous retrieval. After all four seeds have been tried, the result with the smallest value of the wind direction objective function is designated the ML solution.

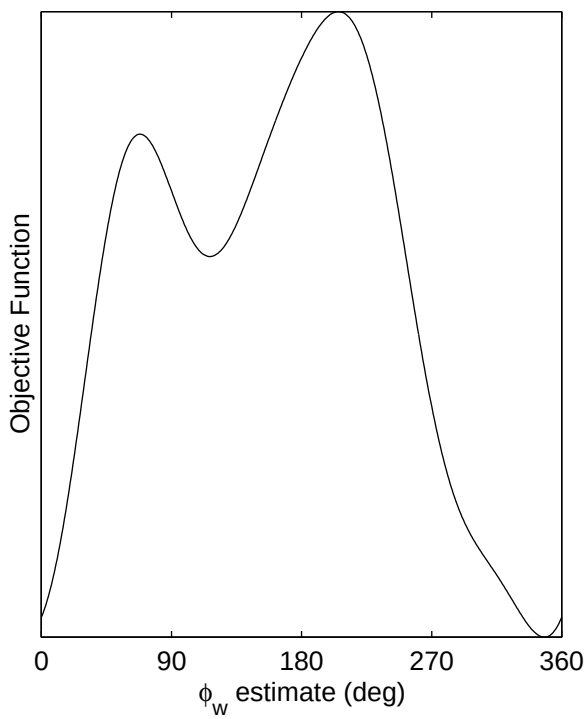

Figure 6.2: Example of wind direction objective function evaluated at estimate wind directions ranging from 0° to 360°. There are two minima, one being local at 117° and the other begin global at 348°.

6.3 Modeling Error and Adaptive Channel Weighting

The weights assigned to the various channels in (6.9) and (6.15) should be based on estimates of both instrument noise and GMF modeling error. The GMF modeling error depends on the specific geophysical states and thus is difficult to determine. A real wind field is typically inhomogeneous in speed and direction, often exhibiting significant structure down to the meso-α spatial scale (i.e., several kilometers). Additionally, inhomogeneities in atmospheric attenuation due to temporal and spatial variability in clouds and water vapor can contribute to geophysical noise in multi-look systems. As an example, the GMF in this study is based on measurements averaged over a geographic area of $\sim$900 km^2, over which the effects of clouds and local convection are to a great extent averaged out. Nonetheless, considerable variability in the harmonic amplitudes can still be seen in Figure 5.5. In order both to estimate and to accommodate the GMF modeling error during the retrieval process, an adaptive channel-weight (ACW) algorithm for multi-look retrievals was developed. The combined ML/ACW wind vector retrieval algorithm provides a means to selectively weight the appropriate radiometer channels in response to geophysical noise resulting from atmospheric and surface inhomogeneities.

The ML/ACW method uses iteration to converge upon both an estimated wind direction and modeling error variance. The goal of the ML/ACW algorithm is to estimate the maximum likelihood wind direction using (6.9) while basing the channel weights ΔT_i^2 on the statistics of the measured brightness temperatures. Specifically, it seeks

$$\widehat{\phi}_w \quad \text{such that} \quad \sum_{m=1}^{M}\sum_{i=1}^{N}\left(\widehat{T}_{i,m} - T_{i,m}\right)^2 \Delta T_i^{-2} \text{ is minimized} \tag{6.17}$$

subject to the condition that:

$$\Delta T_i^2 = \max\left[\frac{1}{M}\sum_{m=1}^{M}\left(\widehat{T}_{i,m} - T_{i,m}\right)^2, \Delta T_{i,RMS}^2\right] \tag{6.18}$$

where the first term in the brackets of (6.18) is the variance estimate of the total noise of the i-th channel over all looks $m = 1..M$. The minimization over $\widehat{\phi}_w$, is implemented using simple recursion as illustrated in Figure 6.3. In the first iteration, the wind direction

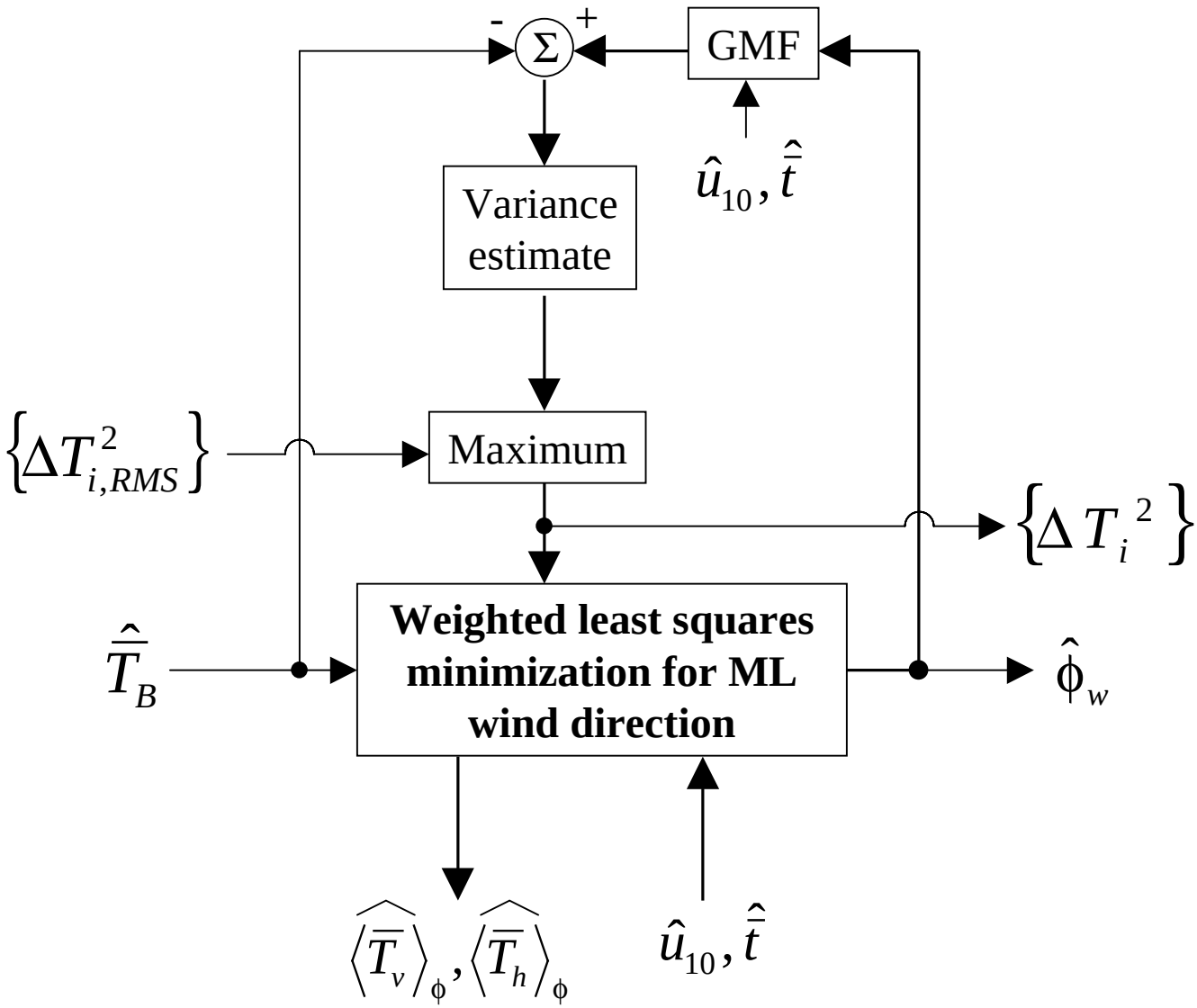

Figure 6.3: Block diagram of the adaptive channel weights recursion algorithm. This algorithm replaces the Wind Direction MLE block in Figure 6.1 to create the full ML/ACW algorithm.

is estimated using channel weights composed of only nominal measurement noise with no modeling error. In all following iterations, the channel weights are the greater of either the nominal measurement noise or the estimated error variances. The error variances for each channel are computed based upon the measured brightness temperatures and the GMF output evaluated at the most recently estimated wind speed and direction. The recursion is repeated until the wind direction converges to a desired precision, in this study 0.1°. To generate the full ML/ACW algorithm, the diagram in Figure 6.3 replaces the Wind Direction MLE block in Figure 6.1.

Under variable cloudiness and/or surface wind inhomogeneity, the vertical and horizontal channels suffer brightness perturbations due to cloud and surface emissions; such perturbations do not appear in the third Stokes parameter channel [22]. Thus, using ACW the third Stokes parameter channel will receive proportionately more weight under these conditions than the vertical and horizontal channels. The ACW technique also helps accommodate the effects of water vapor and temperature inhomogeneity, or variations of any other parameters that impact the baseline vertical and horizontal brightness temperatures.

A useful by-product of the ML/ACW algorithm is is an estimate of the GMF modeling error for each channel. This error can be used in computing Cramer-Rao (CR) minimum variance bound on the direction retrieval accuracy. The CR bound is given by [58]:

$$\sigma^2_{\hat{\phi}_w} \geq -E\left(\left[\frac{\partial^2 \ln L}{\partial \phi_w^2}\right]\right)^{-1} \tag{6.19}$$

where the log likelihood function is given by (6.7). This bound can be analytically derived for the ML wind direction retrieval. Accordingly, the minimum standard deviation for an M-look retrieval is:

$$\sigma_{\hat{\phi}_w} \geq \left[\sum_{m=1}^{M}\sum_{i=1}^{N} F_{i,m}\Delta T_i^{-2}\right]^{-1/2} \tag{6.20}$$

where

$$F_{i,m} = \begin{cases} t^2 \left[a_{1i}\sin(\phi_m - \phi_w) + 2a_{2i}\sin(2\phi_m - 2\phi_w)\right]^2 & \text{if } i \text{ refers to a } v \text{ or } h \text{ channel} \\ t^2 \left[b_{1i}\cos(\phi_m - \phi_w) + 2b_{2i}\cos(2\phi_m - 2\phi_w)\right]^2 & \text{if } i \text{ refers to a } U \text{ or } V \text{ channel} \end{cases} \tag{6.21}$$

where ϕ_m is the azimuth look angle of the m-th look. For example, a wind direction estimate using two looks from a single-frequency fully-polarimetric radiometer would have a minimum standard deviation of:

$$\begin{aligned} \sigma_{\hat{\phi}_w} \geq \Bigg(& t^2 \sum_{m=1}^{2} \left[a_{1v}\sin(\phi_m - \phi_w) + 2a_{2v}\sin(2\phi_m - 2\phi_w)\right]^2 \Delta T_v^{-2} + \\ & \left[a_{1h}\sin(\phi_m - \phi_w) + 2a_{2h}\sin(2\phi_m - 2\phi_w)\right]^2 \Delta T_h^{-2} + \\ & \left[b_{1U}\cos(\phi_m - \phi_w) + 2b_{2U}\cos(2\phi_m - 2\phi_w)\right]^2 \Delta T_U^{-2} + \\ & \left[b_{1V}\cos(\phi_m - \phi_w) + 2b_{2V}\cos(2\phi_m - 2\phi_w)\right]^2 \Delta T_V^{-2} \Bigg)^{-1/2} \end{aligned} \tag{6.22}$$

The CR error bound depends not only upon instrument and modeling noise, but also upon the specific set of azimuth look angles and wind direction. Figure 6.4 shows the minimum bound on the direction standard deviation for a two-look retrieval of 14 $\mathrm{m\,s^{-1}}$ winds using the first three Stokes parameters at 37.0 GHz. The assumed RMS instrument noise is assumed to be 0.2 K for all three polarimetric channels, and the modeling error is 1 K for T_v and T_h. The azimuth look angle is defined as the angle of the fore-look off the starboard side of the aircraft or satellite, and the wind direction is given with respect to the heading. Typically, the minimum standard deviation is $\sim 5^\circ$, however, there exists several points at which the bound exceeds 25°. These points correspond to combinations of wind direction and azimuth look angles at which the objective function (and hence GMF) has a small azimuthal sensitivity. For these conditions a small perturbation in brightness temperature (due to either instrument or modeling noise) produces a rather large change in the estimated wind direction. Perhaps the most extreme example is for the case of the radiometer looking downwind at 90° with respect to the platform track. For this situation, the

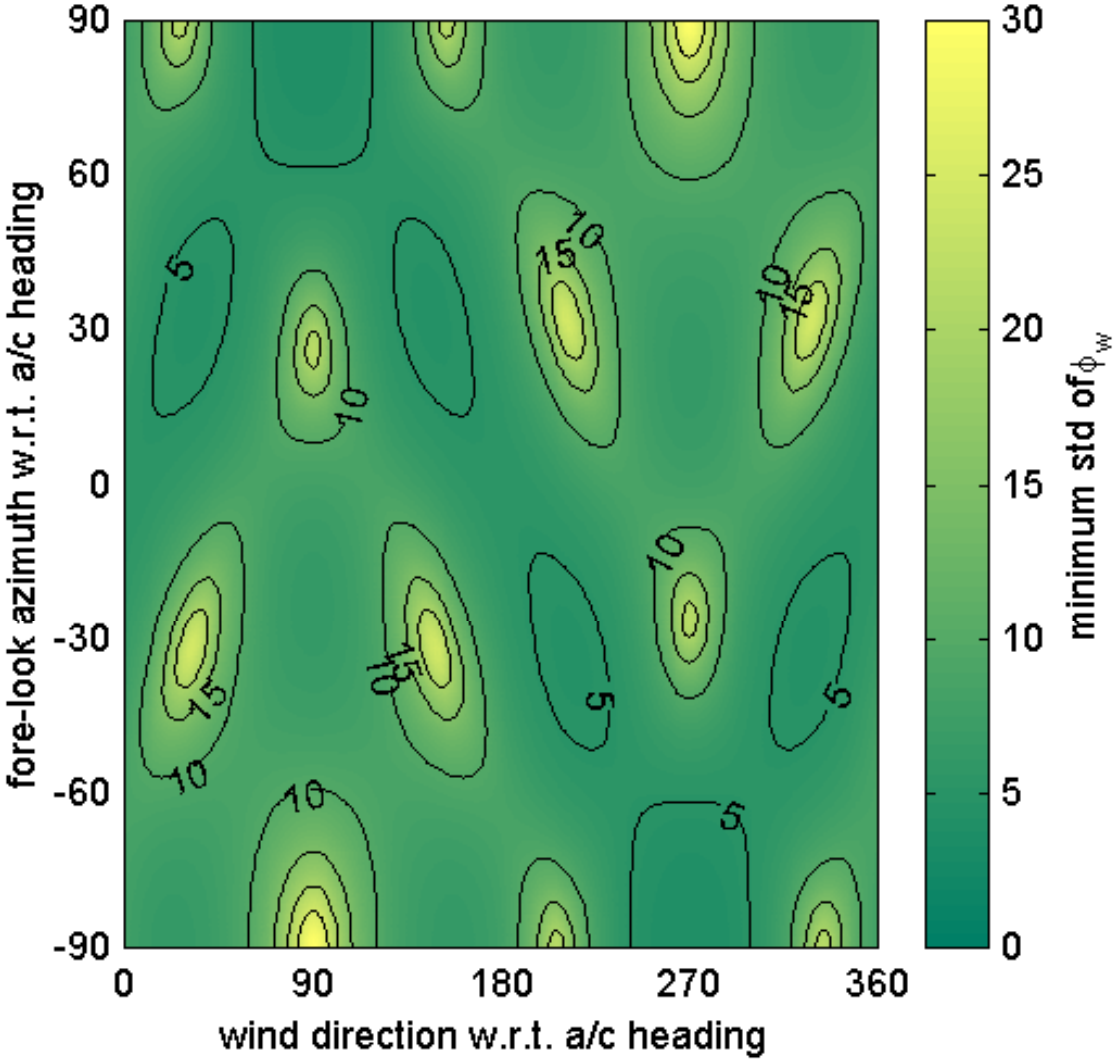

Figure 6.4: Minimum bound on the retrieved wind direction standard deviation for a two-look 37 GHz tri-polarimetric system. The assumed wind speed is 14 $\mathrm{m\,s^{-1}}$, $\Delta T_{RMS} = 0.2$K, and the T_v and T_h modeling error is 1 K RMS.

Table 6.1: PSR Labrador Sea experiment Observations on March 7, 1997.

designation	heading	time	flight track
outbound	102°	1900-1936 UTC	(55.6067°N, 50.0852°W) to (54.7871°N, 44.3091°W)
inbound	288°	1954-2100 UTC	(54.4140°N, 42.1850°W) to (55.7849°N, 51.7862°W)

T_U azimuthal slope is nearly zero (e.g., see Figure 5.4), and from Figure 6.4 the bound on the standard deviation rises to ∼30°. Interestingly, for the opposite case of the radiometer looking upwind at 90° off track, the T_U curve is highly sloped resulting in an error bound of only ∼4°.

6.4 Wind Vector Measurements

During the OWI experiment the P-3 overflew a Canadian-Atlantic low pressure system on March 7 located near 55° 30' N, 47° 00' W and moving northeast towards the southern tip of Greenland. The NOAA AVHRR infrared (channel 4) imagery of clouds associated with this polar low at 1128 UTC is shown in Figure 6.5. The warm air mass flowing southward from Greenland over the Labrador Sea coupled with the cold dry westerly air from the Canadian north to produce a well developed cyclone with surface winds of 15-25 $\mathrm{m\,s^{-1}}$ (30-50 kts) and a central pressure of ∼960 mb. Two P-3 flight tracks (see Table 6.1) intersected the low pressure system and provided unique observations of a mesoscale wind shift across the cyclone center. Surface wind measurements were made by GPS dropsondes at two locations, one on either side of the center. The ML/ACW algorithm was applied to the PSR data in both full conical-scan and two-look (fore and aft) retrieval modes to the multi-band polarimetric imagery. The channels used were 10.7 GHz (v, h, and U), 18.7 GHz (v and h)[1], and 37.0 GHz (v, h, and U). The PSR footprint size was 1400 × 850 m at 10.7 and 18.7 GHz, and 300 × 500 m at 37.0 GHz. The incidence angle was 53.1° from

[1]The 18.7 GHz U-channel was too noisy to be useful in this investigation.

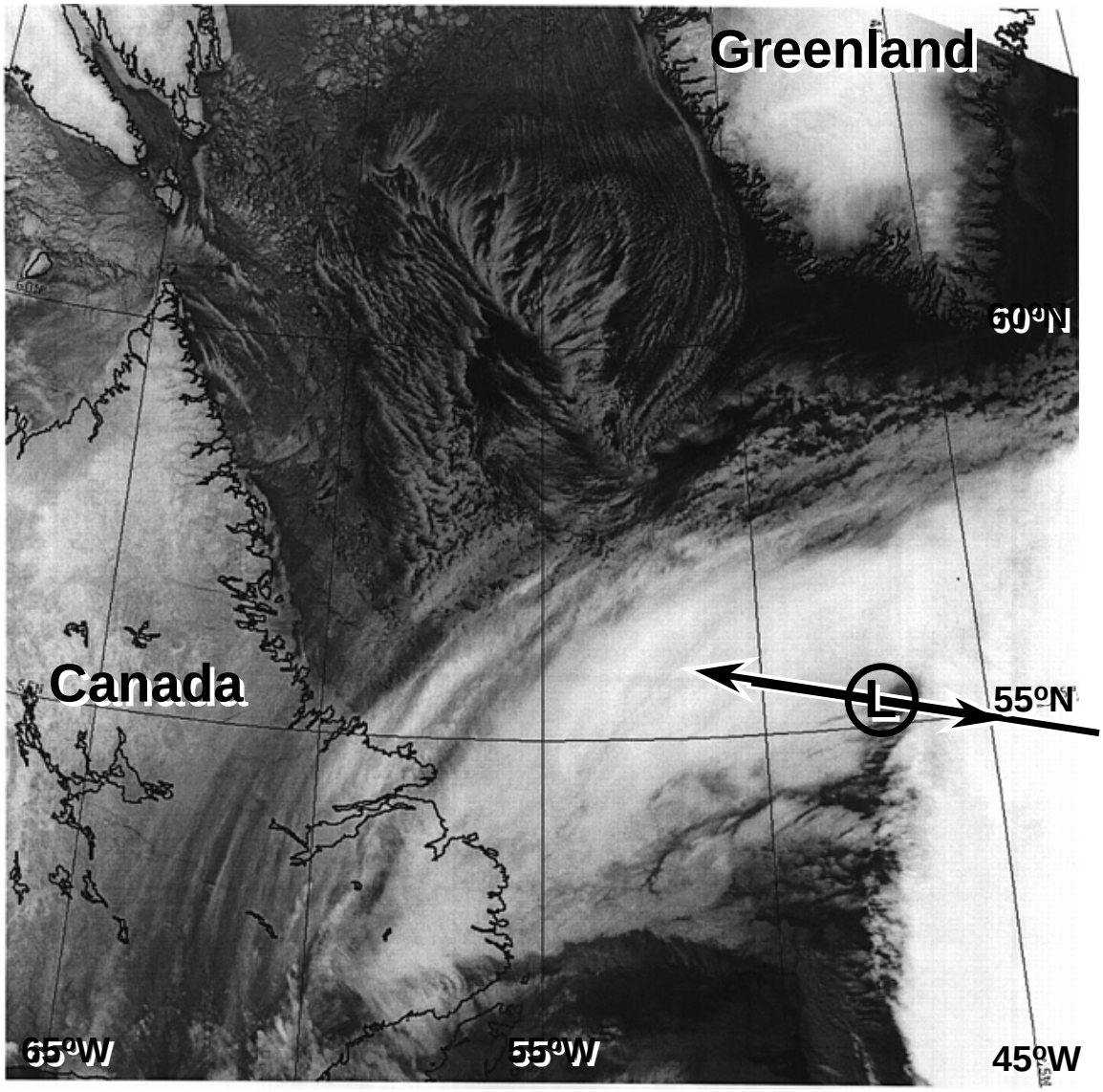

Figure 6.5: The NOAA-12 AVHRR infrared (channel 4, 10.9 μm) imagery at 1128 UTC on March 7, 1997.

nadir, and aircraft altitude was 6,100 m (20,000 ft), thus imaging a swath of width ∼15 km.

6.4.1 Full-Scan Retrievals

One-dimensional 20 km resolution wind vector maps were produced using full azimuthal scans over the inbound (629 km) and outbound (378 km) flight lines. Figure 6.6 displays the results of the full conical averaged-scan wind vector retrieval for the inbound and outbound flight legs overlaid onto 37 GHz radiometric brightness imagery. Each sub-track wind vector was retrieved from an average of seven conical scans, which resulted in 35 seconds of integration time for each scan at a 20 km spacing. There are 19 retrieved wind vectors on the outbound leg and 31 on the inbound leg. The wind measurements show a distinct 180° wind shift in both flight tracks along a frontal boundary associated with the mesoscale cyclone, as indicated in the AVHRR imagery. The two GPS dropsonde measurements obtained during the inbound leg (arrows plotted with stars at the splash points) concur with this wind shift. Table 6.2 lists the wind direction retrieval statistics for the outbound and inbound flight legs. There is a strong southerly flow of ∼15 $\mathrm{m\,s^{-1}}$ (30 kts) at 195° to the east of 47°W longitude. Moving left, or west, across the figure, the wind direction changes from 195° to 22° for the western portion. The dropsonde measurements indicate wind directions of 203° and 9° for the east and west portions of the inbound flight track, respectively. The direction change occurs over a distance of ∼80 km. Comparison of the retrieved wind field with the NOAA National Center for Environmental Prediction (NCEP) Eta numerical weather prediction model [6] analysis at 1800 UTC (blue arrows, two hours prior to the inbound leg) also shows good agreement. Here the higher resolution of the PSR retrieval reveals the wind shift occurring over a much smaller distance (∼50-100 km) than the Eta model.

The low-resolution background field in Figure 6.6 is the 37 GHz horizontally-polarized brightness temperature as measured by the DMSP SSM/I (F-13 spacecraft) during the inbound transect at 2003 UTC. The PSR 37 GHz T_h imagery is also plotted and can be identified as the high-resolution swath of width 15 km running right to left across

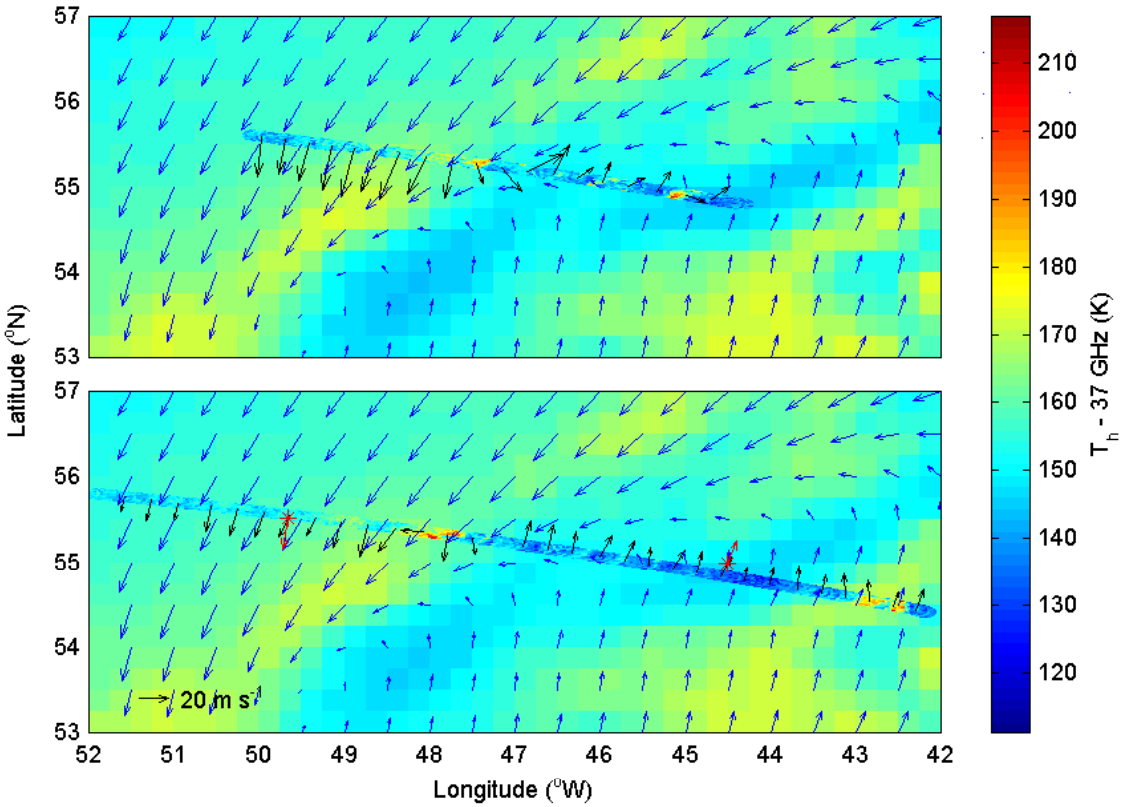

Figure 6.6: Full-scan wind vector retrieval for the outbound (top) and inbound (bottom) flight legs. The wind vectors are overlaid onto the PSR and SSM/I horizontal polarized 37 GHz radiometric brightness imagery. The mean wind direction is 195° to the east of ∼47°W longitude and 22° to the west of this boundary. The dropsonde measurements (plotted as starred arrows) indicate wind directions of 203° and 9° for the east and west portions of the flight track, respectively.

Table 6.2: Wind direction statistics for the transect on March 7, 1997 across the polar low. PSR retrievals used both the 1-dimensional and 2-dimensional ML/ACW methods. The 1-D retrieval statistics were computed using 7 retrieved wind vectors located near each splash point. Eighteen points were used for the 2-D retrievals. The CR bound is stated for the 2-dimensional retrieval. The dropsondes were released on the inbound track. The Eta model data is from the 1800 UTC record.

		East Splash Point		West Splash Point	
		$\langle\phi_w\rangle$	σ_{ϕ_w}	$\langle\phi_w\rangle$	σ_{ϕ_w}
		(degrees)		(degrees)	
Out-	PSR 1-D	230.0	15.4	11.5	3.4
bound	PSR 2-D	217.6	19.8	8.7	11.0
Track	CR bound	-	6.7	-	3.7
	PSR 1-D	195.4	11.6	19.2	5.4
Inbound	PSR 2-D	205.1	18.1	23.8	17.2
Track	CR bound	-	7.0	-	8.8
	GPS	202.6	-	9.3	-
	Eta Model	184.9	-	31.6	-

each figure. Note that the high-resolution details as revealed by the ∼1 km PSR imagery are averaged out by the larger antenna footprint of the SSM/I (∼25 km). In particular, there are several small bright spots ∼ 5 km in size at 48°W longitude (immediately west of the wind direction shift) and 42.5°W longitude that are revealed only in the PSR imagery. These small bright features affected the channel weighting in the ML wind vector retrieval through the ACW algorithm. Figure 6.7 shows the relative weights of the T_U channel versus the sum-squared weights of the T_v and T_h channels for the 10.7 and 37 GHz bands. There are two distinct locations at which the T_U channel is weighted significantly higher than T_v and T_h, both of which correspond to these bright features. Also significant is that the weighting of T_U relative to that of T_v and T_h for 37 GHz is increased more than this same ratio for 10.7 GHz at these locations. This trend is expected because T_v and T_h are more susceptible to variations in both atmospheric and surface absorption and emission at the higher frequency. The above evidence suggests that the 10.7 GHz channels will be useful for wind vector and surface emission mapping in cloudy and convective areas. In

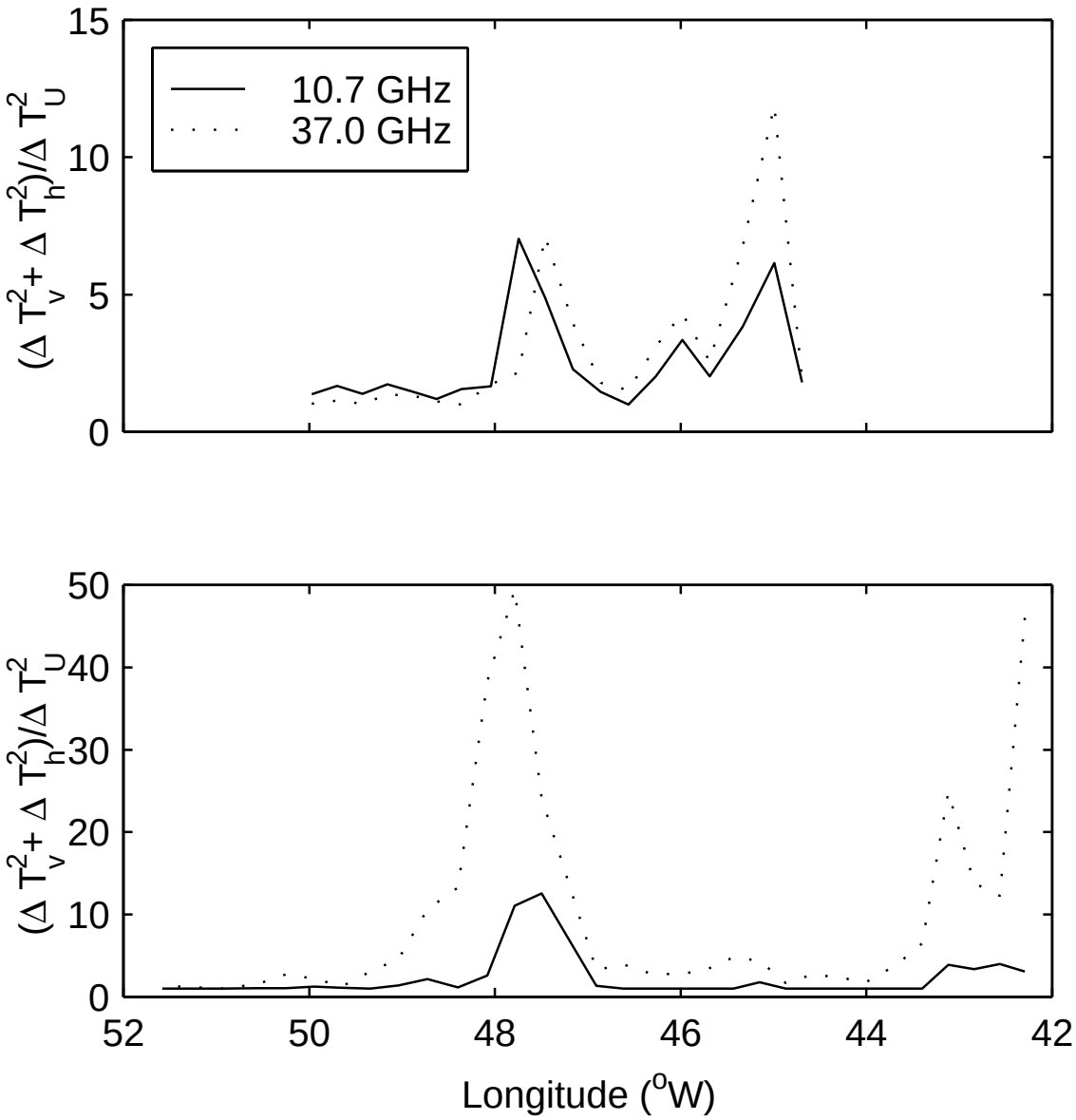

Figure 6.7: Adapted weighting of T_U relative to T_v and T_h ($(\Delta T_v^2 + \Delta T_h^2)/\Delta T_U^2$) for 10.7 GHz (solid line) and 37.0 GHz (dotted line). The top and bottom plots are for the outbound and inbound flight tracks, respectively.

particular, 10.7 GHz T_U will be highly useful for wind direction retrieval.

6.4.2 Two-Look Retrievals

Two-dimensional wind vector maps were also retrieved using the PSR conically-scanned imagery using a two-look technique. The data were separated into fore and aft looks and averaged to produce 2×6 km sized spots. The 629 km inbound flight line yielded fore-look and aft-look images containing 7×105 pixels each. The total radiometric integration time for each pixel was $\sim$0.25 sec. Fore/aft-look pairs were chosen using a nearest neighbor criterion, and the ML/ACW wind vector retrieval was applied to each pair. The resulting wind fields were tested and corrected for directional ambiguities. Generally, the ML estimate is close to the true wind direction. Occasionally, however, a non-ML solution is significantly closer to the true wind direction, thus yielding a gross directional error. This incorrect selection occurs because of instrument noise and geophysical modeling uncertainty, which cause the global maximum of $\ln L$ to occur at the incorrect direction, while one of the local maxima occurs at the correct direction. Directional ambiguities can be resolved using climatology, median filtering (as is common in scatterometry [53, 27]), or available ground truth such as buoys and ship reports. In this study the ambiguities are resolved using the median filtering method described in [27]. The most likely wind direction was determined by passing a 7×7 median filter over the retrieved wind field. If a retrieved wind direction was more than 20° different from the median filter output, the next most likely direction was tested for a better fit. This direction was chosen if it fell within the 20° window, otherwise the original ML estimate was retained. For both the outbound and inbound flight legs, the ML algorithm selected the correct direction to within the 20° window criterion $\gtrsim$90% of the time; thus, the retrieved ambiguity rate was $\lesssim$10%.

Figures 6.8(a) and 6.9(a) show two regions, one to the east and the other to the west of the wind shift, in which the retrieved wind fields were largely homogeneous. The wind images are shown along with corresponding forward-looking brightness maps from the 10.7 and 37.0 GHz channels. The statistics of the retrieved wind fields in the areas close to the

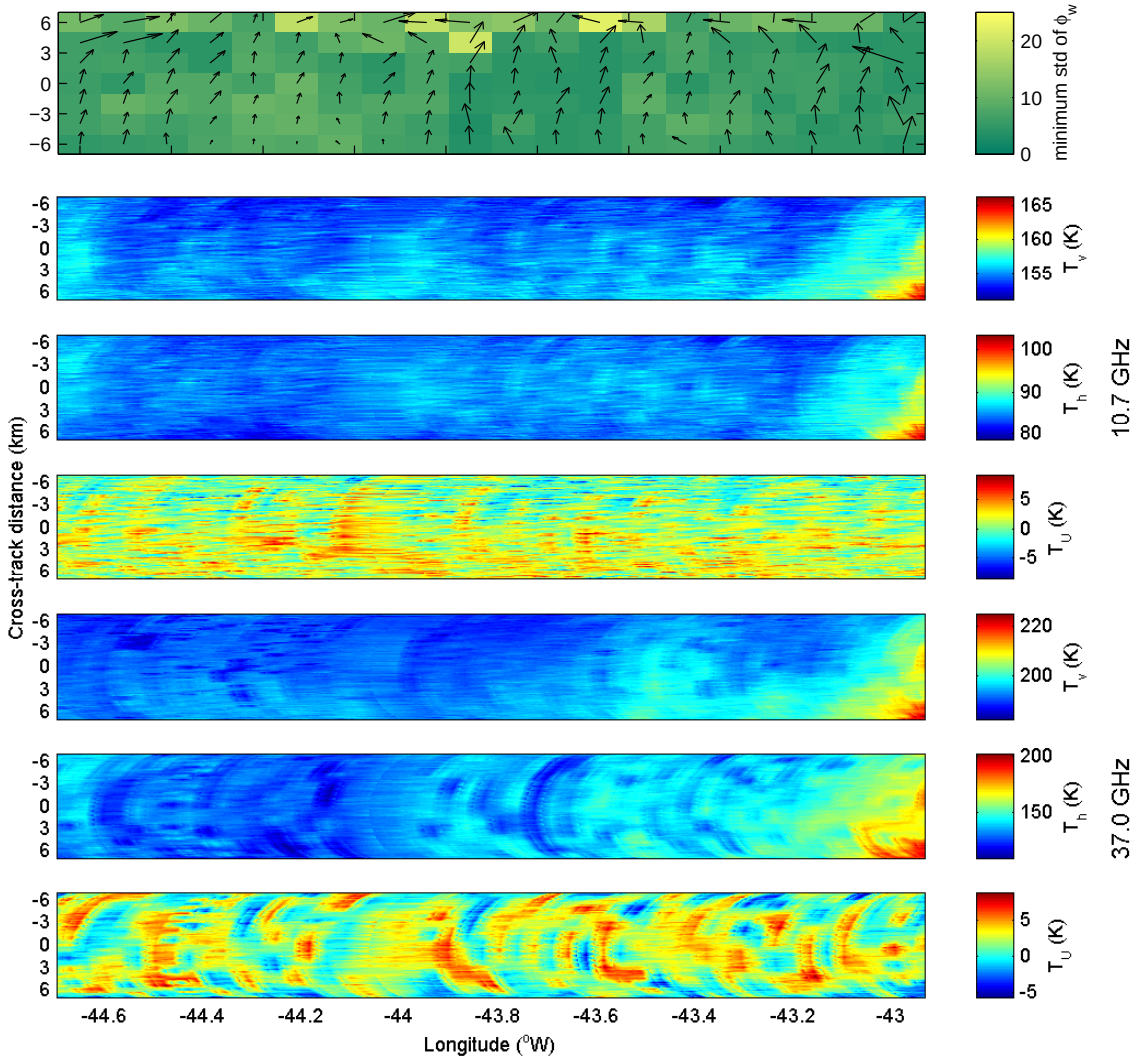

Figure 6.8: High-resolution 2-dimensional wind map and brightness imagery for region east of wind direction shift. The retrieved surface wind field and corresponding CR bound image are plotted in (a). The fore-look polarimetric (T_v, T_h, and T_U) brightness temperatures are displayed in images (b)-(d) (10.7 GHz) and (e)-(g) (37.0 GHz).

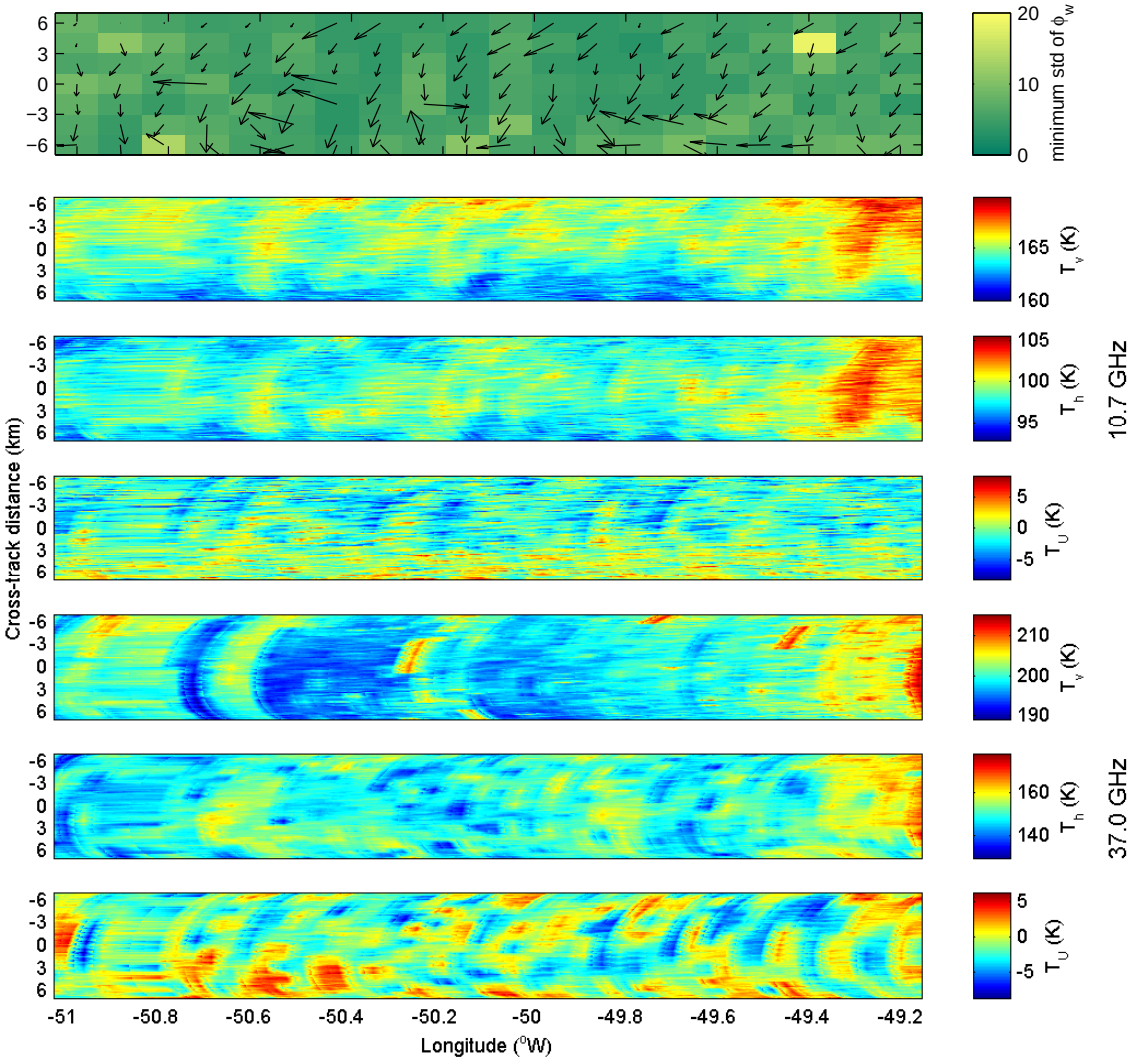

Figure 6.9: Same as Figure 6.8 for the region west of the wind direction shift.

two dropsonde splash-points are compiled in Table 6.2. The absolute difference between the GPS dropsonde measurements and the average retrieved wind direction is only 2° and 9° for the east and west locations, respectively. The RMS variability in the retrieved wind fields is $\sim 18°$, which is about twice the CR bound for the retrieval standard deviation. This difference is not unexpected, since the computed retrieval variability is also affected by the spatial variability present in the actual surface wind field. Furthermore, the variance of the ML estimator only approaches the CR bound asymptotically [58, Section 18.16]; therefore, with only two looks it is quite possible that the retrieval variance will be greater than the CR bound. The homogeneity of the retrieved maps suggests that satellite-based retrievals of surface wind fields that exhibit uniformity over scales of at least one spot size will be retrievable using a two-look technique.

The color background in Figures 6.8(a) and 6.9(a) is the CR bound for each pixel computed from the channel weights estimated by the ML/ACW algorithm. Note that while most of the pixels have a CR bound within 5°-10°, the row across the top of the east image and the bottom of the west image have a larger CR bound. This increase (up to $\gtrsim 20°$) occurs because the combination of azimuth look angle, aircraft heading, and wind direction are such that the radiometer is looking $\sim 90°$ off-track and nearly downwind. This situation is identical to that described in Section 6.3.

The corresponding two-dimensional wind field map for the region containing the wind direction shift is shown in Figure 6.10(a). The winds at both ends of the displayed map are homogeneous as in Figures 6.8(a) and 6.9(a); however, over a track length of ~ 80 km in the vicinity of the wind shift, the retrieved winds are highly variable in direction. Some of the observed variability is presumed to be due to the natural surface wind field. Indeed, non-zero surface divergence and circulation are expected near cyclone eyes. A portion of this variability, however, can be explained by a local increase in geophysical modeling error, resulting in a larger CR bound. Indeed, the bound on direction standard deviation for the pixels in the area from $\sim 47.5°$ to 48.5°W longitude is 10°-20°, contrasted with the 5°-10° bound in the homogeneous regions. As seen in the lower images in Figure 6.10, the

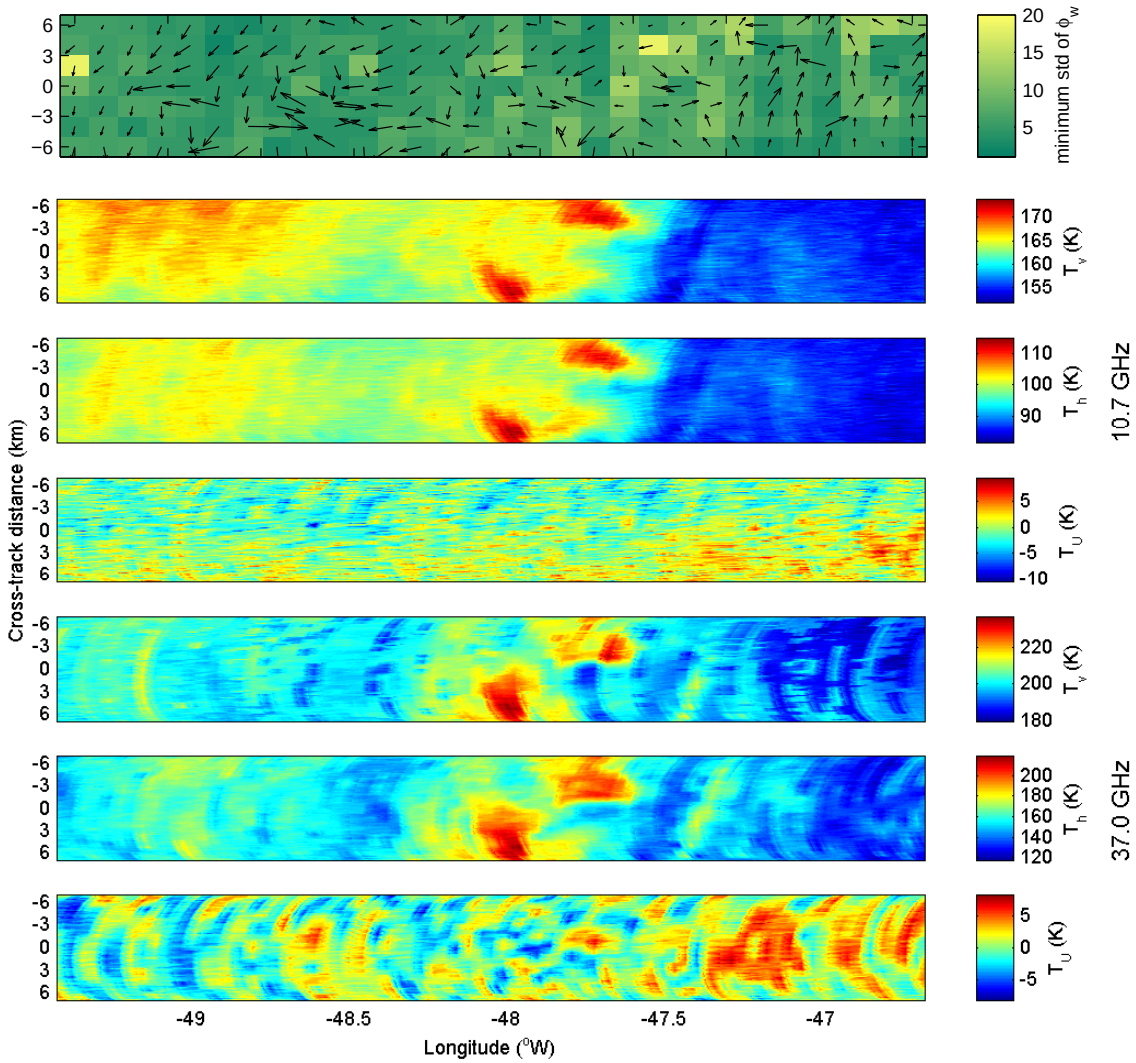

Figure 6.10: Same as Figure 6.8 for the region containing the wind direction shift.

microwave brightness temperature for v and h channels increases in both magnitude and variability around the wind shift. The features seen in the brightness imagery are due to variable cloudiness and surface emission in the region. Convective clouds, in particular, cause the fore and aft-looks to view different liquid water columns. Because the zeroeth order components (5.2) of T_v and T_h are greatly affected by atmospheric absorption, differing cloud content in the paths of the fore- and aft-looks will result in unmodeled brightness temperature fluctuations. A portion of the variability seen in the wind vector map is due to such effects.

Further insight into the nature of the emission process can be gained by considering the calibrated conically-scanned brightness maps from the PSR 10.7 and 37.0 GHz channels in Figures 6.8(b)-(g), 6.9(b)-(g), and 6.10(b)-(g). In the regions of homogeneous wind (Figures 6.8 and 6.9), the observed brightness field is seen to be relatively uniform. Subtle maxima in T_v at both 10.7 and 37.0 GHz can be seen in the upwind directions (+6 km across track in Figures 6.8(b, e) and -6 km across track in Figures 6.9(b, e)), while subtle maxima in T_h can be seen in the cross-wind directions (0 km across track in Figures 6.8(c, f) and 6.9(c, f)). These features are similar to those identified in Section 3.4.1. The phase-quadrature nature of the T_U signature can be seen as subtle minima in directions 45° to the left of the upwind direction (Figures 6.8(d ,g)) and maxima in directions 45° to the right (Figure 6.9(d, g)). We note that perturbations in the vertical and horizontal brightness fields of up to 15 K caused by surface spatially inhomogeneous roughness and/or clouds do not significantly affect the retrieved field. It is particularly important to note that such perturbations are entirely absent in the 10.7 and 37.0 GHz T_U maps. Thus, enhanced regions of surface roughness and/or clouds do not affect the degree of polarization or the orientation of the linearly-polarized component of the upwelling radiation field. It is noted that throughout most of Figures 6.8 and 6.9, the sky below the aircraft was undercast to scattered, indicating rejection of much cloud cover in the retrieved wind fields.

Perhaps the most obvious and important brightness features are the large amplitude brightness perturbations in the vertical and horizontal polarized channels for both 10.7 and

37.0 GHz near and due west of the wind shift in Figures 6.10(b-c) and 6.10(e-f). Two isolated regions extending over ∼4-8 km are noted which cause a perturbation of ∼15 K at 10.7 GHz, and higher (∼60-70 K) at 37.0 GHz. A third extended feature west of the two regions exhibits perturbations mostly in the 10 GHz channels, suggesting that the features are the result of an increase in surface roughness at the scale of approximately one-half electrical wavelength (∼1.5 cm). While these features do affect the retrieval, it is again noted that the T_U signal remained *completely unaffected* (Figures 6.10(d, g)), with the wind shift at ∼47.5°W being clearly seen as an across-track shift in the phase of the T_U imagery.

6.5 Discussion

In this chapter, the first use of conically-scanned microwave polarimetric imagery of the ocean surface at 10.7, 18.7, and 37.0 GHz to generate high-resolution near-surface wind vector maps in both one and two dimensions was demonstrated. While a variety of *ad hoc* wind vector retrieval procedures could be used to develop the retrieval operator, the joint maximum likelihood estimator for wind speed and direction derived here is both fast enough for most operational applications and nearly optimal based on the CR bound. Indeed, since radiometric observations necessarily require integration times of order at least tens of milliseconds, the ML retrieval could easily be implemented in real time. The estimator also allows for straightforward adaptation of the weights assigned to the various channels and polarizations by the estimated geophysical noise. The geophysical noise estimate is itself a valuable by-product of the estimation process and can be further used in either numerical or qualitative weather analyses as a measure of error in the wind vector retrieval. Application of the ML/ACW technique to either full conical scans for 1-dimensional along-track retrievals or partial (sub-swath) scans for 2-dimensional maps is straightforward.

Comparisons of the retrieved wind vector maps with data from dropsondes suggest

that using the ML/ACW technique applied to 10.7, 18.7, and 37.0 GHz full-conical polarimetric scans can provide RMS errors of $\pm 10^\circ$ over footprints covering an area of as little as $\sim$50-100 km^2. The retrieval error using the two-look ML/ACW technique is only slightly worse, but considerably more sensitive to local inhomogeneity in the upwelling brightness field. The two-dimensional retrieval for the case of March 7 shows particularly high variability near a region of major wind shift, an effect possibly resulting from the confused nature of the sea surface at that location. The two-look retrieval achieved a 90% skill in retrieving the non-ambiguous wind direction. The success of this technique demonstrates the viability of airborne and spaceborne wind vector mapping using polarimetric microwave radiometry.

CHAPTER 7

Simulated Satellite Retrievals

This chapter describes a series of simulated satellite retrievals of ocean surface wind vectors. Averaged data from several Labrador Sea hex-cross patterns were used to simulate satellite brightness temperature measurements to study three different satellite sensor configurations: (1) tri-polarimetric one-look, (2) dual-polarization two-look, and (3) tri-polarimetric two-look measurements. Additionally, the simulated radiometric sensitivity of the tri-polarimetric two-look measurements is varied to compare the ML/ACW algorithm performance to its CR bound.

7.1 Design Considerations

Among the various design parameters of a passive wind vector satellite, two major decisions are 1) the choice between a microwave polarimeter or a dual-polarization radiometer and 2) the choice of using a one-look or two-look scan configuration. The incidence angle is also of great importance but is not considered in this study; the investigations herein utilize the SSM/I incidence angle of 53.1°. Two performance measures were chosen to quantitatively study the consequences of using a particular design: RMS retrieval error and retrieval ambiguity rate. Table 7.1 lists the hypothesized effects for the different system combinations based upon examination of the wind direction harmonics. First, the one-look dual-polarization system (e.g., SSM/I) cannot provide instantaneous wind direction measurements. The one-look polarimetric system, on the other hand, can yield a wind direction

Table 7.1: Hypothesized effects of polarization selection and number of looks on mean surface wind vector retrieval ambiguity and RMS error.

	Dual-polarization	Polarimetric
One-look	• No direction information in single look of T_v and T_h • Highest RMS wind speed error	• Two/four-fold directional ambiguity • RMS error based only on one-look, therefore weight adaptation not possible • High RMS wind speed error
Two-look	• Two-fold ambiguity • Lacks T_U for cloud mitigation, but weight adaptation is possible	• Potentially no ambiguity • Wind speed and direction RMS errors reduced by additional information in two looks, and weight adaptation is possible

estimate because directional information is contained in the single sample of T_U (and T_V), yet this system suffers from two- or four-fold ambiguity. Additionally, the adaptive weights algorithm cannot be applied to the one-look retrieval because a proper estimate of mean-square error cannot be made with only one sample point. The two-look dual-polarization system might have lower RMS error than the one-look polarimetric system in clear air, but is missing the third and fourth Stokes parameters, which are useful for both cloud mitigation and breaking the inherent two-fold ambiguity. The adaptive weighting can be applied, however, to the two-look system. Adding the third (and/or presumably the fourth) Stokes parameter not only breaks the two-fold ambiguity (because of the quadrature phase nature of the T_U azimuthal signature), but also improves the RMS error because of the informational content of the additional channels.

In addition to the quality of retrieved winds, the number of azimuthal looks will constrain the design of the conical scanner on the satellite, particularly the placement of the calibration ambient load and cold space mirror. If two different azimuth looks are required for a low-noise measurement, then the calibration targets can be positioned to the sides of the spacecraft such that the side-looking azimuth positions allow the radiometer to

Table 7.2: SSM/I and WindSat Nyquist spot size and the equivalent PSR hex-cross aperture size (for a 9 km $\times$ 15 km spot) at 10.7, 18.7, and 37.0 GHz.

f (GHz)	SSM/I 0.635 m aperture (km^2)	WindSat 1.93 m aperture (km^2)	PSR hex-cross 9.0 km $\times$ 15 km (m)
10.7	–	9.1 $\times$ 15	1.95
18.7	16 $\times$ 26	5.2 $\times$ 8.7	1.12
37.0	8.0 $\times$ 13	2.6 $\times$ 4.4	0.565

view the ambient load or cold space rather than the earth. This placement, however, reduces the swath width on ground. If, on the other hand, only one look is deemed necessary, then the calibration looks could be placed in one of the scan quadrants (such is proposed for WindSat [17]) or in the back-most portion of the scan (effectively, an SSM/I scan geometry with an extended azimuth range and polarimetric channels).

7.2 Simulations

A series of satellite retrieval simulations was performed to quantify the effects of polarization selection and the choice of a one- or two-look system. Using Labrador Sea data, three different design cases were investigated: (1) tri-polarimetric two-look, (2) dual-polarization two-look, and (3) tri-polarimetric one-look. The dual-polarization one-look case (e.g., the SSM/I configuration) was not investigated because wind direction information cannot be extracted from such measurements.

The SSM/I [32] and WindSat [17] instruments were used as satellite sensor models on which to base the simulation. The SSM/I and WindSat altitude is nominally 830 km, the surface incidence angle is 53.1°, and the aperture sizes are 63.5 cm and 1.93 m, respectively. Table 7.2 lists the spot sizes (assuming Nyquist angular sampling) for both instruments. The SSM/I spot sizes range from (16 km $\times$ 26 km) at 18.7 GHz to (8.0 km $\times$ 13 km) at 37.0 GHz. For WindSat, the spot sizes range from (9.1 km $\times$ 15 km) at 10.7 GHz to (2.6

Table 7.3: Four data sets used to study the three satellite design cases.

Data Set #	Date (UTC)	Time ($m\,s^{-1}$)	Wind Speed (deg)	Wind Direction
1	March 3	1344-1423	13.6	314
2	March 4	1502-1557	15.9	270
3	March 7	1638-1728	12.0	351
4	March 7	1731-1823	14.0	345

km $\times$ 4.4 km) at 37.0 GHz. The sensitivities for SSM/I and WindSat are $\sim$0.35 K and $\sim$0.2-0.3 K (planned), respectively.

PSR straight-and-level flight data (i.e., the hex-cross and patrols) were used to generate the simulated satellite brightness temperature measurements. Averaging azimuthal scan data into 10° bins gathered a sufficient number of pixels to cover a (9 km $\times$ 15 km) footprint for each bin. The equivalent satellite aperture diameters needed to obtain this spot size from an 830 km altitude at a 53.1° incidence angle are listed in Table 7.2 for 10.7, 18.7, and 37.0 GHz. The aperture diameter ranges from 1.95 m at 10.7 GHz to 56.5 cm at 37.0 GHz and spans the aperture dimensions of both the SSM/I and WindSat instruments. To generate the simulated measurements $\sim$800 PSR samples were averaged for each azimuth bin for a total integration time of 6.4 sec for the analog channels and 12.8 sec for the digital channels. The equivalent radiometric sensitivity was $\sim$0.03 K. Pseudo-random Gaussian noise of standard deviation 0.246 K was added in a Monte-Carlo fashion to effectively degrade the sensitivity to $\sim$0.25 K.

Four such data sets were generated to test the three satellite design cases. The wind states of each set as measured by the *Knorr* are listed in Table 7.3. Data set 1 is used as a representative set in this chapter; the results for all four data sets can be found in Appendix D. Extra geophysical modeling error was not added to the data, rather the natural variations observed during the hex-cross patterns were retained to model the effect of geophysical noise as averaged over a satellite-scale footprint. To properly cover the possible combinations of relative wind direction and azimuth look angle, several combinations for each of

Table 7.4: Observation parameters used to study the three satellite design cases.

	Design Configuration	Aircraft Heading w.r.t. Wind Direction	Azimuth Look-Angles w.r.t. Aircraft Heading	Total Number of Monte-Carlo Trials
1)	Two-looks Tri-polarimetric	0°, 60°, 120°	(0°,180°) (45°,135°) (-45°, -135°)	135
2)	Two-looks Dual-polarization	0°, 60°, 120°	(0°,180°) (45°,135°) (-45°, -135°)	135
3)	One-look Tri-polarimetric	N/A	0°, 45°, 90°, 135°, 180°, 225°, 270°, 315°	120

the three cases were considered. The observation parameters are listed in Table 7.4. The simulations were run in a Monte-Carlo fashion by adding pseudo-random observational noise with 15 trials for each aircraft heading and look angle combination. Assembling the output of the four sets produced a total of 540 trials each for design cases 1 and 2 and 480 trials for case 3.

The objective function (6.9) inherently has several minima, one of which is the global minimum (i.e., the ML solution). A search, therefore, is required to find and distinguish the different possible points of convergence. An exhaustive search is impractical because of the extremely large number of required objective function evaluations. For example, to search over wind direction (0° to 360°) with 1° resolution, wind speed (0 $\mathrm{m\,s^{-1}}$ to 30 $\mathrm{m\,s^{-1}}$) with 0.1 $\mathrm{m\,s^{-1}}$ resolution, and atmospheric transmissivity (0 to 1) with 0.001 resolution would require $360 \times 300 \times 1000 = 108 \times 10^6$ function evaluations. (Note that this does not even include iteration for channel weight adaptation). Thus, the search was implemented using a quasi-Newton method by initializing the retrieval minimization with four different initial guesses of wind direction: 0°, 90°, 180° and 270°. The multiple initial guesses are used to seed the algorithm at different points so that all the minima of the objective function can be found. Four initial guesses were used because the objective function typically has only two minima, as was empirically determined. This search technique is significantly more efficient than exhaustive searching requiring only ∼1400 function

evaluations for the full ML/ACW algorithm with the four-fold solution search. The the resulting minima are recorded along with the respective values of the objective function. The ML solution is found by choosing the wind direction that has the smallest corresponding value of the objective function from among the four solutions. The remaining solution are spurious or ambiguous results. The 12 plots in Figure 7.1 show the four-fold search results for each of the three design cases of data set 1. (The results for data sets 2-4 can be found in Appendix D.) Note that these results are given prior to ambiguity removal. The ML solutions are plotted as lines pointing in the upwind direction and spurious solutions (caused by convergence at local minima) are plotted as individual points. The percentage of ML solutions for a particular initial guess is printed above each plot. For cases 1 and 2 (Figure 7.1(a-b)), the majority of ML solutions are arrived at by using an initial guess close to the true wind direction. This characteristic indicates that the incorrect wind directions are merely local minima and that the four-fold search method successfully extracts the true ML estimates. The low ambiguity rate expected for case 1 is apparent in that the ML solutions are near the correct direction. The higher ambiguity percentage for case 2 is clearly evidenced by the cluster of ML solutions in several incorrect directions. For design case 3 (Figure 7.1(c)), the ML solutions are almost equally distributed between the four initial guesses. Many (but not a majority) of the ML solutions, however, indicate directions other than the true direction (i.e., ambiguous solutions), as expected for the one-look configuration.

The ML solutions from Figure 7.1 that indicate the wrong wind direction are called identified ambiguities. Many of the identified ambiguities displayed in Figure 7.1 were removed using the ambiguity removal procedure described in Section 6.4.2 and [27]. The procedure is as follows. An ML solution is said to be ambiguous if its direction lies outside a specified window. For an operational satellite algorithm, the width of the window could be based on the expected RMS retrieval accuracy. The center of the window would ideally be the true wind direction, however, in practice the true wind direction is not known. Operationally, the output of a median filter applied to the retrieved wind field could be

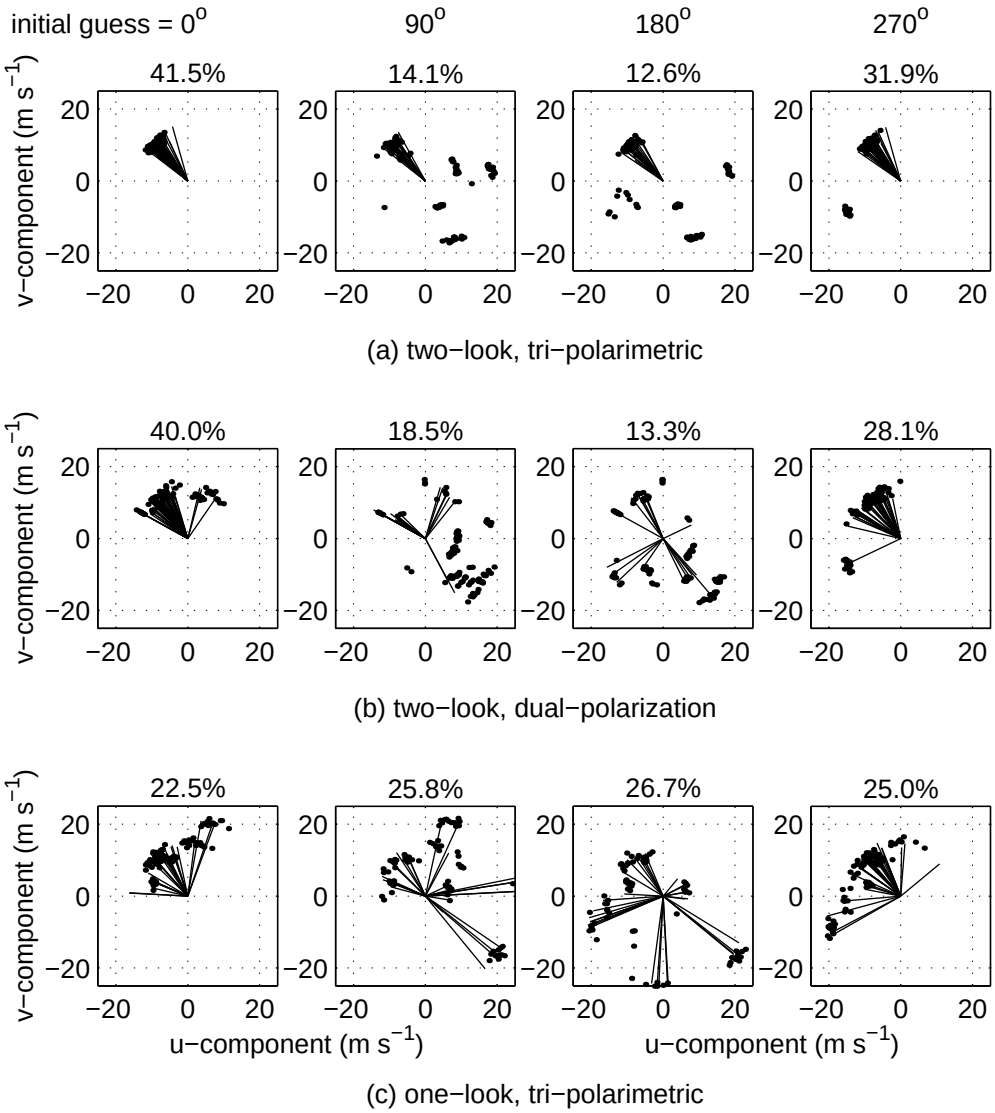

Figure 7.1: Results of the four-fold search for ML solutions before ambiguity removal for data set 1 (March 3, 1344-1423 UTC). The true ML solutions are plotted as lines and the local-minima solutions denoted by individual points. The ML solution is that solution chosen from among the four initial guesses with the smallest corresponding value of the objective function.

used. Provided that more than 50% of the retrieved wind directions are correct, the median filter would produce a reasonable estimate for the window center. Other sources of data for determining the window center include numerical weather prediction models and climatology. Using these sources, however, would bias the retrieval to mimic the model output. For these satellite simulations, the width of the acceptance window was set to $\pm 30°$ with respect to the true wind direction as measured by the *Knorr*. The final retrieved wind vectors after ambiguity removal are given in Figure 7.2 for the four initial guess directions. (The results for data sets 2-4 can be found in Appendix D.) The accepted ML solutions and chosen ambiguities are plotted as lines and the rejected solutions as points. Accepted ML solutions are those that fall within the 30° window about the true wind direction. For those ML solutions that fall outside the window, the local-minima solutions were tested to determine if any were within the acceptance window. Those local-minima solutions falling within the window are called chosen ambiguities. The final wind direction is then either an accepted ML solution or chosen ambiguity. The percentage of final wind directions for each initial guess is printed above each plot. Case 1 provided very few ambiguities, as evidenced by the similarity of Figure 7.2(a) and Figure 7.1(a). As seen in Figure 7.2(b-c), the ambiguity removal procedure, however, significantly improved the retrieval quality of design cases 2 and 3. In case 3 the majority of the retrieved directions were found from the initial guesses closest to the true wind direction only after ambiguity removal (see Figure 7.2(c) and Figure 7.1(c)). Note that there are several instances in Figure 7.1(c) where the retrieval algorithm and ambiguity removal procedure failed to arrive at the correct wind direction. Those retrievals that do not provide a valid ML solution nor an acceptable local-minima solution are cases of unresolved ambiguities. These unresolved ambiguities, or outliers, are obviously undesirable and the satellite design should be chosen accordingly.

Table 7.5 lists, for the four simulated data sets, the solution distribution over the four initial guesses and the ambiguity rates. The post ambiguity removal (PAR) distribution indicates the portion of the combined accepted ML solutions and resolved ambiguities arising from each of the four initial guess directions. The identified ambiguity rate is the

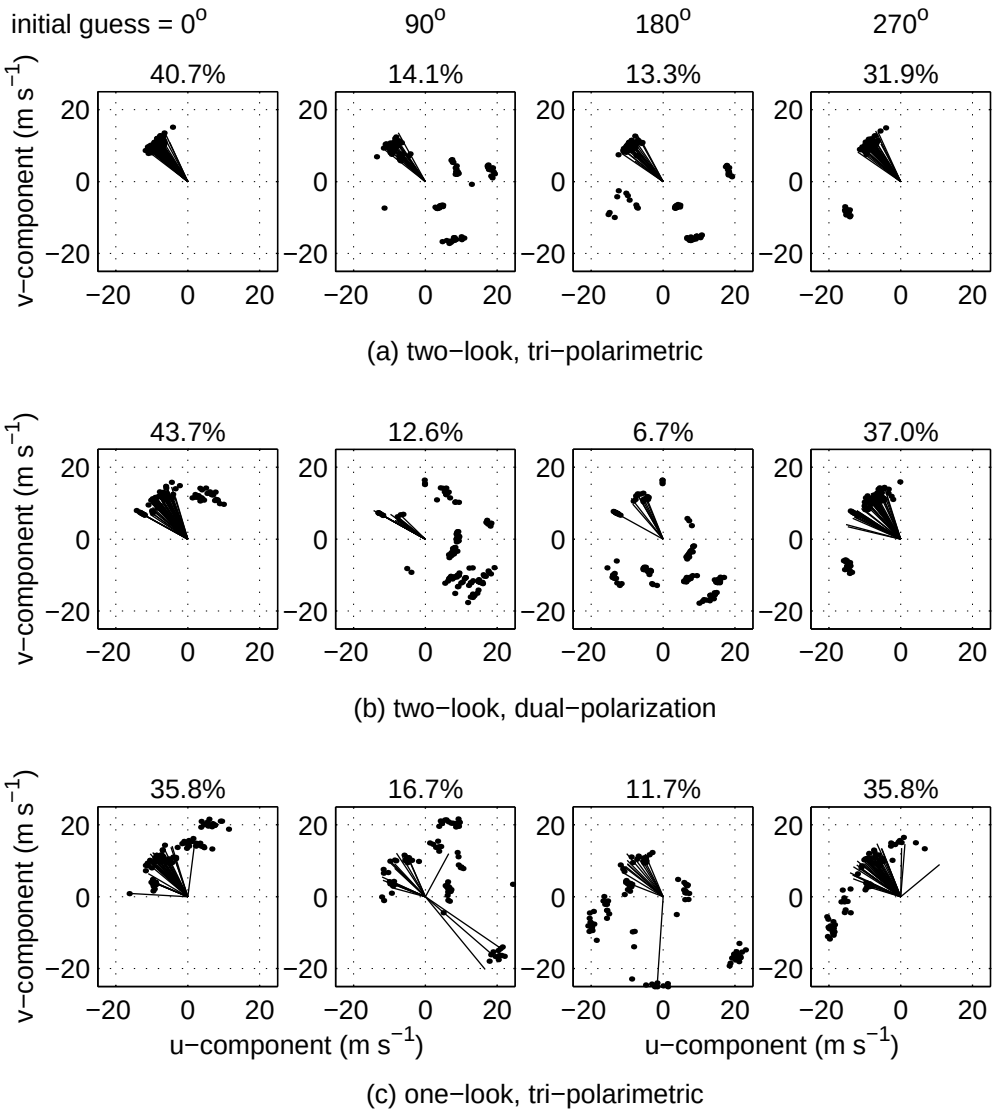

Figure 7.2: Four-fold search results after ambiguity selection. The accepted ML solutions and chosen ambiguities are plotted as lines and the rejected solutions as points.

Table 7.5: Retrieved direction distribution and ambiguity statistics of the four data sets. The two distributions listed are the strict ML solution distribution and the post-ambiguity removal (PAR) distribution. The PAR distribution indicates the portion of combined accepted ML solutions and resolved ambiguities arising from the four initial guess directions.

	Data Set		Initial Guess Direction 0° (%)	90° (%)	180° (%)	270° (%)	% Identified Ambiguities (%)	% Resolved Ambiguities (%)
Case 1: two-look, tri-pol.	1	ML	41.5	14.1	12.6	31.9	1.5	100
		PAR	40.7	14.1	13.3	31.9		
	2	ML	23.0	13.3	24.4	39.3	0	-
		PAR	”	”	”	”		
	3	ML	31.9	23.7	14.1	30.4	0	-
		PAR	”	”	”	”		
	4	ML	32.6	26.7	11.9	28.9	0	-
		PAR	”	”	”	”		
	average						0.4	100
Case 2: two-look, dual-pol.	1	ML	40.0	18.5	13.3	28.1	18.5	96.0
		PAR	43.7	12.6	6.7	37.0		
	2	ML	26.7	17.8	8.9	46.7	31.1	95.2
		PAR	23.0	0.0	12.6	64.4		
	3	ML	34.8	17.8	14.8	32.6	11.1	100
		PAR	42.2	17.8	9.6	30.4		
	4	ML	40.0	20.7	13.3	25.9	20.7	64.3
		PAR	44.4	17.8	8.1	29.6		
	average						20.4	88.9
Case 3: one-look, tri-pol.	1	ML	22.5	25.8	26.7	25.0	49.2	83.1
		PAR	35.8	16.7	11.7	35.8		
	2	ML	23.3	16.7	20.8	39.2	29.2	97.1
		PAR	17.5	6.7	17.5	58.3		
	3	ML	19.2	29.2	26.7	25.0	32.5	100
		PAR	37.5	23.3	16.7	22.5		
	4	ML	30.8	20.0	20.8	28.3	38.3	89.1
		PAR	50.8	13.3	9.2	26.7		
	average						37.3	92.3

ratio of rejected ML solutions (those falling outside the 30° acceptance window) to the total number of retrievals. The resolved ambiguity rate is the ratio of chosen ambiguities to the total number of rejected ML solutions. The two-look polarimeter (case 1) produces the fewest identified ambiguities; in fact, the only ambiguities retrieved for this case were in data set 1 and 100% of these were resolved. Because of the few number of ambiguities, the solution distribution over the four initial guesses remained relatively constant. The two-look dual-polarization system (case 2) performed reasonably well with a $\sim$10-30% identified ambiguity rate. Of those directions labeled as ambiguous typically $\gtrsim$95% were resolved, except for data set 4, in which only $\sim$66% were resolved. The unresolved ambiguities in data set 4 were $\sim$75° away from the true wind direction and could be the result of a systematic retrieval bias due to geophysical modeling error. The PAR distribution for case 2 shows an increase number of solutions arising from the initial guess directions close to the true wind direction. Even though the one-look polarimetric system (case 3) has a relatively high identified ambiguity rate of $\sim$30-50%, the removal procedure is on average capable of resolving 89% of the ambiguities, leaving only 11% uncorrected. Again, the PAR distribution indicates that initial guess directions close to the true wind direction produce most of the accepted solutions.

The final retrievals of data set 1 are displayed as scatter plots in Figure 7.3. (The results for data sets 2-4 can be found in Appendix D.) The final solutions (after ambiguity removal) are plotted as individual points and the unresolved ambiguities are plotted as x's. The arrow indicates the mean retrieved wind vector. The 1-, 2-, and 3-σ contours of a fitted Gaussian (ignoring unresolved ambiguities) are plotted for reference. The outcomes of all three cases have similar mean wind vectors. The retrieved wind vector distributions tend to cluster along a line or an arc of constant radius, indicating a relatively small wind speed variance but a larger wind direction variance. While the wind speed variances are similar for all three cases, the direction variance becomes progressively larger moving from case 1 to 3 (as indicated by the Gaussian contours). The error statistics of the final retrieval sets are presented in Table 7.6. Unresolved ambiguities were not included in the calculation of

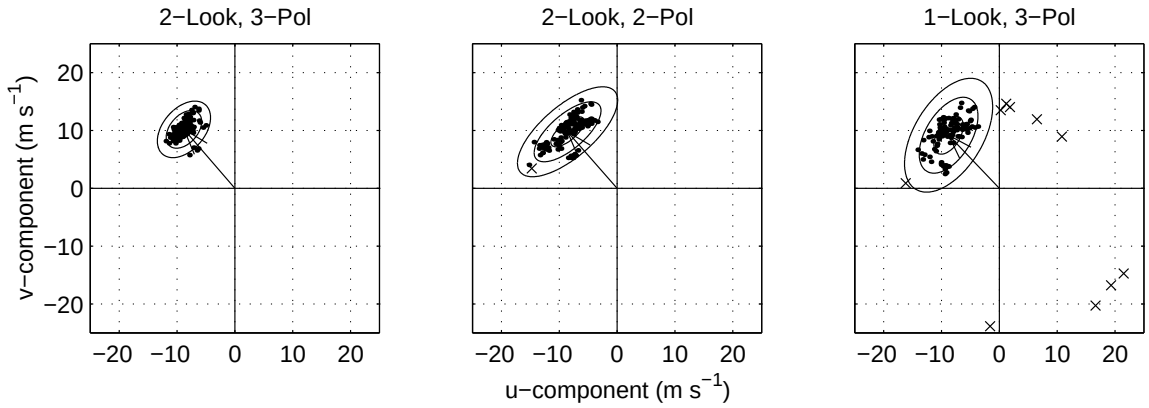

Figure 7.3: Scatter plots of final retrieved wind vectors for data set 1 (March 3, 1344-1423 UTC). The final solutions (after ambiguity removal) are plotted as individual points. The unresolved ambiguities are plotted as x's. The 1-, 2-, and 3-σ contours of a fitted Gaussian (ignoring unresolved ambiguities) are plotted for reference. The mean retrieved wind vector is plotted as an arrow.

Table 7.6: Retrieved wind vector statistics for the four data sets and 3 design cases.

	Data Set	$\langle\widehat{\phi}_w\rangle$ deg	$\langle\widehat{u}_{10}\rangle$ (m s^{-1})	Mean Error deg	Mean Error (m s^{-1})	RMS Error deg	RMS Error (m s^{-1})
Case 1: two-look, tri-pol.	1	319.2	(13.5)	5.2	(-0.1)	8.3	(1.0)
	2	267.3	(15.9)	-2.7	(-0.0)	7.7	(1.0)
	3	348.8	(12.0)	-2.2	(0.0)	8.5	(0.7)
	4	342.4	(13.9)	-2.6	(-0.1)	8.9	(0.6)
	mean	-	-	-	-	8.4	(0.8)
Case 2: two-look, dual-pol.	1	318.8	(13.0)	4.8	(-0.6)	14.7	(1.5)
	2	265.1	(15.8)	-4.9	(-0.1)	11.7	(1.0)
	3	350.2	(11.8)	-0.8	(-0.2)	9.3	(0.8)
	4	344.6	(13.6)	-0.4	(-0.4)	14.7	(0.8)
	mean	-	-	-	-	12.6	(1.0)
Case 3: one-look, tri-pol.	1	316.3	(12.7)	2.3	(-0.9)	14.7	(1.7)
	2	267.8	(15.4)	-2.2	(-0.6)	11.9	(1.7)
	3	347.5	(11.3)	-3.5	(-0.6)	14.5	(1.5)
	4	343.6	(13.7)	-1.4	(-0.3)	14.8	(1.3)
	mean	-	-	-	-	14.0	(1.6)

the retrieval statistics. As expected, case 1 is best in noise performance exhibiting average RMS error of 8.4° (0.8 m s^{-1}). Cases 2 and 3 are comparable in retrieval accuracy and have RMS errors of 12.6° (1.0 m s^{-1}) and 14.0° (1.6 m s^{-1}), respectively. The RMS wind speed accuracy for design cases 1 and 2 is $<$1 m s^{-1}, which is half of the $\sim$2 m s^{-1} accuracy achieved without directional information [28, 52, 66]. Indeed, wind speed accuracy of $<$1.7 m s^{-1} occurs in the cases with the worst RMS direction error, suggesting that knowledge of wind direction to $\pm$15° can significantly enhance the wind speed measurements made by radiometers. Note that the wind direction biases are consistent in sign across all cases. These small biases $\lesssim$5° could be caused by errors in the *Knorr* wind sensor and the P-3 navigation system. It is notable that the biases are negative, except for data set 1; however, the *Knorr* wind sensor was malfunctioning during data set 1 and the stated wind direction was estimated by the science crew. The consistency in the sign of the biases suggests the presence of a height dependence in the wind direction of $\sim$2° per 20 m (the *Knorr* wind sensor was $\sim$20 m above mean sea level). Such a dependence could be the result of either a local boundary layer gradient or possibly Eckman rotation [34]. Although provocative, these measurements are not comprehensive enough to make a statement as to the generality of a wind direction bias in remotely sensed measurements.

The previous simulations used a fixed radiometric sensitivity of $\Delta T_{RMS} = 0.25$ K. The actual value of ΔT_{RMS} significantly affects the RMS retrieval error. In order to study the relationship between RMS direction error and ΔT_{RMS} the two-look polarimeter design case was used for three combinations of different frequency channels: 1) 10.7, 18.7[1] and 37.0 GHz; 2) 10.7 and 18.7 GHz; and 3) 10.7 and 37.0 GHz. The radiometric sensitivities of the channels were simultaneously varied from 0 K to 2 K in 0.25 K increments. The results of data set 2 at a simulated heading of 90° with respect to wind direction and azimuth look angle pairs of (-45°, 135°), (0°, 180°), and (45°, 135°) are plotted in Figure 7.4. For all three channel sets, both the simulated standard deviations and the CR bound exhibit a sensing threshold of $\Delta T_{RMS} \sim 1.1$ K. That is, the wind direction standard deviation

[1]K-band T_U looks were generated by averaging the 10.7 and 37.0 GHz data.

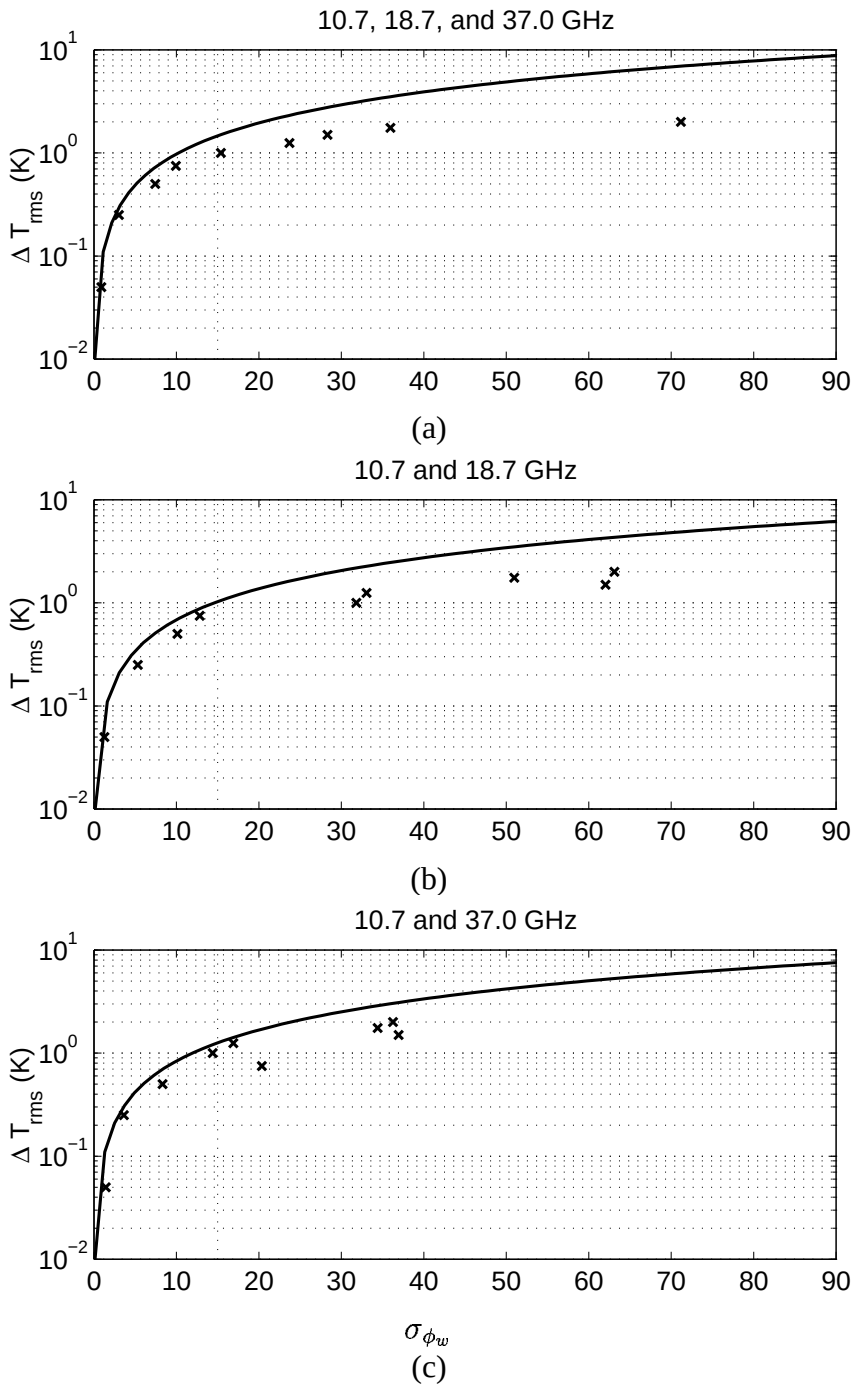

Figure 7.4: Sensitivity of retrieved wind direction to ΔT_{RMS}. These results are for data set 2 at a simulated heading of 90° with respect to wind direction and azimuth look angle pairs of (-45°, 135°), (0°, 180°), and (45°, 135°). The three channel combinations are (a) 10.7, 18.7 and 37.0 GHz; (b) 10.7 and 18.7 GHz; and (c) 10.7 and 37.0 GHz. The retrieval standard deviations are plotted as x's and the CR bound on the direction standard deviation is plotted as a solid line for comparison.

rapidly increases for radiometer noise levels beyond this threshold. The threshold effect is analogous to the detection threshold in FM or phase demodulation [62]. For values of $\Delta T_{RMS} \lesssim 0.7$ K, the retrieval standard deviation is close the CR bound. The retrieval requires a maximum allowable ΔT_{RMS} of $\sim$1 K in order that the direction standard deviation remain $< 15°$. The channel sets with the 37.0 GHz band performed better than the other set because of the large amplitude of the 37.0 GHz azimuthal harmonics. Under conditions of high atmospheric loss (e.g., convection), however, the importance of the 37.0 GHz band is expected to diminish, whereas the 10.7 GHz band is expected to be relatively unaffected. Comparing Figures 7.4(a) and 7.4(c), the utility of the 18.7 GHz channels is relatively small, increasing the required ΔT_{RMS} for a CR error bound of 15° from $\sim$1.2 K (c) to $\sim$1.3 K (a). Thus, the satellite designer must consider carefully the value-added cost and complexity of an additional polarimeter at 18.7 GHz.

In summary, the simulated retrievals support the hypotheses stated in Table 7.1. Average rankings of the three design cases over the four data sets are as follows (from best to worst):

- Identified ambiguity rate: Case 1 (0.4%), Case 2 (20.4%), Case 3 (37.3%)
- Resolved ambiguity rate: Case 1 (100%), Case 3 (92.3%), Case 2 (88.9%)
- RMS wind direction error: Case 1 (8.4°), Case 2 (12.6°), Case 3 (14.0°)
- RMS wind speed error: Case 1 (0.8m s^{-1}), Case 2 (1.0 m s^{-1}), Case 3 (1.6 m s^{-1})

It should be noted that the above RMS error results might be optimistic for the two-look dual-polarization radiometer (case 2) because the simulations did not include the effect of significant geophysical modeling errors caused by clouds and convection. Depending upon the operational requirements, the one-look polarimeter might be acceptable; however, the two-look polarimetric configuration surpasses the performance of the other designs.

CHAPTER 8

Conclusions

A system for high-resolution mapping of ocean surface wind vectors using passive microwave polarimetry was presented in this thesis. As a central component of this system, the PSR was the first technology demonstration of a digital correlation polarimeter. A novel unpolarized two-look calibration method was developed and successfully applied to the PSR Labrador Sea flight data. Observations using the PSR onboard the NASA P3-B research aircraft resulted in the first two-dimensional surface wind fields retrieved from multiband polarimetric microwave imagery of ocean surface emission. The retrievals were based on an empirical GMF derived from averaged brightness variations obtained at wind speeds from 0.4 to 16 $\mathrm{m\,s^{-1}}$. The GMF agrees well with two independent investigations of brightness variations as observed from satellites. The retrieval results compared well with dropsonde measurements and Eta model output. Comparison of the retrieval statistics to its CR bound reveal the capabilities and limitations of the ML/ACW algorithm for retrieving wind directions from two-look observations over homogeneous clouds and convective regions. Simulated satellite retrievals were conducted to study the performance of three spaceborne radiometer/polarimeter configurations. Based on quantitative results, the two-look polarimeter was concluded to be the best design choice. The conclusions drawn from this work will advance techniques in passive microwave polarimetry for remote sensing of ocean winds.

8.1 Summary of Thesis

The digital correlation polarimeter was developed in Chapter 2 and the associated hardware and calibration were presented in Chapters 3 and 4. The polarimeter used a high-speed digital correlator to perform the correlations necessary to measure the third Stokes parameter. The relationships between the signal input statistics and the correlator outputs were derived and used to compute the associated radiometric sensitivities. In practice, the actual ΔT_{RMS} values were $\sim$2 times the fundamental limit. Systematic errors due to system nonidealities and their mitigation through design and calibration were also discussed. A novel calibration technique for the third Stokes parameter channel that uses the hot and ambient loads was presented and applied to the PSR flight data. A fully polarimetric calibration standard was utilized to verify the effectiveness of the technique and the absolute calibration of the U-channel was found to be ~ 0.4 K.

The digital polarimeter is a viable alternative to analog systems that require comprehensive in-situ calibration. Although the gains of the PSR correlators were nonideal and less than unity, the potential causes and their relative importance were identified in the analyses of Chapter 2. The ability to compensate for the correlation offsets without the use of a polarized calibration standard is an extremely desirable feature for space applications. The use of digital correlation in space becomes more practical with time as digital integrated circuit sizes decrease and speeds increase.

The PSR was used to obtain the first multiband polarimetric imagery of ocean surface emission during the Labrador Sea experiment. As described in Chapter 3, the imagery contains both the subtle, yet systematic, wind direction signature as well as brightness inhomogeneities. The inhomogeneities are present in T_v and T_h imagery and are typically a few km in size and a few Kelvin is amplitude. The T_U imagery is quite systematic, lacking the inhomogeneous characteristic. The observed brightness variations are hypothesized to arise from both surface roughness and cloud liquid water variations.

Using Labrador Sea measurements, an empirical GMF for brightness temperature over the ocean was described in Chapter 5. The model contains both the azimuthal wind

direction harmonics and the azimuthally-averaged zeroeth-order components. The first- and second-order harmonic amplitude coefficients of the wind direction harmonics were measured at wind speeds from 0.4 through 16 $\mathrm{m\,s^{-1}}$. The T_v and T_h results are comparable to those obtained using the SSM/I satellite radiometer [66], thus corroborating both measurement techniques. The T_U results are somewhat comparable to recently published fixed-beam radiometer aircraft observations [69]. The differences between the satellite and aircraft measurements of the first three Stokes parameters suggest that additional processes beyond surface wind speed have an influence upon the brightness temperature harmonic amplitudes. While the wind speed is fairly well correlated to the harmonic amplitudes, processes that drive the ocean wave spectral development such as fetch and boundary layer instability might be contributing factors to the environmental dependence of the azimuthal signatures. Nonetheless, the GMF's consistency with the other observations and its fairly high correlation with wind speed is sufficient for meaningful wind direction retrievals in Chapter 6.

The first use of conically-scanned microwave polarimetric imagery of the ocean surface at 10.7, 18.7, and 37.0 GHz to generate high-resolution near-surface wind vector maps was demonstrated in Chapter 6. While a variety of *ad hoc* wind vector retrieval methods could be used, the ML/ACW estimator has two distinct and desirable characteristics: (1) the ability to adaptively modify the channel weights based on the observed process variation and (2) the availability of an analytic CR bound. The ML/ACW algorithm was applied to fore- and aft-look PSR imagery in both full-conical and two-look modes to generate the first one- and two-dimensional passive microwave wind vector maps, respectively. Comparisons of the retrieved wind vector maps with dropsonde measurements and Eta model output suggest that using the ML/ACW technique applied to 10.7, 18.7, and 37.0 GHz full-conical polarimetric scans can provide RMS errors of $\pm 10^\circ$ over footprints covering an area of as little as $\sim$50-100 km^2. The retrieval error using the two-look ML/ACW technique is only slightly worse, but considerably more sensitive to local inhomogeneity in the upwelling brightness field. The two-dimensional retrieval for the case of March 7 shows

particularly high variability near a region of major wind shift, an effect possibly resulting from the confused nature of the sea surface. The two-look retrieval achieved a 90% skill in retrieving the non-ambiguous wind direction.

A byproduct of the ACW technique is an estimate of geophysical modeling error variance. This error estimate can be used to study the relative informational content of the various channels, and clearly reveals the utility of the third Stokes parameter over convection. The algorithm weighted all channels nearly equally over the homogeneous regions of the flight track. In the vicinity of the large brightness features near the wind shift, however, the relative weight of the 37.0 GHz T_U channel was increased by over an order of magnitude, and less so for the 10.7 GHz T_U channel. The smaller increase of the 10.7 GHz channel was expected because losses due to clouds and the atmosphere are less at the lower frequency than at 37.0 GHz. The smaller increase of this channel's weight over its companion T_v and T_h channels also suggests that an X-band polarimeter is useful for probing the surface under cloudy and convective conditions that would otherwise obscure the surface at Ka-band.

Simulated satellite retrievals were conducted to study the performance of three spaceborne radiometer/polarimeter configurations: (1) tri-polarimetric two-look, (2) dual-polarization two-look, and (3) tri-polarimetric one-look systems. The identified ambiguity rate and the RMS direction error were used as quantitative performance measures to judge each system. Based on these quantitative results, the two-look polarimeter was concluded to be the best design choice. Sensitivity studies suggest that the ML/ACW algorithm applied to two-look polarimetric data approaches the CR bound to within a few degrees. Coupled with the retrieval results of Chapter 6, the simulations suggest that such a spaceborne sensor should be able to remotely sense ocean surface winds with an RMS error of $\sim$ 10-20° with fewer than $\sim$10% ambiguities.

8.2 Suggestions for Future Research

This thesis has concentrated on developing technology and techniques for the remote sensing of ocean surface winds by passive microwave polarimetry. However, the system and algorithms presented here are expected to benefit further investigations and advancements in three areas: 1) technology development for a space-qualified digital correlation polarimeter, 2) better understanding of unmodeled geophysical processes that influence the passive wind direction signature, and 3) the development of an operational passive microwave wind vector retrieval algorithm.

The operation of the PSR indicates that accurate and relatively low noise measurements of the third Stokes parameter can indeed be made by digital correlation polarimeters. Efforts needed for further development of a space-qualified digital correlator include (1) low-power and high-speed digital circuits, (2) high-speed, low-noise and precision three-level A/D converters, and (3) integration of the RF, IF, and digital subsystems into a mixed-signal IC or multi-chip module (MCM). Much of this technology is available and is used in commercial and consumer products such as (1) single chip superheterodyne receivers for cellular phones, (2) high-speed A/D converters for wideband digital communications, and (3) high-density mixed packaging of digital and analog components (for example in alphanumeric pagers). The greatest challenge is the qualification of these technologies for space applications. With the growth of satellite based cellular systems, however, space qualified components used for digital communications are expected to become ubiquitous. This investment by the telecommunications industry should be leveraged for the development of satellite based sensors.

The differences of the PSR GMF and satellite measurements indicate that geophysical processes other than just wind speed are affecting the passive wind direction signature. Additional aircraft measurements are needed to study this problem. The experiments should target the effects of at least the following parameters:

- Fetch: Overflights of buoys at varying distances from the shore can provide obser-

vations of varying fetch. One of the important effects of fetch is the evolution of longwaves from nonlinear interaction between shorter waves [43]. Spectral information about the ocean longwaves can be obtained from NDBC buoys and the ROWS radar [63].

- Stability: Overflights of buoys under stable and unstable atmospheric conditions can provide observations useful for determining the effect on the azimuthal brightness signature. Coincident measurements by dropsondes will be useful for determining the boundary layer temperature and humidity profile.

A concerted effort should be made to choose sites at which the conditions are essentially steady-state. For example, an abrupt temporal change in wind direction (perhaps due to a frontal passage) is not desirable because the longwave spectrum could be bi-modal, and thus the effects of longwave amplitude might not be clearly discernible. The flights should also be planned to decouple the parameters under study as much as possible.

The retrieval algorithm presented has the two desirable features of (i) adaptive channel weights technique and (ii) a closed-form Cramer-Rao error bound. The technique, however, operates on single pixels or wind cells, which are inherently coupled by fluid dynamics. Linear and nonlinear techniques along with coupled ocean-atmospheric numerical weather models could be used to exploit the correlations between adjacent cells as governed by the natural variability of near surface divergence and vorticity fields.

APPENDIX A

Correlation Coefficient Inversion

The digital correlation coefficient can be computed by the following:

$$r_{ab} = \sigma_{v_a}\sigma_{v_b}\int_0^{\rho} f(\sigma_{v_a}\theta_a, \sigma_{v_b}\theta_b; \rho') + f(\sigma_{v_a}\theta_a, -\sigma_{v_b}\theta_b; \rho') + f(-\sigma_{v_a}\theta_a, \sigma_{v_b}\theta_b; \rho') + f(-\sigma_{v_a}\theta_a, -\sigma_{v_b}\theta_b; \rho')\ d\rho' \quad \text{(A.1)}$$

Symmetry of the Gaussian probability density function allows us to write:

$$r_{ab} = 2\sigma_{v_a}\sigma_{v_b}\int_0^{\rho} f(\sigma_{v_a}\theta_a, \sigma_{v_b}\theta_b; \rho') + f(\sigma_{v_a}\theta_a, -\sigma_{v_b}\theta_b; \rho')\ d\rho' \quad \text{(A.2)}$$

The function $\sigma_{v_a}\sigma_{v_b} f(\sigma_{v_a}\theta_a, \sigma_{v_b}\theta_b; \rho)$ is recognized as the bivariate normal pdf [1, (26.3.1)]:

$$p(\theta_a, \theta_b; \rho) = \frac{1}{2\pi\sqrt{1-\rho^2}} \exp\left[-\frac{\theta_a^2 - 2\rho\theta_a\theta_b + \theta_b^2}{2\left(1-\rho^2\right)}\right] \quad \text{(A.3)}$$

Rewriting the expression for r_{ab} using the bivariate normal pdf yields:

$$r_{ab} = 2\int_0^{\rho} p(\theta_a, \theta_b; \rho') + p(\theta_a, -\theta_b; \rho')\ d\rho' \quad \text{(A.4)}$$

The task at hand is to expand the integrand in a Taylor series and then integrate. The integrand of the above is

$$I\left(\rho'\right) = 2p(\theta_a, \theta_b; \rho') + 2p(\theta_a, -\theta_b; \rho') \quad \text{(A.5)}$$

This can be expanded in a Taylor series in terms of ρ':

$$I\left(\rho'\right) = I\left(0\right) + I^{(1)}\left(0\right)\rho' + \frac{1}{2!}I^{(2)}\left(0\right)\rho'^2 + \frac{1}{3!}I^{(3)}\left(0\right)\rho'^3 + \frac{1}{4!}I^{(4)}\left(0\right)\rho'^4 + ... \quad \text{(A.6)}$$

The algebra involving the derivatives is quite cumbersome and the computer algebra package *MapleV* was used to evaluate the derivatives. These derivatives are

$$\left.\frac{\partial}{\partial\rho}p(\theta_a,\theta_b,\rho)\right|_{\rho=0} = p(\theta_a,\theta_b,0)\theta_a\theta_b \tag{A.7}$$

$$\left.\frac{\partial^2}{\partial\rho^2}p(\theta_a,\theta_b,\rho)\right|_{\rho=0} = p(\theta_a,\theta_b,0)\left(\theta_a^2-1\right)\left(\theta_b^2-1\right) \tag{A.8}$$

$$\left.\frac{\partial^3}{\partial\rho^3}p(\theta_a,\theta_b,\rho)\right|_{\rho=0} = p(\theta_a,\theta_b,0)\left(3\theta_a-\theta_a^3\right)\left(3\theta_b-\theta_b^3\right) \tag{A.9}$$

$$\left.\frac{\partial^4}{\partial\rho^4}p(\theta_a,\theta_b,\rho)\right|_{\rho=0} = p(\theta_a,\theta_b,0)\left(3-6\theta_a^2+\theta_a^4\right)\left(3-6\theta_b^2+\theta_b^4\right) \tag{A.10}$$

The derivatives of $p(\theta_a,-\theta_b,\rho)$ are easily found by substituting $-\theta_b$ for θ_b in the above. Because the first and third derivatives are odd functions of θ_a and θ_b, it is immediately seen that the Taylor series terms with odd powers of ρ will cancel leaving only the even powers of ρ. Adding the appropriate derivatives yields the following for the integrand:

$$\begin{aligned} I\left(\rho'\right) = 4p(\theta_a,\theta_b,0)\Bigg[1+\frac{1}{2}\left(\theta_a^2-1\right)\left(\theta_b^2-1\right)\rho'^2 \\ +\frac{1}{24}\left(3-6\theta_a^2+\theta_a^4\right)\left(3-6\theta_b^2+\theta_b^4\right)\rho'^4\Bigg]+O\left(\rho'^6\right) \end{aligned} \tag{A.11}$$

Finally, integrating the above yields:

$$\begin{aligned} r_{ab} = \frac{2}{\pi}\exp\left[-\frac{1}{2}\left(\theta_a^2+\theta_b^2\right)\right]\times\Bigg[\rho+\frac{1}{6}\left(\theta_a^2-1\right)\left(\theta_b^2-1\right)\rho^3+ \\ \frac{1}{120}\left(3-6\theta_a^2+\theta_a^4\right)\left(3-6\theta_b^2+\theta_b^4\right)\rho^5\Bigg]+O\left(\rho^7\right) \end{aligned} \tag{A.12}$$

APPENDIX B

Digital Radiometer Sensitivity

This appendix contains a derivation of the sensitivities of both the cross- and autocorrelating channels of the digital polarimeter. These sensitivities are assumed to be optimized with respect to the A/D converter threshold level.

B.1 Cross-correlator Sensitivity

The sensitivity of the third Stokes parameter cross-correlating channel is

$$\Delta T_{U,RMS} = \frac{\sigma_{\hat{r}_{ab}}}{\partial r_{ab}/\partial T_U} \tag{B.1}$$

Using the chain rule, the derivative in the denominator is expanded:

$$\frac{\partial r_{ab}}{\partial T_U} = \frac{\partial r_{ab}}{\partial \rho}\frac{\partial \rho}{\partial T_U} \tag{B.2}$$

The derivative $\partial r_{ab}/\partial \rho$ evaluated for small ρ can be computed using (2.16) and (2.17):

$$\begin{aligned}\lim_{\rho\to 0}\frac{\partial r}{\partial \rho} &= \lim_{\rho\to 0}\sigma_{v_a}\sigma_{v_b}\left[f(\sigma_{v_a}\theta_a,\sigma_{v_b}\theta_b;\rho)+f(-\sigma_{v_a}\theta_a,\sigma_{v_b}\theta_b;\rho)+\right.\\ &\qquad\left. f(\sigma_{v_a}\theta_a,-\sigma_{v_b}\theta_b;\rho)+f(-\sigma_{v_a}\theta_a,-\sigma_{v_b}\theta_b;\rho)\right] \qquad \text{(B.3)}\\ &= \lim_{\rho\to 0}2\sigma_{v_a}\sigma_{v_b}\left[f(\sigma_{v_a}\theta_a,\sigma_{v_b}\theta_b;\rho)+f(-\sigma_{v_a}\theta_a,\sigma_{v_b}\theta_b;\rho)\right]\end{aligned}$$

For the typical correlator, the channels are assumed to be balanced (i.e., $\sigma_{v_a} = \sigma_{v_b} = \sigma$) and the threshold levels for both of the input A/D converters are assumed to be equal (i.e.,

$\theta_a = \theta_b = \theta$). Simplifying the above:

$$\begin{aligned}\lim_{\rho\to 0}\frac{\partial r}{\partial \rho} &= \lim_{\rho\to 0} 2\sigma^2\left[f(\sigma\theta,\sigma\theta;\rho)+f(-\sigma\theta,\sigma\theta;\rho)\right]\\ &= 2\sigma^2\left[f(\sigma\theta,\sigma\theta;0)+f(-\sigma\theta,\sigma\theta;0)\right]\\ &= 4\sigma^2 f(\sigma\theta,\sigma\theta;0)\end{aligned} \tag{B.4}$$

The remaining derivative is obtained from (2.5):

$$\frac{\partial \rho}{\partial T_U} = \frac{1}{2\sqrt{T_{v,sys}T_{h,sys}}} \tag{B.5}$$

In the numerator of (B.1), the standard deviation of $\widehat{r}_{ab}$ is found by definition:

$$\sigma_{\widehat{r}_{ab}} = \sqrt{\langle \widehat{r}_{ab}^2\rangle - \langle \widehat{r}_{ab}\rangle^2} \tag{B.6}$$

Under the limiting case of $\rho \to 0$, the expected value of the digital covariance is zero:

$$\lim_{\rho\to 0}\langle \widehat{r}_{ab}\rangle = 0. \tag{B.7}$$

The standard deviation now is

$$\lim_{\rho\to 0}\sigma_{\widehat{r}_{ab}} = \lim_{\rho\to 0}\sqrt{\langle \widehat{r}_{ab}^2\rangle}. \tag{B.8}$$

Expanding the quantity $\langle \widehat{r}_{ab}^2\rangle$ results in:

$$\begin{aligned}\lim_{\rho\to 0}\langle \widehat{r}_{ab}^2\rangle &= \lim_{\rho\to 0}\left\langle \left[\frac{1}{N}\sum_{n=1}^{N} h(v_a(nT))h(v_b(nT))\right]\left[\frac{1}{N}\sum_{m=1}^{N} h(v_a(mT))h(v_b(mT))\right]\right\rangle\\ &= \lim_{\rho\to 0}\left\langle \frac{1}{N^2}\sum_{n=1}^{N}\sum_{m=1}^{N} h(v_a(nT))\cdot h(v_b(nT))\cdot h(v_a(mT))\cdot h(v_b(mT))\right\rangle\\ &= \lim_{\rho\to 0}\frac{1}{N^2}\sum_{n=1}^{N}\sum_{m=1}^{N}\langle h(v_a(nT))\cdot h(v_b(nT))\cdot h(v_a(mT))\cdot h(v_b(mT))\rangle\end{aligned} \tag{B.9}$$

Evaluating the limit allows the expected value within the double sum to be separated into two parts because v_a and v_b are statistically independent when $\rho \to 0$:

$$\lim_{\rho\to 0}\langle \widehat{r}_{ab}^2\rangle = \frac{1}{N^2}\sum_{n=1}^{N}\sum_{m=1}^{N}\langle h(v_a(nT))h(v_a(mT))\rangle\langle h(v_b(nT))h(v_b(mT))\rangle \tag{B.10}$$

Furthermore, because the samples are independent and identically distributed, all non-zero lag products are zero; $\langle h(v_a(nT))h(v_a(mT))\rangle = 0$ for $n \neq m$. The above double summation becomes

$$\begin{aligned}\lim_{\rho\to 0}\langle \widehat{r}_{ab}^2\rangle &= \frac{1}{N^2}\sum_{n=1}^{N}\left\langle h^2(v_a(nT))\right\rangle\left\langle h^2(v_b(nT))\right\rangle \\ &= \frac{1}{N}\langle h^2(v_a)\rangle\langle h^2(v_b)\rangle \\ &= \frac{1}{N}\langle \widehat{s}_a^2\rangle\langle \widehat{s}_b^2\rangle.\end{aligned} \tag{B.11}$$

Finally, by combining the previous results, the radiometric sensitivity is found:

$$\lim_{\rho\to 0}\Delta T_{U,RMS} = \frac{\sqrt{\langle \widehat{s}_a^2\rangle\langle \widehat{s}_b^2\rangle T_{v,sys}T_{h,sys}}}{2\sigma^2 f(\sigma\theta,\sigma\theta;0)\sqrt{N}} \tag{B.12}$$

The above expression can be written in terms of θ by substituting in (2.8) and (2.12):

$$\lim_{\rho\to 0}\Delta T_{U,RMS} = \frac{2\pi e^{\theta^2}}{\sqrt{N}}\left[1-\Phi(\theta)\right]\sqrt{T_{v,sys}T_{h,sys}} \tag{B.13}$$

Computing the value of θ for the minimum $\Delta T_{U,RMS}$ can be done using Newton's method. The optimal θ is 0.61 with

$$\Delta T_{U,RMS} = \frac{2.47}{\sqrt{N}}\sqrt{T_{v,sys}T_{h,sys}} \tag{B.14}$$

Compare this to the continuous correlator

$$\Delta T_{U,RMS} = \frac{2}{\sqrt{N}}\sqrt{T_{v,sys}T_{h,sys}} \tag{B.15}$$

B.2 Total-power Sensitivity

The sensitivity of the total-power channel is found similarly:

$$\Delta T_{\alpha,RMS} = \frac{\sqrt{\langle(\widehat{s}_\alpha^2)^2\rangle - \langle \widehat{s}_\alpha^2\rangle^2}}{\partial\langle \widehat{s}_\alpha^2\rangle/\partial T_{ANT,\alpha}} \tag{B.16}$$

Once again, the denominator is expanded using the chain rule:

$$\frac{\partial\langle \widehat{s}_\alpha^2\rangle}{\partial T_{ANT,\alpha}} = \frac{\partial\langle \widehat{s}_\alpha^2\rangle}{\partial(\sigma_{v_\alpha}^2)}\frac{\partial(\sigma_{v_\alpha}^2)}{\partial T_{ANT,\alpha}} \tag{B.17}$$

The first term in the product is the differential relationship between the input voltage variance and the output of the total-power channel of the digital correlator. From (2.12),

$$\begin{aligned}\frac{\partial\langle\widehat{s}_\alpha^2\rangle}{\partial(\sigma_{v_\alpha}^2)} &= 2\frac{\partial}{\partial(\sigma_{v_\alpha}^2)}\left[1-\Phi\left(\frac{v_{th,\alpha}}{\sqrt{\sigma_{v_\alpha}^2}}\right)\right] \\ &= \frac{v_{th,\alpha}}{\sigma_{v_\alpha}^3\sqrt{2\pi}}\exp\left[-\frac{1}{2}\left(\frac{v_{th,\alpha}}{\sigma_{v_\alpha}}\right)^2\right]\end{aligned} \tag{B.18}$$

Recalling (2.15), the variance of the input voltage signal is

$$\sigma_{v_\alpha}^2 = R_0 kBG_\alpha(T_{ANT,\alpha}+T_{REC,\alpha}) \tag{B.19}$$

so that

$$\frac{\partial(\sigma_{v_\alpha}^2)}{\partial T_{ANT,\alpha}} = \frac{\sigma_{v_\alpha}^2}{T_{\alpha,sys}} \tag{B.20}$$

where $T_{\alpha,sys} = T_{REC,\alpha}+T_{ANT,\alpha}$. Combining the two derivatives yields

$$\begin{aligned}\frac{\partial\langle\widehat{s}_\alpha^2\rangle}{\partial T_{ANT,\alpha}} &= \frac{1}{T_{sys,\alpha}\sqrt{2\pi}}\left(\frac{v_{th,\alpha}}{\sigma_{v_\alpha}}\right)\exp\left[-\frac{1}{2}\left(\frac{v_{th,\alpha}}{\sigma_{v_\alpha}}\right)^2\right] \\ &= \frac{1}{T_{sys,\alpha}\sqrt{2\pi}}\theta_\alpha e^{-\frac{1}{2}\theta_\alpha^2}.\end{aligned} \tag{B.21}$$

In the numerator of (B.21), the standard deviation of $\widehat{s}_\alpha^2$ is found by definition:

$$\sqrt{\langle(\widehat{s}_\alpha^2)^2\rangle - \langle\widehat{s}_\alpha^2\rangle^2} \tag{B.22}$$

This is computed by first expanding the expected value of $(\widehat{s}_\alpha^2)^2$:

$$\begin{aligned}\langle(\widehat{s}_\alpha^2)^2\rangle &= \left\langle\left[\frac{1}{N}\sum_{n=1}^{N}h^2(v_\alpha(nT))\right]\left[\frac{1}{N}\sum_{m=1}^{N}h^2(v_\alpha(mT))\right]\right\rangle \\ &= \left\langle\frac{1}{N^2}\sum_{n=1}^{N}\sum_{m=1}^{N}h^2(v_\alpha(nT))h^2(v_\alpha(mT))\right\rangle \\ &= \frac{1}{N^2}\sum_{n=1}^{N}\sum_{m=1}^{N}\left\langle h^2(v_\alpha(nT))h^2(v_\alpha(mT))\right\rangle\end{aligned} \tag{B.23}$$

Because the samples of v_α are independent and identically distributed, the above expected value can be written:

$$\left\langle h^2(v_\alpha(nT))h^2(v_\alpha(mT))\right\rangle = \begin{cases} \langle h^2(v_\alpha(nT))\rangle \langle h^2(v_\alpha(mT))\rangle & \text{for } n \neq m \\ \langle h^4(v_\alpha(nT))\rangle & \text{for } n = m \end{cases} \tag{B.24}$$

Conveniently, by the definition of $h(v)$, $h^4(v) = h^2(v)$. Substituting these two cases into the double summation yields

$$\begin{aligned} \langle(\widehat{s}_\alpha^2)^2\rangle &= \frac{1}{N^2}\sum_{n=1}^{N}\left\langle h^2(v_\alpha(nT))\right\rangle + \frac{1}{N^2}\sum_{\substack{n=1\\n\neq m}}^{N}\sum_{m=1}^{N}\left\langle h^2(v_\alpha(nT))\right\rangle\left\langle h^2(v_\alpha(mT))\right\rangle \\ &= \frac{1}{N}\langle\widehat{s}_\alpha^2\rangle + \left(1-\frac{1}{N}\right)\langle\widehat{s}_\alpha^2\rangle^2 \end{aligned} \tag{B.25}$$

The variance of $\widehat{s}_\alpha^2$ is

$$\begin{aligned} \sqrt{\langle(\widehat{s}_\alpha^2)^2\rangle - \langle\widehat{s}_\alpha^2\rangle^2} &= \sqrt{\frac{1}{N}\langle\widehat{s}_\alpha^2\rangle + \left(1-\frac{1}{N}\right)\langle\widehat{s}_\alpha^2\rangle^2 - \langle\widehat{s}_\alpha^2\rangle^2} \\ &= \sqrt{\frac{1}{N}\langle\widehat{s}_\alpha^2\rangle\left(1-\langle\widehat{s}_\alpha^2\rangle\right)} \\ &= \sqrt{\frac{1}{N}\left[1-\Phi\left(\theta_\alpha\right)\right]\Phi\left(\theta_\alpha\right)} \end{aligned} \tag{B.26}$$

Forming the quotient (B.16) with the variance (B.26) and the derivative (B.21) produces

$$\Delta T_{\alpha,RMS} = \frac{\sqrt{2\pi}}{\theta_\alpha}e^{\frac{1}{2}\theta_\alpha^2}\sqrt{\Phi\left(\theta_\alpha\right)-\Phi^2\left(\theta_\alpha\right)}\frac{T_{sys,\alpha}}{\sqrt{N}}. \tag{B.27}$$

The optimum value of θ_α for best total-power radiometer sensitivity is found by minimizing $\Delta T_{\alpha,RMS}$ with respect to θ_α. Again, this can be done numerically. The sensitivity is minimized at $\theta_\alpha = 1.58$ such that

$$\Delta T_{\alpha,RMS} = 1.28\frac{T_{sys,\alpha}}{\sqrt{N}} \tag{B.28}$$

For operation of the polarization correlating radiometer, however, the value of θ_α is set to minimize the noise of the T_U measurement. At the optimal point for T_U where $\theta_\alpha = 0.61$, the sensitivity of the total-power channel is

$$\Delta T_{\alpha,RMS} = 2.20\frac{T_{sys,\alpha}}{\sqrt{N}} \tag{B.29}$$

APPENDIX C

Threshold Offset Effects

Perturbations in the threshold voltages will change the output of the digital correlator. With asymmetric threshold levels, the digital correlation coefficient can be computed by the following:

$$r_{ab} = r_{ab}|_{\rho=0} + \sigma_{v_a}\sigma_{v_b}\int_0^{\rho} f(\sigma_{v_a}(\theta_a+\delta_a),\sigma_{v_b}(\theta_b+\delta_b),\rho') + f(\sigma_{v_a}(\theta_a+\delta_a),\sigma_{v_b}(-\theta_b+\delta_b),\rho') + f(\sigma_{v_a}(-\theta_a+\delta_a),\sigma_{v_b}(\theta_b+\delta_b),\rho') + f(\sigma_{v_a}(-\theta_a+\delta_a),\sigma_{v_b}(-\theta_b+\delta_b),\rho')d\rho'. \quad \text{(C.1)}$$

Using the definition for the bivariate normal pdf (A.3), the above becomes

$$r_{ab} = r_{ab}|_{\rho=0} + \int_0^{\rho} p(\theta_a+\delta_a,\theta_b+\delta_b,\rho') + p(\theta_a+\delta_a,-\theta_b+\delta_b,\rho') + p(-\theta_a+\delta_a,\theta_b+\delta_b,\rho') + p(-\theta_a+\delta_a,-\theta_b+\delta_b,\rho')d\rho'. \quad \text{(C.2)}$$

To determine the behavior of r_{ab} with respect to δ_a and δ_b, we need to express the integrand in a three-dimensional power series in ρ, δ_a and δ_b. The integrand is

$$I(\rho') = p(\theta_a+\delta_a,\theta_b+\delta_b,\rho') + p(\theta_a+\delta_a,-\theta_b+\delta_b,\rho') + p(-\theta_a+\delta_a,\theta_b+\delta_b,\rho') + p(-\theta_a+\delta_a,-\theta_b+\delta_b,\rho') \quad \text{(C.3)}$$

and its expansion in ρ' is nearly identical to that in section A. The Taylor series expansion is

$$I(\rho') = I(0) + I^{(1)}(0)\rho' + \frac{1}{2!}I^{(2)}(0)\rho'^2 + \frac{1}{3!}I^{(3)}(0)\rho'^3 + \frac{1}{4!}I^{(4)}(0)\rho'^4 + \ldots \quad \text{(C.4)}$$

What remains is to determine the two-dimensional Taylor series in δ_a and δ_b of each of the terms of the integrand. Throughout it is assumed that δ_a and δ_b are $O(\delta)$ and the Taylor series are generally truncated beyond $O\left(\delta^2\right)$.

The first term of $I\left(\rho'\right)$ is

$$I\left(0\right) = p(\theta_a + \delta_a, \theta_b + \delta_b, 0) + p(\theta_a + \delta_a, -\theta_b + \delta_b, 0) + \\ p(-\theta_a + \delta_a, \theta_b + \delta_b, 0) + p(-\theta_a + \delta_a, -\theta_b + \delta_b, 0) \quad \text{(C.5)}$$

There are four instances of a term with the form $p(x + a, y + b, 0)$, where $x = \pm\theta_a$, $y = \pm\theta_b$, $a = \delta_a$, $b = \delta_b$. The two-dimensional Taylor series about x and y will be derived then applied to the above.

The expression $p(x + a, y + b, 0)$ is the product of two standard normal pdfs: $p(x + a, y + b, 0) = Z(x + a)Z(y + b)$, where $Z(x) = \frac{1}{\sqrt{2\pi}}e^{-x^2/2}$ is the standard normal curve [1, (26.2.1)]. The Taylor series of this product is

$$p(x + a, y + b, 0) = Z(x)Z(y) + Z^{(1)}(x)Z(y)a + Z(x)Z^{(1)}(y)b + \\ \frac{1}{2!}\left[Z^{(2)}(x)Z(y)a^2 + 2Z^{(1)}(x)Z^{(1)}(y)ab + Z(x)Z^{(2)}(y)b^2\right] + \ldots \quad \text{(C.6)}$$

The derivatives $Z^{(n)}(x)$ of the standard normal pdf can be expressed in terms of Hermite polynomials [1, (26.2.32)]:

$$Z^{(n)}(x) = (-1)^{-n}2^{-n/2}Z(x)H_n(\frac{x}{\sqrt{2}}), \quad \text{(C.7)}$$

where the first three Hermite polynomials are $H_0(x) = 1$, $H_1(x) = 2x$, and $H_2(x) = 4x^2 - 2$. For example, the second derivative of $Z(x)$ is

$$\begin{aligned} Z^{(2)}(x) &= (-1)^{-2}2^{-2/2}Z(x)H_2(\frac{x}{\sqrt{2}}) \\ &= Z(x)\left(x^2 - 1\right) \end{aligned} \quad \text{(C.8)}$$

Substituting these results into (C.5), the first term of the integrand is

$$
\begin{aligned}
I\left(0\right) = {} & Z(\theta_a)Z(\theta_b) + Z^{(1)}(\theta_a)Z(\theta_b)\delta_a + Z(\theta_a)Z^{(1)}(\theta_b)\delta_b + \\
& \frac{1}{2!}\left[Z^{(2)}(\theta_a)Z(\theta_b)\delta_a^2 + 2Z^{(1)}(\theta_a)Z^{(1)}(\theta_b)\delta_a\delta_b + Z(\theta_a)Z^{(2)}(\theta_b)\delta_b^2\right] + \\
& Z(\theta_a)Z(\theta_b) + Z^{(1)}(\theta_a)Z(\theta_b)\delta_a - Z(\theta_a)Z^{(1)}(\theta_b)\delta_b + \\
& \frac{1}{2!}\left[Z^{(2)}(\theta_a)Z(\theta_b)\delta_a^2 - 2Z^{(1)}(\theta_a)Z^{(1)}(\theta_b)\delta_a\delta_b + Z(\theta_a)Z^{(2)}(\theta_b)\delta_b^2\right] + \\
& Z(\theta_a)Z(\theta_b) - Z^{(1)}(\theta_a)Z(\theta_b)\delta_a + Z(\theta_a)Z^{(1)}(\theta_b)\delta_b + \\
& \frac{1}{2!}\left[Z^{(2)}(\theta_a)Z(\theta_b)\delta_a^2 - 2Z^{(1)}(\theta_a)Z^{(1)}(\theta_b)\delta_a\delta_b + Z(\theta_a)Z^{(2)}(\theta_b)\delta_b^2\right] + \\
& Z(\theta_a)Z(\theta_b) - Z^{(1)}(\theta_a)Z(\theta_b)\delta_a - Z(\theta_a)Z^{(1)}(\theta_b)\delta_b + \\
& \frac{1}{2!}\left[Z^{(2)}(\theta_a)Z(\theta_b)\delta_a^2 + 2Z^{(1)}(\theta_a)Z^{(1)}(\theta_b)\delta_a\delta_b + Z(\theta_a)Z^{(2)}(\theta_b)\delta_b^2\right] + \ldots
\end{aligned}
\tag{C.9}
$$

Because $Z(x)$ and $H_2(x)$ are even functions, $Z^{(2)}(x)$ is also even; conversely, $H_1(x)$ is odd, which makes $Z^{(1)}(x)$ odd. This allows the above to be greatly simplified:

$$
\begin{aligned}
I\left(0\right) &= 4\left(Z(\theta_a)Z(\theta_b) + \frac{1}{2!}\left[Z^{(2)}(\theta_a)Z(\theta_b)\delta_a^2 + Z(\theta_a)Z^{(2)}(\theta_b)\delta_b^2\right]\right) + \ldots \\
&= 4p(x,y,0)\left(1 - \frac{1}{2}\left[\left(1-\theta_a^2\right)\delta_a^2 + \left(1-\theta_b^2\right)\delta_b^2\right]\right) + O(\delta^3)
\end{aligned}
\tag{C.10}
$$

The second term in the Taylor series of $I\left(\rho'\right)$ is

$$
\begin{aligned}
I^{(1)}\left(0\right)\rho' = {} & \left[\frac{\partial}{\partial\rho}p(\theta_a+\delta_a,\theta_b+\delta_b,\rho)\bigg|_{\rho=0} + \frac{\partial}{\partial\rho}p(\theta_a+\delta_a,-\theta_b+\delta_b,\rho)\bigg|_{\rho=0} + \right. \\
& \left. \frac{\partial}{\partial\rho}p(-\theta_a+\delta_a,\theta_b+\delta_b,\rho)\bigg|_{\rho=0} + \frac{\partial}{\partial\rho}p(-\theta_a+\delta_a,-\theta_b+\delta_b,\rho)\bigg|_{\rho=0}\right]\rho'
\end{aligned}
\tag{C.11}
$$

The first partial derivative with respect to ρ, evaluated at zero, of the bivariate normal pdf is

$$
\begin{aligned}
\frac{\partial}{\partial\rho}p(\theta_a,\theta_b,\rho)\bigg|_{\rho=0} &= p(\theta_a,\theta_b,0)\theta_a\theta_b \\
&= \theta_a Z(\theta_a)\theta_b Z(\theta_b)
\end{aligned}
\tag{C.12}
$$

Thus,

$$
\begin{aligned}
I^{(1)}(0) = {} & (\theta_a+\delta_a)Z(\theta_a+\delta_a)(\theta_b+\delta_b)Z(\theta_b+\delta_b) + \\
& (\theta_a+\delta_a)Z(\theta_a+\delta_a)(-\theta_b+\delta_b)Z(-\theta_b+\delta_b) + \\
& (-\theta_a+\delta_a)Z(-\theta_a+\delta_a)(\theta_b+\delta_b)Z(\theta_b+\delta_b) + \\
& (-\theta_a+\delta_a)Z(-\theta_a+\delta_a)(-\theta_b+\delta_b)Z(-\theta_b+\delta_b) \\
= {} & [(\theta_a+\delta_a)Z(\theta_a+\delta_a)+(-\theta_a+\delta_a)Z(-\theta_a+\delta_a)] \times \\
& [(\theta_b+\delta_b)Z(\theta_b+\delta_b)+(-\theta_b+\delta_b)Z(-\theta_b+\delta_b)]
\end{aligned}
\tag{C.13}
$$

Next, consider the expression $(\theta_\alpha+\delta_\alpha)Z(\theta_\alpha+\delta_\alpha)+(-\theta_\alpha+\delta_\alpha)Z(-\theta_\alpha+\delta_\alpha)$ by expanding the standard normal pdfs in one dimensional Taylor series:

$$
\begin{aligned}
& (\theta_\alpha+\delta_\alpha)\left[Z(\theta_\alpha)+Z^{(1)}(\theta_\alpha)\delta_\alpha+\frac{1}{2!}Z^{(2)}(\theta_\alpha)\delta_\alpha+\ldots\right] + \\
& \quad (-\theta_\alpha+\delta_\alpha)\left[Z(-\theta_\alpha)+Z^{(1)}(-\theta_\alpha)\delta_\alpha+\frac{1}{2!}Z^{(2)}(-\theta_\alpha)\delta_\alpha^2+\ldots\right] \\
& \quad = \theta_\alpha\left[Z(\theta_\alpha)+Z^{(1)}(\theta_\alpha)\delta_\alpha+\frac{1}{2!}Z^{(2)}(\theta_\alpha)\delta_\alpha^2+\ldots\right] \\
& \qquad - \theta_\alpha\left[Z(\theta_\alpha)-Z^{(1)}(\theta_\alpha)\delta_\alpha+\frac{1}{2!}Z^{(2)}(\theta_\alpha)\delta_\alpha^2+\ldots\right] \\
& \quad + \delta_\alpha\left[Z(\theta_\alpha)+Z^{(1)}(\theta_\alpha)\delta_\alpha+\frac{1}{2!}Z^{(2)}(\theta_\alpha)\delta_\alpha^2+\ldots\right] \\
& \qquad + \delta_\alpha\left[Z(\theta_\alpha)-Z^{(1)}(\theta_\alpha)\delta_\alpha+\frac{1}{2!}Z^{(2)}(\theta_\alpha)\delta_\alpha^2+\ldots\right] \\
& \quad = \theta_\alpha\left(2Z^{(1)}(\theta_\alpha)\delta_\alpha+\ldots\right)+2\delta_\alpha\left[Z(\theta_\alpha)+\frac{1}{2!}Z^{(2)}(\theta_\alpha)\delta_\alpha^2+\ldots\right] \\
& = Z(\theta_\alpha)\delta_\alpha\left(1-2\theta_\alpha^2\right)+O\left(\delta_\alpha^3\right)
\end{aligned}
\tag{C.14}
$$

Finally, substituting the above series into the a and b terms of (C.13) yields the following:

$$
I^{(1)}(0) = 2\delta_a\delta_b p(\theta_a,\theta_b,0)\left(1-2\theta_a^2\right)\left(1-2\theta_b^2\right)+O(\delta^3) \tag{C.15}
$$

The third term in the series expansion of $I\left(\rho'\right)$ contains

$$
\begin{aligned}
I^{(2)}(0) = & \left[(\theta_a+\delta_a)^2-1\right] Z(\theta_a+\delta_a)\left[(\theta_b+\delta_b)^2-1\right] Z(\theta_b+\delta_b) + \\
& \left[(\theta_a+\delta_a)^2-1\right] Z(\theta_a+\delta_a)\left[(-\theta_b+\delta_b)^2-1\right] Z(-\theta_b+\delta_b) + \\
& \left[(-\theta_a+\delta_a)^2-1\right] Z(-\theta_a+\delta_a)\left[(\theta_b+\delta_b)^2-1\right] Z(\theta_b+\delta_b) + \\
& \left[(-\theta_a+\delta_a)^2-1\right] Z(-\theta_a+\delta_a)\left[(-\theta_b+\delta_b)^2-1\right] Z(-\theta_b+\delta_b) \\
= & \left[\left(\theta_a^2+2\theta_a\delta_a+\delta_a^2-1\right) Z(\theta_a+\delta_a)+\left(\theta_a^2-2\theta_a\delta_a+\delta_a^2-1\right) Z(-\theta_a+\delta_a)\right] \times \\
& \left[\left(\theta_b^2+2\theta_b\delta_b+\delta_b^2-1\right) Z(\theta_b+\delta_b)+\left(\theta_b^2-2\theta_b\delta_b+\delta_b^2-1\right) Z(-\theta_b+\delta_b)\right]
\end{aligned}
\tag{C.16}
$$

Consider the following expression by expanding Z in a power series:

$$
\begin{aligned}
& \left(\theta_\alpha^2+2\theta_\alpha\delta_\alpha+\delta_\alpha^2-1\right) Z(\theta_\alpha+\delta_\alpha)+\left(\theta_\alpha^2-2\theta_\alpha\delta_\alpha+\delta_\alpha^2-1\right) Z(-\theta_\alpha+\delta_\alpha) \\
= & \left(\theta_\alpha^2+2\theta_\alpha\delta_\alpha+\delta_\alpha^2-1\right)\left[Z(\theta_\alpha)+Z^{(1)}(\theta_\alpha)\delta_\alpha+\frac{1}{2!}Z^{(2)}(\theta_\alpha)\delta_\alpha^2+\ldots\right]+ \\
& \left(\theta_\alpha^2-2\theta_\alpha\delta_\alpha+\delta_\alpha^2-1\right)\left[Z(-\theta_\alpha)+Z^{(1)}(-\theta_\alpha)\delta_\alpha+\frac{1}{2!}Z^{(2)}(-\theta_\alpha)\delta_\alpha^2+\ldots\right] \\
= & 2\left(\theta_\alpha^2+\delta_\alpha^2-1\right)\left[Z(\theta_\alpha)+\frac{1}{2!}Z^{(2)}(\theta_\alpha)\delta_\alpha^2+\ldots\right]+4\theta_\alpha\delta_\alpha\left[Z^{(1)}(\theta_\alpha)\delta_\alpha+\ldots\right]+ \\
= & 2\left(\theta_\alpha^2+\delta_\alpha^2-1\right)\left[Z(\theta_\alpha)+\frac{1}{2!}Z(\theta_\alpha)\left(\theta_\alpha^2-1\right)\delta_\alpha^2\right]+8\theta_\alpha\delta_\alpha\theta_\alpha Z(\theta_\alpha)\delta_\alpha+\ldots \\
= & Z\left(\theta_\alpha\right)\left(\left(\theta_\alpha^2-1\right)\delta_\alpha^4+\left(6\theta_\alpha^2+\theta_\alpha^4+3\right)\delta_\alpha^2+2\theta_\alpha^2-2\right)+\ldots
\end{aligned}
\tag{C.17}
$$

Substituting the above result into (C.16) produces,

$$
\begin{aligned}
I^{(2)}(0) = p\left(\theta_a,\theta_b,0\right)\left[\left(6\theta_a^2+\theta_a^4+3\right)\delta_a^2+2\theta_a^2-2\right] \times \\
\left[\left(6\theta_b^2+\theta_b^4+3\right)\delta_b^2+2\theta_b^2-2\right]+O\left(\delta^4\right)
\end{aligned}
\tag{C.18}
$$

Combining and integrating the first three terms of the integrand (C.10), (C.15), and

(C.18) results in

$$
\begin{aligned}
r_{ab} = {} & r_{ab}|_{\rho=0} + 4p(\theta_a,\theta_b,0)\left(1-\frac{1}{2}\left[\left(1-\theta_a^2\right)\delta_a^2+\left(1-\theta_b^2\right)\delta_b^2\right]\right)\rho + \\
& \delta_a\delta_b p(\theta_a,\theta_b,0)\left(1-2\theta_a^2\right)\left(1-2\theta_b^2\right)\rho^2 + \\
& \frac{1}{3}p\left(\theta_a,\theta_b,0\right)\left(\left(6\theta_a^2+\theta_a^4+3\right)\delta_a^2+2\theta_a^2-2\right)\left(\left(6\theta_b^2+\theta_b^4+3\right)\delta_b^2+2\theta_b^2-2\right)\rho^3 + \\
& O\left(\rho^4,\delta^3\right) \\
& = r_{ab}|_{\rho=0} + 4p(\theta_a,\theta_b,0)\left[\rho+\frac{1}{6}\left(\theta_a^2-1\right)\left(\theta_b^2-1\right)\rho^3\right] + \\
& 4p(\theta_a,\theta_b,0)\left[-\frac{1}{2}\left[\left(1-\theta_a^2\right)\delta_a^2+\left(1-\theta_b^2\right)\delta_b^2\right]\rho + \right. \\
& \qquad\qquad \frac{1}{4}\delta_a\delta_b\left(1-2\theta_a^2\right)\left(1-2\theta_b^2\right)\rho^2 + \\
& \left. -\frac{1}{6}\left[\left(6\theta_a^2+\theta_a^4+3\right)\left(1-\theta_b^2\right)\delta_a^2+\left(1-\theta_a^2\right)\left(6\theta_b^2+\theta_b^4+3\right)\delta_b^2\right]\rho^3\right] + \\
& \qquad O\left(\rho^4,\delta^3\right)
\end{aligned}
\tag{C.19}
$$

There are two different power series in ρ that can be identified in the above. These are the ideal relationship between ρ and r and an error series caused by nonzero threshold offsets δ_a and δ_b:

$$
\begin{aligned}
r_{ab} = {} & r_{ab}|_{\rho=0} + r_{ab}|_{\delta_a=\delta_b=0} + \frac{2}{\pi}\exp\left[-\frac{1}{2}\left(\theta_a^2+\theta_b^2\right)\right]\times \\
& \left[-\frac{1}{2}\left[\left(1-\theta_a^2\right)\delta_a^2+\left(1-\theta_b^2\right)\delta_b^2\right]\rho+\frac{1}{4}\delta_a\delta_b\left(1-2\theta_a^2\right)\left(1-2\theta_b^2\right)\rho^2 + \right. \\
& \left. -\frac{1}{6}[\left(6\theta_a^2+\theta_a^4+3\right)\left(1-\theta_b^2\right)\delta_a^2+\left(1-\theta_a^2\right)\left(6\theta_b^2+\theta_b^4+3\right)\delta_b^2]\rho^3\right] + O\left(\rho^4,\delta^3\right)
\end{aligned}
\tag{C.20}
$$

APPENDIX D

Simulated Satellite Retrievals

This appendix contains the simulation results of the four data sets and three cases discussed in Chapter 7.

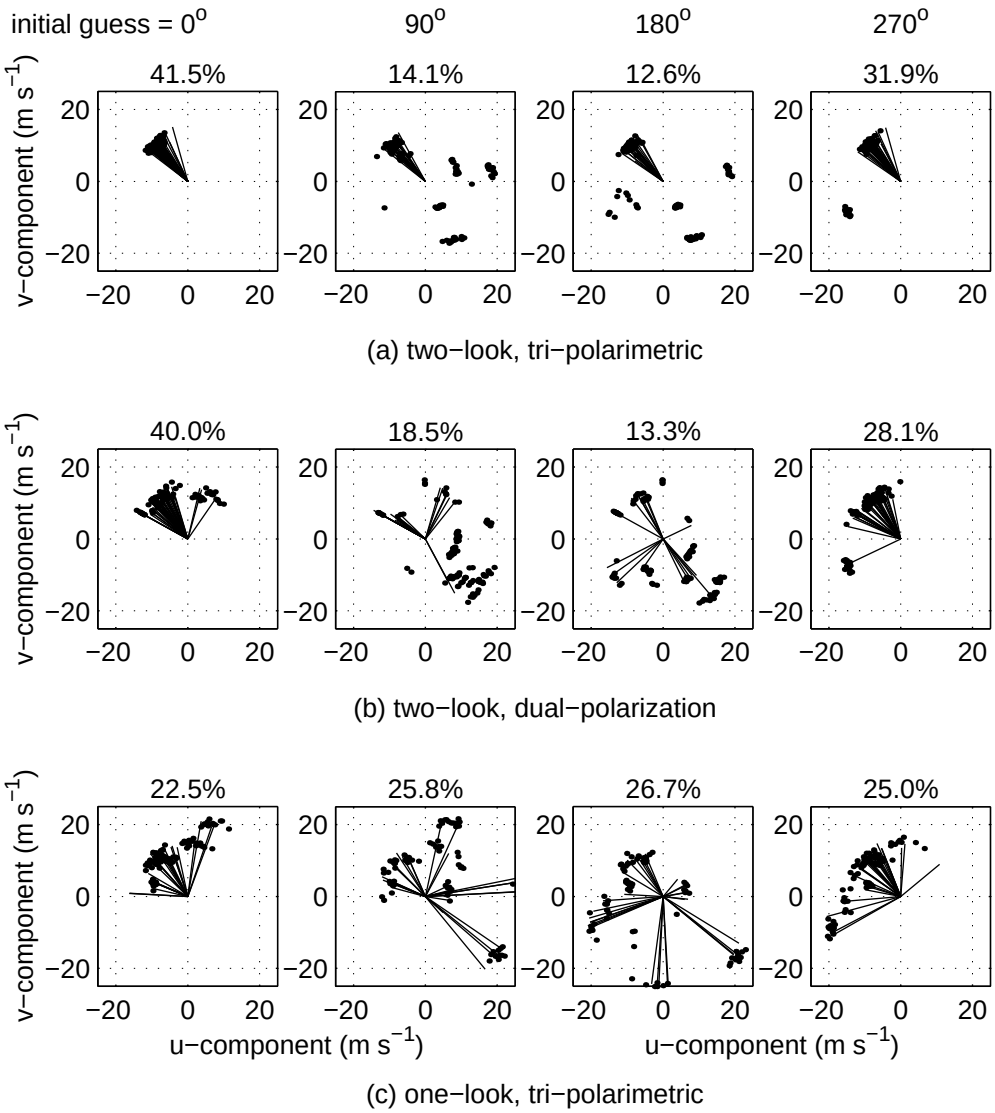

Figure D.1: Results of the four-fold search for ML solutions before ambiguity removal for data set 1. The true ML solutions are plotted as lines and the local-minima solutions denoted by individual points.

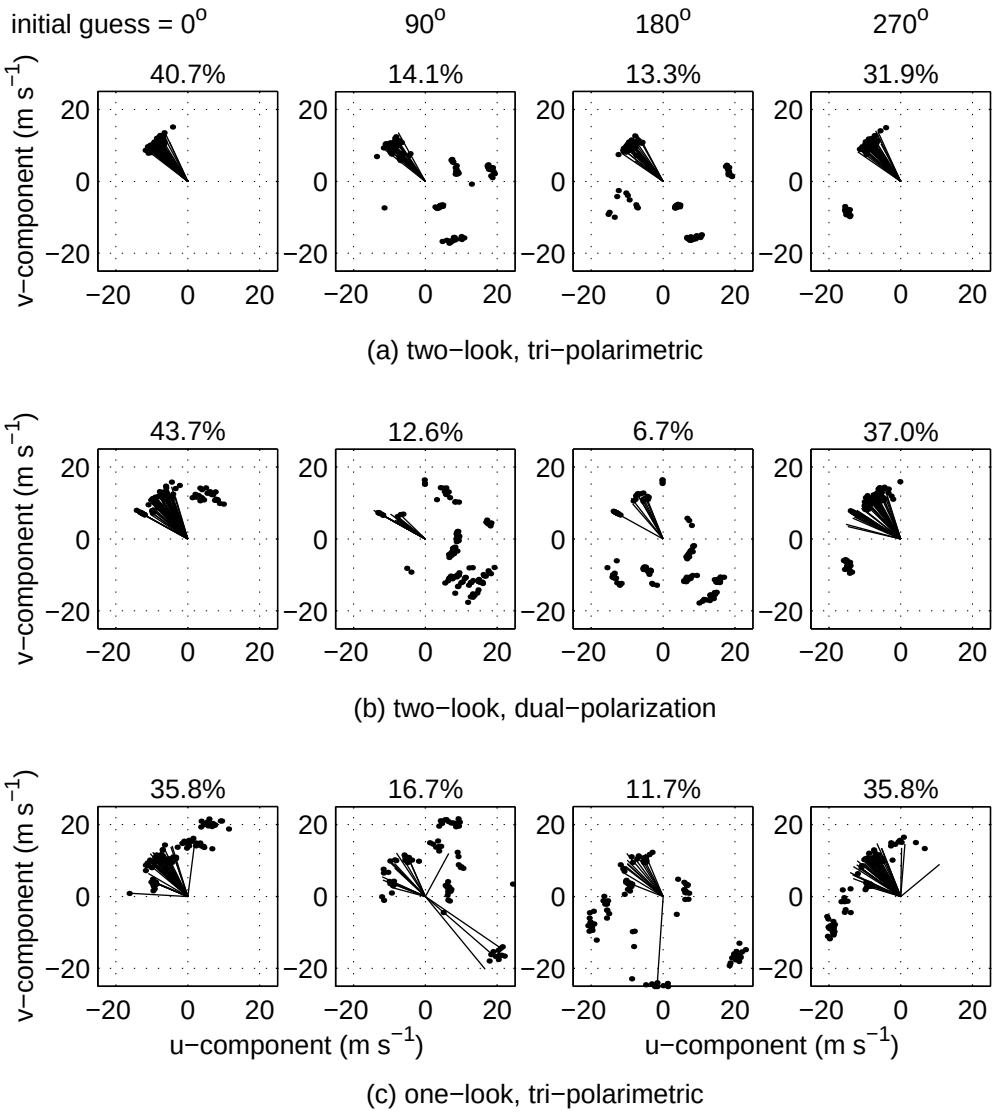

Figure D.2: Four-fold search results after ambiguity selection for data set 1. The accepted ML solutions and chosen ambiguities are plotted as lines and the rejected solutions as points.

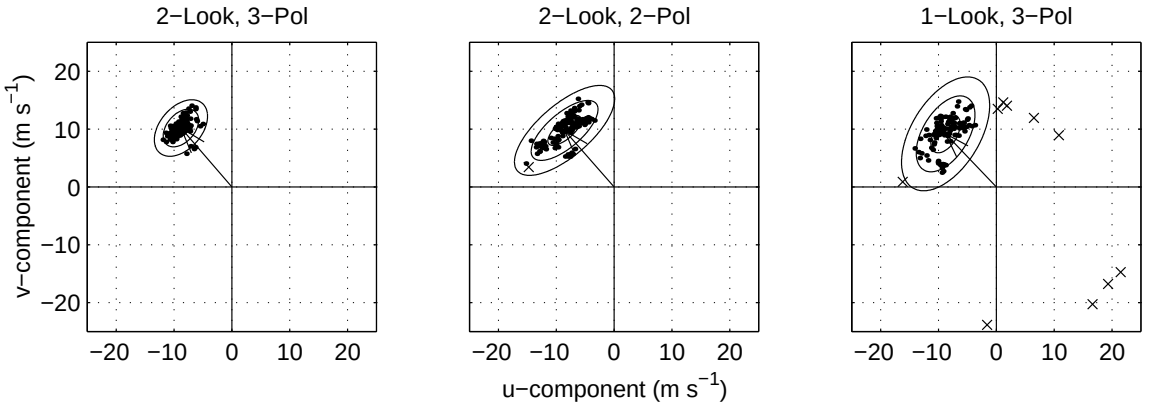

Figure D.3: Scatter plots of final retrieved wind vectors for data set 1. The final solutions (after ambiguity removal) are plotted as individual points. The unresolved ambiguities are plotted as x's. The 1-, 2-, and 3-σ contours of a fitted Gaussian (ignoring unresolved ambiguities) are plotted for reference. The mean retrieved wind vector is plotted as an arrow.

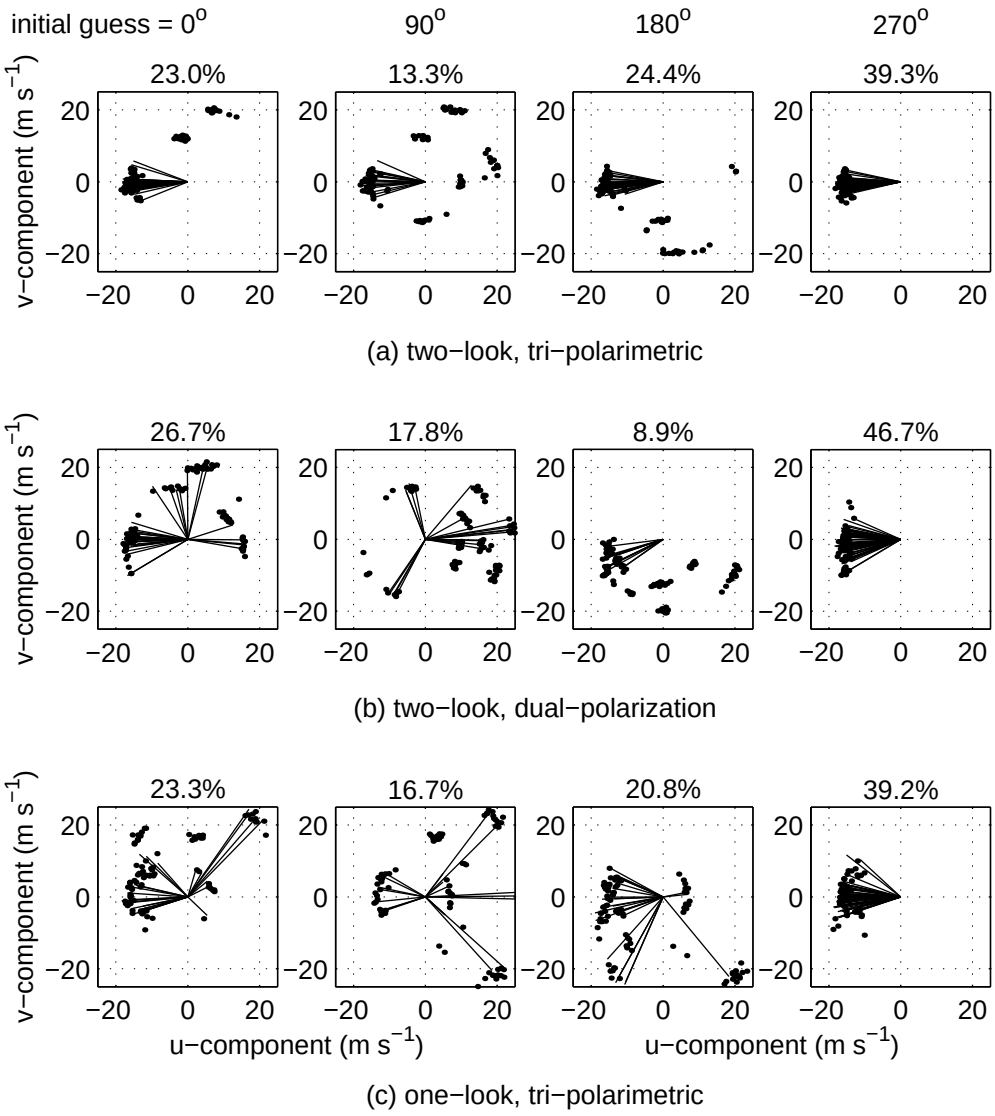

Figure D.4: Same as Figure D.1 except for data set 2.

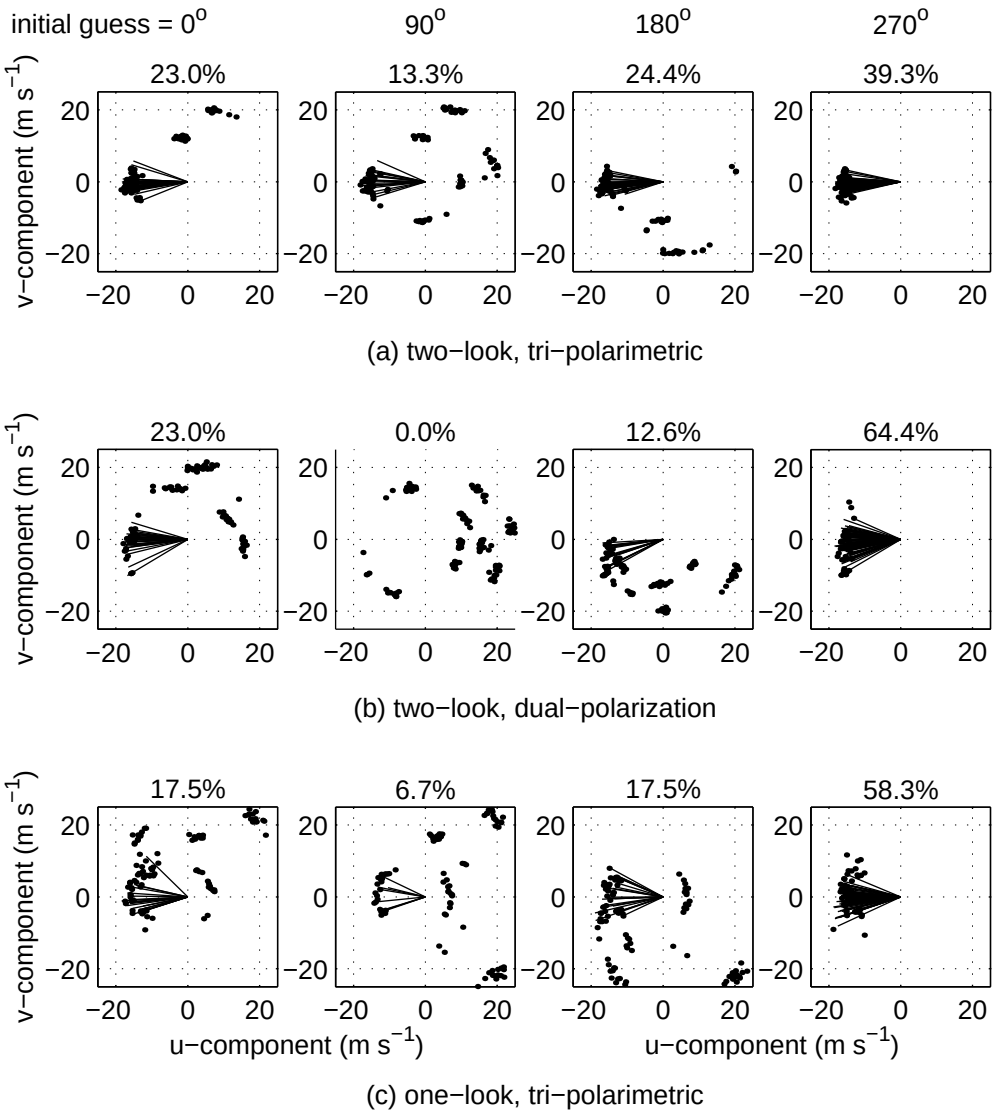

Figure D.5: Same as Figure D.2 except for data set 2.

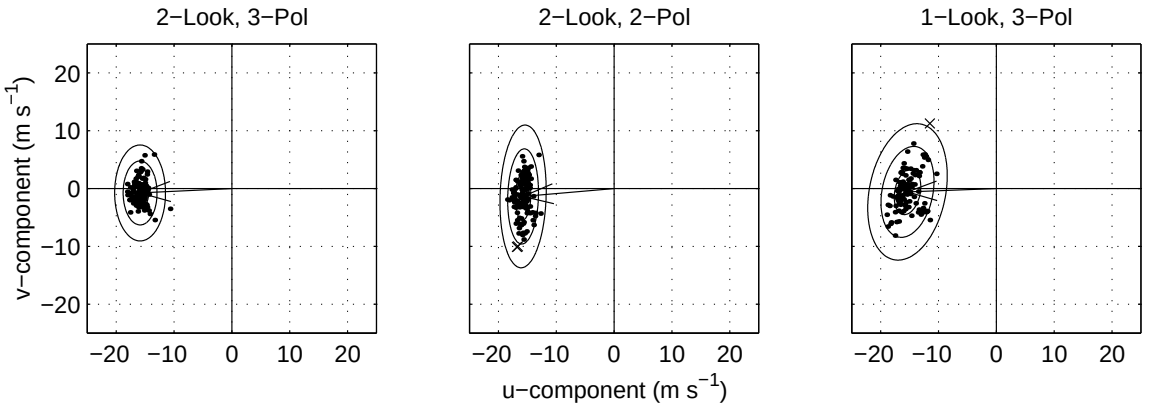

Figure D.6: Same as Figure D.3 except for data set 2.

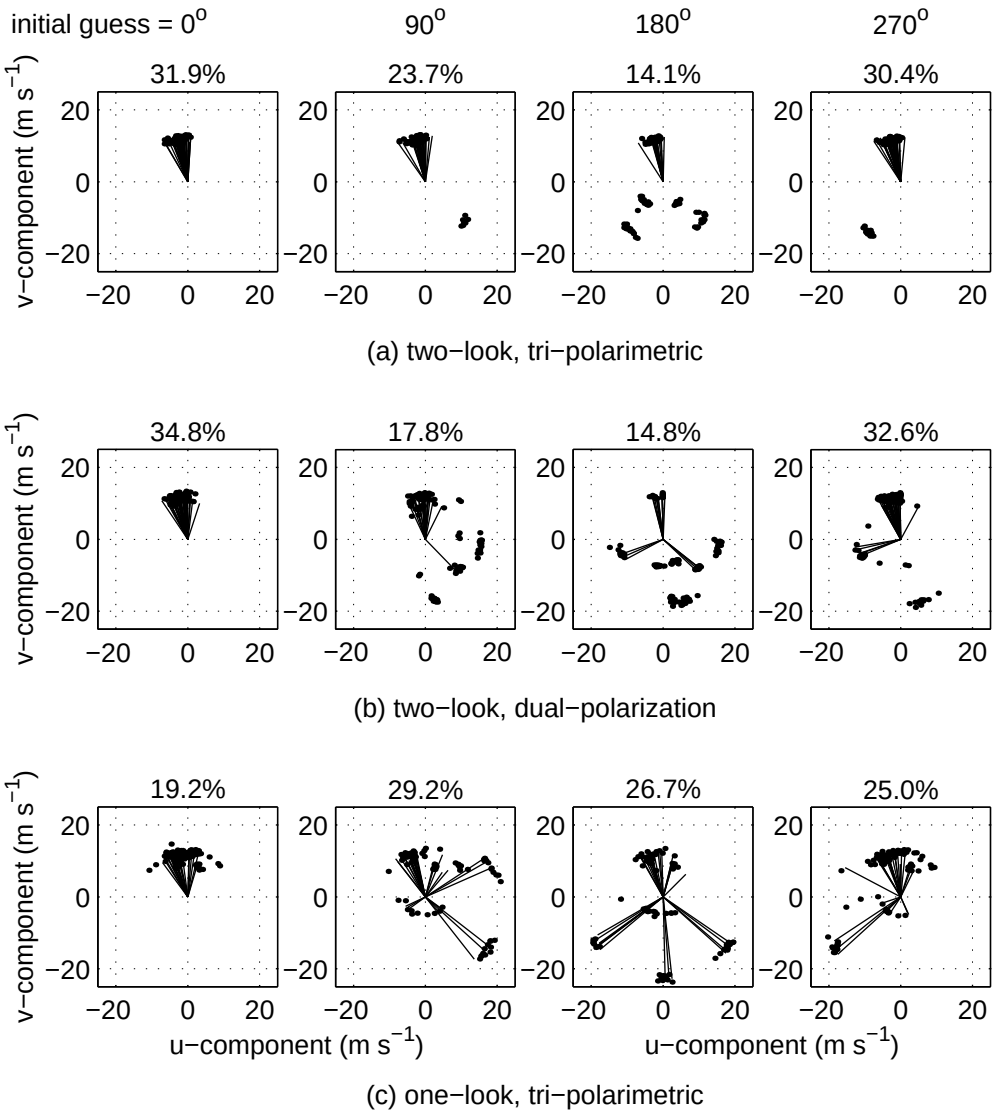

Figure D.7: Same as Figure D.1 except for data set 3.

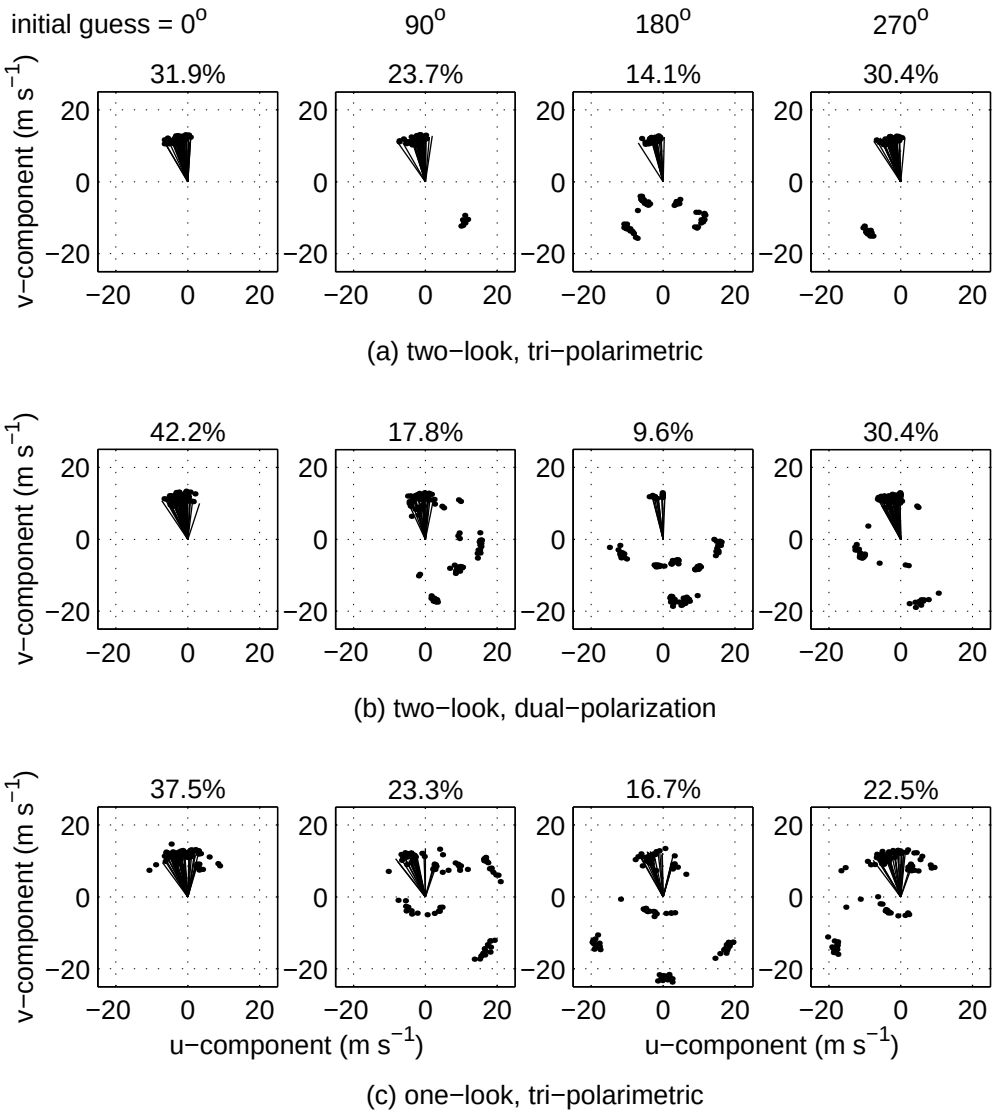

Figure D.8: Same as Figure D.2 except for data set 3.

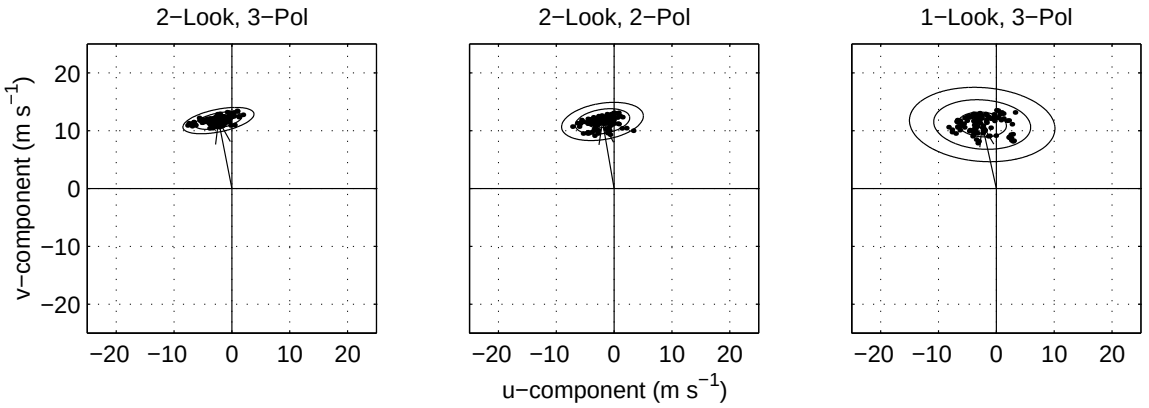

Figure D.9: Same as Figure D.3 except for data set 3.

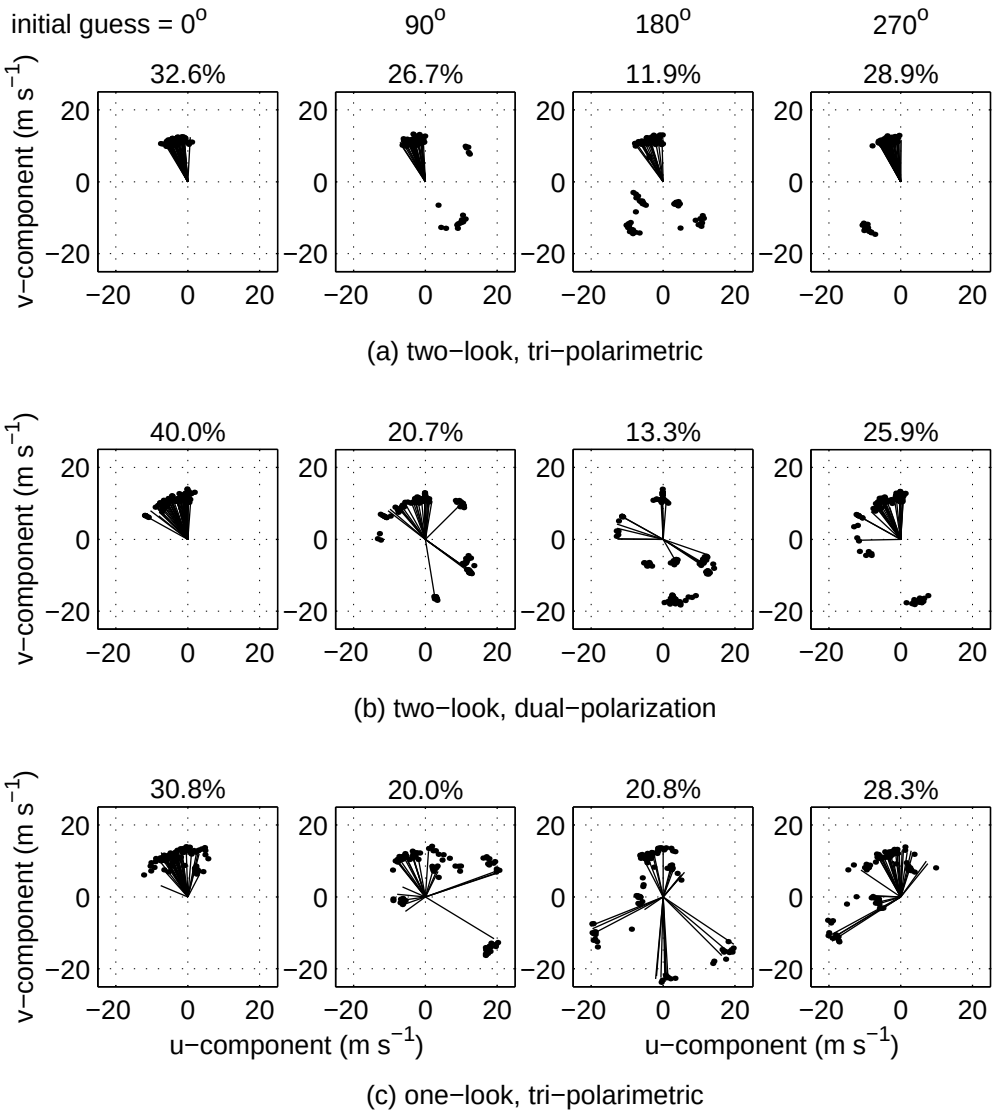

Figure D.10: Same as Figure D.1 except for data set 4.

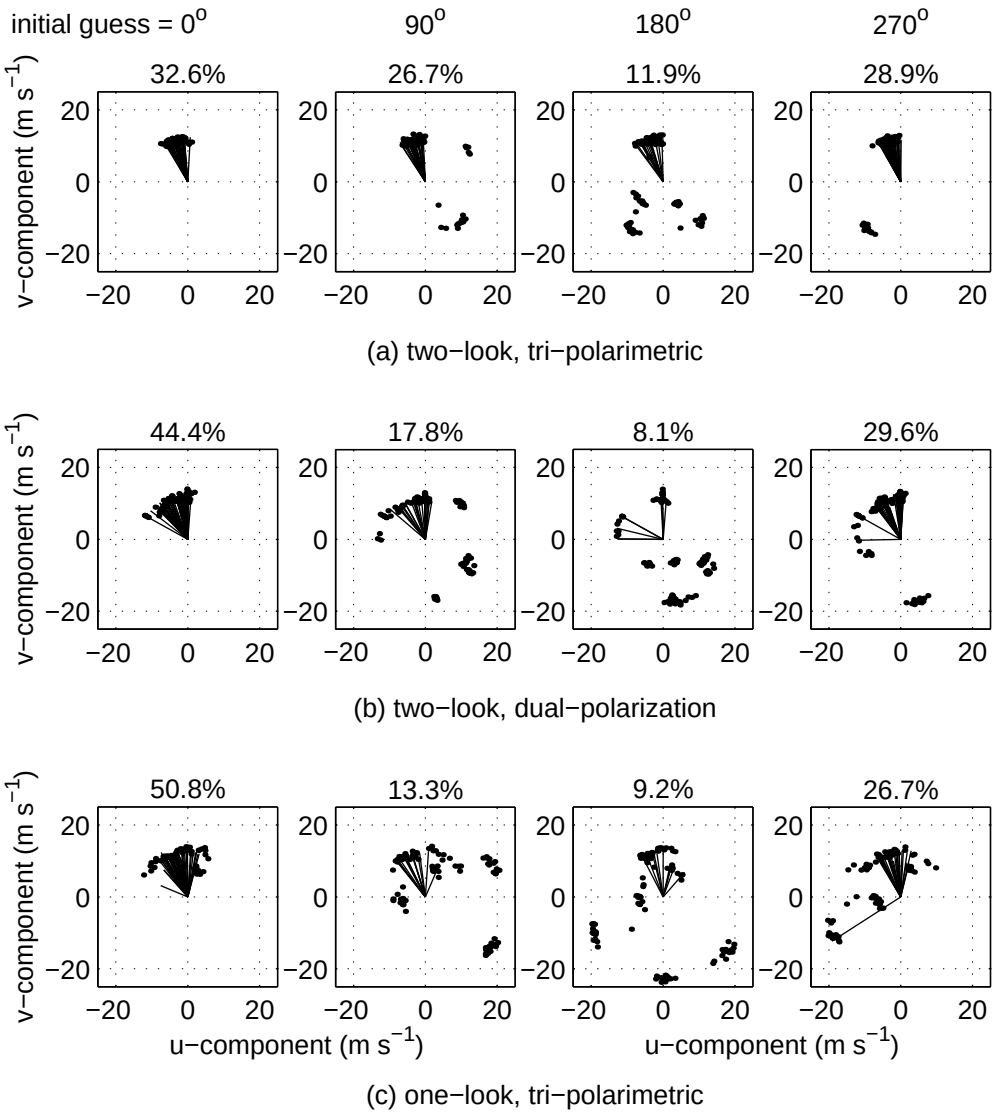

Figure D.11: Same as Figure D.2 except for data set 4.

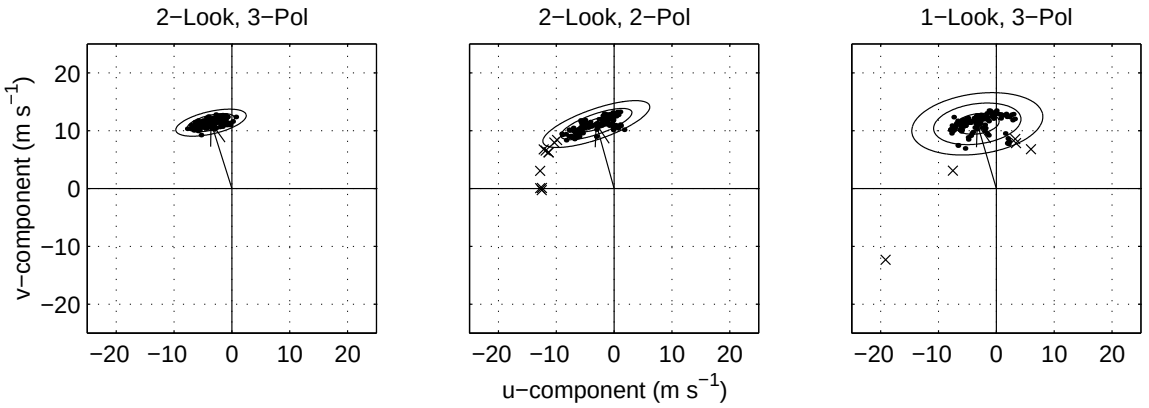

Figure D.12: Same as Figure D.3 except for data set 4.

Bibliography

[1] Milton Abramowitz and Irene A. Stegun. *Handbook of Mathematical Functions*. Dover Publications, New York, 1964.

[2] L. K. Adelberg, A. J. Gasiewski, and D. M. Jackson. Optimal calibration of radiometer using wiener filters. In *Proc. Int. Geosci. and Remote Sens. Symp. (IGARSS)*, page 1444, Tokyo, Japan, 1993.

[3] E.P.W. Attema and P. Lecomte. The ERS-1 and ERS-2 wind scatterometers, system performance and data products. In *Proc. Int. Geosci. and Remote Sens. Symp. (IGARSS)*, pages 1967–1969, Seattle, WA, 1998.

[4] J. J. Bates, G. A. Wick, and C. C. Gottschall. Passive microwave remote sensing of wind direction using SSM/I data. In *Proc. Int. Geosci. and Remote Sens. Symp. (IGARSS)*, pages 363–365, Seattle, WA, 1998.

[5] E. A. Bespalova *et al.*. Sea-ripple anisotropy estimates from variations in polarized thermal emission of the sea. *Soviet Physics Reports*, 246(6):1482–1485, 1979. (in Russian).

[6] Thomas Black. The new NMC mesoscale Eta-model - Description and forecast examples. *Weather and Forecasting*, 9(2):265–278, 1994.

[7] J. Canaris. NASA CERC digital correlator projects. In *Fourth NASA Symposium on VLSI Design*, Idaho Univ., 1992. N94-21708.

[8] S. Chandrasekhar. *Radiative Transfer*. Dover Publications, New York, 1960.

[9] G. Chattopadhyay *et al.*. A 96-GHz ortho-mode transducer for the Polatron. *IEEE Microwave Guided Wave Lett.*, 8(12):421–423, 1998.

[10] Robert E. Collin. *Foundations for Microwave Engineering*. McGraw-Hill, New York, 2nd edition, 1992.

[11] B. F. C. Cooper. Correlators with two-bit quantization. *Aust. J. Phys.*, 23:521–527, 1970.

[12] L. R. D'Addario *et al.*. Complex cross correlators with three-level quantization: Design tolerances. *Radio Science*, 19(3):931–945, 1984.

[13] Peter Duffett-Smith. *Practical Astronomy with Your Calculator*. Cambridge University Press, New York, 1988.

[14] M. S. Dzura *et al.*. Radiometers-polarimeters: Principles of design and applications for sea surface microwave emission polarimetry. In *Proc. Int. Geosci. and Remote Sens. Symp. (IGARSS)*, Houston, TX, 1992.

[15] V. S. Etkin *et al.*. Discovering critical phenomena under thermal microwave emission of the uneven water surface. *Radiophysics and Quantum Electronics*, 21(3):454–456, 1978. (in Russian).

[16] V. S. Etkin *et al.*. Radiohydrophysical aerospace research of ocean. Report 1749, Academy of Sciences, Space Research Institute, Moscow, Russia, 1991.

[17] P. Gaiser, G. Poe, and K. St. Germain. Critical design issues for space borne polarimetric radiometry. In *Proc. Int. Geosci. and Remote Sens. Symp. (IGARSS)*, pages 1698–1700, Seattle, WA, July 1998.

[18] P. W. Gaiser, P. Chang, and Li Li. Ocean surface wind direction retrievals using microwave polarimetric radiometer. In *Proc. Int. Geosci. and Remote Sens. Symp. (IGARSS)*, pages 1123–1125, Lincoln, NE, 1996.

[19] A. J. Gasiewski. Ocean Winds Imaging (OWI) experiment, final report on NASA/WFF Orion P-3 integration and Labrador Sea aircraft measurements. Technical report, NOAA Environmental Technology Laboratory, Boulder, CO, October 1997. Available on the World Wide Web at *http://www1.etl.noaa.gov/radiom/owi.html*.

[20] A. J. Gasiewski and D. B. Kunkee. Calibration and applications of polarization-correlating radiometers. *IEEE Trans. Microwave Theory Tech.*, 41(5):767–773, 1993.

[21] A. J. Gasiewski and D. B. Kunkee. Polarized microwave emission from water waves. *Radio Science*, 29(6):1449–1466, 1994.

[22] A. J. Gasiewski and J. R. Piepmeier. High resolution multiband passive microwave imagery of ocean surface wind features. In *Proc. Int. Geosci. and Remote Sens. Symp. (IGARSS)*, Seattle, WA, July 1998.

[23] A. J. Gasiewski and D. H. Staelin. Numerical modeling of passive microwave O_2 observations over precipitation. *Radio Science*, 25(3):217–235, 1990.

[24] A. J. Gasiewski *et al.*. Combined high-resolution active and passive imaging of ocean surface winds from aircraft. In *Proc. Int. Geosci. and Remote Sens. Symp. (IGARSS)*, pages 1001–1005, Singapore, August 1997.

[25] K. St. Germain, G. Poe, and P. Gaiser. Modeling of the polarimetric microwave signal due to ocean surface wind vector. In *Proc. Int. Geosci. and Remote Sens. Symp. (IGARSS)*, pages 2304–2306, Seattle, WA, July 1998.

[26] Jerry H. Ginsberg. *Advanced Engineering Dynamics*. Harper and Row Publishers, New York, 1988.

[27] B. S. Gohil. Extraction of ocean surface wind field from simulated ERS-1 Scatterometer data. *Int. J. Remote Sensing*, 13(17):3311–3327, 1992.

[28] Mark A. Goodberlet, Calvin T. Swift, and J. C. Wilkerson. Ocean surface wind speed measurements of the Special Sensor Microwave/Imager (SSM/I). *IEEE Trans. Geosci. Remote Sensing*, 28(5):823–827, 1990.

[29] J. E. Graf, Tsi Wu-yang, and L. Jones. Overview of QuikSCAT mission - a quick deployment of a high resolution, wide swath scanning scatterometer for ocean wind measurement. In *Proc. IEEE Southeastcon*, pages 314–317, Orlando, FL, 1998.

[30] J. B. Hagen and D. T. Farley. Digital-correlation techniques in radio science. *Radio Science*, 8(8, 9):775–784, 1973.

[31] D. W. Hawkins and D. P. Woody. A 500 mhz bandwidth, 512 lag, digital cross correlator. In *Proc. National Radio Science Meeting*, page 160, Boulder, CO, 1998.

[32] J. P. Hollinger, J. L. Pierce, and G. A. Poe. SSM/I instrument evaluation. *IEEE Trans. Geosci. Remote Sensing*, 28(5):781–790, 1990.

[33] J. P. Holman. *Heat Transfer*. McGraw-Hill, Inc., New York, 7th edition, 1990.

[34] James R. Holton. *An Introduction to Dynamic Meteorology*. Academic Press, New York, 3rd edition, 1992.

[35] V. G. Irisov, A. V. Kuzmin, M. N. Pospelov, Y. G. Trokhimovsky, and V. S. Etkin. The dependence of sea brightness temperature on surface wind direction and speed: Theory and experiment. In *Proc. Int. Geosci. and Remote Sens. Symp. (IGARSS)*, pages 1297–1300, Espoo, Finland, 1991.

[36] David M. Jackson. *Calibration of Millimeter-Wave Radiometers with Application to Clear-Air Remote Sensing of the Atmosphere*. Ph.D. thesis, Georgia Institute of Technology, 1999.

[37] L. A. Klein and C. T. Swift. An improved model for the dielectric constant of sea water at microwave frequencies. *IEEE Trans. Antennas and Propagation*, 25(1):104–111, 1977.

[38] John D. Kraus. *Radio Astronomy*. Cygnus-Quasar Books, Powell, Ohio, 2nd edition, 1986.

[39] Yu. A. Kravstov *et al.*. Critcal effects in the thermal radiation of a perdiodically uneven water surface. *Atmospheric and Oceanic Physics*, 14(7):733–739, 1978. (in Russian).

[40] S. R. Kulkarni and C. Heiles. How to obtain the true correlation from a 3-level digital correlator. *The Astronomical Journal*, 85(10):1413–1420, October 1980.

[41] D. B. Kunkee and A. J. Gasiewski. Simulation of passive microwave wind direction signatures over the ocean using an asymmetric-wave geometrical optics model. *Radio Science*, 32(1):59–77, 1997.

[42] David B. Kunkee. *Polarimetric millimeter-wave thermal emission from anisotropic water surfaces: Application to remote sensing of ocean surface wind direction*. Ph.D. thesis, Georgia Institute of Technology, 1995.

[43] P. H. LeBlond and L. A. Mysak, editors. *Waves in the Ocean*. Elsevier Scientific Pub. Co., New York, 1978.

[44] J. R. Miller, J. E. Geyser, A. T. C. Chang, and T. T. Wilheit. Observations of oceanic surface-wind fields from the Nimbus-7 microwave radiometer. *IEEE Trans. Geosci. Remote Sensing*, 20(4):549–554, 1982.

[45] F. M. Naderi, M. H. Freilich, and D. G. Long. Spaceborne radar measurement of wind velocity over the ocean – an overview of the NSCAT scatterometer system. *Proc. of the IEEE*, 79(6):850–866, June 1991.

[46] S. K. Okumura, M. Momose, T. Tsutsumi, and N. Kawaguchi. 1-GHz bandwidth digital spetro-correlator system for Nobeyama millimeter array. In *Proc. National Radio Science Meeting*, page 162, Boulder, CO, 1998.

[47] S. Padin *et al.*. High-speed digital correlator for radio astronomy. *IEEE Trans. Instr. Measure.*, 42(4):793–798, 1993.

[48] J. R. Piepmeier and A. J. Gasiewski. Polarimetric scanning radiometer for airborne microwave imaging studies. In *Proc. Int. Geosci. and Remote Sens. Symp. (IGARSS)*, pages 1688–1691, University of Nebraska, Lincoln, NE, 1996.

[49] J. R. Piepmeier and A. J. Gasiewski. Digital correlation polarimetry: Analysis and demonstration. *in preparation*, 1999.

[50] J. R. Piepmeier *et al.*. Ocean surface wind direction measurement by scanning polarimetric microwave radiometry. In *Proc. Int. Geosci. and Remote Sens. Symp. (IGARSS)*, volume 5, pages 2307–2310, Seattle, WA, July 1998.

[51] R. Price. A useful theorem for nonlinear devices having gaussian inputs. *IRE Trans. Info. Theory*, 4:69–72, 1958.

[52] Peter Schluessel and Hans Luthardt. Surface wind speeds over the North Sea from Special Sensor Microwave/Imager observations. *J. Geophys. Res.*, 96(C3):4845–4853, 1991.

[53] H. Schultz. A circular median filter approach for resolving directional ambiguities in wind fields retrieved from spaceborne scatterometer data. *J. Geophys. Res.*, 95(C4):5291–5303, 1990.

[54] Henry Stark and John W. Woods. *Probability, Random Processes, and Estimation Theory for Engineers*. Prentice Hall, Englewood Cliffs, N.J., 2nd edition, 1994.

[55] A. Stoffelen and D. Anderson. Ambiguity removal and assimilation of scatterometer data. *Quarterly J. Royal Meteorological Society*, 123(538):491–518, 1997.

[56] A. Stogryn. The apparent temperature of the sea at microwave frequencies. *IEEE Trans. Antennas and Propagation*, 15(2):278–286, 1967.

[57] Gilbert Strang. *Linear Algebra and Its Applications*. Harcourt, Brace, Jovanovich, San Diego, 3rd edition, 1988.

[58] Alan Stuart and J. Keith Ord. *Kendall's Advanced Theory of Statistics*, volume 2. Oxford University Press, New York, 5th edition, 1991.

[59] C. Timoc and T. Tran. Digital correlation spectrometer with 1 GHz sampling rate. In *Proc. National Radio Science Meeting*, page 161, Boulder, CO, 1998.

[60] L. Tsang, J. A. Kong, and R. T. Shin. *Theory of Microwave Remote Sensing*. John Wiley and Sons, New York, 1985.

[61] F. T. Ulaby, R. K. Moore, and A. K. Fung. *Microwave Remote Sensing: Active and Passive*. Addison-Wesley Pub. Co., Reading, Mass., 1986.

[62] Harry L. Van Trees. *Detection, Estimation, and Modulation Theory*. Wiley, New York, 1968.

[63] D. Vandemark, F. C. Jackson, E. J. Walsh, and B. Chapron. Airborne measurements of ocean wave spectra and wind speed during the Grand Banks ERS-1 SAR Wave Experiment. *Atmosphere-Ocean*, 32(1):143–178, 1994.

[64] S. Weinreb. Digital radiometer. *Proc. IEEE*, 49(6):1099, 1961.

[65] F. J. Wentz. A two-scale scattering model for foam-free sea microwave brightness temperatures. *J. Geophys. Res.*, 80(24):3441–3446, 1975.

[66] F. J. Wentz. Measurement of oceanic wind vector using satellite microwave radiometers. *IEEE Trans. Geosci. Remote Sensing*, 30(5):960–972, 1992.

[67] T. T. Wilheit. A model for the microwave emissivity of the ocean's surface as a function of wind speed. *IEEE Trans. Geosci. Electron.*, 17(4):244–249, 1979.

[68] C. Wu *et al.*. The SeaWinds scatterometer instrument. In *Proc. Int. Geosci. and Remote Sens. Symp. (IGARSS)*, pages 1511–1515, Pasadena, CA, 1994.

[69] S. Yueh, W. Wilson, F. Li, S. Dinardo, and F. Li. Polarimetric microwave brightness signatures of ocean wind directions. *IEEE Trans. Geosci. Remote Sensing*, 37(2):949–959, 1999.

[70] S. Yueh, W. Wilson, F. Li, S. Nghiem, and W. Ricketts. Polarimetric measurements of sea surface brightness temperatures using an aircraft K-band radiometer. *IEEE Trans. Geosci. Remote Sensing*, 33(1):85–92, 1995.

[71] S. Yueh, W. Wilson, S. Nghiem, F. Li, and W. Ricketts. Polarimetric passive remote sensing of ocean wind vectors. In *Proc. Int. Geosci. and Remote Sens. Symp. (IGARSS)*, pages 2416–2418, Pasadena, CA, 1994.